

---

# Theoretical approaches to realistic strongly correlated nanosystems

Malte Schüler

---



Bremen 2016



---

# Theoretical approaches to realistic strongly correlated nanosystems

Malte Schüler

---

Dissertation  
an dem Institut für theoretische Physik  
der Universität  
Bremen

vorgelegt von  
Malte Schüler  
aus Lübeck

Bremen, den 27. April 2016

Erstgutachter: Prof. Tim Wehling

Zweitgutachter: Prof. Gerd Czycholl

Tag der mündlichen Prüfung: 23. Juni 2016



... a tymczasem myśmy do niego nawet nie weszli. Skazani do końca na domysł, odłamawszy z pieczętujących go zamknięć kilka okruchów, zachwycaliśmy się blaskiem, jakim, roztrzaskane, pozłociły nam końce palców.

... whereas in fact we did not get as far as the entrance. Doomed forever to conjecture, having chipped a few flecks from the lock that seals the gate, we delighted in the glitter that gilded our fingertips.

... dabei haben wir es nicht einmal betreten. Bis zuletzt auf Vermutungen angewiesen, haben wir ein paar Splitter von den Siegeln abgekrazt, die es verschließen, und uns an dem Glanz entzückt, der uns, als wir sie zerrieben hatten, die Fingerkuppen vergoldete.

Stanisław Lem [130, 129, 128]



# Abstract

Recent developments in methods and computational power render it possible to realistically simulate nanoscopic systems such as surfaces, two-dimensional materials, and nanodots including strong electronic correlations. Nanoscopic structuring enables the tailoring of the electronic structure which can be the basis of future electronic devices. This thesis addresses method developments and applications at the interface of ab-initio methods and model based many-body methods for the case of nanoscopically structured systems with strong correlations.

In contrast to bulk materials, low-dimensional materials exhibit long-range interactions due to reduced screening. In this work, the general question how these long-range interactions affect electronic properties is investigated. To this end, a variational approach which approximates models with long-range interactions by models with only local interactions is introduced. For the case of an ab-initio derived model of graphene it is found that nonlocal interactions stabilize the semimetallic phase. The quality of this approach is discussed using a simple test case.

Realistic models of interacting impurities embedded in an extended solid involve a large amount of bath sites and low symmetries regarding the impurity, which renders an exact treatment impossible. A variational algorithm is presented which optimizes corresponding exactly solvable effective models. Thus, the method is a proposition to an unambiguous solution of the so-called bath-discretization problem in exact diagonalization approaches to the Anderson impurity model. The method is benchmarked for a simple test case and applied to realistic models of Co atoms in Cu hosts and Fe atoms on alkali surfaces.

Finally, the (001) surface of Cr is investigated by incorporating local correlation effects into a material realistic description derived from density functional theory. To this end, the LDA+DMFT method is used to calculate spectral functions, which are compared to spectroscopic experimental data. So far open experimental features are thereby clarified. Cr(001) exemplifies a situation where correlation effects are determined by the geometric structure of a material: While correlations effects are weak in bulk Cr, they are key for the electronic structure of the Cr(001) surface.

# Zusammenfassung

Entwicklungen im Bereich Methoden und Rechenleistung haben die realistische Berechnungen von Eigenschaften nanoskopischer Systeme wie Oberflächen, zweidimensionale Materialien und Nanopunkte mit starker elektronischer Wechselwirkung ermöglicht. Strukturierungen auf der Nanoskala erlauben es elektronische Eigenschaften direkt zu beeinflussen, was eine Basis für zukünftige elektronische Bauelemente darstellt. Diese Arbeit beschäftigt sich mit der Methodenentwicklung und deren Anwendung an der Schnittstelle von ab-initio Methoden und modellbasierten Vielteilchen-Methoden in Bezug auf Nanosysteme mit starken Korrelationseffekten.

Durch eine im Gegensatz zu Volumenmaterialien kleinere Abschirmung weisen niederdimensionale Systeme langreichweitige Wechselwirkung auf. In dieser Arbeit wird der Frage nachgegangen, wie diese elektronische Eigenschaften beeinflussen. Dazu wird eine auf dem Variationsprinzip basierende Methode eingeführt, Modelle mit langreichweitiger Wechselwirkung durch Modelle mit nur lokaler Wechselwirkung zu approximieren. An einem ab-initio basierten Modell für Graphen wird gezeigt, wie die halbmetallische Phase durch langreichweitige Wechselwirkung stabilisiert wird. Die Qualität dieses Ansatzes wird anhand einfacher Systeme diskutiert.

Realistische Modelle von in ausgedehnten Festkörpern eingebetteten wechselwirkenden Störstellen sind auf Grund der großen Anzahl an Badzuständen und niedriger Symmetrie nicht exakt lösbar. Es wird ein variationeller Algorithmus eingeführt, der diese Modelle auf exakt lösbare, effektive Modelle abbildet. Damit wird eine eindeutige Lösung des sogenannten Baddiskretisierungsproblems vorgeschlagen, welches in der exakten Diagonalisierungsmethode im Bezug auf das Anderson Störstellenmodell auftritt. Die Methode wird anhand eines einfachen Systems untersucht und auf realistische Modelle für Co-Störstellen in Cu und Fe-Atome auf Alkali-Oberflächen angewendet.

Schließlich soll die (001)-Oberfläche von Cr auf Basis der Kombination von ab-initio basierten materialspezifischen Bandstrukturen und lokalen Korrelationseffekten untersucht werden. Dazu werden mit der LDA+DMFT-Methode Spektralfunktionen berechnet, mit experimentellen Daten verglichen und bisher ungeklärte experimentelle Befunde aufgeklärt. An der Cr(001)-Oberfläche werden Korrelationseffekte durch Strukturierung maßgeblich beeinflusst: Korrelationseffekte spielen im Volumen eine untergeordnete Rolle, an der Oberfläche jedoch eine Hauptrolle.

# Contents

<b>Abstract</b>	<b>vii</b>
<b>1. Introduction</b>	<b>1</b>
<b>2. Theory and methods</b>	<b>5</b>
2.1. Models for solid-state systems . . . . .	5
2.1.1. The Hubbard model . . . . .	6
2.1.2. The Anderson impurity model . . . . .	10
2.2. Density functional theory . . . . .	13
2.2.1. Local and semilocal density approximations . . . . .	16
2.2.2. One-particle basis for the Kohn-Sham equations . . . . .	17
2.3. Dynamical mean-field theory . . . . .	19
2.4. LDA+DMFT . . . . .	22
2.4.1. Correlated bands and localized basis . . . . .	23
2.4.2. Hybridization functions . . . . .	27
2.4.3. Interaction terms . . . . .	28
2.5. Monte Carlo methods . . . . .	32
2.5.1. Determinant quantum Monte Carlo . . . . .	35
2.5.2. Continuous-time quantum Monte Carlo . . . . .	38
2.5.3. The sign problem . . . . .	42
2.5.4. Analytic continuation . . . . .	42
2.6. Exact diagonalization . . . . .	45
2.6.1. Lanczos method . . . . .	47
2.7. Random-phase approximation . . . . .	49
2.7.1. Computational details . . . . .	51
2.8. Hartree-Fock . . . . .	53
2.9. The variational principle . . . . .	53
2.9.1. Ritz variational method . . . . .	54
2.9.2. Variational principle for the grand canonical potential . . . . .	55
<b>3. Renormalizations of the Hubbard model by nonlocal interactions</b>	<b>57</b>
3.1. Introduction . . . . .	57

3.2.	Theoretical framework . . . . .	58
3.3.	One-dimensional systems . . . . .	62
3.4.	Square lattices . . . . .	66
3.5.	Honeycomb lattices . . . . .	69
3.6.	Models for realistic materials: Graphene, silicene and benzene . . . . .	73
3.6.1.	Real space convergence of the effective interaction . . . . .	75
3.6.2.	Finite-size analysis for graphene . . . . .	76
3.6.3.	Temperature dependence of $\tilde{U}$ for graphene . . . . .	77
3.7.	Filling dependence . . . . .	79
3.8.	Benchmark for the case of benzene . . . . .	82
3.9.	Low-level approximations of the effective system . . . . .	83
3.9.1.	Hartree-Fock . . . . .	84
3.9.2.	Random-phase approximation . . . . .	88
3.10.	Conclusion . . . . .	90
<b>4.</b>	<b>Variational exact diagonalization method for the AIM</b>	<b>93</b>
4.1.	Introduction . . . . .	93
4.2.	The effective model . . . . .	95
4.2.1.	Implementation of minimization . . . . .	97
4.3.	Benchmark for a single-orbital Anderson impurity model . . . . .	98
4.4.	Spectral functions . . . . .	101
4.5.	Co impurities in Cu: Application to a realistic five-orbital system . . . . .	103
4.5.1.	The Anderson impurity model derived from LDA . . . . .	104
4.5.2.	Implementation of the var. ED method for the five-orbital AIM . . . . .	105
4.5.3.	Results . . . . .	107
4.6.	Fe on alkali surfaces . . . . .	111
4.6.1.	X-ray magnetic circular dichroism measurements . . . . .	112
4.6.2.	Anderson impurity model derived from LDA . . . . .	114
4.6.3.	Calculation of magnetization . . . . .	115
4.7.	Fit of hybridization functions on the Matsubara axis . . . . .	119
<b>5.</b>	<b>Many-body effects on Cr(001) surfaces: An LDA+DMFT study</b>	<b>121</b>
5.1.	Introduction . . . . .	121
5.2.	Overview of Cr physics . . . . .	122
5.3.	Models and Methods . . . . .	126
5.3.1.	Cr(001) surface . . . . .	126
5.3.2.	Details of the LDA+DMFT method for Cr(001) . . . . .	127

5.4. Results . . . . .	129
5.4.1. LDA and LSDA spectra . . . . .	129
5.4.2. DMFT spectra . . . . .	131
5.4.3. Self-energy . . . . .	138
5.5. Conclusion . . . . .	140
<b>6. Summary and outlook</b>	<b>141</b>
<b>A. Appendix</b>	<b>145</b>
A.1. Smoothing QMC data: Savitzky-Golay filter . . . . .	145
A.2. In depth benchmark of correlation functions for benzene . . . . .	147
A.3. Spectral function of a single-orbital AIM . . . . .	148
A.4. Self-energy of Cr(001) for the case of trace double counting . . . . .	150
<b>List of publications</b>	<b>153</b>
<b>List of changes</b>	<b>155</b>
<b>Bibliography</b>	<b>157</b>
<b>Acknowledgments</b>	<b>175</b>



# 1. Introduction

In the context of solid-state physics, strong electronic correlations occur in materials with partially filled  $d$  and  $f$  shells and lead to a conglomerate of phenomena, such as the Mott metal-insulator transition [90], the Kondo effect [81, 111], heavy fermion behavior [64], band ferromagnetism [89], and high-temperature superconductivity [194]. Related phase transitions lead to a sensitive dependence on external parameters, such as temperature, pressure, and fields [217] and can be exploited, e.g., for technologically relevant sensor and switching applications. The phenomena are not only technologically and fundamentally intriguing but unfortunately also extremely difficult to understand theoretically. The phenomena's mutual constituents are valence electrons subject to considerable interaction.

While for weak interactions, electrons are well described in a band picture as independent particles, strongly interacting electrons, e.g., in the atomic case, are successfully described in a multiplet picture. It is the region where kinetic and interaction energy are of similar magnitude which is theoretically most complicated and requires sophisticated methods to gain insight to. The theoretical treatment of relatively simple representatives of this class of complicated materials can nowadays be considered state of the art. Bulk transition metals [134, 18, 25], their oxides [78, 215, 98] and sulfides [125], and bulk  $f$  electron materials [233, 79] are well understood by combining the accurate description of correlation effects in the framework of many-body models with the material specific information from band-theory methods, the so called LDA+DMFT method [8, 133].

More involving is the treatment of correlations in nanoscopically structured materials, such as two-dimensional materials [99], heterostructures of layered materials [161], surfaces [74], and clusters and chains of adatoms on surfaces [82, 50, 165] as, e.g., long-range interactions and low-symmetries hinder the straight-forward application of the LDA+DMFT approach. However, the geometry of correlated materials can nowadays be manipulated by self-assembled growth and scanning probes on the scale of atoms which enables a new level of experimental and technological possibilities. Therefore, the development of novel methods in the realm of strongly correlated nanostructured materials promises to be highly rewarding.

This work is devoted to the accurate description of correlation effects for nanoscop-

ically structured materials in a material specific manner. In a greater context, the goal is to develop methods which enable a direct comparison of theoretical and experimental studies and thus lead to a deeper understanding of correlation effects in real materials. Ideally, these methods will have predictive power and guide the quest for technological devices. Here, we consider the effect of long-range interactions on the properties of two-dimensional materials (i.e., graphene and silicene), methods to treat correlated impurities with low-symmetries, and the electronic structure of the Cr(001) surface.

The thesis is structured as follows: In section (2) we present the methods and models of consideration. Starting with the introduction of the basic solid-state Hamiltonian, we go on to introduce the low energy models of concern: the Hubbard model and Anderson impurity model. Subsequently, we discuss the density functional theory (DFT), an ab initio approach to the many-body Hamiltonian, and in particular the projector augmented wave method. After introducing the dynamical mean-field theory (DMFT), which links lattice and impurity models in certain regimes, we consider the combination of DFT and many-body models by the LDA+DMFT method. In order to solve interacting quantum lattice models, at least approximately, we introduce two Monte Carlo based methods, the determinant and continuous-time quantum Monte Carlo methods (for lattice and impurity models, respectively), the exact diagonalization method (for finite systems), the random-phase approximation for the Hubbard model, and the Hartree-Fock method. Preceding the introduction of the Monte Carlo based methods, we give a more general introduction to the Monte Carlo approach. We complete the methods section by elaborating on the variational principle, which is the foundation of the novel methods we present in sections (3) and (4).

The first of these new methods, presented in section (3), is designed to analyze the role of nonlocal interactions by means of the Hubbard model and its extensions. After introducing the method for general cases, we apply it to low-dimensional models. In particular, we study an ab initio derived model of graphene and find that nonlocal interactions stabilize the semimetallic phase.

The second method, presented in section (4), constitutes a new approach to solving the Anderson impurity model by means of exact diagonalization: We use a variational approach to map Anderson impurity models with an arbitrary number of bath sites, complicated interaction terms, and low symmetries to exactly solvable models. Benchmarking the method for one and five orbital models, we establish the method and then apply it to realistic impurity systems such as Fe on alkali metals.

Finally, in section (5), we go on to an intriguing example of a strongly correlated nanostructured material: the Cr(001) surface. We employ the LDA+DMFT methodology to simulate electronic spectral properties of the Cr(001) surface in order to compare

---

them to experimental data. The comparison reveals that the electronic structure is determined by the complex interplay of the reconstruction of single-particle states at the surface and local correlation effects.



## 2. Theory and methods

This chapter covers the methods and models used in this work. It is assumed that the reader has basic knowledge of quantum mechanics, quantum field theory (“second quantization”, “action formalism”) and solid-state theory. Exemplary literature covering these topics are Refs. [163, 162] for basic quantum mechanics, Refs. [42, 146] for second quantization and solid state theory, and Ref. [5] for field theory and the action formalism.

### 2.1. Models for solid-state systems

In this work, we deal with model systems for interacting electrons. Model systems neglect the complexity of real materials but grasp the essential physics to describe a certain effect. In this section we rationalize the use of models and their relationship to the full electronic problem. In the remainder of the section we introduce the Hubbard model and the Anderson impurity model, which are both of central concern in this work.

Let us consider the electronic structure of a solid. Assuming all atoms at rest<sup>1</sup> we deal with the following Hamiltonian for the electronic degrees of freedom [42]

$$H = \sum_i^{N_e} \frac{\mathbf{p}_i^2}{2m} - \sum_i^{N_e} \sum_k^{N_c} \frac{Z_k e^2}{|\mathbf{r}_i - \mathbf{R}_k|} + \frac{1}{2} \sum_{i,j}^{N_e} \frac{e^2}{|\mathbf{r}_i - \mathbf{r}_j|}, \quad (2.1)$$

where  $N_e$  and  $N_c$  are the number of electrons and atomic cores, respectively,  $e$  is the elementary charge,  $\mathbf{p}_i$  and  $\mathbf{r}_i$  are the momentum and position operators of the  $i$ 'th electron,  $\mathbf{R}_k$  and  $Z_k$  are the position and atomic number of the  $k$ 'th atom. The first term is the kinetic energy of the electrons and the second the static atomic potential in which the electrons move. The last term is the Coulomb repulsion between each pair of electrons. This Hamiltonian describes all electrons in the system: from tightly bound inner shell electrons to potentially delocalized electrons near the Fermi level. To describe macroscopic properties of a solid related to electronic degrees of freedom, e.g., magnetic states, electrical conductivity, or superconductivity it is often sufficient

---

<sup>1</sup>more accurately, we use the Born-Oppenheimer approximation, compare Ref. [23].

to neglect the dynamics of inner-shell electrons and focus on those near the Fermi energy. One calls such an approach low-energy approach, as it only treats electrons in a narrow energetic region around the Fermi energy.

Propose we have accomplished to solve a low-energy version of the Hamiltonian (2.1) for a certain configuration of atoms and we have found that the system is superconducting. What would we have learned from such a calculation? The reason and systematics why exactly that compound is superconducting would still be as unclear as the general mechanism leading to superconductivity. A route for a systematic analysis of quantum mechanical systems is the use of parametric models. Let us write the electronic part of the Hamiltonian (2.1) in second quantization, assuming we have solved the single-particle part, with respect to a quantum number  $k$ :

$$H = \sum_k t_k c_k^\dagger c_k + \frac{1}{2} \sum_{\alpha\beta\gamma\delta} U_{k_1 k_2 k_3 k_4} c_{k_1}^\dagger c_{k_2}^\dagger c_{k_3} c_{k_4}, \quad (2.2)$$

where

$$t_k = \langle k | \frac{\mathbf{p}^2}{2m} - \sum_i^{N_c} \frac{Z_i e^2}{|\mathbf{r} - \mathbf{R}_i|} | k \rangle$$

is the matrix element of the single-particle part and

$$U_{k_1 k_2 k_3 k_4} = {}^{(1)}\langle k_1 | {}^{(2)}\langle k_2 | \frac{e^2}{|\mathbf{r}_1 - \mathbf{r}_2|} | k_3 \rangle {}^{(2)}| k_4 \rangle {}^{(1)}$$

is the matrix element of the two-particle part. Up to now, the Hamiltonian is only rewritten into a more convenient form and includes the same amount of complexity as before. Let us come back to our superconducting compound: We could start and neglect certain matrix elements (i.e., setting them to zero) and observe if the superconductivity survives. Thereby we can find a minimal model, which still describes the physics we are interested in and thus identify the crucial ingredients of the physical system. Once we have found a minimal model, we can also change the values of the matrix elements to learn for which combinations the models shows superconductivity. In practice, this approach works in the exact opposite direction, as we can never solve the Hamiltonian of the full system. In the following, we introduce two parametric low-energy models which we deal with in this work.

### 2.1.1. The Hubbard model

The Hubbard model was introduced to clarify the formation of ferromagnetism in materials with strong local interaction [89]. It can be motivated in two ways: First, as

the simplest possible extension of a tight binding model with local Coulomb interaction. Secondly, in the spirit of the introductory section (2.1) by neglecting all non-local interaction matrix elements. The second way is how Hubbard motivates the model in [89]. There, the magnitude of different interaction matrix elements is estimated with the conclusion that local interaction terms dominate all others for systems in which mobile electrons exist to screen non-local terms efficiently. We don't reproduce the excellent discussion of Hubbard but follow the first route to introduce the model. We briefly remember the tight binding model: It is a single-particle lattice model with the basic assumption of well localized basis functions. Electrons have a certain probability to hop from one atom to another. Depending on the details of the model, the number of orbitals on each atom and the range of hopping processes can be varied. A tight binding model describing a single band reads

$$H_{\text{tight binding}} = - \sum_{ij\sigma} t_{ij} c_{i\sigma}^\dagger c_{j\sigma}, \quad (2.3)$$

where  $t_{ij}$  are the hopping amplitudes from atom  $i$  to atom  $j$  for an electron with spin  $\sigma$ . By including the simplest possible interaction term, namely the Coulomb interaction  $U_i$  for two electrons on the same atom  $i$ , we arrive at the Hubbard model

$$H_{\text{Hubbard}} = - \sum_{ij\sigma} t_{ij} c_{i\sigma}^\dagger c_{j\sigma} + \sum_i U_i c_{i\uparrow}^\dagger c_{i\uparrow} c_{i\downarrow}^\dagger c_{i\downarrow}. \quad (2.4)$$

The Hubbard model is key to understanding the Mott metal-insulator transition [59]. This transition is depicted schematically in Fig. (2.1) by means of the spectral function for half-filled Hubbard models with weak, intermediate and strong interaction. For weak interaction, the electrons can freely hop to neighboring sites and form bands: the system is metallic. For strong interaction, electrons pay an energy penalty of  $U$  when occupying the same site. Two bands appear which correspond to atomic excitations of isolated atoms: the system is insulating. The intermediate regime shows a quasiparticle peak at the Fermi energy and two broad peaks, the upper and the lower Hubbard band, which are precursors of the atomic peaks at stronger interaction strengths. The intermediate case is certainly the most interesting but also the most difficult to handle theoretically. We can put this qualitative discussion into context by regarding the  $T = 0$  phase diagram of the two-dimensional Hubbard model with fixed nearest neighbor hopping  $t$  and next-nearest neighbor hopping  $t'$ , reproduced from [232] and depicted in Fig. (2.2). For all interaction strengths  $U$ , the particle-hole symmetric case ( $t' = 0$ ) is an antiferromagnetically ordered insulator for half filling. Away from half filling the phase diagram is richer: next to the metallic phase, phases

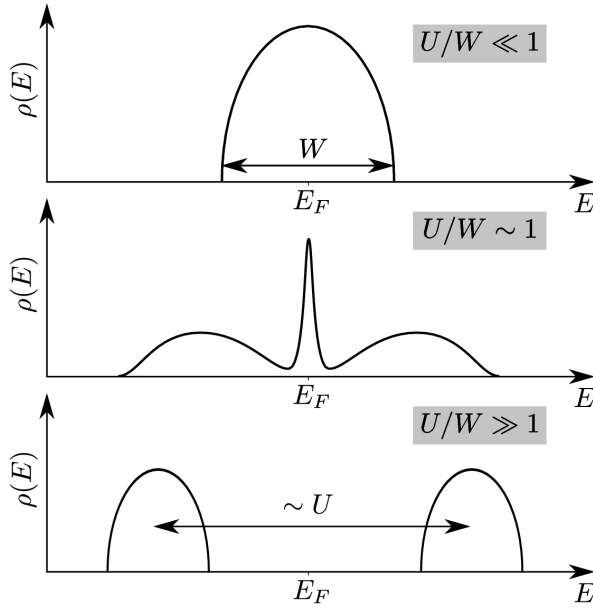


**Figure 2.1.:** Sketch of the spectral functions of half filled Hubbard models with a semicircular non-interacting density of states with a band width of  $W$  and interaction  $U$  for three different regimes: The non-interacting case ( $U/W \ll 1$ ), Mott insulator ( $U/W \gg 1$ ), and the regime where kinetic and interaction energy are competing ( $U/W \sim 1$ ). Figure inspired by Ref. [114]. For quantitatively correct spectral functions for a Hubbard model in infinite dimensions see for example [29].

with antiferromagnetic ordering, superconducting order and inhomogeneous order are present. For  $t' \neq 0$ , there is a metallic behavior of the half-filled system for weak interactions.

A nice motivation, introduction and discussion of some properties of the Hubbard model can also be found in Ref. [5]. The Hubbard model is known to be analytically solvable in one dimension by the Bethe ansatz [136, 135] and is in infinite dimensions equivalent to a self-consistently defined Anderson impurity model [152, 24, 60], which we introduce in the next section. For interaction strengths dominating the hopping,  $U/t \gg 1$ , double occupation is suppressed, which leads to a quenching of hopping possibilities and an insulating behavior. In this regime, no charge fluctuations are possible because of the large interaction, but virtual charge fluctuations still allow spin fluctuations. In this regime, the half filled Hubbard model is well approximated by a spin model, the Heisenberg model [77], with a coupling of the spins of the magnitude  $J \sim t^2/U$  [38].

By including interaction terms between electrons on different sites (non-local inter-

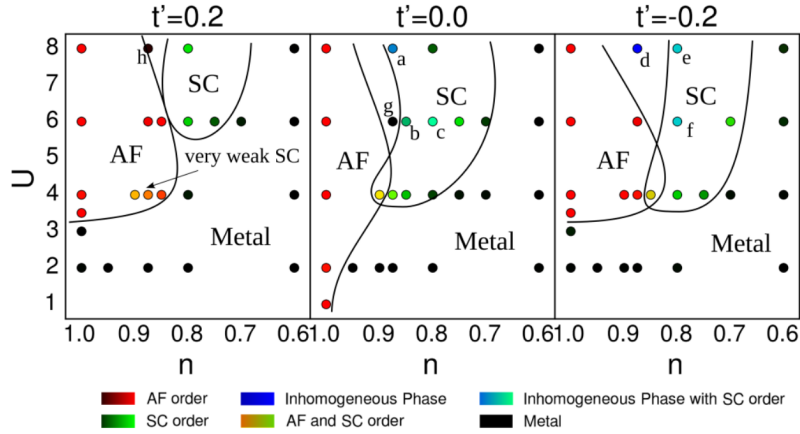


**Figure 2.2.:** Zero temperature phase diagrams of the Hubbard models on the square lattice with next-nearest neighbor hopping  $t'$  calculated from density matrix embedding theory [105, 104]. Orders are represented with three primary colors: red (antiferromagnetism), green (d-wave superconductivity), and blue (inhomogeneity), with the brightness proportional to the robustness of the order. For details see original reference. Reprinted figure with permissions from [Bo-Xiao Zheng and Garnet Kin-Lic Chan, Phys. Rev. B, **93**, 035126 (2016), [232]]. Copyright 2016 by the American Physical Society.

action), we arrive at the so called extended Hubbard model or the Pariser-Parr-Pople model (PPP model [167, 177])<sup>2</sup>. The Hamiltonian reads

$$H_{exHub} = H_{Hub} + \frac{1}{2} \sum_{\substack{i \neq j \\ \sigma, \sigma'}} V_{ij} c_{i\sigma}^\dagger c_{i\sigma} c_{j\sigma'}^\dagger c_{j\sigma'}, \quad (2.5)$$

where  $V_{ij}$  are Coulomb matrix elements for electrons at sites  $i$  and  $j$ . The introduction of non-local interaction extends the phase diagram of the Hubbard model with the charge-density wave phase [85], which can be reasoned by a simple physical picture: For the case of only two electrons on two sites, it is energetically less favorable for both electrons to occupy different lattice sites than to doubly occupy the same lattice site, as soon as the non-local interaction is larger than the local interaction. Thus, a charge order is established. This argument also holds for more general systems. Thereby, e.g., an order where every second site is doubly occupied and every other site is empty can minimize the energy of an extended Hubbard model. The according phase diagram for a half-filled two-dimensional Hubbard model with nearest-neighbor interaction  $V$

<sup>2</sup>The name extended Hubbard model is used in the community of solid-state physics whereas PPP model is used in quantum chemistry.

is presented in Fig. (2.3): Approximately, for  $V > U/2$ , the charge-density wave phase is energetically more favorable than the spin-density wave phase.

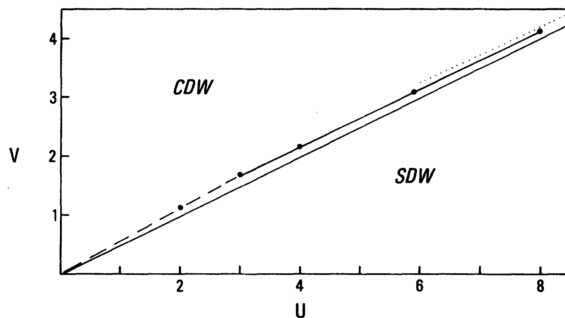


**Figure 2.3.:** Phase boundary between charge density wave (CDW) and spin density wave (SDW) regions in the half-filled extended Hubbard model on the square lattice with nearest neighbor interaction  $V$  from DQMC simulations (compare Sec. (2.5.1)). The solid line is  $U = 2V$ , the dotted line a strong-coupling prediction. For details see Ref. [85]. Reprinted figure with permissions from [J. E. Hirsch, Phys. Rev. Lett., **53**, 2327 (1984), [85]]. Copyright 1984 by the American Physical Society.

### 2.1.2. The Anderson impurity model

The Anderson impurity model (AIM) is a general model for impurities with local interactions in non-interacting host systems [7]. Originally, it was developed to describe single atoms with open  $d$  or  $f$  shells embedded in bulk materials and to understand the formation of their magnetic moments [7]. Furthermore, the model includes the widely discussed Kondo physics [116, 111, 120]. Multi-orbital variants of the AIM gained considerable attention in the context of rare-earth impurity systems [222, 69] as well as more recently magnetic adatoms or molecules on surfaces [91, 223, 210, 122]. Finally, dynamical mean-field theory (DMFT, Sec. (2.3)) links Hubbard models (models with nonlocal self-energy, multiple interacting sites) to Anderson impurity models (models with local self-energy, one interacting site).

The model consists of an impurity site, subject to Coulomb interaction, and non-interacting bath sites. Impurity and bath sites are coupled by the so called hybridization. The Hamiltonian of the AIM reads

$$H = H_{\text{bath}} + H_{\text{hyb}} + H_{\text{imp}}. \quad (2.6)$$

The bath is described by

$$H_{\text{bath}} = \sum_{\alpha k, \sigma} \varepsilon_k n_{\alpha k \sigma}^c, \quad (2.7)$$

where  $\varepsilon_{\alpha k}$  is the energy of the bath state with band/orbital index  $\alpha$  and the wave vector  $k$ .  $n_{\alpha k \sigma}^c = c_{\alpha k \sigma}^\dagger c_{\alpha k \sigma}$  is the corresponding particle number operator. The hybridization part

$$H_{\text{hyb}} = \sum_{\alpha k, \sigma} V_{\alpha k} \left( c_{\alpha k \sigma}^\dagger d_{\alpha \sigma} + d_{\alpha \sigma}^\dagger c_{\alpha k \sigma} \right) \quad (2.8)$$

ouples the bath sites of one band to an orbital of the impurity with a coupling strength  $V_{\alpha k}$ . The bath electrons with spin  $\sigma$  are created and annihilated by  $c_{\alpha k \sigma}^\dagger$  and  $c_{\alpha k \sigma}$ , respectively, while  $d_{\alpha \sigma}^\dagger$  ( $d_{\alpha \sigma}$ ) denote the creation (annihilation) operators of the impurity electrons. The impurity site is described by

$$H_{\text{imp}} = \sum_{\alpha, \sigma} \varepsilon_\alpha^d n_{\alpha \sigma}^d + \sum_{\alpha, \beta, \gamma, \delta, \sigma, \sigma'} U_{\alpha \beta \gamma \delta} d_{\alpha \sigma}^\dagger d_{\beta \sigma'}^\dagger d_{\gamma \sigma'} d_{\delta \sigma}, \quad (2.9)$$

which contains the on-site Coulomb interaction  $U_{\alpha \beta \gamma \delta}$  and the on-site energies  $\varepsilon_\alpha^d$ .

Let us calculate the impurity Green function  $G_{dd}^0$  of a non-interacting single-orbital AIM (compare Ref. [7]), defined by

$$H = \sum_k \varepsilon_k |k\rangle \langle k| + \sum_k V_k (|k\rangle \langle d| + |d\rangle \langle k|) + \varepsilon_d |d\rangle \langle d|. \quad (2.10)$$

The non-interacting Green function  $G_{\mu\kappa}^0 = \langle \mu | G^0 | \kappa \rangle$  is defined by

$$\sum_\mu \langle \nu | z - H | \mu \rangle G_{\mu\kappa}^0 = \delta_{\nu\kappa}, \quad (2.11)$$

where  $z$  is a shorthand for  $\omega + i0^+$  and the indices run over  $d$  and all  $k$ . By writing down the equations for  $\mu = d, \kappa = d$  and  $\mu = k, \kappa = d$ , we arrive at

$$(z - \varepsilon_d) G_{dd}^0 - \sum_k V_k G_{kd}^0 = 1 \quad \text{and} \quad (2.12)$$

$$(z - \varepsilon_k) G_{kd}^0 - V_{kd} G_{dd}^0 = 0. \quad (2.13)$$

We solve for  $G_{dd}^0$  and get

$$[G_{dd}^0]^{-1} = z - \varepsilon_d - \sum_k \frac{V_k V_k^*}{z - \varepsilon_k} = z - \varepsilon_d - \Delta(z). \quad (2.14)$$

Here, we have introduced the hybridization function  $\Delta(z)$ , which characterizes the energy-dependent coupling between impurity and bath. The generalized hybridization function for multi-orbital systems reads

$$\Delta_{\alpha\alpha'}(\omega) = \sum_k \frac{V_{\alpha k}^* V_{\alpha' k}}{\omega + i0^+ - \varepsilon_k}. \quad (2.15)$$

We further define the bath Green function  $\mathcal{G}_0$  by

$$[\mathcal{G}_{\alpha\alpha'}^0(\omega)]^{-1} = \omega\delta_{\alpha\alpha'} - \Delta_{\alpha\alpha'}(\omega). \quad (2.16)$$

Let us consider the impurity spectral functions of two analytically solvable limits of the single-orbital Anderson impurity level: For the non-interacting case, we calculate

$$A(\omega) = -\frac{1}{\pi} \text{Im} [G_{dd}^0(\omega + i0^+)]. \quad (2.17)$$

By comparing to the former result for the Green function (Eq. (2.14)), we observe that the spectral function has a pole at  $\varepsilon_d + \text{Re}[\Delta(\varepsilon)]$  which is broadened by  $\text{Im}[\Delta(\varepsilon)]$ . The effect of the hybridization function is to shift and broaden the impurity resonance. In the atomic limit, the impurity part of the Hamiltonian,  $H_{\text{imp}}$ , is diagonalized by the four states  $|0\rangle$ ,  $|\uparrow\rangle$ ,  $|\downarrow\rangle$ , and  $|\uparrow\downarrow\rangle$  with energies 0,  $\varepsilon_d$ ,  $\varepsilon_d$ , and  $2\varepsilon_d + U$ . We calculate the Green function at half filling from the Lehmann representation (Eq. (2.126)) and obtain two poles in the spectral function,

$$A(\omega) = \frac{1}{2}\delta(\omega - \varepsilon_d) + \frac{1}{2}\delta(\omega - \varepsilon_d - U), \quad (2.18)$$

one at  $\varepsilon_d$  for removing an electron from the impurity and one at  $\varepsilon_d + U$  for adding an electron. Due to its spin degree of freedom, a singly occupied impurity in the atomic limit, has a magnetic moment of  $1/2$ . Here, it is possible to exactly map the model to a spin  $1/2$  Kondo-model [111] by a Schrieffer-Wolf transformation [195], i.e., integrating out the empty and doubly occupied states.

For the case of strong hybridization, the moment is screened by bath electrons to form a singlet. Essentially, this is the famous Kondo effect. In this case, the spectral function shows a pronounced resonance at the Fermi energy, which is a fingerprint of the screened moment. The evolution of the numerically calculated spectral function of a particle-hole symmetric single-orbital AIM<sup>3</sup> between the discussed limits, i.e., from the weakly to the strongly interacting case, is presented in Fig. (2.4). For weak interaction a single peak broadened by the hybridization at the Fermi energy is visible.

---

<sup>3</sup>The model is defined by  $\varepsilon_d = -U/2$  and a constant hybridization function of  $\Delta(\omega) = 1$  for  $-40 < \omega < 40$  in dimensionless units.

For stronger interactions a three peak structure emerges: with growing interaction strength, the central quasiparticle peak narrows and the upper and lower broad peak shift in energy. We note the similarities to the evolution of the Hubbard model's spectral function with increasing interaction strength, compare Fig. (2.1). This is related to the close connection of the Anderson impurity model and the Hubbard model: In infinite dimensions, the Hubbard model can be mapped exactly to an AIM by a self-consistency relation [152, 24, 60]. In all other cases, an adequately chosen Anderson model approximates the local physics of the Hubbard model to certain degrees. We discuss this in more detail in the framework of dynamical mean-field theory in section (2.3).

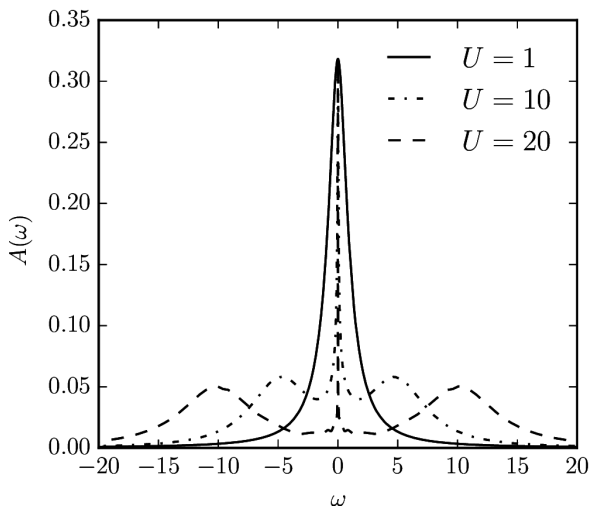


**Figure 2.4:** Spectral function of particle-hole symmetric single-orbital Anderson impurity models with different interaction strengths  $U = 1, 10, 20$  in dimensionless units and constant hybridization function  $\Delta = 1$ . Originally calculated in Ref. [197]. Compare original work for details.

## 2.2. Density functional theory

Next to the model approach introduced in the preceding section, the complexity and enormous amount of degrees of freedom in the solid-state Hamiltonian (Eq. (2.1)) can also be tackled differently: Density functional theory changes the perception on what the basic quantity in quantum mechanics is. We show that we can resign the wavefunction of a system and rely only on the density to find the ground-state energy of a system. This comes with a greatly reduced complexity such that certain additional approximations permit to tackle the full electronic many-body problem stated in Eq. (2.1) directly. This is called an *ab initio* approach to solid-state problems. This is in contrast but also is complementary to the model approach (Sec. (2.1)) of understanding solid-state systems. Complementary, because recently the combination of model and

ab initio methods has led to the LDA++ method which we introduce in Sec. (2.4) and use throughout this work. Here, we cover the main ideas and approximations on which the method builds upon.

The solution of the many-body problem of  $N$  electrons involves finding the ground-state wavefunction  $\Psi(\mathbf{r}_1, \mathbf{r}_2, \dots, \mathbf{r}_N)$ , which is an intractable object due to the  $N$  space coordinates, which themselves consist of three space dimensions. The fundamental idea of density functional theory is instead to use the electronic density defined by

$$n(\mathbf{r}) = \langle \Psi | \sum_i^N \delta(\mathbf{r} - \mathbf{r}_i) | \Psi \rangle \quad (2.19)$$

as central object to solve the many-body problem. Following [146] and [93] we derive the results of Hohenberg and Kohn, who showed in [86] that it is indeed sufficient to know the electronic density of the ground state to specify the ground state entirely.

We consider the general electronic many-body Hamiltonian

$$H = T + U + \sum_{i=1}^N V_{\text{ext}}(r_i), \quad (2.20)$$

where  $T$  and  $U$  are the kinetic and potential energy and  $V_{\text{ext}}$  is an external potential. The first Hohenberg-Kohn theorem states that the ground state energy  $E_0$  of  $H$  is a unique functional of the electronic density of the ground state  $n_0(\mathbf{r})$ :

$$E_0 = E[n_0(\mathbf{r})]. \quad (2.21)$$

The second Hohenberg-Kohn theorem states that the density of the ground state,  $n_0(\mathbf{r})$ , minimizes the energy functional leading to the ground state energy:

$$E_0 = E[n_0(\mathbf{r})] \leq E[n(\mathbf{r})]. \quad (2.22)$$

In order to prove both theorems, we introduce the universal functional

$$F[n(\mathbf{r})] = \min_{|\Psi\rangle \rightarrow n} \langle \Psi | T + U | \Psi \rangle. \quad (2.23)$$

The minimum is taken with respect to all wavefunctions  $|\Psi\rangle$  which lead to the density  $n(\mathbf{r})$  via Eq. (2.19). These  $|\Psi\rangle$  are also called  $N$ -representable. We can write the ground-state energy  $E_0$  as the expectation value of the Hamiltonian with the wavefunction of the ground state  $|\Psi_0\rangle$ . The wavefunction of the ground state leads to the density of the ground state  $n_0(\mathbf{r})$ . We can then use the Ritz variational principle, Eq. (2.167), to show

$$E_0 = \langle \Psi_0 | H | \Psi_0 \rangle = \min_{|\Psi\rangle \rightarrow n_0} \langle \Psi | H | \Psi \rangle = F[n_0] + \int d^3r V_{\text{ext}}(\mathbf{r})n_0(\mathbf{r}) = E[n_0(\mathbf{r})], \quad (2.24)$$

which proves the first Hohenberg-Kohn theorem.

For any  $n(\mathbf{r})$  we introduce  $|\Psi_{\min}^n\rangle$ , which minimizes the functional  $F[n(\mathbf{r})]$ . We can then evaluate the energy functional for any density and prove the second theorem using the Ritz principle again:

$$E[n(\mathbf{r})] = F[n(\mathbf{r})] + \int d^3r V_{\text{ext}}(\mathbf{r})n(\mathbf{r}) = \langle \Psi_{\min}^n | H | \Psi_{\min}^n \rangle \geq E_0 = E[n_0(\mathbf{r})]. \quad (2.25)$$

We could now solve the many-body problem (at least regarding total energies) by minimizing the functional  $E[n(\mathbf{r})]$  with respect to all possible electron densities. However, calculating the energy from the density via its definition with Eq. (2.23), requires the knowledge of the many-body wavefunction. Thus, for practical calculations we need an approximation leading to a functional which depends analytically on the density. In order to arrive at such approximation we first introduce an auxiliary non-interacting system. The idea of the so called Kohn-Sham ansatz [107] is to represent the ground-state density of the many-body system by the ground state of an non-interacting system with some *effective* single-particle potential. The Schrödinger equation of the auxiliary system reads

$$H_{\text{KS}}\psi_i(\mathbf{r}) = \left( -\frac{\hbar^2}{2m}\nabla^2 + V_{\text{eff}}(\mathbf{r}) \right) \psi_i(\mathbf{r}) = \varepsilon_i\psi_i(\mathbf{r}). \quad (2.26)$$

The effective potential  $V_{\text{eff}}(\mathbf{r})$  has to be determined such that the electron density by filling the effective one-particle states,

$$n(\mathbf{r}) = \sum_{i=1}^N |\psi_i(\mathbf{r})|^2, \quad (2.27)$$

coincides with the true ground-state density  $n_0(\mathbf{r})$ . The Kohn-Sham ansatz consists of writing the Hohenberg-Kohn functional for the energy in the following way

$$E[n(\mathbf{r})] = T_s[n(\mathbf{r})] + E_{\text{ext}} + E_H[n(\mathbf{r})] + E_{\text{xc}}[n(\mathbf{r})], \quad (2.28)$$

where  $T_s$  is the kinetic energy of the non-interacting system

$$T_s = -\frac{\hbar^2}{2m} \sum_{i=1}^N \langle \psi_i | \nabla^2 | \psi_i \rangle, \quad (2.29)$$

$E_{\text{ext}} = \int d^3r V_{\text{ext}}(\mathbf{r})n(\mathbf{r})$  is the potential energy,  $E_H$  is the classical (Hartree) part of the electron-electron repulsion

$$E_H[n(\mathbf{r})] = \frac{1}{2} \int d^3r d^3r' \frac{n(\mathbf{r})n(\mathbf{r}')}{|\mathbf{r} - \mathbf{r}'|}, \quad (2.30)$$

and  $E_{\text{xc}}$  is the exchange-correlation energy, defined as the difference between the prior energies and the full  $E[n(\mathbf{r})]$ :

$$E_{\text{xc}}[n(\mathbf{r})] = \langle T \rangle - T_s[n(\mathbf{r})] + \langle U \rangle - E_H[n(\mathbf{r})]. \quad (2.31)$$

The minimization of  $E[n(\mathbf{r})]$  in the form of Eq. (2.28) with respect to the density can be reformulated into a minimization with respect to the non-interacting wavefunctions via the chain rule. We then obtain

$$\begin{aligned} \frac{\delta E[n(\mathbf{r})]}{\delta \psi_i^*(\mathbf{r})} &= \frac{\delta T_s}{\delta \psi_i^*(\mathbf{r})} + \left( \frac{\delta E_{\text{ext}}}{\delta n(\mathbf{r})} + \frac{\delta E_H}{\delta n(\mathbf{r})} + \frac{\delta E_{\text{xc}}}{\delta n(\mathbf{r})} \right) \frac{\delta n(\mathbf{r})}{\delta \psi_i^*(\mathbf{r})} \\ &= -\frac{\hbar^2}{2m} \nabla^2 \psi_i(\mathbf{r}) + \left( V_{\text{ext}} + \int d^3r' \frac{n(\mathbf{r}')}{|\mathbf{r} - \mathbf{r}'|} + V_{\text{xc}} \right) \psi_i(\mathbf{r}) = 0, \end{aligned} \quad (2.32)$$

which we solve under the constraint of orthonormalized wavefunctions  $\langle \psi_i | \psi_j \rangle = \delta_{ij}$  using Lagrange multipliers  $\varepsilon_i$ . We end up with a Schrödinger equation in the form of Eq. (2.26) and identify the effective one-particle potential

$$V_{\text{eff}}(\mathbf{r}) = V_{\text{ext}}(\mathbf{r}) + V_H(\mathbf{r}) + V_{\text{xc}}(\mathbf{r}). \quad (2.33)$$

Thus, Eqs. (2.26), the Kohn-Sham equations, have to be solved self-consistently.

So far, we have replaced the problem of finding the ground state energy of a many-body problem by the self-consistent solution of a single-particle problem. However, evaluating  $V_{\text{xc}}(\mathbf{r})$  still involves the knowledge of the exact solution of the many-body problem.

### 2.2.1. Local and semilocal density approximations

A simple approximation for the exchange-correlation energy  $E_{\text{xc}}[n(\mathbf{r})]$  follows from the assumption that it coincides at every point with the exchange-correlation energy of the homogeneous electron gas

$$E_{\text{xc}}^{\text{LDA}}[n(\mathbf{r})] = \int d^3r n(\mathbf{r}) \varepsilon_{\text{xc}}^{\text{hom}}(n(\mathbf{r})), \quad (2.34)$$

where  $\varepsilon_{\text{xc}}^{\text{hom}}$  is the sum of the correlation energy  $\varepsilon_{\text{c}}^{\text{hom}}$  and the exchange energy  $\varepsilon_{\text{x}}^{\text{hom}}$ . As the exchange-correlation energy is assumed to depend only locally on the density, this approach is called local density approximation (LDA). The exchange energy of the homogeneous electron gas is known analytically and the correlation energy is computed to great accuracy by Monte Carlo sampling and parametrized in terms of the density [36].

Taking the ideas of the LDA one step further results in the generalized gradient approximation (GGA), which assumes that the exchange correlation energy can be expressed in terms of the density and its gradient

$$E_{xc}^{GGA}[n(\mathbf{r})] = \int d^3r n(\mathbf{r}) \varepsilon_{xc}(n(\mathbf{r}), \nabla n(\mathbf{r})). \quad (2.35)$$

In contrast to the LDA, where the assumption of the locality is equivalent of using the exchange energy of the homogeneous electron gas, the GGA leaves ambiguities in defining a specific functional. Different flavors exist: Commonly used ones are the functional of Perdew and Wang [173] or that of Perdew, Burke and Enzerhof [172], which is used in this work.

### 2.2.2. One-particle basis for the Kohn-Sham equations

To solve the Kohn-Sham equations (Eqs. (2.26)) the wavefunctions have to be expanded in some infinite set of basis functions. In practical calculations this set has to be truncated, which leads to a truncation error. This has to be checked carefully by converging calculations with respect to the truncation. The speed of the convergence, i.e., the number of states needed to describe a system adequately, depends on both the system at hand and the basis functions we choose. For molecules or atoms localized basis functions seem more reasonable than plane waves, for solids vice versa. For translationally invariant solids an expansion using the Bloch theorem

$$\psi_{i\mathbf{k}}(\mathbf{r}) = \sum_{\mathbf{G}} c_{i\mathbf{k}}(\mathbf{G}) e^{i(\mathbf{k}+\mathbf{G})\mathbf{r}}, \quad (2.36)$$

is reasonable.

The nature of wavefunctions in the case of solids is very different for the interstitial region, where they vary slowly, and regions in the vicinity of atoms, where we expect rapid oscillations due to large gradients of the potential. These strong oscillations lead to a poor convergence of results with respect to the truncation in the number of plane waves. This is demonstrated for a bound and a free solution of a numerically solved one-dimensional box potential in the left panel of Fig. (2.5). The atomic potential is modeled by a region of attractive constant potential. Bound states exist, which are far from plane wave-like. Only outside of the attractive (“atomic”) potential the free solution is in good approximation a plane wave. The right panel shows the poor convergence of the expansion in plane waves for both the bound and the free state. A method to tackle this problem is the projector augmented wave method (PAW, [21]). In the following, we introduce the basic idea of the PAW following [21].

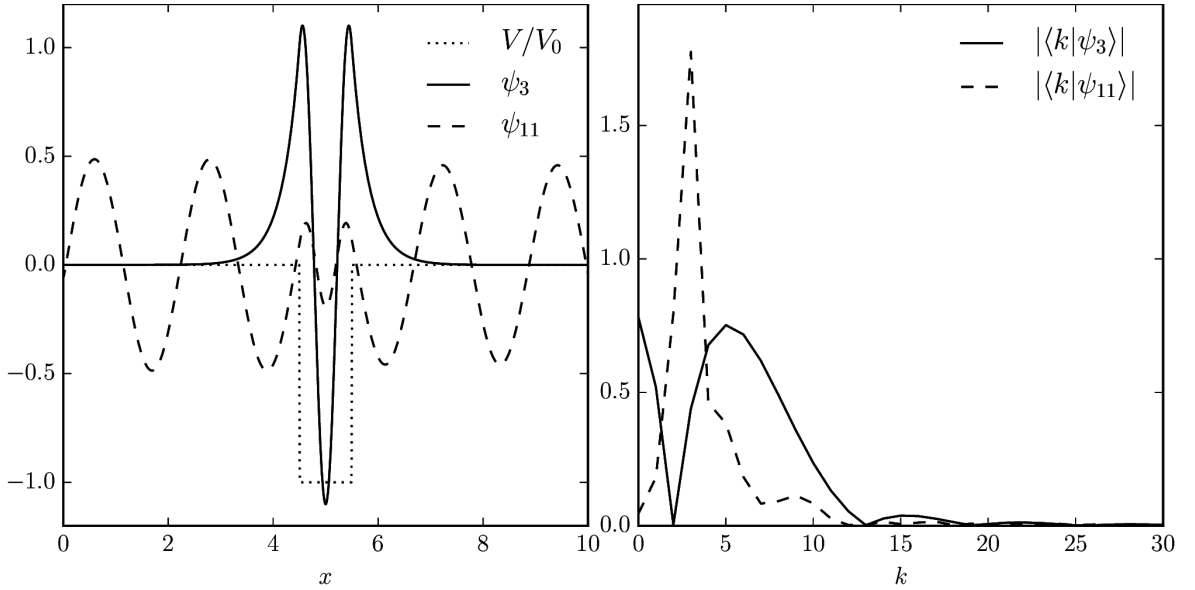


**Figure 2.5.:** Left panel: Third and eleventh eigenfunction of the one-dimensional single-particle Schrödinger equation for the box potential  $V(x)$  for  $V_0 = 30$ . The solution is obtained numerically by discretization of the space. Right panel: plane wave expansion coefficients  $\langle k|\psi_i\rangle = \int dx \exp(ikx)\psi_i(x)$ .

Given Kohn-Sham wavefunctions  $|\psi\rangle$ , we introduce a linear transformation  $T$  to computationally more convenient (i.e., smoother) functions  $|\tilde{\psi}\rangle$ , called pseudo wavefunctions, by

$$|\psi\rangle = T |\tilde{\psi}\rangle. \quad (2.37)$$

The transformation is defined on the Hilbert space of the valence states, which is assumed to be orthogonal to the Hilbert space of the core states. Thus the PAW is a so called frozen core method, which means the core states are assumed to be not affected by valence electrons. Because  $T$  is a linear transformation, we can perform all calculations with pseudo functions by transforming operators into the new basis. We compute observables via  $\langle A \rangle = \sum_n f_n \langle \psi_n | A | \psi_n \rangle = \sum_n f_n \langle \tilde{\psi}_n | \tilde{A} | \tilde{\psi}_n \rangle$ , where  $\tilde{A} = T^\dagger A T$  and  $f_n$  is the occupation of the  $n$ 'th state.

The transformation is designed to affect the Kohn-Sham wavefunctions only in the vicinity of the atoms at  $\mathbf{R}$ , called augmentation region  $\Omega_{\mathbf{R}}$ . We note this by defining  $T$  as a deviation of unity by terms acting only in the respective  $\Omega_{\mathbf{R}}$ :

$$T = \mathbb{1} + \sum_{\mathbf{R}} T_{\mathbf{R}}. \quad (2.38)$$

The atom-centered transformations  $T_{\mathbf{R}}$  are defined by specifying target functions  $|\phi_i\rangle$  of  $T_{\mathbf{R}}$  for initial functions  $|\tilde{\phi}_i\rangle$  by  $|\phi_i\rangle = (\mathbb{1} + T_{\mathbf{R}}) |\tilde{\phi}_i\rangle$ . Outside of  $\Omega_{\mathbf{R}}$  target and initial functions coincide. Inside of  $\Omega_{\mathbf{R}}$  both functions are complete. The index  $i$  is a combined index the atomic position  $\mathbf{R}$  and all quantum numbers at the respective atomic position. One choice of the target functions are solutions of the radial Schrödinger equation for a certain energy. The target functions are assumed to be orthogonal to core states.

In order to specify the transformation, we expand the pseudo wavefunction within  $\Omega_{\mathbf{R}}$  in initial functions:

$$|\tilde{\psi}\rangle = \sum_i c_i |\tilde{\phi}_i\rangle. \quad (2.39)$$

By acting with  $T$  on this equation we get

$$|\psi\rangle = T |\tilde{\psi}\rangle = \sum_i c_i |\phi_i\rangle. \quad (2.40)$$

We subtract Eq. (2.39) from Eq. (2.40) and arrive at

$$|\psi\rangle = |\tilde{\psi}\rangle - \sum_i c_i |\tilde{\phi}_i\rangle + \sum_i c_i |\phi_i\rangle, \quad (2.41)$$

which defines the transformation up to the unknown coefficients  $c_i$ . Because  $T$  is linear, we can write the  $c_i$  as scalar products  $c_i = \langle \tilde{p}_i | \tilde{\phi}_i \rangle$ , where the so called projector functions  $|\tilde{p}_i\rangle$  fulfill  $\sum_i |\tilde{\phi}_i\rangle \langle \tilde{p}_i| = \mathbb{1}$ . We choose the projector functions to be localized in  $\Omega_{\mathbf{R}}$ . Finally, the transformation  $T$  reads

$$T = \mathbb{1} + \sum_i \left( |\phi_i\rangle - |\tilde{\phi}_i\rangle \right) \langle \tilde{p}_i| \quad (2.42)$$

and is defined by the target functions  $|\phi_i\rangle$ , the initial functions  $|\tilde{\phi}_i\rangle$  and the projector functions  $|\tilde{p}_i\rangle$ . The specific choice and parametrization of the three defining functions in the Vienna ab initio simulation package (VASP), which we use for all DFT calculations in this work, is documented in Ref. [119]. Beside the frozen core approximation, practical implementations come with the inevitable approximations of a plane wave cut-off energy and the limited number of projector functions (also called augmentation channels). However, these approximations are controllable as calculations can be systematically checked for convergence with respect to both cut-offs.

## 2.3. Dynamical mean-field theory

Density functional theory in LDA or GGA, discussed in the prior section, fails to describe the electronic structure of strongly correlated systems. The remaining sections of

this work's methodological part are devoted to methods designed to solve many-body models, which include strong correlation effects. We begin by introducing the dynamical mean-field theory (DMFT, [61]): DMFT is a non-perturbative method based on Green functions to approximate the solution of the Hubbard model. It is based on the observation that the Hubbard model on lattices with infinite coordination number can be mapped exactly to an Anderson impurity model (AIM) [60]. This is equivalent to the statement, that the self-energy in the Hubbard model becomes purely local (i.e.,  $k$  independent) in infinite dimensions. The DMFT approximation consists of mapping the Hubbard model with *arbitrary* coordination number to a self-consistently defined AIM. Again, this statement can be reformulated in terms of the approximation for the self-energy: DMFT approximates the exact,  $k$ -dependent self-energy  $\Sigma(k, \omega)$ , by a  $k$ -independent self-energy  $\Sigma(\omega)$ . Due to the finite number of interacting states, the AIM is far simpler to solve than the Hubbard model.

To further motivate the method, let us analyze the possible dynamics of the electrons at one lattice site for the one band Hubbard model (compare left side of Fig. (2.6)). The lattice site can be empty, populated by one electron, or doubly occupied, in which case an energy penalty of  $U$  is paid. Electrons leaving the lattice site propagate through the rest of the interacting system and come back after some time. In this time the population of the lattice site may have changed or not. In dynamical mean-field theory, the rest of the system is replaced by effective *non-interacting* sites (called bath sites) to which electrons from the lattice site can hop on and off again (compare left side of Fig. (2.6)). This non-interacting bath and its coupling to the lattice site is tuned to mimic the dynamics of the interacting rest of the system as close as possible. This tuning is done by a self-consistency condition based on matching Green functions of the lattice and the effective system, which is introduced in the remainder of this section.

The central object in DMFT is the Green function and self-energy of the lattice. In order to formulate the DMFT self-consistency cycle, we first define all relevant objects. The lattice Matsubara Green function is connected to the single-particle Hamiltonian  $H(k)$  and the lattice self-energy  $\Sigma^{\text{lat}}(k, i\omega_n)$  via

$$G^{\text{lat}}(k, i\omega_n) = \frac{1}{i\omega_n + \mu - H(k) + \Sigma^{\text{lat}}(k, i\omega_n)}, \quad (2.43)$$

where  $\mu$  is the chemical potential. We obtain the local Green function of the lattice by summing over all  $k$  points

$$G^{\text{loc}}(i\omega_n) = \frac{1}{N_k} \sum_k G^{\text{lat}}(k, i\omega_n). \quad (2.44)$$

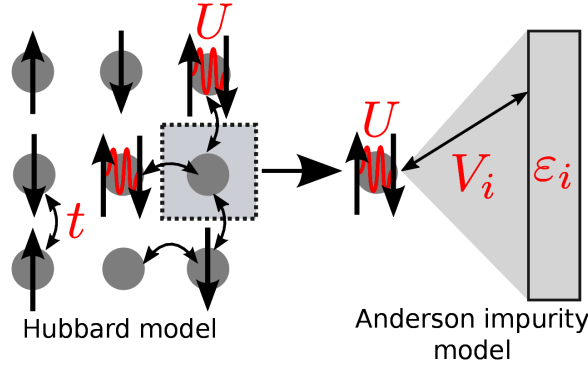


**Figure 2.6.:** In dynamical mean-field theory, the Hubbard model is approximated by a single interacting site embedded in a non-interacting bath. The hybridization of the impurity and the bath is defined self-consistently from the parameters of the Hubbard model. Hopping processes in both models are depicted as arrows

The impurity Green function  $G^{\text{imp}}(i\omega_n)$  is connected to its self-energy  $\Sigma^{\text{imp}}(i\omega_n)$  and the bath Green function  $\mathcal{G}_0^{\text{imp}}(i\omega_n)$  by the impurity Dyson equation

$$\left[\mathcal{G}_0^{\text{imp}}(i\omega_n)\right]^{-1} = \left[G^{\text{imp}}(i\omega_n)\right]^{-1} + \Sigma^{\text{imp}}(i\omega_n). \quad (2.45)$$

The hybridization function  $\Delta(i\omega_n)$  defines the Anderson impurity model together with the onsite energy  $\varepsilon_d$  and the interaction tensor  $U$  and is related to the bath Green function by

$$\Delta(i\omega_n) = i\omega_n - \mu + \left[\mathcal{G}_0^{\text{imp}}(i\omega_n)\right]^{-1}. \quad (2.46)$$

The DMFT approximation consists in setting

$$\Sigma^{\text{lat}}(k, i\omega_n) = \Sigma^{\text{imp}}(i\omega_n) \quad (2.47)$$

and such neglecting all  $k$ -dependence of the lattice self-energy. The hybridization function of the effective Anderson model is found by calculating a non-interacting impurity Green function from the difference of the local lattice Green function and the self-energy. This is done by solving above equations self-consistently using the approximation (2.47). In practice we start such an iteration by initializing the self-energy to zero. We then get the local non-interacting Green function via Eqs. (2.43), (2.44) and a lattice Dyson equation. The lattice Green function is used to calculate the  $\Delta(i\omega_n)$  using Eq.(2.46). This hybridization function defines an Anderson impurity model, which we solve through a method of our choice<sup>4</sup>. The solution provides the

<sup>4</sup>The method used in this work is the continuous-time quantum Monte Carlo method introduced in Sec. (2.5.2)

impurity Green function and self-energy for the next iteration via the impurity Dyson equation. The loop is also depicted in Fig. (2.7).

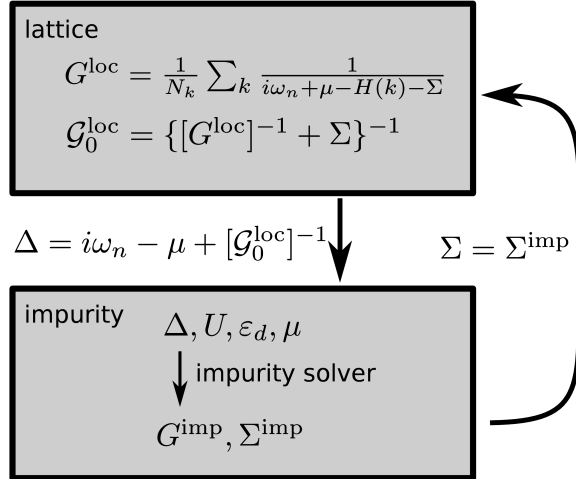


**Figure 2.7.:** Self consistency loop to solve the DMFT equations.

## 2.4. LDA+DMFT

So far, we have introduced two methods to simplify the many-body problem: density-functional theory in local density approximation and dynamical mean-field theory. Both LDA and DMFT have shortcomings: LDA fails in describing correlated electrons, for example, in open shell transition metal compounds where localized electrons are present. Due to its bad scaling of numerical complexity with the number of orbitals in the treated Hubbard model, DMFT is restricted to model systems with a limited number of orbitals and can not be directly used to describe realistic materials. A method to combine the best of both worlds is the LDA+DMFT or LDA++ scheme which was first introduced in Refs. [8] and [133]. Introductions and possible applications can be found in two reviews on DMFT [61, 113]. A detailed introduction and discussion of most of the ideas can also be found in Ref. [169], which we follow in this chapter.

The general idea of LDA+DMFT is to add explicit correlation terms in the form of a Hubbard model or an extended Hubbard model onto the DFT description of a material. This is done in three steps: First, we choose a subset of Kohn-Sham bands, which are most prone to interaction effects. We call these the correlated bands as only they are affected by correlations in the LDA+DMFT scheme. Secondly, we transform these

Kohn-Sham states to a set of localized orbitals  $\{|L\rangle\}$ . Thirdly, we augment a subset of these orbitals, the correlated orbitals  $\{|C\rangle\} \subseteq \{|L\rangle\}$ , with explicit Coulomb interaction. We call the remaining orbitals the uncorrelated orbitals  $\{|U\rangle\} \subset \{|L\rangle\}$ . We need a *localized* basis, because it fulfills the approximations of purely local interactions best. The Hamiltonian of the DFT+DMFT approach reads

$$H^{\text{DFT+DMFT}} = H^{\text{LDA}} - H^{\text{DC}} + \frac{1}{2} \sum_i \sum_{\sigma\sigma'} \sum_{\alpha\beta\gamma\delta} U_{\alpha\beta\gamma\delta}^i d_{i\alpha\sigma}^\dagger d_{i\beta\sigma'}^\dagger d_{i\gamma\sigma'} d_{i\delta\sigma}, \quad (2.48)$$

where  $H^{\text{LDA}}$  is the Kohn-Sham Hamiltonian, the index  $i$  is a site index,  $\sigma$  and  $\sigma'$  are spin indices and Greek indices relate to correlated orbitals ( $\{|C\rangle\}$ ) on the same site. The annihilation and creation operators correspond to the localized basis on the respective sites  $i$ . The two-particle matrix elements  $U_{\alpha\beta\gamma\delta}^i$  are site-dependent elements of the Coulomb interaction tensor.  $H^{\text{DC}}$  is introduced as a correction term to subtract the amount of local interaction already included in  $H^{\text{LDA}}$  through Hartree and exchange terms. This term is called double-counting correction. As DFT is not a diagrammatic theory, no analytic expression for the double counting correction exists. This double-counting problem is currently an open question which has been tackled through different strategies [137, 8, 43, 97]. We introduce the scheme used in this work in chapter (5).

The single-particle part of the DFT+DMFT Hamiltonian is readily available from a DFT calculation in the Kohn-Sham basis. We get single-particle energies  $\varepsilon_{n,\mathbf{k}}$  and Bloch functions  $|n, \mathbf{k}\rangle$  which diagonalize the Kohn-Sham Hamiltonian

$$H_{nn'}^{\text{LDA}}(\mathbf{k}) = \varepsilon_{n,\mathbf{k}} \delta_{nn'}, \quad (2.49)$$

where

$$\varepsilon_{n,\mathbf{k}} = \langle n, \mathbf{k} | H^{\text{LDA}} | n, \mathbf{k} \rangle. \quad (2.50)$$

The essence of LDA+DMFT is to choose the correlated bands and a corresponding localized basis and to calculate the Coulomb matrix elements. We deal with both issues in the next two sections.

### 2.4.1. Correlated bands and localized basis

The construction of the localized basis consists of two steps: First, the choice of the correlated bands and secondly, the choice of the localized basis states. We choose the correlated bands by selecting a subset of Kohn-Sham bands and label them by  $\{|m\rangle\}$ . The criterion for the excluded bands is that they are sufficiently well described by the

LDA and have a low overlap with the correlated orbitals  $\{|C\rangle\}$ . This criterion is rather weak and leads to ambiguities in the choice. In practice, the choice has to be reasoned by physical considerations. We follow Refs. [98, 6] to discuss the choice of the localized basis. More details about projecting Bloch states on localized orbitals can be found in appendix A and B of Ref. [3]. After reproducing the main results of [98], we discuss disadvantages of this approach and show a route to circumvent some of them.

As first guess to a localized basis we use the first order target functions  $|\phi_0\rangle$  from the PAW formalism (Sec. (2.2.2), Eq. (2.38)). The advantage of the PAW target functions is that their projection onto Bloch functions are readily available as standard output from VASP. The physical advantage to use the first order PAW target functions is that they are localized by definition. The downside of the first order target functions is that they are not orthonormal to the remaining PAW target functions, which is one reason why we cannot use the target functions directly.

Let us specify the notation for the localized basis: We have basis functions  $|L_\alpha^{\mathbf{R}}\rangle$  with orbital indices  $\alpha$  for each site  $\mathbf{R}$ . The DFT Hamiltonian (2.49) in the localized basis reads

$$H_{\alpha\alpha'}^{\mathcal{C}}(\mathbf{k}) = \sum_m \langle L_\alpha^{\mathbf{R}} | m, \mathbf{k} \rangle \varepsilon_{m,\mathbf{k}} \langle m, \mathbf{k} | L_{\alpha'}^{\mathbf{R}} \rangle, \quad (2.51)$$

where  $m$  are the correlated bands<sup>5</sup>. Obviously, the object of interest is  $P_{m,\alpha}^{\mathcal{C}}(\mathbf{k}) = \langle L_\alpha^{\mathbf{R}} | m, \mathbf{k} \rangle$ . The PAW decomposition (compare Eq. (2.42)) of the projection reads

$$\langle L_\alpha^{\mathbf{R}} | m, \mathbf{k} \rangle = \langle L_\alpha^{\mathbf{R}} | m, \tilde{\mathbf{k}} \rangle + \langle L_\alpha^{\mathbf{R}} | \left( \sum_i \left( |\phi_i\rangle - |\tilde{\phi}_i\rangle \right) \langle \tilde{p}_i | m, \tilde{\mathbf{k}} \rangle \right), \quad (2.52)$$

where  $i$  is a combined index for the site, orbital and augmentation order  $\nu$ . For  $|L_\alpha^{\mathbf{R}}\rangle$ , which are well localized inside the PAW sphere, the first and last term cancel and we get

$$\langle L_\alpha^{\mathbf{R}} | m, \mathbf{k} \rangle = \sum_i \langle L_\alpha^{\mathbf{R}} | \phi_i \rangle \langle \tilde{p}_i | m, \tilde{\mathbf{k}} \rangle. \quad (2.53)$$

By choosing the first order target functions as localized orbitals, we fix the orbital and site indices of  $|L_\alpha^{\mathbf{R}}\rangle$  and  $|\phi_i\rangle$  and only retain the augmentation order index  $\nu$ :

$$\langle L_\alpha^{\mathbf{R}} | m, \mathbf{k} \rangle = \sum_\nu \langle \phi_{\nu'=0} | \phi_\nu \rangle \langle \tilde{p}_\nu | m, \tilde{\mathbf{k}} \rangle. \quad (2.54)$$

---

<sup>5</sup>The restriction of the sum to the correlated bands only is denoted by the superscript  $\mathcal{C}$  in  $H^{\mathcal{C}}$ .

Following the implementation in VASP, we choose following definition for the projections: The absolute value of the projections is

$$|\langle L_{\alpha}^{\mathbf{R}} | m, \mathbf{k} \rangle|^2 = \sum_{\nu\nu'} \langle m, \tilde{\mathbf{k}} | \tilde{p}_{\nu} \rangle \langle \phi_{\nu} | \phi_{\nu'} \rangle \langle \tilde{p}_{\nu'} | m, \tilde{\mathbf{k}} \rangle \quad (2.55)$$

and the phase is

$$\arg(\langle L_{\alpha}^{\mathbf{R}} | m, \mathbf{k} \rangle) = \arg(\langle \tilde{p}_{\nu=0} | m, \tilde{\mathbf{k}} \rangle), \quad (2.56)$$

which is an unambiguous definition of the phase. The summation of the phase over more than one augmentation order may lead to erroneous cancellation of the phases belonging to each augmentation order. A comparison of different definitions of the projector is done in Ref. [98].

As mentioned in the beginning of this section, the  $\langle L_{\alpha}^{\mathbf{R}} | m, \mathbf{k} \rangle$  defined by Eqs. (2.55) and (2.56) do not correspond to orthonormal localized basis functions, because of the finite number of Bloch functions and because the PAW augmentation functions are not orthonormal. We can promote the basis to an orthonormal system by a Bloch transform and an orthonormalization. The Bloch transform reads

$$|L_{\alpha, \mathbf{k}}^{\mathbf{R}'}\rangle = \sum_{\mathbf{T}} e^{i\mathbf{k}\cdot\mathbf{T}} |L_{\alpha}^{\mathbf{R}'+\mathbf{T}}\rangle, \quad (2.57)$$

where we have split the site index  $\mathbf{R}$  into  $\mathbf{T}$ , a Bravais lattice vector, and  $\mathbf{R}'$ , the position of an atom in the unit cell. We orthonormalize the projections  $P_{m, \alpha}^{\mathcal{C}}(\mathbf{k})$  by

$$\bar{P}_{m, \alpha}^{\mathcal{C}}(\mathbf{k}) = \sum_{\alpha'} [O(\mathbf{k})]_{\alpha\alpha'}^{-1/2} P_{m, \alpha'}^{\mathcal{C}}(\mathbf{k}), \quad (2.58)$$

where  $O(\mathbf{k})_{\alpha\alpha'}$  is the overlap matrix defined by

$$O_{\alpha\alpha'}(\mathbf{k}) = \sum_m P_{m, \alpha}^{\mathcal{C}}(\mathbf{k}) (P_{m, \alpha'}^{\mathcal{C}}(\mathbf{k}))^*. \quad (2.59)$$

In principle we could orthonormalize by a Gram-Schmidt process or a QR-factorization, but the first has numerical deficiencies and the latter is prone to destroy symmetries of the orbitals. In practice, we calculate the inverse square root of the overlap matrix by a singular value decomposition of the overlap matrix, which allows us to calculate the pseudo inverse of  $O(\mathbf{k})$ .

So far, we have simply reproduced the result from Refs. [98, 6]. In the following, we discuss issues of this scheme and a route to deal with them. In order to define unitary projectors, the number of localized states has to be the same as the number

of correlated bands. This number determines the shape of the localized basis states after the orthonormalization: more bands lead to stronger localized states, less bands to stronger delocalized states. Consider the following: We augment the  $d$  states of a system with Coulomb interaction and therefore choose the five atomic  $d$  states to be part of the localized basis. The bands with  $d$  character are entangled with other bands such that we have to include more states with, e.g.,  $s$  or  $p$  symmetry in the localized basis. This choice naturally affects the number of correlated bands. Using  $d$  and  $s$  states leads to a six-dimensional space, using  $d$  and  $p$  states leads to an eight-dimensional space: the choice of additional uncorrelated states affects the shape of the  $d$  states via the number of correlated bands. A more controlled approach is to fix the number of correlated bands by considering the  $d$  states only and to *calculate* the remaining localized states needed to span the correlated space. We do this by calculating the orthogonal complement of the states of interest with respect to the space spanned by the correlated bands.

We distinguish between *correlated* localized states  $|C\rangle$  subject to explicit Coulomb interaction in the LDA+DMFT Hamiltonian (Eq. (2.48)) and *uncorrelated* localized states  $|U\rangle$ . The uncorrelated states are defined by spanning the space defined by the projector

$$\sum_U |U\rangle \langle U| = \mathbb{1} - \sum_C |C\rangle \langle C|, \quad (2.60)$$

where  $\mathbb{1} = \sum_m |m, \mathbf{k}\rangle \langle m, \mathbf{k}|$  is the unity operator with respect to the correlated bands. To calculate the projections of the  $|U\rangle$  on the Kohn-Sham states, we start from the orthonormalized projectors on  $\{|C\rangle\}$ ,

$$\bar{P}_{m,\alpha}^C(\mathbf{k}) = \langle U|m\rangle, \quad (2.61)$$

which are obtained from the PAW projectors as presented above. In order to keep the following expressions concise, we suppress all irrelevant indices. We calculate the first state,  $|U\rangle^{(1)}$ , of the uncorrelated orbitals by letting the projector defined in Eq. (2.60) act on a Bloch state  $|m'\rangle$

$$|U\rangle^{(1)} = \sum_U |U\rangle \langle U|m'\rangle = |m'\rangle - \sum_C |C\rangle \langle C|m'\rangle. \quad (2.62)$$

The scalar products of  $|U\rangle^{(1)}$  and the Bloch states  $|m\rangle$  are the projection matrix  $\bar{P}_{m,\alpha}^{U(1)}(\mathbf{k})$  which explicitly reads

$$\begin{aligned} \bar{P}_{m,\alpha}^{U(1)}(\mathbf{k}) &= \langle U|^{(1)} |m\rangle = \delta_{m',m} - \sum_C \langle m'|C\rangle \langle C|m\rangle \\ &= \delta_{m',m} - \sum_\alpha \langle m', \mathbf{k}|L_{\alpha,\mathbf{k}}^{\mathbf{R}'}\rangle \langle L_{\alpha,\mathbf{k}}^{\mathbf{R}'}|m, \mathbf{k}\rangle. \end{aligned} \quad (2.63)$$

We calculate the projections onto the remaining states,  $|U\rangle^{(n>1)}$ , iteratively by using the projectors

$$\mathbb{1}^C - \sum_C |C\rangle \langle C| - \sum_i |U\rangle^{(i)} \langle U|^{(i)} \quad (2.64)$$

with the remaining Bloch states. Actually, this is a Gram-Schmidt process. In each iteration of the Gram-Schmidt process, we get orthogonal states to some given orthonormal basis, which is what we have described above. In practice, we do not perform a Gram-Schmidt process, but a QR decomposition of an otherwise empty matrix but the upper rows equal to  $\bar{P}_{m,\alpha}^C(\mathbf{k})$ .

A downside of this method is the uncontrolled shape and symmetry of the uncorrelated localized states. However, as long as we are only interested in orbital resolved properties of the correlated orbitals this is no real issue. An additional advantage of not using PAW  $s$  or  $p$  states is that they may have low overlap with the Bloch bands. This can lead to serious issues in obtaining a band structure resembling the DFT band structure (for a more detailed discussion of projections with low overlap see, e.g., Refs. [2, 3])

An alternative approach is a Wannier projection [147, 207], where the localized states can be arbitrary. In the framework of Wannier projection the localized states can even be iteratively calculated to be maximally localized. This scheme is computationally rather demanding and has issues for entangled band structures.

### 2.4.2. Hybridization functions

So far, we have discussed the transformation of Kohn-Sham Hamiltonians in the case of correlated lattice systems leading to Hubbard models. For correlated impurities in weakly interacting hosts we can use a similar approach which leads to an Anderson impurity model. This is, e.g., done in Ref. [210] for Co atoms in a Cu crystal. The AIM can then be solved by methods we introduce in the next two sections. In principle, we extract the hybridization function (compare Eq. (2.15)) of an AIM in a basis localized on the impurity. Following Ref. [6], the Kohn-Sham Green function  $G_{\text{KS}}(\omega)$  reads

$$G_{\text{KS}}(z) = \sum_{m,\mathbf{k}} \frac{|m, \mathbf{k}\rangle \langle m, \mathbf{k}|}{z - \varepsilon_{m,\mathbf{k}}}. \quad (2.65)$$

Equivalently to the construction of a Hamiltonian in the localized basis in Sec. (2.4.1), we use projectors to localized basis states  $\bar{P}_{m,\alpha}^C(\mathbf{k})$ , derived from the impurities' target functions in the PAW formalism. We obtain the Green function in the localized basis

$$[G_{\text{KS}}^C]_{\alpha\alpha'}(z) = \sum_{m,\mathbf{k}} \frac{\bar{P}_{m,\alpha}^C(\mathbf{k}) [\bar{P}_{m,\alpha'}^C(\mathbf{k})]^*}{z - \varepsilon_{m,\mathbf{k}}}, \quad (2.66)$$

which is related to the hybridization function via Eq. (2.16).

### 2.4.3. Interaction terms

The brute force calculation of the Coulomb interaction matrix elements from their definition

$$U_{\alpha\beta\gamma\delta} = \int d^3r \int d^3r' v(\mathbf{r} - \mathbf{r}') \psi_{\alpha}^*(\mathbf{r}) \psi_{\beta}^*(\mathbf{r}') \psi_{\gamma}(\mathbf{r}') \psi_{\delta}(\mathbf{r}). \quad (2.67)$$

using the localized basis states from the last section is not very helpful in the case of solids, as the corresponding Hubbard model on a low-energy subspace is embedded in a sea of high-energy electrons. The biggest shortcoming of this approach is that we neglect the screening of the interaction terms in the Hubbard model by high-energy electrons. We take this screening into account by using interactions which carry the information about their high-energy environment: we calculate *effective* Coulomb interaction matrix elements. Two routes are basically possible: The first one, discussed in the next section, relies on a parametrization of the Coulomb interaction to fit the model to experimental results. The second route is to calculate the screening from the available DFT information, i.e., in an ab initio way. This is described in the subsequent section.

#### Coulomb interaction as parameter

A useful attempt to parametrize the Coulomb interaction is to use the Coulomb interaction of the bare atom and to scale the matrix elements to our convenience. Later, we will see that for  $d$  electrons basically only two parameters enter the expressions for all matrix elements  $U_{\alpha\beta\gamma\delta}$ . To this end, we calculate  $U_{\alpha\beta\gamma\delta}$  with atomic orbitals  $\Psi_{nml}(\mathbf{r}) = R_{nl}(r)Y_{lm}(\theta, \phi)$  using the definition (2.67) with the bare Coulomb interaction  $v(\mathbf{r}_1 - \mathbf{r}_2) = |\mathbf{r}_1 - \mathbf{r}_2|^{-1}$ . We start by writing the Coulomb interaction in spherical harmonics

$$\frac{1}{|\mathbf{r}_1 - \mathbf{r}_2|} = \sum_{k=0}^{\infty} \frac{r_{<}^k}{r_{>}^{k+1}} \frac{4\pi}{2k+1} \sum_{q=-k}^k Y_{kq}(\theta_2, \phi_2) Y_{kq}^*(\theta_1, \phi_1), \quad (2.68)$$

where  $r_{<} = \min(r_1, r_2)$  and  $r_{>} = \max(r_1, r_2)$ . In the following we restrict our discussion to the  $3d$  shell, i.e., we fix  $n = 2$  and  $l = 2$  in the combined index  $\alpha = (n_{\alpha}, l_{\alpha}, m_{\alpha})$ , such that  $m$  is restricted to  $m = -2, -1, \dots, 2$ . The Coulomb interaction then reads

$$U_{m_{\alpha}m_{\beta}m_{\gamma}m_{\delta}} = \sum_{k=0}^{2l} a_k(m_{\alpha}m_{\delta}, m_{\beta}m_{\gamma}) F_k, \quad (2.69)$$

where the angular integrals  $a_k$  are shorthands for

$$a_k(m_\alpha m_\delta, m_\beta m_\gamma) = \frac{4\pi}{2k+1} \sum_{q=-k}^k \langle l m_\alpha | Y_{kq} | l m_\delta \rangle \langle l m_\beta | Y_{kq}^* | l m_\gamma \rangle. \quad (2.70)$$

The integrals  $\langle l_1 m_1 | Y_{l_2 m_2} | l_3 m_3 \rangle$  are also called Gaunt coefficients<sup>6</sup>. The  $F_k$  are radial Slater integrals defined by

$$F_k = \int dr \int dr' r^2 r'^2 R_{nl}^2(r) R_{nl}^2(r') \frac{r^k}{r^{k+1}}. \quad (2.71)$$

The rotational symmetry leads to two simplifications: First, many angular integrals are zero, such that only few of the  $U_{m_\alpha m_\beta m_\gamma m_\delta}$  in Eq. (2.69) are non-zero. Secondly, only  $F_0$ ,  $F_2$  and  $F_4$  are non-zero. In practice, we assume that the angular part of the integrals is the same as in the atom. The severeness of this approximation is discussed in Ref. [181] for the examples of SrVO<sub>3</sub> and BaOsO<sub>3</sub>. We treat the remaining three radial integrals as parameters. More commonly, the average direct and exchange term  $U$  and  $J$  are used. They are defined by

$$U = \frac{1}{(2l+1)^2} \sum_{m,m'} U_{mm'm'm}, \quad (2.72)$$

$$U - J = \frac{1}{2l(2l+1)} \sum_{m,m'} U_{mm'm'm} - U_{mm'mm'}. \quad (2.73)$$

We can show that  $U$  is equal to  $F^0$ . For  $d$  electrons  $J$  is equal to  $(F^2 + F^4)/14$ . Calculations have shown, that the ratio of  $F^2$  and  $F^4$  is almost constant for  $d$  electrons [10, 45]. For  $3d$  electrons the ratio is  $F^4 \approx 0.625F^2$ . In summary, we use the following relation between average Coulomb interaction and Slater integrals throughout the work:

$$F^0 = U, \quad (2.74)$$

$$F^2 = \frac{14}{1.625} J, \quad (2.75)$$

$$F^4 = 0.625F^2. \quad (2.76)$$

This leaves only two free parameters, namely  $U$  and  $J$  or  $F^0$  and  $F^2$ , to fix the Coulomb interaction tensor defined in Eq. (2.69).

<sup>6</sup>The Gaunt coefficients are proportional to products of Clebsh-Gordon coefficients, which are easily calculated and are also tabulated in [62].

### Ab initio Coulomb interaction and screening from a high-energy subspace

As mentioned in the beginning of this section, the brute force calculation of the Coulomb matrix elements from some wavefunctions via Eq. (2.67) leads to too big matrix elements as it neglects screening from high-energy electrons. We can take this screening into account on a different, simpler, level of approximation by using interactions which carry the information about their high-energy environment. In order to take into account the effects of high-energy electrons on the low-energy model, we assume the electronic structure of the high-energy region to be fixed and calculate the screening of the interaction between low-energy electrons by electrons from the high-energy subspace. Commonly this screening is calculated in the random-phase approximation (RPA [208, 112], also introduced in more detail in Sec. (2.7) to calculate susceptibilities). Strictly speaking, a method called constrained RPA (cRPA, [13]) is used to cure a double counting of screening effects in RPA and the subsequent treatment<sup>7</sup> of the Hubbard model. The RPA approximation, in its essence, means to neglect correlations between the screening electrons, i.e., to treat screening electrons as classical charges.

The dielectric function  $\varepsilon(r)$  relates the bare interaction  $U$  with the screened interaction  $W$  by  $W = \varepsilon^{-1}U$ . The dielectric function is related to the polarization function  $P$  via  $\varepsilon = 1 - UP$ . The RPA approximation is used to calculate the polarization in linear response, which gives  $P^0 = G^0G^0$ , where  $G^0$  is the non-interacting Green function. More explicitly,  $P^0$  reads

$$P^0(\omega) = \sum_i^{\text{occ}} \sum_j^{\text{unocc}} \psi_i(r)\psi_i^*(r')\psi_j^*(r)\psi_j(r') \left( \frac{1}{\omega - \varepsilon_j + \varepsilon_i + i0^+} - \frac{1}{\omega + \varepsilon_j - \varepsilon_i + i0^+} \right), \quad (2.77)$$

compare Refs. [208] or [70]. In cRPA, we exclude contributions where  $i$  and  $j$  *both* belong to orbitals of the low-energy subspace. This is depicted for the example of a three band model in Fig. (2.8). The screened Coulomb matrix elements in (c)RPA are

$$W(\omega) = (1 - UP^0(\omega))^{-1}U. \quad (2.78)$$

In contrast to the bare Coulomb interaction  $U$ , the screened Coulomb interaction is frequency dependent. An inspection of Eq. (2.78) shows that  $\lim_{\omega \rightarrow \infty} W(\omega) = U$ . If a Hubbard model with a non-frequency-dependent interaction is desired, the screened interaction at  $\omega = 0$  is commonly used for simplicity. However, this may not be the optimal choice.

---

<sup>7</sup>The subsequent treatment is usually on a higher level of approximation than RPA.

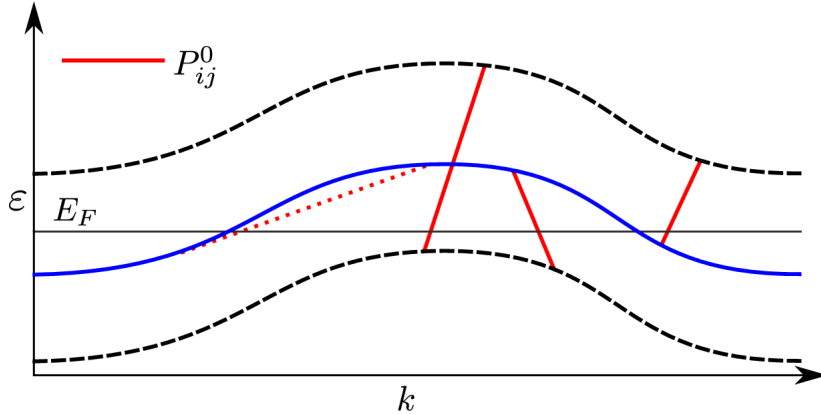


**Figure 2.8.:** Depiction of included (solid lines) and excluded (dotted lines) terms for the calculation of screening in constrained RPA by Eq. (2.77). Each line connects two non-interacting Green functions  $G_{ii}^0(k)$  and  $G_{jj}^0(k+q)$ . Terms of  $P_0$  including two  $G^0$  from the low-energy band (solid blue) are discarded. Terms containing at least one  $G^0$  from the high-energy bands (dashed black) are kept.

As remarked in Ref. [164], when DMFT is used to solve the resulting Hubbard model, i.e., only local screening is included, non-local terms where  $i$  and  $j$  both belong to the low-energy subspace should be included in the calculation of  $P^0$  in Eq. (2.77). Ref. [199] benchmarks the cRPA screening and shows that its quality depends on the model's details and can sometimes be poor.

An alternative to cRPA is the constrained local-density approximation (cLDA, [149, 68, 9, 39]), where screening effects are calculated entirely in the DFT formalism by calculating the energy difference of systems with different occupations in the correlated subspace. For the simple case of on-site density-density interaction, the Coulomb interaction matrix element is calculated by

$$W_{\text{eff}} = E(n+1) + E(n-1) - 2E(n), \quad (2.79)$$

where  $E(n)$  is the ground state energy of a super cell system with  $n$  electrons in the correlated subspace. The  $E(n \pm 1)$  are ground state energies of the system with 1 added/removed electron in the correlated subspace on one specific atom, while the occupation in the correlated subspace of all other atoms is kept fixed. In this way, the electronic response in the uncorrelated subspace is included on a DFT level. As this method is not used in this work, the details of the implementation of the method are not discussed here. Detailed information is contained in the references given above.

A comparison for the case of the  $3d$  transition metal Cr shows only minor differences of the effective Coulomb interaction between cRPA ( $W \sim 4.5$  eV, [189]) and cLDA ( $W \sim 5$  eV, [157])

## 2.5. Monte Carlo methods

Before we introduce two Monte Carlo based many-body methods, we take some time and consider the basic concept of Monte Carlo methods. Monte Carlo methods are a wide class of methods, which have in common the random sampling of a big phase space. Examples are numerical integrations of high dimensional integrals or optimizations dependent on many variables with a complicated function to minimize. The method is also widely used in statistical mechanics to calculate ground-state properties. In this section, we give a general introduction to Monte Carlo methods in statistical mechanics. We mainly follow Refs. [219, 159]. For in depth overviews we refer to Ref. [159], which mainly focuses on classical spin lattice systems and non-equilibrium dynamics, Ref. [124] with similar topics but which also contains a chapter about quantum Monte Carlo techniques, and Ref. [118] which gives an excellent overview over Monte-Carlo methods in general and its application to statistical mechanics with many code examples. Here, we lay out the principle of Monte Carlo methods to be able to first apply them in the determinant Monte Carlo method in Sec. (2.5.1) to solve the Hubbard model and secondly in the continuous-time quantum Monte Carlo method in Sec. (2.5.2) to solve the Anderson impurity model.

Consider some physical system that takes configurations  $\{i\}$ . Specific examples for configurations are a certain arrangement of spins on a lattice or a set of position and momentum values for particles. The system is governed by physical laws which determine the system's probability  $p_i$  for each configuration  $i$  in thermal equilibrium at a given temperature  $T$ . Specifically, the probabilities are governed by the partition function of the system. However, in practice the number configurations is often too large to calculate the partition function exactly. The key idea of the Monte Carlo technique is to perform an *importance sampling* of the phase space, i.e., to find those configurations which contribute most to the partition function. We do this by a so called random walk through the phase space: We start with some configuration  $i$  and randomly generate new configurations based only on the prior configuration. We show that setting up the rules to find the new configurations correctly, ensures that, on average, the random walk visits configurations with their physical probabilities  $p_i$ .

The transition probability to change the system from configuration  $i$  to  $j$  is  $T_{ji}$ . As  $T_{ij}$  are probabilities we can state rather trivially

$$T_{ji} \geq 0, \tag{2.80}$$

$$\sum_j T_{ji} = 1. \tag{2.81}$$

We show that  $T_{ji}$  always has an eigenvalue of  $\lambda = 1$  by assuming a vector  $\mathbf{v}$  with unit

entries,  $v_i = 1$ , and show that it is a left eigenvector using (2.81)

$$\sum_j v_j T_{ji} = v_i. \quad (2.82)$$

Starting with the (right) eigenvector equation

$$\sum_i T_{ji} v_i = \lambda v_j,$$

we show that the eigenvalues  $\lambda$  of  $T_{ji}$  obey  $|\lambda| \leq 1$ . Taking the absolute value of both sides, using (2.80) and the triangle inequality, we arrive at

$$\sum_i T_{ji} |v_i| \geq |\lambda| |v_j|. \quad (2.83)$$

Summing both sides over  $j$  and using (2.81), we arrive at

$$\sum_i |v_i| \geq |\lambda| \sum_j |v_j|, \quad (2.84)$$

from which  $|\lambda| \leq 1$  follows directly. We can now state that  $\lambda = 1$  is always the largest eigenvalue of  $T_{ij}$ .

Consider a vector  $v_i^N$ , which encodes the relative number of times a random walk governed by  $T_{ij}$  has visited the configuration  $i$  after  $N$  updates. In the following, we derive a condition for  $T_{ij}$  which guaranties, that all configurations are visited according to their physical probability, i.e.,  $v_i^\infty = p_i$ . If we set up  $T_{ij}$  such that  $p_i$  is a right eigenvector to the (largest) eigenvalue 1, we can use the fact that multiple action of a matrix on any vector  $v_i^N$  projects out the eigenvector to the largest eigenvalue, as long as  $v_i^N$  has non zero overlap with that eigenvector. The requirement for  $p_i$  to be the right eigenvector to the eigenvalue 1 of the matrix  $T_{ji}$  is equivalent to the requirement for  $T_{ji}$  to obey the so called *detailed balance*

$$T_{ji} p_i = T_{ij} p_j. \quad (2.85)$$

Using the detailed balance condition and (2.81) we can show  $\sum_i T_{ji} p_i = p_j$  by

$$\sum_i T_{ji} p_i = \sum_i T_{ij} p_j = p_j \sum_i T_{ij} = p_j. \quad (2.86)$$

We can for example ensure detailed balance by constructing  $T_{ij}$  by the famous Metropolis algorithm [151]. In the Metropolis algorithm the transition probability from one configuration  $i$  to another  $j$  is

$$T_{ji} = \begin{cases} p_j/p_i & \text{if } p_i \geq p_j \\ 1 & \text{if } p_i < p_j \end{cases}. \quad (2.87)$$

To check Eq. (2.85) we assume  $p_i > p_j$  without loss of generality and get  $T_{ji} = p_j/p_i$  and  $T_{ij} = 1$ . Evaluating (2.85) then gives  $p_j/p_i \cdot p_i = p_j$ . Now we have to ensure that every starting vector has non-zero overlap with the eigenvector  $p_i$ . This is equivalent to requiring ergodicity for  $T_{ji}$ , i.e., there is a non zero probability to reach every configuration  $j$  from any configuration  $i$  in a finite number of steps. The Metropolis suggestion for  $T_{ji}$  is ergodic since it assigns a non zero probability for any  $j$ . Note that the Metropolis algorithm does not require the calculation of  $p_i$  in any step but only the *ratio* of probabilities of consecutive steps. The ratio is in most cases much simpler to calculate. In the case of the Ising lattice, calculating the probability of a configuration involves calculating the partition function, i.e., solving the system. The ratio  $p_i/p_j$  is the fraction of Boltzmann factors  $p_i/p_j = \exp(-\beta(E_i - E_j))$ , where  $\beta$  is the inverse temperature and  $E_i$  and  $E_j$  are the energies of the configurations  $i$  and  $j$ , such that only energy differences have to be calculated. Alternative algorithms to Metropolis exist, one is the heat bath algorithm [153], where  $T_{ij}$  is defined by

$$T_{ji} = \frac{p_j}{p_i + p_j}. \quad (2.88)$$

In summary, any algorithm to update configurations has to obey

- detailed balance and
- ergodicity.

So far, our discussion has left out which next configuration  $j$  to suggest. This is of course dependent on the physical system at hand and the specific choice determines the efficiency of the sampling. However, there is no simple recipe to find efficient algorithms so that this task is left to our ingenuity and intuition.

Another point worth noting is that the use of random walks leads to correlations between subsequent steps, because a new configuration is generated based on the prior step. But when measuring physical quantities from a Monte Carlo simulation, we average over *independent* configurations. The usual technique to obtain independent configurations is to measure only after every  $m$ 'th step. We choose  $m$  to be bigger than the so called auto-correlation time of the system. This correlation time again depends very much on the algorithm of updating configurations and the physical system at hand.

A related technical problem is that the simulation has to be initialized with some configuration. This configuration can be in a region of the phase space with low  $p_i$ . Since the simulation does not run infinitely long and we approximate the true  $p_i$  with the relative number of times configurations are visited, the early configurations lead to a bias of the results. We avoid this systematical error by neglecting the first

configurations for measurements. The so called warm-up period has again to be chosen with the details of the simulated physical system in mind and should at least be some multiple of the correlation time.

### 2.5.1. Determinant quantum Monte Carlo

In this section, we shortly discuss a method, first introduced in Ref. [20], to statistically solve the Hubbard model. We use this method to obtain approximate solutions of the ground state of Hubbard models on finite honeycomb and square lattices in section (3). We follow an introduction from Ref. [230]. For reasons we discuss later, the method is especially efficient in the case of the half-filled Hubbard model. The method is formulated in the grand canonical ensemble, where the filling is adjusted by the chemical potential. The usual way of writing the Hubbard model for half filling is

$$H = \underbrace{-t \sum_{i,j,\sigma} (c_{i\sigma}^\dagger c_{j\sigma} + c_{j\sigma}^\dagger c_{i\sigma})}_{=H_K} + U \underbrace{\sum_i \left( n_{i\uparrow} - \frac{1}{2} \right) \left( n_{i\downarrow} - \frac{1}{2} \right)}_{=H_U}, \quad (2.89)$$

which corresponds to a chemical potential of  $\mu = -U/2$ .

In order to calculate thermodynamic expectation values, we approximate the operator  $P = 1/Z \exp(-\beta H)$ , where  $Z = \text{Tr} \exp(-\beta H)$  is the partition function. The starting point of the method is the so called Suzuki-Trotter decomposition of the imaginary time. Let us apply the decomposition to the partition function

$$\begin{aligned} Z &= \text{Tr} e^{-\beta H} \\ &= \text{Tr} \left( \prod_{l=1}^L e^{-\Delta\tau H} \right) \\ &= \text{Tr} \left( \prod_{l=1}^L e^{-\Delta\tau H_K} e^{-\Delta\tau H_U} \right) + \mathcal{O}(\Delta\tau^2), \end{aligned} \quad (2.90)$$

where  $L\Delta\tau = \beta$ . Since  $H_K$  and  $H_U$  do not commute, the last step is an approximation, at least for a finite step size  $\Delta\tau$ . As for numerical applications the step size is always finite, this introduces a systematic but controllable<sup>8</sup> error. The kinetic part of the term is quadratic in the fermionic operators and can therefore be written as

$$e^{-\Delta\tau H_K} = e^{-\Delta\tau H_{K\uparrow}} e^{-\Delta\tau H_{K\downarrow}}. \quad (2.91)$$

<sup>8</sup>The error is controllable, because the solution can be extrapolated to infinitesimally small  $\Delta\tau$ . Compare for example [184].

We write kinetic terms of the Hamiltonian in the following way

$$H_{K\sigma} = -t\mathbf{c}_\sigma^\dagger K \mathbf{c}_\sigma, \quad (2.92)$$

where  $K$  is a matrix containing the geometry of the lattice and  $\mathbf{c}^{(\dagger)} = (c_1^{(\dagger)}, c_2^{(\dagger)}, \dots, c_N^{(\dagger)})$ .

The interaction term is quartic in the fermionic operators which prohibits us to use single-particle methods to calculate the partition function straight forwardly. However, having separated the kinetic term and the interaction term in the exponent by the Suzuki-Trotter decomposition, we can apply the discrete Hubbard-Stratonovich transformation. We can apply the transformation for each lattice site independently since the sites decouple by

$$\begin{aligned} e^{-\Delta\tau H_U} &= e^{-U\Delta\tau \sum_{i=1}^N (n_{i\uparrow} - \frac{1}{2})(n_{i\downarrow} - \frac{1}{2})} \\ &= \prod_{i=1}^N e^{-U\Delta\tau (n_{i\uparrow} - \frac{1}{2})(n_{i\downarrow} - \frac{1}{2})}. \end{aligned} \quad (2.93)$$

The Hubbard-Stratonovich transformation for a lattice site  $i$  reads

$$e^{-U\Delta\tau (n_{i\uparrow} - \frac{1}{2})(n_{i\downarrow} - \frac{1}{2})} = \frac{1}{2} e^{-\frac{U\Delta\tau}{4}} \sum_{h_i = \pm 1} e^{\nu h_i (n_{i\uparrow} - n_{i\downarrow})}, \quad (2.94)$$

where  $\nu$  is defined by  $\cosh \nu = \exp(U\Delta\tau/2)$ . This identity is proven explicitly by letting the right and left side of the equation act on the four possible local states ( $|0\rangle$ ,  $|\uparrow\rangle$ ,  $|\downarrow\rangle$ , and  $|\uparrow\downarrow\rangle$ ), respectively. The transformation is only valid for  $U > 0$ , since otherwise no  $\nu$  can be found to solve  $\cosh \nu = \exp(U\Delta\tau/2)$ . However, a similar transformation exists for negative  $U$  [83]. By inserting the transformation into the exponential in Eq. (2.93) we get

$$\begin{aligned} e^{-\Delta\tau H_U} &= \prod_{i=1}^N \frac{1}{2} e^{-\frac{U\Delta\tau}{4}} \sum_{h_i = \pm 1} e^{\nu h_i (n_{i\uparrow} - n_{i\downarrow})} \\ &= \left( \frac{1}{2} e^{-\frac{U\Delta\tau}{4}} \right)^N \sum_{h_i = \pm 1} e^{\sum_{i=1}^N \nu h_i (n_{i\uparrow} - n_{i\downarrow})} \\ &= \left( \frac{1}{2} e^{-\frac{U\Delta\tau}{4}} \right)^N \text{Tr}_h e^{\sum_{i=1}^N \nu h_i (n_{i\uparrow} - n_{i\downarrow})}, \end{aligned} \quad (2.95)$$

where  $\text{Tr}_h$  denotes the trace over all variables  $h_i$ . As in the case of the kinetic part of the Hamiltonian, we split the interaction part into separate spin parts and write it in matrix form:

$$H_{V\sigma} = \pm \sum_i^N \nu h_i n_{i\sigma} = \pm \nu \mathbf{c}_\sigma^\dagger V(h) \mathbf{c}_\sigma, \quad (2.96)$$

where the plus (minus) sign is for  $\sigma = \uparrow (\downarrow)$  and  $V(h) = \text{diag}(h_1, h_2, \dots, h_N)$ . We insert the current results into the (approximate) expression for the partition function (2.90):

$$Z = \left(\frac{1}{2}e^{-\frac{U\Delta\tau}{4}}\right)^{NL} \text{Tr}_h \text{Tr} \left( \prod_{l=1}^L e^{-\Delta\tau H_{K\uparrow} + H_{V\uparrow}^l} \right) \left( \prod_{l=1}^L e^{-\Delta\tau H_{K\downarrow} + H_{V\downarrow}^l} \right), \quad (2.97)$$

where we have introduced the index  $l$  in the interaction part, which means that each time slice  $l$  has its own set of auxiliary variables  $h_i^l$ . We are left with a trace over products of exponentials of operators which are *quadratic* in the fermionic operators. Thus, we can apply the following identity for quadratic operators,  $H_l = \mathbf{c}^\dagger \underline{H}_l \mathbf{c}$ , reading

$$\text{Tr} (e^{-H_1} e^{-H_2} \dots e^{-H_L}) = \det \left( I + e^{-\underline{H}_L} e^{-\underline{H}_{L-1}} \dots e^{-\underline{H}_1} \right). \quad (2.98)$$

The right side of the equation is much easier to compute, as the  $\underline{H}_l$  are quadratic matrices with the dimension  $N$ , where  $N$  is the number of lattice sites, whereas the  $H_l$  are operators on the Hilbert space with dimension  $4^N$ . A proof of Eq. (2.98) is given in elementary notation in Ref. [84] and using Grassmann numbers in Ref. [20]. Using the identity we write the partition function in the following simple way:

$$Z = \left(\frac{1}{2}e^{-\frac{U\Delta\tau}{4}}\right)^{NL} \text{Tr}_h \det (M_\uparrow(h)) \det (M_\downarrow(h)), \quad (2.99)$$

where the matrices  $M_\sigma(h)$  are defined as

$$M_\sigma(h) = I + e^{t\Delta\tau K} e^{\mp\nu V(h^L)} e^{t\Delta\tau K} e^{\mp\nu V(h^{L-1})} \dots e^{t\Delta\tau K} e^{\mp\nu V(h^1)}. \quad (2.100)$$

We can also write down the approximate expression for the operator  $P = 1/Z \exp(-\beta H)$ :

$$P_h = \frac{1}{Z} \left(\frac{1}{2}e^{-\frac{U\Delta\tau}{4}}\right)^{NL} \det (M_\uparrow(h)) \det (M_\downarrow(h)). \quad (2.101)$$

We note that we have eliminated the quartic terms, i.e., arrived at a single-particle Hamiltonian, for the cost of introducing an auxiliary field defined by the variables  $h_i^l$  at each time slice. The solution to this problem is much easier and related to the Ising problem of classical spins on a lattice. The Ising lattice we have to solve does however not have the dimension of the lattice of the original problem but one dimension more. The extra dimension has the size  $L$  as it is the axis introduced by partitioning  $\beta$  into  $L$  slices. The configurations  $\{h\}$  can be sampled by the Metropolis-Hastings algorithm using the Metropolis ratio from one configuration  $h$  to another configuration  $h'$

$$r_{l,i} = \frac{\det (M_\uparrow(h')) \det (M_\downarrow(h'))}{\det (M_\uparrow(h)) \det (M_\downarrow(h))}. \quad (2.102)$$

In order to perform measurements, e.g., the time averaged one-particle Green function  $G_{ij}^\sigma$ , we have to calculate  $\langle c_{i\sigma} c_{j\sigma}^\dagger \rangle$  in the framework of the approximations we have done. Using similar techniques as in the proof of equation (2.98), compare Ref. [188], one can show that the Green function is related to the inverse of the matrices  $M_\sigma(h)$  by

$$G_{ij}^\sigma = [M_\sigma^{-1}(h)]_{ij}. \quad (2.103)$$

All DQMC results in this work are obtained with the implementation ‘‘QUantum Electron Simulation Toolbox’’ (QUEST 1.3.0)<sup>9</sup>.

### 2.5.2. Continuous-time quantum Monte Carlo

The method introduced in this section is able to solve Anderson impurity models by stochastically sampling diagrams contributing to the partition function. In contrast to the determinant quantum Monte Carlo method introduced in the last section, which suffers from systematic time-discretization errors, this method does not have any systematic errors at all; it is numerically exact. Given an infinite amount of computational resources, the solution is exact. However, the method comes with certain restrictions on the nature of the Anderson impurity models to solve. Complicated Coulomb interaction, low symmetries of the hybridization and spin-orbit coupling limit the applicability of the method. An extensive review of most flavors, applications and problems of continuous-time Quantum Monte Carlo (CT-QMC) is available in Ref. [66]. The flavor used in this work is the so-called hybridization expansion CT-QMC (CT-Hyb [225]) which we introduce for a one-band model following a lecture of Phillip Werner in 2015. We use this method to solve five-orbital Anderson impurity models in the context of DMFT in chapter (5) and as a method to benchmark a novel approximation scheme to the AIM in chapter (4).

The method is introduced in the action formalism. We start with the case of a spinless Anderson impurity model without interaction. The model is defined by a hybridization function  $\Delta(\tau)$  in imaginary time and a chemical potential  $\mu$ . The impurity action in this case is defined by

$$S_{\text{imp}} = \int_0^\beta d\tau d\tau' c^\dagger(\tau) \Delta(\tau - \tau') c(\tau') - \mu \int_0^\beta d\tau n(\tau), \quad (2.104)$$

where time dependent operators are in the Heisenberg picture with respect to the impurity part of the AIM Hamiltonian, i.e.,  $c^{(\dagger)}(\tau) = \exp(\tau H_{\text{imp}}) c^{(\dagger)} \exp(-\tau H_{\text{imp}})$ . We

---

<sup>9</sup>A. Tomas, C-C. Chang, Z-J. Bai, and R. Scalettar, QUEST code (<http://quest.ucdavis.edu/>)

arrive at the impurity action by starting at the action for the full AIM Hamiltonian and integrating out the bath degrees of freedom, which generates the hybridization terms proportional to  $\Delta(\tau - \tau')$ . The corresponding partition function is

$$\begin{aligned} Z &= \text{Tr} [T e^{-S_{\text{imp}}}] \\ &= \text{Tr} \left[ T \exp \left( - \int_0^\beta d\tau d\tau' c^\dagger(\tau) \Delta(\tau - \tau') c(\tau') + \mu \int_0^\beta d\tau n(\tau) \right) \right], \end{aligned} \quad (2.105)$$

where  $T$  is the time ordering operator. In order to generate diagrams, we expand the partition function in powers of the hybridization function  $\Delta(\tau)$ . An alternative is to expand in powers of the interaction leading to the interaction expansion CT-QMC (CT-Int, compare Ref. [185]). A Taylor expansion of (2.105) gives

$$\begin{aligned} Z &= \sum_n \int d\tau_1 d\tau'_1 \cdots \int d\tau_n d\tau'_n \frac{(-1)^n}{n!} \text{Tr} \left[ T \exp \left( \int_0^\beta d\tau \mu n(\tau) \right) \times \right. \\ &\quad \left. \times c^\dagger(\tau_1) c(\tau'_1) \cdots c^\dagger(\tau_n) c(\tau'_n) \right] \Delta(\tau_1 - \tau'_1) \cdots \Delta(\tau_n - \tau'_n), \end{aligned} \quad (2.106)$$

which is a sum over traces over an increasing number of creation and annihilation operators weighted with hybridization events and an exponential factor. Possible terms of zeroth, first and second order in the hybridization function are depicted in Fig. (2.9). The possible states in the trace are the empty and filled impurity ( $|0\rangle$  and  $|1\rangle$ ). Because the system evolves in imaginary time along lines between these states, we call the lines connecting  $\langle 0|1\rangle$  and  $|0\rangle 1\rangle$  world lines. Creation and annihilation operators  $c^\dagger(\tau)$  and  $c(\tau')$  at times  $\tau$  and  $\tau'$  are connected through hybridization functions  $\Delta(\tau - \tau')$ . The corresponding intuitive physical picture of these arrows is electrons leaving the impurity to the bath at times depicted by empty circles and reentering the impurity at times depicted by full circles. This process is of course governed by the hybridization function. We can now exemplarily calculate the weights of the  $\langle 0| \dots |0\rangle$  diagrams. The zeroth order diagram has the weight  $\exp(0)$ . The first order diagram  $-(d\tau)^2 \exp(\mu l) \Delta(\tau_1 - \tau'_1)$ , where  $l$  is the length of the segment of the line in which the impurity is occupied. The weights of the two depicted second order diagrams are

$$(-1)^2 \exp(\mu(l_1 + l_2)) \Delta(\tau_1 - \tau'_1) \Delta(\tau_2 - \tau'_2) d\tau^4$$

and

$$-(-1)^2 \exp(\mu(l_1 + l_2)) \Delta(\tau_1 - \tau'_2) \Delta(\tau_2 - \tau'_1) d\tau^4.$$

The last two weights, belonging to diagrams of the same segment structure but different orderings of the times, can be generated by the determinant of the matrix

$$\underline{\Delta}^c = \begin{pmatrix} \Delta(\tau_1 - \tau'_1) & \Delta(\tau_2 - \tau'_1) \\ \Delta(\tau_1 - \tau'_2) & \Delta(\tau_2 - \tau'_2) \end{pmatrix}.$$

The determinant vastly simplifies practical calculations as it takes care of all possible

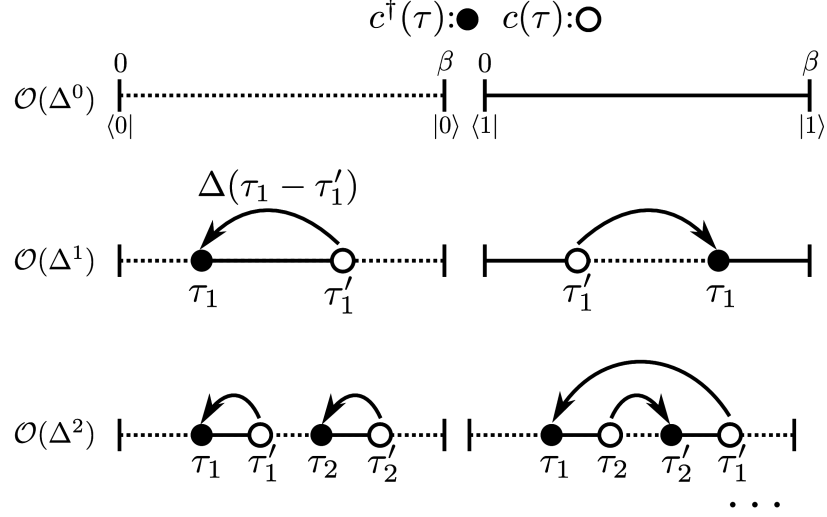


**Figure 2.9.:** Graphical representation of the first few terms in Eq. (2.106). Full/empty dots depict creation/annihilation operators, arrows represent hybridization functions. Full lines denote times with an electron on the impurity and dashed lines denote times where the impurity is empty. The lines connecting the outer states are called world lines.

time orderings for each configuration of segments. We can now write the partition function as a sum over all *segment* configurations with weights proportional to

$$w_c \propto e^{\mu l_{\text{seg}}} \det(\underline{\Delta}^c). \quad (2.107)$$

We can use these weights to sample the diagrams using the Metropolis Hastings algorithm using the ratio from one segment configuration  $c$  to another  $c'$

$$r = \frac{\exp(\mu l_{\text{seg}}) \det(\underline{\Delta}^c)}{\exp(\mu l'_{\text{seg}}) \det(\underline{\Delta}^{c'})}. \quad (2.108)$$

The single-particle Green function can be calculated by writing down its definition in the hybridization expansion of the trace

$$\begin{aligned} G(\tau, \tau') &= \frac{1}{Z} \text{Tr} [T e^{-S_{\text{imp}}} c(\tau) c^\dagger(\tau')] \\ &= \frac{1}{Z} \sum_n \int d\tau_1 d\tau'_1 \cdots \int d\tau_n d\tau'_n \frac{(-1)^n}{n!} \text{Tr} \left[ T \exp \left( \int_0^\beta d\tau \mu n(\tau) \right) \times \right. \\ &\quad \left. \times c(\tau) c^\dagger(\tau') c^\dagger(\tau_1) c(\tau'_1) \cdots c^\dagger(\tau_n) c(\tau'_n) \right] \Delta(\tau_1 - \tau'_1) \cdots \Delta(\tau_n - \tau'_n) \end{aligned} \quad (2.109)$$

and sampling the trace with the configurations suggested by the Monte-Carlo algorithm.

The more interesting case of a one-orbital Anderson impurity model including spin and local interaction  $U$  on the impurity is described by the action

$$S_{\text{imp}} = \sum_{\sigma} \left[ \int_0^{\beta} d\tau d\tau' c_{\sigma}^{\dagger}(\tau) \Delta(\tau - \tau') c_{\sigma}(\tau') - \mu \int_0^{\beta} d\tau n_{\sigma}(\tau) \right] + U \int_0^{\beta} d\tau n_{\uparrow}(\tau) n_{\downarrow}(\tau). \quad (2.110)$$

In contrast to the spinless case we arrive at two expectation values for each config-

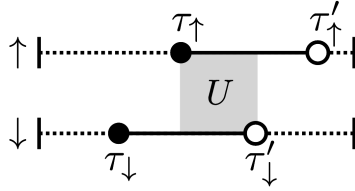


**Figure 2.10.:** Example for a configuration including spins where two electrons simultaneously occupy the impurity from  $\tau_{\uparrow}$  to  $\tau'_{\downarrow}$ .

uration: one for spin up and one for spin down. The interaction between electrons leads to an additional term in the exponential for those times at which the impurity is doubly occupied. An exemplary first order configuration is depicted in Fig. (2.10). By defining an overlap time  $l_{\text{overlap}} = \tau'_{\downarrow} - \tau_{\uparrow}$  and the occupation time  $l_{\sigma} = \tau'_{\sigma} - \tau_{\sigma}$  we arrive at the weight

$$e^{-\mu(l_{\uparrow}+l_{\downarrow})-U l_{\text{overlap}}} \det(\underline{\Delta}_{\uparrow}^c) \det(\underline{\Delta}_{\downarrow}^c). \quad (2.111)$$

Again, we can sample the configurations stochastically using the Metropolis Hastings algorithm.

In the case of multi-orbital Anderson models, more complicated interaction terms can appear which are not proportional to density-density type terms, such as  $n_i n_j$ . Arbitrary interaction terms can be dealt with in alternative schemes like the Krylov method [143] or a method described in Ref. [76]. Then, the simple picture of overlapping world lines breaks down and alternative ways of calculating the trace have to be found (see for example Ref. [66]). For all QMC solutions of AIMs in this work, the implementation of CT-Hyb in *w2dynamics* of the groups of Prof. Karsten Held (TU Vienna) and Prof. Giorgio Sangiovanni (University of Würzburg) is used [168]. A documentation is available in Ref. [160].

### 2.5.3. The sign problem

In quantum Monte Carlo methods a severe problem arises: the so called sign problem. Here, following Ref. [46], we shortly introduce this issue. In classical systems, as introduced in Sec. (2.5), we evaluate expectation values of observables  $A$  by summing over the weights  $p_i$  and the values of the observable  $A_i$  for all configurations  $i$ :

$$\langle A \rangle = \sum_i p_i A_i. \quad (2.112)$$

In contrast to classical systems, where the  $p_i$  can be interpreted as probabilities because they are positive definite,  $p_i$  can be positive and negative in the case of quantum systems. To be able to do an importance sampling anyway, we have to take care of the negative weights. We introduce a new weight defined by  $\tilde{p}_i = |p_i| / \sum_j |p_j|$  and absorb the sign of the weight into the observable we measure

$$\langle A \rangle = \frac{\sum_i A_i \text{sign}(p_i) \tilde{p}_i}{\sum_i \text{sign}(p_i) \tilde{p}_i} = \frac{\langle A \cdot s \rangle}{\langle s \rangle}, \quad (2.113)$$

where  $s$  is the sign operator with  $s_i = \text{sign}(p_i)$ . While this route is mathematically correct, random walks based on  $\tilde{p}_i$  instead of  $p_i$  may include unimportant regions of the phase space disproportionately high. If the average sign is close to zero, measurements of  $\langle A \cdot s \rangle$  tend to cancel each other leading to prohibitively bad statistics. However, for certain systems one can show that the sign problem is absent. In other cases numerical tests have shown that it is not severe.

In the case of DQMC, the half filled repulsive Hubbard model is sign-problem free. Additionally, certain fillings are favorable, e.g., when the non-interacting ground-state is non-degenerate [227]. In cases where the sign problem is present, the average sign scales as  $\langle s \rangle \propto \exp(-\beta N U \gamma)$ , where  $N$  is the system size and  $\gamma$  depends on the filling. The problems gets exponentially worse with lower temperature. [46, 188].

In the case of CT-QMC the sign problem is governed by the structure of the hybridization function (2.15). For strictly diagonal hybridization functions with respect to the orbital indices no sign problem occurs. Large off diagonal elements can lead to a sign problem which can be partly circumvented by a rotation of the orbital basis [54]. However, this is not entirely possible as the hybridization function is energy dependent. Here, a similar aggravation with lower temperatures as in the former case can be observed [54].

### 2.5.4. Analytic continuation

In this section, we introduce a method, called maximum entropy method, to cope with the problem of transforming noisy data from the imaginary axis to the real frequency

axis. Doing so we follow Ref. [92]. The CT-QMC algorithm samples the Green function on imaginary time (compare Eq. (2.109)). In order to compare results from the calculation to photo emission experiments (i.e., spectral information) we have to calculate the spectrum  $A(\omega) = -\frac{1}{\pi} \text{Im} G(\omega)$  on real frequencies. The transformation from the spectral function in real frequency to the Green function in imaginary time reads

$$G(\tau) = \int d\omega A(\omega) K(\tau, \omega), \quad (2.114)$$

where  $K(\tau, \omega)$ , the kernel, is defined by

$$K(\tau, \omega) = \frac{e^{-\tau\omega}}{1 + e^{-\beta\omega}}. \quad (2.115)$$

For discrete samples of  $\tau \rightarrow \tau_n$  and  $\omega \rightarrow \omega_m$  in a numerical implementation, the kernel is a matrix ( $K(\tau, \omega) \rightarrow K_{nm}$ ) which has to be inverted in order to get  $A(\omega_n) \rightarrow A_m$  from a measured  $G(\tau) \rightarrow G_n$ . The condition number of  $K$ , defined by the quotient of the largest and the smallest singular value, grows exponentially, making a straight forward (pseudo) inversion impossible<sup>10</sup>. That the measured  $G(\tau_n)$  are only known up to a statistical uncertainty worsens the problem considerably. A simple least square fit of  $\sum_m K_{nm} A_n$  to  $G_n$  leads to an overfitting of statistical noise. The singular values of an exemplary  $K$  are shown in Fig. (2.11): they fall exponentially.

Inverting the kernel is an example for an ill defined problem. This problem is tightly connected to so called inverse problems. Similar problems also arise in the reconstruction of volume data from noisy tomography measurements. Inverse problems have spawned quite an interest in mathematics. In that context, the maximum entropy method can also be seen as a generalized Tikhonov-Phillips regularization under the constraint of strictly positive spectral functions  $A_n$  using the entropy of  $A_n$  as a punishing term for the overfitting of noise [182, 155].

A possible route for finding an appropriate solution is to search for the most probable spectrum  $A(\omega)$  given a measured  $G(\tau)$  in a Bayesian sense. Mathematically spoken, we maximize the probability

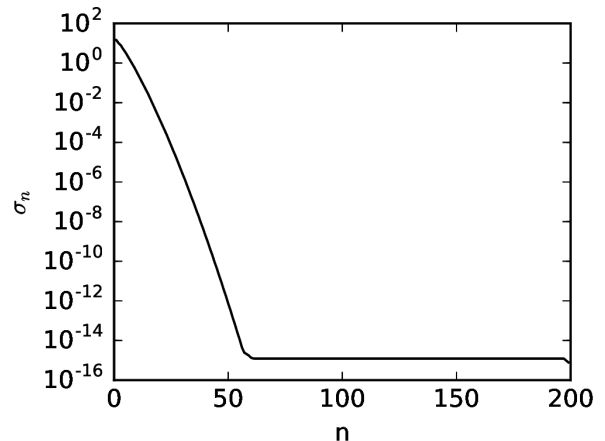
$$P(A|G) = \frac{P(G|A)P(A)}{P(G)}, \quad (2.116)$$

using Bayes theorem<sup>11</sup>, where  $P(G|A)$  is the likelihood function,  $P(A)$  is the prior probability and  $P(G)$  is constant, as we only deal with one measured  $G$  at a time,

<sup>10</sup>The calculation of the pseudo inverse is in fact equivalent to performing a least square fit.

<sup>11</sup>Bayes theorem states that the probability of finding  $a$  under the condition of  $b$ , times the probability of  $b$  is the same as the probability of finding  $b$  under the condition of  $a$ , times the probability of  $a$ :  $P(a|b)P(b) = P(b|a)P(a)$ .

**Figure 2.11:** Singular values of the Kernel  $K_{nm}$  (see Eq. (2.115)) for  $\beta = 100$  and a grid of 200 discretization points for  $\tau$  and  $\omega$  ranging from -4 to 4. The singular values for  $n \gtrsim 50$  are below machine accuracy.



and can therefore be ignored. The heart of the maximum entropy method is to define the prior probability with the help of the entropy  $S$  of  $A$  with respect to some default model  $m$ . This is possible because the spectrum is positive definite and, as its integral over the frequency is finite, can be normalized. Thus,  $A$  can be interpreted as a probability. The prior probability is then defined (compare [203] for a rigorous proof that the following form of the prior probability leads to the desired results) as

$$P(A|m(\omega), \alpha) = e^{\alpha S} \quad (2.117)$$

with

$$S = \int d\omega \left( A(\omega) - m(\omega) - A(\omega) \ln \left( \frac{A(\omega)}{m(\omega)} \right) \right). \quad (2.118)$$

Given uncorrelated data (see [92] for details on obtaining uncorrelated data from QMC simulations), the likelihood function  $P(G|A)$  is obtained by a least square fit weighted with the statistical uncertainty of the spectrum to the data:

$$P(G|A) = e^{-\chi^2/2} \quad (2.119)$$

with

$$\chi^2 = \sum_n \left( \frac{G_n - \sum_m K_{nm} A_m}{\sigma_n} \right)^2, \quad (2.120)$$

where  $\sigma_n$  is the error estimate of the measurement of  $G_n$ . Finally, we find the most probable spectrum  $A_m$  by maximizing

$$P(A|G) = e^{\alpha S - \chi^2/2}. \quad (2.121)$$

If some prior knowledge of the spectrum is available it can be used to choose a default model  $m$ . In practice this is seldomly the case, therefore a featureless flat or Gaussian model is used to obtain unbiased results.

The factor  $\alpha$ , which balances between the maximization of  $\exp(\chi^2/2)$  (overfitting of the data) and  $\exp(S)$  (reproduction of the default model), is a priori unknown. Two routes for determining  $\alpha$  are popular: In the so-called historic maximum entropy method [204, 67]  $\alpha$  is chosen such that  $\chi^2 = L$ , where  $L$  is the number of data points. This, however, tends to underfit the data [92]. The classic maximum entropy method (compare Ref. [203]) finds the most probable value of  $\alpha$  by maximizing

$$P(\alpha|G, m) = \int \frac{d^N A}{\prod_i \sqrt{A_i}} P(A, \alpha|G, m), \quad (2.122)$$

where

$$P(A, \alpha|G, m) \sim e^{\alpha S - \chi^2/2} P(\alpha), \quad (2.123)$$

and  $P(\alpha)$  is empirically assumed to be  $P(\alpha) = 1/\alpha$ . As the maximum of  $P(\alpha|G, m)$  is often not representative for the mean value of  $P(\alpha|G, m)$ , most modern implementations of the maximum entropy method use a generalized version of the classical maximum entropy method called Bryan's method [27]. It consists of averaging optimal spectra for many  $\alpha$  in the "classical" sense weighted with their respective probability. This gives

$$\bar{A} = \int d\alpha A(\alpha) P(\alpha|G, m). \quad (2.124)$$

Alternative approaches to the analytic continuation are stochastic sampling methods, e.g., the first implementation from Sandvik [186] or an implementation by Beach [16] who also proves that the maximum entropy method is in some sense a mean-field solution of a stochastic sampling algorithm. A stochastic method using no default model is the stochastic optimization method (SOM, [154], for a more pedagogical introduction and an overview of stochastic sampling methods see Ref. [155]). A comparison of the maximum entropy method and specifically the method introduced by Beach is done in Ref. [56]. In this work we use Bryan's maximum entropy method to obtain all analytic continuations.

## 2.6. Exact diagonalization

In its essence, exact diagonalization is the most straightforward method of solving the many-body problem that one can think of. The method consists of setting up the

full many-body Hamiltonian of a system in some basis (e.g., the occupation number basis) and solving it numerically. However, the size of the Fock-space (which is the size of the matrix we have to diagonalize) is  $2^N$  for a system of  $N$  single-particle states. Although conserved quantities of the Hamiltonian lead to a block diagonal structure of the Hamiltonian and reduce the size of the matrices considerably, each block matrix still grows exponentially with the system size. This makes it impossible to solve systems with more than  $\sim 20$  single-particle states exactly on modern computers. For larger systems of about  $\sim 30$  single-particle states, the use of iterative solvers for sparse matrices such as the Lanczos method (see [123] and Sec. (2.6.1)) or the Arnoldi method [127] give access to certain regions (e.g., the few lowest eigenvalues) of the spectrum. In the context of quantum chemistry<sup>12</sup> many methods exist which truncate the number of many-body basis states included in the calculation. This is often based on the number of excitations in the used Slater determinants relative to some non-interacting starting point [231]. Alternative schemes rely on an automatic selection of included basis states based on the overlap of the many-body states with the ground state (e.g., a method tailored for the use as impurity solver in the context of DMFT [141]). Such truncated methods can deal with several hundreds of single-particle states.

In this work, we use exact diagonalization to solve the Anderson impurity model (AIM, Sec. (2.1.2)). As exact diagonalization can only cope with very few states, solving the AIM with ED involves truncating the infinite-dimensional Hilbert space of the AIM to a dramatically smaller Hilbert space. This problem is known as the bath-discretization problem<sup>13</sup>. We introduce a novel approach to this problem in chapter (4). We also use exact diagonalization to solve Hubbard models on small one-dimensional lattices in Sec. (3), where we discuss nonlocal interaction effects in benzene.

The diagonalization of a Hamiltonian  $H$  gives eigenenergies  $E_n$  and eigenstates  $|n\rangle$  such that we can calculate thermodynamical expectation values of an operator  $A$  through

$$\langle A \rangle = \frac{1}{Z} \sum_n \langle n | A | n \rangle e^{-\beta E_n}. \quad (2.125)$$

We calculate the single-particle Green function  $G_{\alpha\beta}(z)$  from the Lehmann representa-

---

<sup>12</sup>In quantum chemistry exact diagonalization is known as full configuration interaction, full CI.

<sup>13</sup>The name stems from approximating the infinite number of bath sites of the AIM with only a few, i.e., discretizing the bath.

tion by

$$\begin{aligned} G_{\alpha\beta}(z) &= \frac{1}{Z} \sum_{nm} \frac{\langle m | c_\beta | n \rangle \langle n | c_\alpha^\dagger | m \rangle}{z - E_n + E_m} [e^{-\beta E_n} + e^{-\beta E_m}] \\ &= \frac{1}{Z} \sum_n e^{-\beta E_n} [G_{\alpha\beta}^{m+}(z) + G_{\alpha\beta}^{m-}(z)], \end{aligned} \quad (2.126)$$

with the excited Green functions

$$\begin{aligned} G_{\alpha\beta}^{m+}(z) &= \sum_m \frac{\langle n | c_\beta | m \rangle \langle m | c_\alpha^\dagger | n \rangle}{z - E_n + E_m} \\ G_{\alpha\beta}^{m-}(z) &= \sum_m \frac{\langle n | c_\beta^\dagger | m \rangle \langle m | c_\alpha | n \rangle}{z - E_m + E_n}, \end{aligned} \quad (2.127)$$

compare for example [174].

### 2.6.1. Lanczos method

The Lanczos method [123] is designed to find a subset of eigenvalues of sparse matrices. It deals with vastly larger matrices than methods to calculate the full spectrum. Most commonly, the method is used to find extremal eigenvalues which makes it attractive to find the  $T = 0$  ground state of a sparse Hamiltonian<sup>14</sup>. We follow Ref. [106] for the introduction of this method.

The  $N$  dimensional Hilbert space of a Hamiltonian  $H$  is spanned by a set of states  $\{|n_i\rangle\}$ . The basic idea of the Lanczos method is to approximate the ground state by the ground state of the Hamiltonian projected onto a set of only  $M$  states  $\{|m_i\rangle\} \subseteq \{|n_i\rangle\}$ .

In the case of the Lanczos method, this subset is the  $L$ 'th Krylov space [121] of a starting vector  $|\psi\rangle$ :  $\mathcal{K}^L(|\psi\rangle)$  is spanned by the vectors  $|m_0\rangle = |\psi\rangle$ ,  $|m_1\rangle = H|\psi\rangle$ ,  $|m_2\rangle = H^2|\psi\rangle, \dots, |m_L\rangle = H^L|\psi\rangle$ . We can construct an orthonormal basis of  $\mathcal{K}^L(|\psi\rangle)$  by orthogonalizing every vector to all subsequent vectors

$$b_{n+1} |m_{n+1}\rangle = H |m_n\rangle - \sum_{i=0}^n |m_i\rangle \langle m_i | H |m_n\rangle = H |m_n\rangle - a_n |m_n\rangle - b_n |m_{n-1}\rangle, \quad (2.128)$$

where  $a_n = \langle m_n | H |m_n\rangle$  and  $b_n = \langle m_n | H |m_{n-1}\rangle$ . By rearranging Eq. (2.128),

$$H |m_n\rangle = b_{n+1} |n+1\rangle + a_n |m_n\rangle + b_n |m_{n-1}\rangle \quad (2.129)$$

<sup>14</sup>A Hamiltonian which is sparse in some basis.

we immediately recognize that  $H$  is tridiagonal in the Lanczos space. In practice, the Hamiltonian in the subspace of only the first few hundred Lanczos states is used to approximate the true ground state. We reason the methods' fast convergence by analyzing the Ritz variational principle for the energy functional defined in Eq. (2.167),  $\tilde{\Phi}[\Psi] = E[\Psi]$ ,

$$E[\Psi] = \frac{\langle \Psi | H | \Psi \rangle}{\langle \Psi | \Psi \rangle}. \quad (2.130)$$

The functional gradient,

$$\frac{\delta E[\Psi]}{\delta \langle \Psi |} = \frac{H | \Psi \rangle - E[\Psi] | \Psi \rangle}{\langle \Psi | \Psi \rangle}, \quad (2.131)$$

is a vector in the direction of the steepest ascent of the functional. We therefore minimize the functional in the space spanned by  $|\Psi\rangle$  and  $H|\Psi\rangle$  to obtain a new wavefunction with lower energy  $|\Psi_1\rangle = \sin(\theta)|\Psi\rangle + \cos(\theta)H|\Psi\rangle$ . Using the same argument once more, we find a wavefunction with again lower energy by minimizing the functional in the space spanned by  $|\Psi_1\rangle$  and  $H|\Psi_1\rangle$ . We observe that the space spanned by  $|\Psi\rangle$ ,  $H|\Psi\rangle$ , and  $H^2|\Psi\rangle$  is equal to the space spanned by  $|\Psi_1\rangle$  and  $H|\Psi_1\rangle$ . We can therefore also directly minimize the functional in the three dimensional space, as we then have more variational degrees of freedom. The Krylov space is the natural space in which to search for the minimum of the energy as it is in each step enlarged by that vector which assures the best convergence in energy.

The Lanczos method is also used to efficiently calculate spectral functions via

$$G_c = \langle \Psi_c | \frac{1}{z - H} | \Psi_c \rangle \quad (2.132)$$

by setting up the Hamiltonian in the Krylov space of  $|\Psi_c\rangle$  which results in an approximation of  $z - H$  by a tridiagonal matrix

$$z - H \approx \begin{pmatrix} z - a_0 & -b_1 & 0 & 0 & \dots \\ -b_1 & z - a_1 & -b_2 & 0 & \dots \\ 0 & -b_2 & z - a_2 & -b_3 & \dots \\ \vdots & \vdots & \vdots & \vdots & \ddots \end{pmatrix}. \quad (2.133)$$

We find the first element of the inverted matrix recursively, which results in a continued fraction

$$[G_c]_{00} = [(z - H)^{-1}]_{00} \approx \frac{1}{z - a_0 - \frac{b_1^2}{z - a_1 - \frac{b_2^2}{z - a_2 - \dots}}}. \quad (2.134)$$

## 2.7. Random-phase approximation

In this section we derive the so called random-phase approximation (RPA) for two-particle Green functions in order to calculate charge and spin correlation functions for Hubbard models. The derivation is based on Ref. [47]. In Sec. (3), we use the RPA to compare the resulting correlation function with those from DQMC for Hubbard models on finite lattices.

The random-phase approximation is also called generalized Hartree-Fock approximation. While in Hartree-Fock we decouple two-particle terms on a static basis, i.e., directly in the Hamiltonian, we do this in RPA in a dynamical fashion. The decoupling is done only in the equation of motion of two-particle Green functions. Physically speaking, we treat the screening charges classically (see also Sec. (2.4.3) on cRPA). The RPA can also be derived in the language of diagrams, where it is based on neglecting all screening diagrams which are not “bubble” like (only bare particle-hole processes). The remaining “bubble” diagrams can then be summed to infinite order analytically [26].

The RPA is most easily derived in momentum space (the quantum number diagonalizing the one-particle part of the Hamiltonian,  $H_0$ ), in which the Hubbard model (2.4) reads

$$H = H_0 + H_1, \quad (2.135)$$

where

$$H_0 = \sum_{\mathbf{p}\sigma} \varepsilon_{\mathbf{p}} c_{\mathbf{p}\sigma}^\dagger c_{\mathbf{p}\sigma}, \quad (2.136)$$

$$H_1 = \frac{U}{N} \sum_{\mathbf{p}\mathbf{p}'\mathbf{q}} c_{\mathbf{p}+\mathbf{q}\uparrow}^\dagger c_{\mathbf{p}\uparrow} c_{\mathbf{p}'-\mathbf{q}\downarrow}^\dagger c_{\mathbf{p}'\downarrow}. \quad (2.137)$$

We closely follow the derivation in Ref. [47] for the transverse susceptibility  $\chi^{-+}$ : Here, we calculate the charge and spin susceptibility defined by

$$\chi^{c/s}(\mathbf{p}, \mathbf{q}, t) = i\Theta(t) \langle [c_{\mathbf{p}+\mathbf{q}\uparrow}^\dagger(t) c_{\mathbf{p}\uparrow}(t) \pm c_{\mathbf{p}+\mathbf{q}\downarrow}^\dagger(t) c_{\mathbf{p}\downarrow}(t), n(0, 0)] \rangle, \quad (2.138)$$

where  $n(0, 0) = \sum_{\mathbf{p}\mathbf{q}} c_{\mathbf{p}+\mathbf{q}\uparrow}^\dagger c_{\mathbf{p}\uparrow}$  is the local density. The respective equations of motion of the charge and spin susceptibility read

$$\begin{aligned} i \frac{\partial}{\partial t} \chi^{c/s}(\mathbf{p}, \mathbf{q}, t) = & -\delta(t) \langle [c_{\mathbf{p}+\mathbf{q}\uparrow}^\dagger c_{\mathbf{p}\uparrow} \pm c_{\mathbf{p}+\mathbf{q}\downarrow}^\dagger c_{\mathbf{p}\downarrow}, n(0, 0)] \rangle \\ & + i\Theta(t) \langle [[c_{\mathbf{p}+\mathbf{q}\uparrow}^\dagger(t) c_{\mathbf{p}\uparrow}(t) \pm c_{\mathbf{p}+\mathbf{q}\downarrow}^\dagger(t) c_{\mathbf{p}\downarrow}(t), H], n(0, 0)] \rangle. \end{aligned} \quad (2.139)$$

In order to solve the equations we calculate all commutators in the prior equation. We start with

$$[c_{\mathbf{p}+\mathbf{q}\sigma}^\dagger c_{\mathbf{p}\sigma}, H_0] = -(\varepsilon_{\mathbf{p}+\mathbf{q}} - \varepsilon_{\mathbf{p}})c_{\mathbf{p}+\mathbf{q}\sigma}^\dagger c_{\mathbf{p}\sigma}. \quad (2.140)$$

In the spin up case the commutator with the interacting  $H_1$  is

$$[c_{\mathbf{p}+\mathbf{q}\uparrow}^\dagger c_{\mathbf{p}\uparrow}, H_1] = U \sum_{\mathbf{p}'\mathbf{q}'} \left( c_{\mathbf{p}+\mathbf{q}+\mathbf{q}'\uparrow}^\dagger c_{\mathbf{p}'-\mathbf{q}'\downarrow}^\dagger c_{\mathbf{p}\uparrow} c_{\mathbf{p}'\downarrow} - c_{\mathbf{p}+\mathbf{q}\uparrow}^\dagger c_{\mathbf{p}'-\mathbf{q}'\downarrow}^\dagger c_{\mathbf{p}-\mathbf{q}'\uparrow} c_{\mathbf{p}'\downarrow} \right). \quad (2.141)$$

In the spin down case it is

$$[c_{\mathbf{p}+\mathbf{q}\downarrow}^\dagger c_{\mathbf{p}\downarrow}, H_1] = U \sum_{\mathbf{p}'\mathbf{q}'} \left( c_{\mathbf{p}'+\mathbf{q}'\uparrow}^\dagger c_{\mathbf{p}+\mathbf{q}-\mathbf{q}'\downarrow}^\dagger c_{\mathbf{p}'\uparrow} c_{\mathbf{p}\downarrow} - c_{\mathbf{p}'+\mathbf{q}'\uparrow}^\dagger c_{\mathbf{p}+\mathbf{q}\downarrow}^\dagger c_{\mathbf{p}'\uparrow} c_{\mathbf{p}+\mathbf{q}'\downarrow} \right). \quad (2.142)$$

In the RPA approximation we decouple the two-particle terms in Eqs. (2.141) and (2.142), which gives

$$[c_{\mathbf{p}+\mathbf{q}\uparrow}^\dagger c_{\mathbf{p}\uparrow}, H_1] \stackrel{\text{RPA}}{=} U \sum_{\mathbf{p}'} c_{\mathbf{p}'+\mathbf{q}\downarrow}^\dagger c_{\mathbf{p}'\downarrow} (\langle n_{\mathbf{p}+\mathbf{q}\uparrow} \rangle - \langle n_{\mathbf{p}\uparrow} \rangle) \quad (2.143)$$

and

$$[c_{\mathbf{p}+\mathbf{q}\downarrow}^\dagger c_{\mathbf{p}\downarrow}, H_1] \stackrel{\text{RPA}}{=} U \sum_{\mathbf{p}'} c_{\mathbf{p}'+\mathbf{q}\uparrow}^\dagger c_{\mathbf{p}'\uparrow} (\langle n_{\mathbf{p}+\mathbf{q}\downarrow} \rangle - \langle n_{\mathbf{p}\downarrow} \rangle). \quad (2.144)$$

The commutator with the density gives

$$[c_{\mathbf{p}+\mathbf{q}\sigma}^\dagger c_{\mathbf{p}\sigma}, n(0, 0)] = \delta_{\sigma\uparrow} \sum_{\mathbf{q}'} \left( c_{\mathbf{p}+\mathbf{q}\uparrow}^\dagger c_{\mathbf{p}-\mathbf{q}'\uparrow} - c_{\mathbf{p}+\mathbf{q}+\mathbf{q}'\uparrow}^\dagger c_{\mathbf{p}\uparrow} \right), \quad (2.145)$$

which results in this expectation value:

$$\langle [c_{\mathbf{p}+\mathbf{q}\sigma}^\dagger c_{\mathbf{p}\sigma}, n(0, 0)] \rangle = \delta_{\sigma\uparrow} (\langle n_{\mathbf{p}+\mathbf{q}\uparrow} \rangle - \langle n_{\mathbf{p}\uparrow} \rangle). \quad (2.146)$$

Inserting the expressions (2.140), (2.143), (2.144) and (2.146) into the equation of motion (2.139) and assuming  $\langle n_{\mathbf{p}} \rangle = \langle n_{\mathbf{p}\uparrow} \rangle = \langle n_{\mathbf{p}\downarrow} \rangle$  gives

$$\begin{aligned} & \left( i \frac{\partial}{\partial t} + (\varepsilon_{\mathbf{p}+\mathbf{q}} - \varepsilon_{\mathbf{p}}) \right) \chi^{c/s}(\mathbf{p}, \mathbf{q}, t) \\ & = -\delta(t) (\langle n_{\mathbf{p}+\mathbf{q}} \rangle - \langle n_{\mathbf{p}} \rangle) \pm (\langle n_{\mathbf{p}+\mathbf{q}} \rangle - \langle n_{\mathbf{p}} \rangle) U \sum_{\mathbf{p}'} \chi^{c/s}(\mathbf{p}', \mathbf{q}, t). \end{aligned} \quad (2.147)$$

We solve this equation by introducing the Fourier transform in time domain,

$$\chi(\omega) = \int dt \chi(t) e^{i\omega t}, \quad (2.148)$$

which results in

$$\chi^{c/s}(\mathbf{p}, \mathbf{q}, \omega) = \frac{(\langle n_{\mathbf{p}\uparrow} \rangle - \langle n_{\mathbf{p}+\mathbf{q}\uparrow} \rangle) (1 \mp U \chi^c(\mathbf{q}, \omega))}{\omega + \varepsilon_{\mathbf{p}+\mathbf{q}} - \varepsilon_{\mathbf{p}}}, \quad (2.149)$$

where  $\chi(\mathbf{q}, \omega) = \sum_{\mathbf{p}} \chi(\mathbf{p}, \mathbf{q}, \omega)$ . We trivially find an expression for  $\chi(\mathbf{q}, \omega)$ :

$$\chi^{c/s}(\mathbf{q}, \omega) = \frac{\Gamma(\mathbf{q}, \omega)}{1 \pm U \Gamma(\mathbf{q}, \omega)}, \quad (2.150)$$

where  $\Gamma$  is defined by

$$\Gamma(\mathbf{q}, \omega) = \frac{1}{N} \sum_{\mathbf{p}} \frac{\langle n_{\mathbf{p}} \rangle - \langle n_{\mathbf{p}+\mathbf{q}} \rangle}{\omega - (\varepsilon_{\mathbf{p}} - \varepsilon_{\mathbf{p}+\mathbf{q}}) + i\eta}. \quad (2.151)$$

We note that in this case the spin susceptibility  $\chi^s$  is actually equal to the transverse susceptibility (compare Ref. [47, Chapter 7.3]). We get the static correlation functions in real space by a Fourier transform and a frequency summation:

$$\langle n_{0\uparrow} n_{i\uparrow} \rangle \pm \langle n_{0\uparrow} n_{i\downarrow} \rangle - \langle n_{0\uparrow} \rangle \langle n_{i\downarrow} \rangle = \int d\omega \sum_{\mathbf{q}} e^{i\mathbf{q}\mathbf{r}_i} \chi^{c/s}(\mathbf{q}, \omega), \quad (2.152)$$

where we subtract the uncorrelated part of the correlation function. Because of the asymptotic  $1/\omega$  behavior of  $\text{Re } \Gamma^{s/c}(\mathbf{q}, \omega)$  for large  $\omega$ , a frequency summation on real frequencies is numerically rather impractical. Instead, an analytic continuation to (bosonic) Matsubara frequencies defined by  $\omega_n = (2n)\pi/\beta$  is done, as the high frequency behavior is  $1/\omega_n^2$ . The correlation functions are calculated by

$$\langle n_{0\uparrow} n_{i\uparrow} \rangle \pm \langle n_{0\uparrow} n_{i\downarrow} \rangle - \langle n_{0\uparrow} \rangle \langle n_{i\downarrow} \rangle = \frac{1}{\beta} \sum_n \sum_{\mathbf{q}} e^{i\mathbf{q}\mathbf{r}_i} \chi^{c/s}(\mathbf{q}, i\omega_n). \quad (2.153)$$

## 2.7.1. Computational details

### High frequency tail

In practice, we approximately cure the error of summing over only a finite number of Matsubara frequencies by fitting the  $1/\omega_n^2$  behavior for high frequencies at the highest Matsubara frequency  $\omega_{n_{\max}}$  used in the calculation. I.e., we assume

$$\chi(\mathbf{q}, \omega_n) = \frac{\alpha}{\omega_n^2} \quad (2.154)$$

is valid for  $n > n_{\max}$ . We approximate the constant of proportionality by

$$\alpha = \chi(\mathbf{q}, \omega_{n_{\max}}) \omega_{n_{\max}}^2. \quad (2.155)$$

We then use

$$\sum_{n=1}^{\infty} \frac{1}{n^2} = \frac{\pi^2}{6} \quad (2.156)$$

and the definition of bosonic Matsubara frequencies,  $\omega_n = 2n\pi/\beta$ , to obtain

$$\sum_{n=0}^{\infty} \chi(\mathbf{q}, \omega_n) \approx \sum_{n=0}^{n_{\max}} \chi(\mathbf{q}, \omega_n) + \alpha \left( \frac{\beta^2}{24} - \sum_{n=1}^{n_{\max}} \frac{1}{\omega_n^2} \right). \quad (2.157)$$

### Treatment of special $\mathbf{q}$ points

For special  $\mathbf{q}$  points ( $\mathbf{q} = \mathbf{0}$  in general and, e.g.,  $\mathbf{q} = (\pi, \pi)$  for a nearest-neighbor tight binding model on the square lattice), we replace the sum over the reciprocal space by an energy integral over the density of states (compare Ref. [84]),

$$\frac{1}{N_k} \sum_p \rightarrow \int d\varepsilon \rho(\varepsilon), \quad (2.158)$$

which leads to significantly less computational effort, especially when the density of states is known analytically, as in the case of the nearest neighbor tight binding model on the square lattice (derived in Refs. [175, 176]), which is

$$\rho(\varepsilon) = \frac{1}{2\pi^2} K\left(1 - \frac{\varepsilon^2}{16}\right), \quad (2.159)$$

where the energy is measured in units of  $2t$  and  $K(x)$  is the complete elliptic integral of the first kind

$$K(x) = \int_0^{\pi/2} \frac{d\phi}{\sqrt{1 - x \sin^2 \phi}}. \quad (2.160)$$

### Treatment of $\omega_n = 0$

We have to take care of the zeroth frequency in  $\chi(\mathbf{q}, \omega_n)$ , as the case  $\varepsilon_{\mathbf{p}} = \varepsilon_{\mathbf{p}+\mathbf{q}}$  leads to a division by zero in Eq. (2.151). In this case, we can use the Taylor expansion of the Fermi function

$$\langle n_{\mathbf{p}+\mathbf{q}} \rangle = \langle n_{\mathbf{p}} \rangle + \frac{d\langle n_{\mathbf{p}} \rangle}{d\varepsilon_{\mathbf{p}}} \frac{d\varepsilon_{\mathbf{p}}}{d\mathbf{p}} \cdot \mathbf{q} \quad (2.161)$$

and that of the dispersion

$$\varepsilon_{\mathbf{p}+\mathbf{q}} = \varepsilon_{\mathbf{p}} + \frac{d\varepsilon_{\mathbf{p}}}{d\mathbf{p}} \cdot \mathbf{q} \quad (2.162)$$

to obtain

$$\frac{\langle n_{\mathbf{p}} \rangle - \langle n_{\mathbf{p}+\mathbf{q}} \rangle}{\varepsilon_{\mathbf{p}+\mathbf{q}} - \varepsilon_{\mathbf{p}}} = -\frac{d\langle n_{\mathbf{p}} \rangle}{d\varepsilon_{\mathbf{p}}}. \quad (2.163)$$

Numerically, we can handle the last expression much better.

## 2.8. Hartree-Fock

We introduce the Hartree-Fock (HF) method, which is the simplest approximation of an interacting system possible. We use it throughout the work to benchmark more involved approximations. It is most natural to compare the novel variational methods we develop in chapters (3) and (4) to Hartree-Fock, as HF is a variational method, too.

Hartree-Fock is a method to approximate many-body systems by the best possible single-particle description in the sense of the variational principle introduced in Sec. (2.9). Derivations using both the Ritz variational method (Sec. (2.9.1)) and the variational principle for the grand potential (Sec. (2.9.2)) are available in Ref. [42]. In the case of the Ritz method, the ansatz for the wavefunction is a single Slater determinant. In the case of the variational principle for the grand potential, the ansatz for the effective Hamiltonian is a general one-particle system. Both routes lead to a decoupling rule for two-particle terms reading

$$\begin{aligned} d_{\alpha\sigma}^\dagger d_{\beta\sigma'}^\dagger d_{\gamma\sigma'} d_{\delta\sigma} &\rightarrow \langle d_{\alpha\sigma}^\dagger d_{\delta\sigma} \rangle d_{\beta\sigma'}^\dagger d_{\gamma\sigma'} + \langle d_{\beta\sigma'}^\dagger d_{\gamma\sigma'} \rangle d_{\alpha\sigma}^\dagger d_{\delta\sigma} \\ &\quad - \langle d_{\alpha\sigma}^\dagger d_{\gamma\sigma'} \rangle d_{\beta\sigma'}^\dagger d_{\delta\sigma} - \langle d_{\beta\sigma'}^\dagger d_{\delta\sigma} \rangle d_{\alpha\sigma}^\dagger d_{\gamma\sigma'}, \end{aligned} \quad (2.164)$$

where the expectation values are taken with respect to the effective non-interacting system and therefore have to be calculated self-consistently.

## 2.9. The variational principle

We end this work's methods part by introducing the variational principle, which plays a central role in the results of this work. In chapter (3), we use it to derive optimal effective Hubbard models with purely local interactions for Hubbard models including nonlocal interactions. In chapter (4), we define optimally truncated Anderson impurity models, which are solved by means of exact diagonalization.

Consider a system, defined by some Hamiltonian  $H$ , which is too complicated to be solved exactly. The central idea of the variational principle is to set up a space of trial solutions. This space is usually spanned by parameters  $(\alpha_0, \alpha_1, \dots)$  defining each trial solution. The best approximation to the true solution within this space is then found by minimizing a functional  $\tilde{\Phi}[\alpha_0, \alpha_1, \dots]$ . In this section we derive two forms of variational principles based on thermodynamic potentials, which in certain limits are equivalent.

### 2.9.1. Ritz variational method

The Ritz variational method (compare, e.g., Ref. [162]) approximates the ground-state wavefunction by minimizing the expectation value of  $H$  with a trial wavefunction. Let the ground state of  $H$  be

$$H |n_0\rangle = E_0 |n_0\rangle. \quad (2.165)$$

The space of trial solutions is spanned by parameters  $(\alpha_0, \alpha_1, \dots)$  specifying trial wavefunctions  $|\Psi(\alpha_0, \alpha_1, \dots)\rangle$ . The parameters could, e.g., be the coefficients of an expansion in orthogonal basis functions or parameters of functions chosen to suit the problem in mind. Let us evaluate the expectation value of  $H$  with a trial wavefunction using a complete set of eigenfunctions  $H |n\rangle = E_n |n\rangle$  of  $H$  and the decomposition of unity in that basis ( $\mathbb{1} = \sum_n |n\rangle \langle n|$ ):

$$\begin{aligned} \langle \Psi | H | \Psi \rangle &= \sum_n \langle \Psi | H | n \rangle \langle n | \Psi \rangle \\ &= \sum_n E_n \langle \Psi | n \rangle \langle n | \Psi \rangle \\ &\geq E_0 \sum_n \langle \Psi | n \rangle \langle n | \Psi \rangle \\ &= E_0 \langle \Psi | \Psi \rangle. \end{aligned} \quad (2.166)$$

The inequality holds because  $E_n \geq E_0 \forall n$ . This is the essence of the Ritz variational principle:

$$\tilde{\Phi}_{\text{Ritz}} = \frac{\langle \Psi | H | \Psi \rangle}{\langle \Psi | \Psi \rangle} \geq E_0. \quad (2.167)$$

We can use this inequality to find the optimal trial wavefunction by minimizing  $\tilde{\Phi}_{\text{Ritz}}$  with respect to all parameters.

### 2.9.2. Variational principle for the grand canonical potential

This section follows Ref. [42]. We introduce an alternative to the Ritz method in this section. It relies on varying trial Hamiltonians (which, once solved, correspond to trial density matrix) rather than a density matrix directly. This method is often called Peierls-Feynman-Bogoliubov variational principle [171, 22, 53]. The space of trial solutions is spanned by parameters  $(\alpha_0, \alpha_1, \dots)$  of a trial Hamiltonian  $\tilde{H}(\alpha_0, \alpha_1, \dots)$ . For a general Hamiltonian in second quantization

$$\tilde{H} = \sum_{ij} h_{ij}^1 c_i^\dagger c_j + \sum_{ijkl} h_{ijkl}^2 c_i^\dagger c_j^\dagger c_k c_l, \quad (2.168)$$

we identify the one and two-particle matrix elements  $h_{ij}^1$  and  $h_{ijkl}^2$  as the parameters  $(\alpha_0, \alpha_1, \dots)$ . Let us first write the functional and the inequality to prove:

$$\tilde{\Phi}_{\text{GP}} = \langle H - \tilde{H} \rangle_{\tilde{H}} + \Phi_{\tilde{H}} \geq \Phi_H, \quad (2.169)$$

where  $\Phi_{\tilde{H}/H} = -1/\beta \ln Z_{H/\tilde{H}}$  is the free energy ( $Z_H = \text{Tr} \exp(-\beta H)$  is the partition function and  $\rho_H = 1/Z_H e^{-\beta(H-\mu N)}$  is the density operator) of  $H$  and  $\langle A \rangle_{\tilde{H}} = \text{Tr} [\rho_{\tilde{H}} A]$  denotes a thermodynamic expectation value with respect to the system  $\tilde{H}$ . To prove the inequality (2.169), we rewrite  $\tilde{\Phi}_{\text{GP}}$ :

$$\begin{aligned} & \langle H - \mu N + \frac{1}{\beta} \ln \rho_{\tilde{H}} \rangle_{\tilde{H}} \\ &= \langle H - \mu N - \frac{1}{\beta} \beta (\tilde{H} - \mu N) - 1/\beta \ln Z_{\tilde{H}} \rangle_{\tilde{H}} \\ &= \langle H - \tilde{H} \rangle_{\tilde{H}} + \Phi_{\tilde{H}} = \tilde{\Phi}_{\text{GP}}. \end{aligned} \quad (2.170)$$

We use the general inequality

$$\text{Tr} \{ \rho \ln \rho \} \geq \text{Tr} \{ \rho \ln \rho' \} \quad (2.171)$$

of two density operators  $\rho$  and  $\rho'$ , which we prove in the following. Let  $|\alpha\rangle$  and  $|\beta\rangle$  be eigenfunctions and  $\rho_\alpha$  and  $\rho'_\beta$  the eigenvalues of the density operators, respectively.

We can then show

$$\begin{aligned}
\text{Tr} \{ \rho (\ln \rho' - \ln \rho) \} &= \sum_{\alpha} \rho_{\alpha} (\langle \alpha | \ln \rho' | \alpha \rangle - \ln \rho_{\alpha}) \\
&= \sum_{\alpha\beta} \rho_{\alpha} (\langle \alpha | \beta \rangle \ln \rho'_{\beta} \langle \beta | \alpha \rangle - \ln \rho_{\alpha}) \\
&= \sum_{\alpha\beta} \rho_{\alpha} |\langle \beta | \alpha \rangle|^2 (\ln \rho'_{\beta} - \ln \rho_{\alpha}) \\
&= \sum_{\alpha\beta} \rho_{\alpha} |\langle \beta | \alpha \rangle|^2 \left( \ln \frac{\rho'_{\beta}}{\rho_{\alpha}} \right) \\
&\leq \sum_{\alpha\beta} \rho_{\alpha} |\langle \beta | \alpha \rangle|^2 \left( \frac{\rho'_{\beta}}{\rho_{\alpha}} - 1 \right) \\
&= \sum_{\alpha\beta} \rho'_{\beta} |\langle \beta | \alpha \rangle|^2 - \rho_{\alpha} |\langle \beta | \alpha \rangle|^2 \\
&= \text{Tr} \rho' - \text{Tr} \rho = 0,
\end{aligned} \tag{2.172}$$

where we have used the basic inequality  $\ln x \leq x - 1$ . Using Eq. (2.171) and starting from the expression in Eq. (2.170), we show

$$\begin{aligned}
\tilde{\Phi}_{\text{GP}} &= \langle H - \mu N + \frac{1}{\beta} \ln \rho_{\tilde{H}} \rangle_{\tilde{H}} \\
&= \langle H - \mu N \rangle_{\tilde{H}} + \text{Tr} \left[ \rho_{\tilde{H}} \frac{1}{\beta} \ln \rho_{\tilde{H}} \right] \\
&\geq \langle H - \mu N \rangle_{\tilde{H}} + \text{Tr} \left[ \rho_{\tilde{H}} \frac{1}{\beta} \ln \rho_H \right] \\
&= \langle H - \mu N + \frac{1}{\beta} \ln \rho_H \rangle_{\tilde{H}} \\
&= \langle H - \mu N + \frac{1}{\beta} [-\beta (H + \mu N) - \ln Z_H] \rangle_{\tilde{H}} \\
&= \Phi_H.
\end{aligned} \tag{2.173}$$

By minimizing  $\tilde{\Phi}_{\text{GP}}$  with respect to its parameters, we find the effective density matrix which approximates the original one as closest as possible.

# 3. Renormalizations of the Hubbard model by nonlocal interactions

M. Schüler, M. Rösner, T. O. Wehling, A. I. Lichtenstein, and M. I. Katsnelson, **Optimal Hubbard models for materials with nonlocal Coulomb interactions: graphene, silicene and benzene**, Phys Rev. Lett. **111** 036601 (2013)

Sections (3.1), (3.2), (3.6), (3.7), (3.8) and (3.10) of this chapter are based on the publication given above and show considerable amount of overlap with the original manuscript, concerning both text and figures. The original text is mainly written by M. Schüler and proofread by all authors. The cRPA calculations for graphene and silicene presented in Tab. (3.1) are done by M. Rösner. All other calculations and figures presented in the manuscript have been created by M. Schüler.

## 3.1. Introduction

Low dimensional *sp*-electron systems like graphene [224, 115, 99], systems of adatoms on semiconductor surfaces, such as Si(111):X with X=C, Si, Sn, Pb [74], Bechgaard salts or aromatic molecules [167, 177] and polymers [55, 206] feature simultaneously strong local and nonlocal Coulomb interactions. In graphene for instance, the on-site interactions  $U/t \sim 3.3$ , the nearest neighbor Coulomb repulsion  $V/t \sim 2$  as well as further sizable nonlocal Coulomb terms exceed the nearest neighbor hopping  $t = 2.8$  eV [224]. Considering on-site interactions  $U/t \sim 3.3$  alone would put graphene close to the boundary of a gapped spin-liquid [150], which could be even crossed by applying strain on the order of a few percent [224]. It is a priori unclear, whether [94] or not [87, 193] nonlocal Coulomb interaction stabilize the semimetallic Dirac phase in graphene. To rephrase the problem: It is unclear which Hubbard model with strictly local interactions would yield the best approximation to the ground state of graphene. To judge the stability of the Dirac electron phase in graphene but also to understand Mott transitions on surfaces like Si:X (111), a quantitative well defined link from models

with local and nonlocal Coulomb interactions to those with purely local interactions is desirable.

In Sec. (3.2), we present a method to map a *general* extended Hubbard model with nonlocal Coulomb interactions onto an effective Hubbard model with on-site interactions  $\tilde{U}$  only. In Secs. (3.3)-(3.5) we apply this method to simple generic one- and two-dimensional extended Hubbard models (i.e., models on a chain, a square, and a honeycomb lattice) with nearest neighbor interaction only to gain insight to general properties of these models and the renormalizations taking place in them for a wide range of interaction parameters. We analyze the effect of dimensionality and geometry of the Hubbard model on the strength of the renormalization. To answer the questions about physical systems stated above, we apply the method to graphene, silicene and benzene in Sec. (3.6) and show that nonlocal terms reduce the effective on-site interaction by more than a factor of two. Thus, nonlocal Coulomb interactions stabilize the Dirac electron phases in graphene and silicene against spin-liquid and antiferromagnetic phases. In Sec. (3.7) we analyze the dependence of the renormalization on the filling of the system for the case of benzene, where we show the robustness of our result in a wide doping range around half filling. However, in the almost empty and nearly filled case strictly repulsive nonlocal Coulomb interactions can effectively increase the local interaction. In Sec. (3.8) we benchmark our method for different dopings by comparing observables of the effective Hubbard model and the original extended Hubbard model and find that spin-related ground-state properties are described better by the effective model than charge-related properties.

The variational method involves the solution of the effective Hubbard model to calculate the renormalization. In this chapter all results have been obtained with either exact diagonalization or determinant quantum Monte Carlo. In Sec. (3.9) we investigate the applicability of approximations on lower levels, namely Hartree-Fock and the random-phase approximation to calculate charge correlation functions.

## 3.2. Theoretical framework

We use the Peierls-Feynman-Bogoliubov variational principle introduced in Sec. (2.9.2) to find the best approximation of an extended Hubbard model (Eq. (2.5)) by means of an effective purely local Hubbard model (Eq. (2.4)). In the language of the variational principle, the extended Hubbard model is the original model  $H$ , which, in its translationally invariant version with next nearest neighbor hopping  $t$ , reads

$$H = t \sum_{\langle ij \rangle \sigma} c_{i\sigma}^\dagger c_{j\sigma} + U \sum_i n_{i\uparrow} n_{i\downarrow} + \frac{1}{2} \sum_{\sigma\sigma'} \sum_{i \neq j} V_{ij} n_{i\sigma} n_{j\sigma'}. \quad (3.1)$$

The effective system  $\tilde{H}$  is given by the Hubbard model with the same single-particle part and reads

$$\tilde{H} = t \sum_{\langle ij \rangle \sigma} c_{i\sigma}^\dagger c_{j\sigma} + \tilde{U} \sum_i n_{i\uparrow} n_{i\downarrow}. \quad (3.2)$$

To find the best possible effective  $\tilde{U}$  we apply the variational principle for the grand potential introduced in Sec. (2.9.2). We minimize the functional (2.169) by solving the equation  $\partial/\partial\tilde{U}\tilde{\Phi}[\tilde{U}] = 0$ . In the following, we simplify the equation

$$\frac{\partial}{\partial\tilde{U}}\tilde{\Phi} = \frac{\partial}{\partial\tilde{U}}(\langle H - \tilde{H} \rangle_{\tilde{H}} + \Phi_{\tilde{H}}) \quad (3.3)$$

considerably. We calculate the derivatives of the difference of the Hamiltonians and the free energy separately. The derivative of the free energy<sup>1</sup> with respect to  $\tilde{U}$  is

$$\begin{aligned} \frac{\partial}{\partial\tilde{U}}\Phi_{\tilde{H}} &= -\frac{\partial}{\partial\tilde{U}}\frac{1}{\beta}\ln Z_{\tilde{H}} \\ &= -\frac{1}{\beta}\frac{1}{Z_{\tilde{H}}}\frac{\partial}{\partial\tilde{U}}\text{Tr}e^{-\beta\tilde{H}} \\ &= -\frac{1}{\beta}\frac{1}{Z_{\tilde{H}}}\text{Tr}\left(-\beta\sum_i n_{i\uparrow}n_{i\downarrow}e^{-\beta\tilde{H}}\right) \\ &= \sum_i \langle n_{i\uparrow}n_{i\downarrow} \rangle_{\tilde{H}}. \end{aligned} \quad (3.4)$$

As the single-particle parts of  $H$  and  $\tilde{H}$  are equal, they drop out in the first part of the functional:

$$H - \tilde{H} = (U - \tilde{U}) \sum_i n_{i\uparrow}n_{i\downarrow} + \frac{1}{2} \sum_{ij\sigma\sigma'} V_{ij} n_{i\sigma} n_{j\sigma'}. \quad (3.5)$$

The derivative of the expectation value of this part is

$$\begin{aligned} \frac{\partial}{\partial\tilde{U}}\langle H - \tilde{H} \rangle_{\tilde{H}} &= \frac{\partial}{\partial\tilde{U}} \left( (U - \tilde{U}) \sum_i \langle n_{i\uparrow}n_{i\downarrow} \rangle_{\tilde{H}} + \frac{1}{2} \sum_{ij\sigma\sigma'} V_{ij} \langle n_{i\sigma}n_{j\sigma'} \rangle_{\tilde{H}} \right) \\ &= -\sum_i \langle n_{i\uparrow}n_{i\downarrow} \rangle_{\tilde{H}} + (U - \tilde{U}) \sum_i \frac{\partial}{\partial\tilde{U}} \langle n_{i\uparrow}n_{i\downarrow} \rangle_{\tilde{H}} \\ &\quad + \frac{1}{2} \sum_{ij\sigma\sigma'} V_{ij} \frac{\partial}{\partial\tilde{U}} \langle n_{i\sigma}n_{j\sigma'} \rangle_{\tilde{H}}, \end{aligned} \quad (3.6)$$

<sup>1</sup>Here, in contrast to the definition of the functional (Eq. (2.169)), we use the canonical definition of the partition function, in order to fix the particle number of the effective system to that of the original system. The formal dependence of the chemical potential in a grand canonical approach (e.g.,  $\mu = -\tilde{U}/2$  for half filling) would lead to an additional factor of  $\langle N \rangle/2$  in Eq. (3.4).

using the product rule. By collecting Eqs. (3.4) and (3.6), we observe that the free energy derivative cancels with the term from the product rule and solve the equation for  $\tilde{U}$ :

$$\tilde{U} = U + \frac{1}{2} \frac{\sum_{ij\sigma\sigma'} V_{ij} \partial/\partial\tilde{U} \langle n_{i\sigma} n_{j\sigma'} \rangle_{\tilde{H}}}{\sum_i \partial/\partial\tilde{U} \langle n_{i\uparrow} n_{i\downarrow} \rangle_{\tilde{H}}}. \quad (3.7)$$

Introducing the charge operator  $n_i = n_{i\uparrow} + n_{i\downarrow}$ , the exact relation  $\partial/\partial\tilde{U} \langle n_{i\sigma} n_{i\sigma} \rangle_{\tilde{H}} = 0$ , and assuming translationally invariant systems ( $n_{i+k} n_{j+k} = n_i n_j$ ), we arrive at a simplified equation:

$$\tilde{U} = U + \sum_{j \neq 0} V_{0j} \frac{\partial/\partial\tilde{U} \langle n_0 n_j \rangle_{\tilde{H}}}{\partial/\partial\tilde{U} \langle n_0 n_0 \rangle_{\tilde{H}}}. \quad (3.8)$$

If we assume spin symmetry ( $n_{\uparrow} n_{\downarrow} = n_{\downarrow} n_{\uparrow}$  and  $n_{\uparrow} n_{\uparrow} = n_{\downarrow} n_{\downarrow}$ ) of the expectation values, we arrive at

$$\tilde{U} = U + \sum_{j \neq 0, \sigma'} V_{0j} \frac{\partial/\partial\tilde{U} \langle n_{0\uparrow} n_{j\sigma'} \rangle_{\tilde{H}}}{\partial/\partial\tilde{U} \langle n_{0\uparrow} n_{0\downarrow} \rangle_{\tilde{H}}}. \quad (3.9)$$

Eq. (3.8) is a central result of this section, as it presents a general rule to calculate the Coulomb parameter  $\tilde{U}$  of an effective Hubbard model, approximating an extended Hubbard model with local *and* nonlocal Coulomb interactions  $U$  and  $V_{ij}$ . This equation has an intuitive physical interpretation: Increasing the on-site interaction strength  $\tilde{U}$  reduces the double occupancy  $\langle n_{i\uparrow} n_{i\downarrow} \rangle$  and pushes away electrons approaching an already occupied site at  $i = 0$  to other sites. In the case of purely local Coulomb interactions there is an energy gain of  $\tilde{U}$  upon suppressing the double occupancy. When there are, however, nonlocal Coulomb interactions with surrounding lattice sites  $j$ , the electrons which are displaced from the site  $i = 0$  to the surrounding sites  $j$  raise the energy of the system by terms proportional to  $V_{0j}$ . This process is depicted in a simplified way for a half-filled system in Fig. (3.1).

The total double occupation of the lattice  $D = \sum_{ij,\sigma\sigma'} n_{i\sigma} n_{j\sigma'}$  is conserved, since its commutator with the Hamiltonian is zero,  $[\tilde{H}, D] = 0$ . Thus,  $\langle D \rangle$  is constant and independent of  $U$  in the case of the canonical ensemble<sup>2</sup>. For a translationally invariant system we find  $\sum_{j\sigma} \langle n_{0\uparrow} n_{j\sigma} \rangle_{\tilde{H}} = \text{const.}$  Taking the derivative with respect to  $\tilde{U}$  leads to

$$\partial/\partial\tilde{U} \langle n_{0\uparrow} n_{0\downarrow} \rangle_{\tilde{H}} = - \sum_{j \neq 0, \sigma} \partial/\partial\tilde{U} \langle n_{0\uparrow} n_{j\sigma} \rangle_{\tilde{H}}. \quad (3.10)$$

---

<sup>2</sup>For the grand canonical ensemble, this holds only for  $\beta$  such that grand canonical and canonical expectation values are approximately equal, i.e., fluctuations of the total particle number are thermally prohibited.

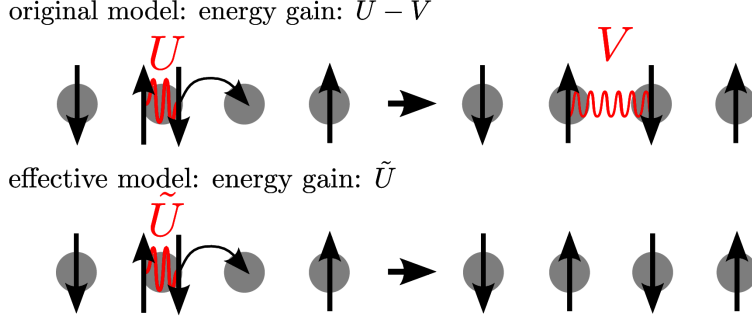


**Figure 3.1.:** Illustration of the physical process underlying Eq. (3.8) for half-filled systems: An electron hops from a doubly occupied site to an empty one, gaining an energy  $U - V$  in the original model and  $\tilde{U}$  in the effective model.

This means, that the second summand in the equation for  $\tilde{U}$ , Eq. (3.8), is a weighted average of the nonlocal Coulomb interactions.

Before solving Eq. (3.8) for special cases numerically, let us analyze simple cases which we can solve analytically or at least simplify: (i) By assuming that an increasing  $\tilde{U}$  displaces electrons only to next neighbors we find

$$\partial/\partial\tilde{U}\langle n_{0\uparrow}n_{0\downarrow}\rangle_{\tilde{H}} = -N_n \sum_{\sigma} \partial/\partial\tilde{U}\langle n_{0\uparrow}n_{1\sigma}\rangle_{\tilde{H}}, \quad (3.11)$$

where  $N_n$  is the coordination number. Equation (3.8) then yields

$$\tilde{U} = U - V_{01}. \quad (3.12)$$

(ii) For spatially slowly decaying Coulomb interactions, we may assume a uniform Coulomb interaction  $V_{0j} = V$  and arrive at a very similar result as in the former case

$$\tilde{U} = U - V. \quad (3.13)$$

For these strongly simplifying assumptions, the effective local Coulomb interaction is reduced exactly by the neighboring nonlocal interaction term. (iii) If we assume that only the nearest neighbor is subject to nonlocal interaction,

$$V_{0j} = \begin{cases} V & \text{if } j = 1 \\ 0 & \text{else,} \end{cases} \quad (3.14)$$

we can simplify Eq. (3.8) to

$$\tilde{U} = U - N_n V \frac{\partial/\partial\tilde{U}\langle n_0 n_1 \rangle_{\tilde{H}}}{\partial/\partial\tilde{U}\langle n_0 n_0 \rangle_{\tilde{H}}} = U - V\alpha(\tilde{U}), \quad (3.15)$$

where we have introduced the nearest neighbor renormalization strength  $\alpha(\tilde{U})$ , which is a universal property of the effective system.

In the next sections we present more rigorous solutions of  $\tilde{U}$  based on exact or stochastic solutions of finite Hubbard models. First, density-density correlation functions are calculated and analyzed for the case of the one-dimensional Hubbard model and Hubbard models on the square lattice and honeycomb lattice. In all cases, only nearest-neighbor hopping is included. For simplicity, we assume only nearest-neighbor Coulomb interaction for the solution of Eq. (3.8), such that we can analyze the universal renormalization by means of investigating  $\alpha(\tilde{U})$  (Eq. (3.15)). We proceed to calculate effective models for Hubbard models of graphene, silicene, and benzene derived from first principles. Here, the nonlocal Coulomb interaction is not restricted to next nearest-neighbor terms. For the case of benzene, we analyze the case away from half filling and additionally benchmark the effective model against the exact solution of the extended Hubbard model on the basis of charge and spin correlation functions. We also analyze the usage of approximate methods (Hartree-Fock and RPA) for calculating the correlation functions. This is important as exact solutions are computationally not accessible in the case of more complicated Hubbard models (e.g., for realistic multi-band systems).

### 3.3. One-dimensional systems

The one-dimensional Hubbard model is exactly solvable by the Bethe ansatz [17, 136, 135] so we can draw some general conclusions how the renormalization behaves in one dimension. We can thus perform a first check of the above approximations. While the expression for the eigenvalues in the Bethe ansatz is very simple, the eigenfunctions are rather complicated. Thus, the exact computation of the correlation functions is difficult but general results for the spatial behavior of  $\langle n_0 n_j \rangle$  are known in special cases. For gapped systems<sup>3</sup>, the density-density correlation functions decay exponentially [51]. For systems which are not gapped, the correlation functions show a power law behavior, where the exponent  $K$  is independent of  $U$  for half filling [196]. One can show that for large  $j$  the correlation functions show an oscillating behavior  $\langle n_0 n_j \rangle \sim \cos(4k_F x_j) x_j^K$ , where  $k_F$  is the Fermi wave vector and  $x_j$  is the position of the lattice site  $j$  [196]. This means the approximation which neglects all correlation functions but that for the nearest neighbor, leading to Eq. (3.12), should hold better for systems which are

---

<sup>3</sup>e.g., half filled systems on bipartite lattices for interactions  $U$  beyond the Mott-Transition [51]. If a system is gapped or not can in general not be deduced from a simple inspection of the Hamiltonian [41].

described by large  $\tilde{U}$ , due to the exponential spatial decay of the correlation functions. The approximation may break down for metallic systems if the oscillations of the correlation functions do not help to cancel neighboring correlation functions like  $\langle n_0 n_j \rangle$  and  $\langle n_0 n_{j+1} \rangle$ .

To make more explicit statements for one-dimensional systems, we calculate the correlation functions for finite effective systems exactly. We solve half-filled systems with six sites, periodic boundary conditions, and local Coulomb interactions in the range from  $\tilde{U}/t = 0$  to  $\tilde{U}/t = 15$ . The correlation functions and the derivative with respect to  $\tilde{U}/t$  are depicted in Fig. (3.2). The charge correlation functions for different interaction strengths are presented in Fig. (3.2) (a-b).

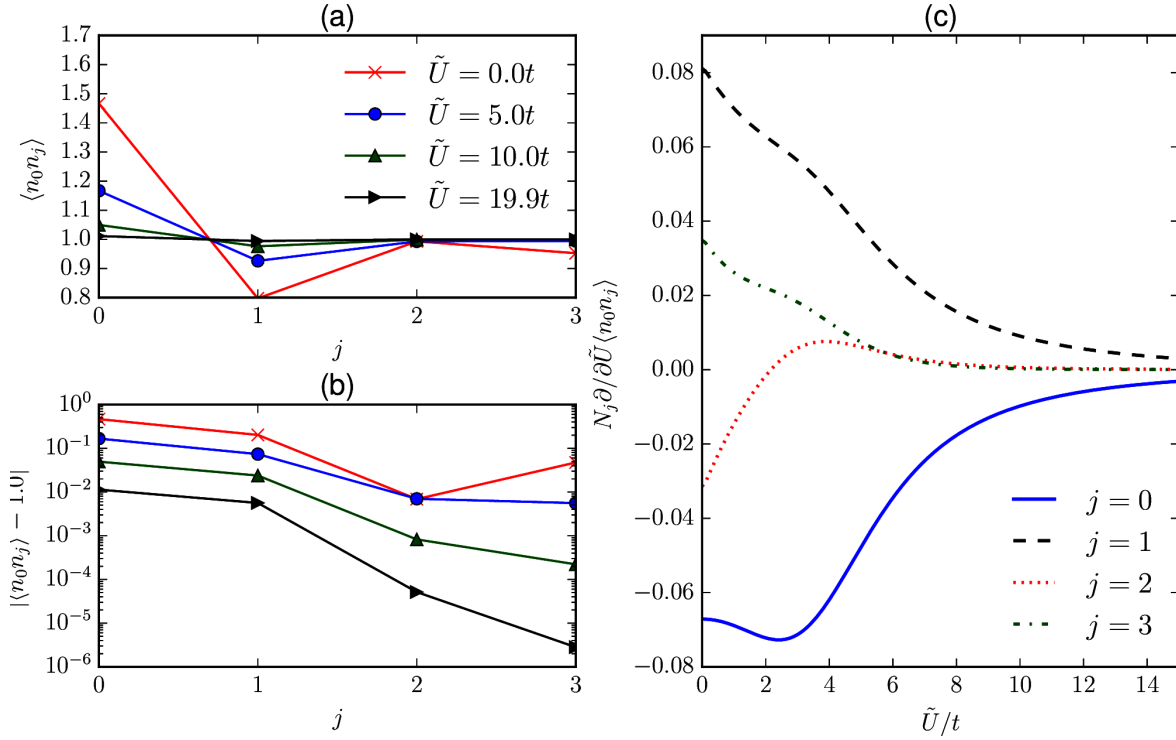


**Figure 3.2.:** Charge correlation functions of the 6 site one-dimensional Hubbard model with periodic boundary conditions: (a) and (b) show the spatial behavior for different interaction strengths for the  $j$ th neighbor shell. The semilogarithmic plot in (b) shows the absolute difference to 1.0. Panel (c) shows the derivative with respect to  $\tilde{U}$  multiplied with the coordination number, for different neighbors  $j$ .

We observe two features: First, the oscillating nature of the  $\langle n_0 n_j \rangle$  and secondly, the dependence of the spatial decay of  $\langle n_0 n_j \rangle$  on  $\tilde{U}$ . The linear behavior in the semilogarithmic plot in Fig. (3.2) (b) shows an exponential spatial decay for large interaction

### 3. Renormalizations of the Hubbard model by nonlocal interactions

strengths,  $\tilde{U}/t \gtrsim 10$ . Fig. (3.2) (c) shows the derivative with respect to  $\tilde{U}$  multiplied by the coordination number  $N_j$  in dependence of  $\tilde{U}$ . For small  $\tilde{U}$  ( $\tilde{U}/t \lesssim 4$ ), the derivatives of the local and nonlocal correlation are of the same order for all  $j$ . For larger  $\tilde{U}$ , the derivatives  $\partial/\partial\tilde{U}\langle n_0n_0 \rangle$  and  $\partial/\partial\tilde{U}\langle n_0n_1 \rangle$  are by orders of magnitude larger than those for  $j > 1$ , which renders the approximation of electrons only being displaced to nearest neighbors very good in this region. The local term ( $j = 0$ ) shows a minimum at  $\tilde{U}/t \sim 2.5$ . We find shoulders or maxima for the other terms at the same interaction strength.

The graphical representations in Fig. (3.3) show the long-range correlations for Coulomb interactions up to  $\tilde{U}/t = 6$ . This representation stresses the difference between systems with larger and smaller interactions than  $\tilde{U}/t \sim 2.5$ : For small local interaction ( $\tilde{U}/t = 0.1, 2.0$ ) we observe oscillations of the sign in the derivatives (the local and the next-nearest neighbor derivatives are negative), whereas for  $\tilde{U}/t = 6.0$ , only the local derivative is negative.

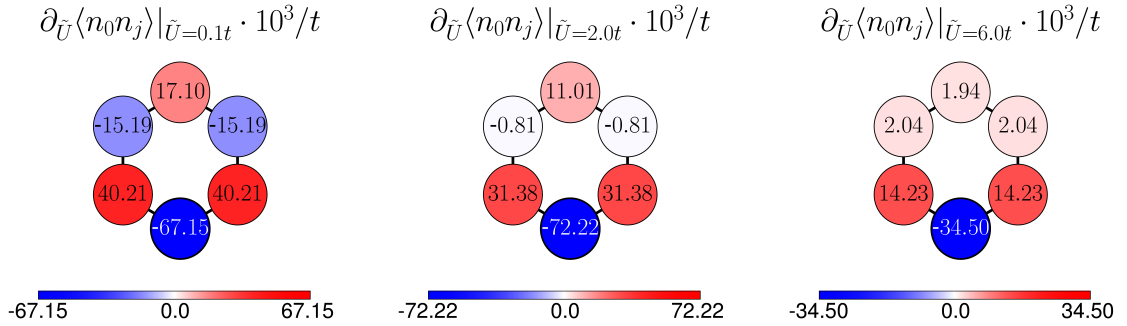


**Figure 3.3.:** Graphical representation of  $\partial/\partial\tilde{U}\langle n_0n_j \rangle$  for  $\tilde{U}/t = 0.1, 2.0, 6.0$ .

By using the numerical results discussed above we solve Eq. (3.8) to obtain the optimal  $\tilde{U}$  for a set of extended Hubbard models, defined by local Coulomb interactions in the range from  $U/t = 0$  to  $U/t = 15$  and next nearest neighbor interactions in the range from  $V_{01} = 0$  to  $V_{01} = 0.8U$ , respectively. In order to compare all models on equal footing, we analyze the renormalization  $\tilde{U}/U$ . This is shown in Fig. (3.4) (a). For  $V = 0$  there is no renormalization ( $\tilde{U}/U = 1$ ), as it should be. The gradient of the renormalization in direction of  $V/U$  is strongest for  $U/t \rightarrow 0$  and smallest in the region of  $2 \lesssim U/t \lesssim 6$ .

For  $V/U > 0.8$  (not shown here) the renormalization can lead to negative  $\tilde{U}$ . However, we do not discuss this here, as such large nonlocal interaction are rather unphysical. For large  $U/t$ , also more than one solution of Eq. (3.8) can exist. This is obvious

from the parabolic behavior of  $\alpha(\tilde{U})$  around  $\tilde{U}/t \sim 4$ , shown in Fig. (3.4) (c). In the case of multiple solutions we cannot decide (from Eq. (3.8) only) which solution leads to the global minimum of  $\tilde{\Phi}(\tilde{U})$  and have to calculate the functional  $\tilde{\Phi}(\tilde{U})$  directly. In all cases considered in this work, only one solution of Eq. (3.8) was found.

The difference between the exact and the approximate solution ( $\tilde{U} = U - V$ ) is shown in Fig. (3.4) (b). For small  $V_{01}$ , the nearest neighbor approximation is better the bigger  $U/t$  is, as the analysis of the general long-range behavior of the correlation functions already suggested. Interestingly, the exact renormalization for the finite system is larger than the approximate result for  $U/t \lesssim 1 - 2$  and smaller for  $U/t \gtrsim 1 - 2$ .

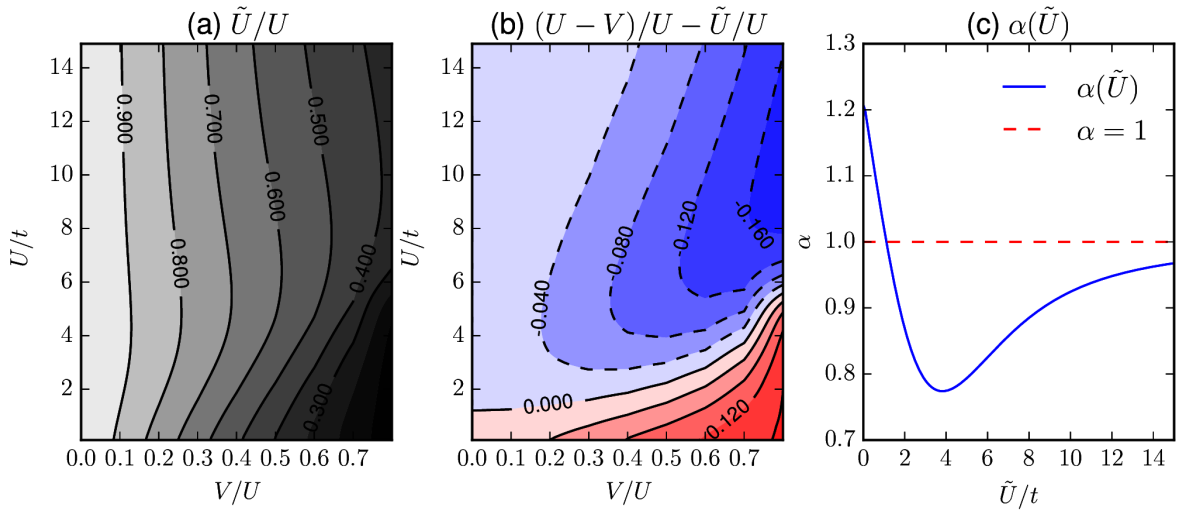


**Figure 3.4.:** (a) Renormalization of the local Coulomb interaction  $\tilde{U}/U$  for half filled one-dimensional Hubbard models (defined by  $U/t$  and  $V/U$ ) calculated from Eq. (3.8). (b) shows the deviation of the approximation that electrons are only displaced to nearest neighbors (Eq. (3.12)) to the exact treatment. (c) shows the nearest neighbor renormalization strength  $\alpha(\tilde{U})$ , compare Eq. (3.15). The red dashed line corresponds to the approximation  $\tilde{U} = U - V$ , i.e.,  $\alpha = 1$ .

Finally, we analyze the nearest neighbor renormalization strength  $\alpha(\tilde{U})$ , which allows us to understand the preceding discussion on the basis of the behavior of the effective system. This quantity is calculated by dividing the  $j = 1$  and  $j = 0$  data from Fig. (3.2) (c) and is shown in Fig. (3.4) (c) together with  $\alpha = 1$ , which corresponds to the approximation that electrons are displaced to the nearest neighbors only ( $\tilde{U} = U - V$ ). We find the strongest renormalizations for effective Hubbard models with  $\tilde{U}/t = 0$  and the smallest for  $\tilde{U}/t \sim 4$ . For large effective interactions, we observe that the renormalization approaches  $\alpha = 1$ . That explains why for intermediate  $V/U$ , the

approximation ( $\tilde{U} = U - V$ ) leads to better results for large  $U/t$ . Due to the sum rule (Eq. (3.10)), values of  $\alpha(\tilde{U})$  larger than one are only possible if derivatives of correlation functions for  $j > 1$  are negative. Thus, the region where  $\alpha > 1$  roughly matches the region where  $\partial/\partial\tilde{U}\langle n_0n_2 \rangle < 0$ , compare Fig. (3.2) (c).

### 3.4. Square lattices

We continue the discussion on generic Hubbard models with only nearest neighbor interaction with Hubbard models on the square lattice, i.e., with a two-dimensional system. There is no general analytical solution of the Hubbard model in two dimensions. As in the case of one dimension we could rely on exact diagonalization techniques, e.g., using a 8 site cluster in [140]. However, the small number of lattice sites accessible restricts us from drawing any conclusions near the thermodynamic limit [84]. We instead use the determinant quantum Monte Carlo technique introduced in Sec. (2.5.1) for the cost of noisy data<sup>4</sup>. We obtain the correlation functions on a relatively course mesh of  $\tilde{U}$  with a discretization of  $\delta\tilde{U} = 0.1t$ . We calculate the correlation functions for finite lattices with periodic boundary conditions on a  $8 \times 8$  lattice for  $\beta t = 9$ ,  $\Delta\tau = 0.05$ ,  $10^4$  warm-up sweeps and  $10^5$  measurement sweeps.

Let us start the analysis of the square model with the density-density correlation functions and their derivatives with respect to  $\tilde{U}$ . Fig. (3.5) shows these quantities in the same manner as before, i.e., the charge correlations for different interactions in panel (a) and (b) and their derivative with respect to  $\tilde{U}$  in panel (c). In Fig. (3.5) (a) and (b) we can see that the general spatial behavior of the correlation functions is exponential, as in the one-dimensional case. In contrast to the one-dimensional case, for small  $\tilde{U}$ , the correlations do not drop monotonically, but show oscillations.

The noise of the data is apparent in the (finite difference) derivative in panel (c). We use a Savitzky-Golay filter [191] with  $\Delta\tilde{U}/t = 1.0$  and quadratic polynomials (Compare appendix (A.1) for a comparison of different methods to overcome the noise) of the charge correlation function with respect to  $\tilde{U}$ . The result of filtering is shown as lines in the respective colors. The derivative of the local correlation functions is negative for all  $\tilde{U}$  and looks very similar to the one-dimensional case with a pronounced minimum around  $\tilde{U}_M = 3$ . The next nearest neighbor derivative is again positive for all examined  $\tilde{U}$  values. Negative derivatives on other sites but  $j = 0$  only occur for interaction strengths below  $\tilde{U}_M$ . In relation to the local term, the nonlocal terms are slightly

---

<sup>4</sup>DQMC works with a grand canonical ensemble. We approximate the canonical expectation value with the grand canonical expectation values, which is a good approximation for  $\beta t \gtrsim 5$  as discussed in section (3.6.3).

smaller than in the one-dimensional case. However, the nearest-neighbor derivative dominates all other nonlocal derivatives. We observe a checker-board like symmetry of the sign below  $\tilde{U}_M$ , obvious in the two dimensional representation of the derivatives in Fig. (3.6).

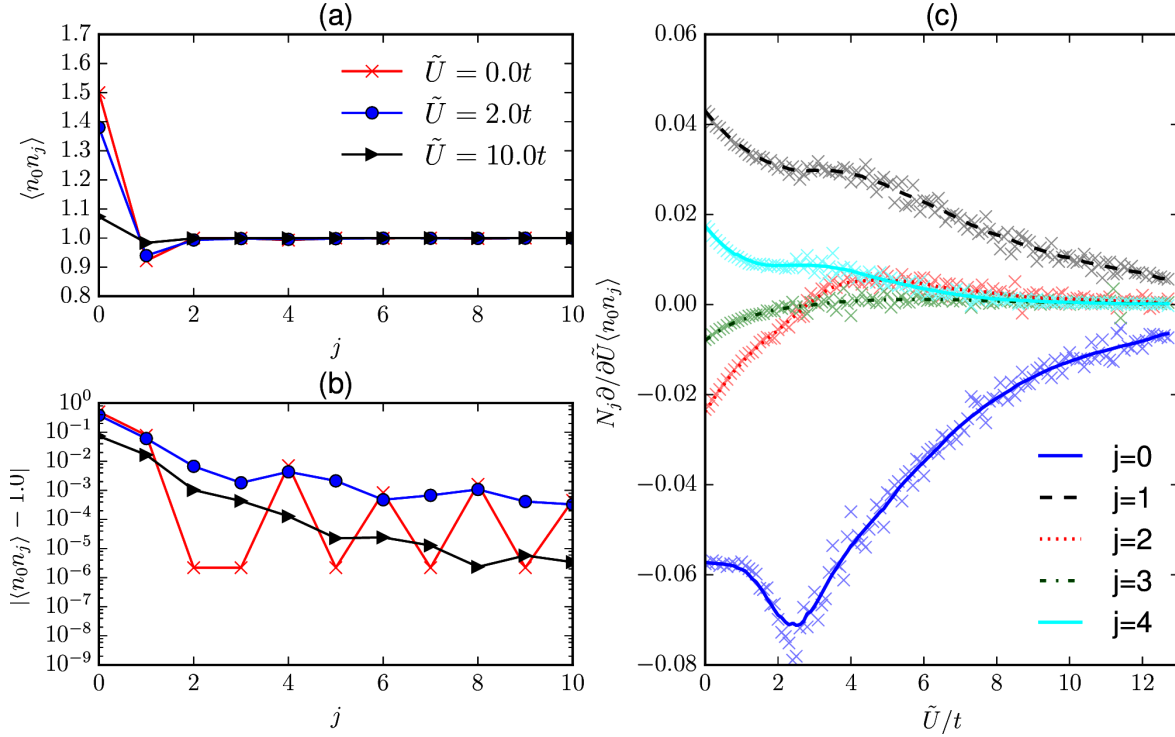


**Figure 3.5.:** Density-density correlation functions of a  $8 \times 8$  site square Hubbard model: (a) and (b) show the spatial behavior for different interaction strengths for the  $j$ th neighbor shell. The semilogarithmic plot in (b) shows the difference to a value of 1.0. Panel (c) shows the derivative with respect to  $\tilde{U}$  multiplied with the coordination number, for the first few nearest neighbors  $j$ . The crosses are from finite differences and the line is from analytic derivatives of the result of a Savitzky-Golay filtering.

Using the derivatives of the correlations functions we calculate the optimal effective Coulomb interaction for a set of extended Hubbard models with only nearest neighbor interaction. We study a similar set of models as in the case of the one-dimensional lattice and analyze the results in the exactly same way. The results are displayed in Fig. (3.7) by showing (a) the amount of renormalization of the local Coulomb interaction  $\tilde{U}/U$ , (b) the difference of  $\tilde{U}/U$  from the exact solution and the approximation  $\tilde{U} = (U - V)/U$  and (c) the nearest neighbor renormalization strength  $\alpha(\tilde{U})$ . We find the

### 3. Renormalizations of the Hubbard model by nonlocal interactions

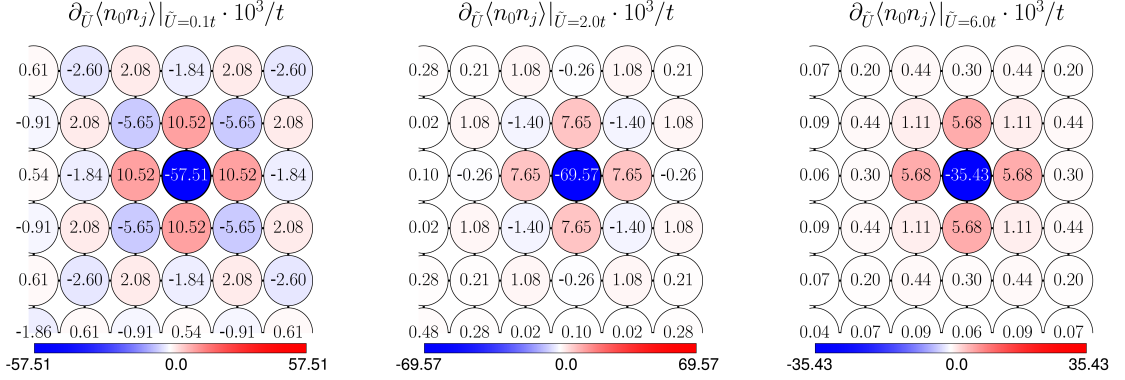


**Figure 3.6.:** Graphical representation of  $\partial/\partial\tilde{U}\langle n_0 n_j \rangle$  for  $\tilde{U}/t = 0.1, 2.0, 6.0$ .

smallest renormalization for  $U/t \sim 3$  considering small nonlocal interaction and local interactions up to  $U/t \sim 4$  for larger nonlocal interactions. The comparison with the approximative result shows that in the case of the square lattice, no renormalizations stronger than  $U - V$  is found. That is also apparent from the analysis of the nearest-neighbor renormalization strength shown in Fig. (3.7) (c), where  $\alpha(\tilde{U}) < 1 \forall \tilde{U}$ . This is very different to the one-dimensional case, where we have found nearly twice as strong renormalizations. We can understand this behavior regarding the graphical representations of the correlations functions (Fig. (3.6)) on the respective lattices. The response of the system at small  $\tilde{U}$  is more spread out than in the case of the 6-site ring, leading to a smaller derivative at the nearest neighbor.

The nearest-neighbor renormalization strength  $\alpha(\tilde{U})$  presented in Fig. (3.7) (c) shows a similar trend as in the one-dimensional case. The renormalization is weakest for  $\tilde{U}/t \sim 3$  and reaches asymptotically  $\alpha = 1$  for large interaction strengths. Strikingly, the renormalization in the non-interacting limit is  $\alpha(0) \approx 0.8$  in contrast to  $\alpha(0) \approx 1.2$  in the case of one dimension.

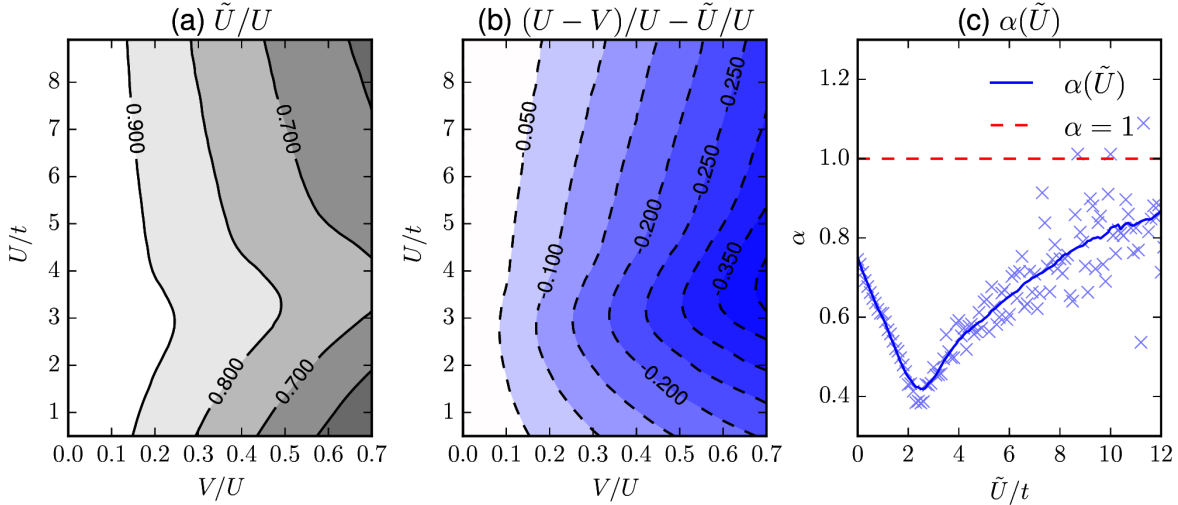


**Figure 3.7.:** (a) Renormalization of the local Coulomb interaction  $\tilde{U}/U$  for half-filled Hubbard models (defined by  $U/t$  and  $V/U$ ) on a  $12 \times 12$  square lattice calculated from Eq. (3.8). (b) shows the deviation of the approximation that electrons are only displaced to nearest neighbors (Eq. (3.12)) to the exact treatment. (c) shows the nearest neighbor renormalization strength  $\alpha(\tilde{U})$ , compare Eq. (3.15). The crosses are from finite differences and the line is from analytic derivatives of fits. The red dashed line corresponds to the approximation  $\tilde{U} = U - V$ , i.e.,  $\alpha = 1$ .

### 3.5. Honeycomb lattices

The honeycomb lattice is especially relevant as it is the lattice of graphene. We discuss the honeycomb lattice with realistic long-range interactions in the next section. Here, we analyze the properties of the effective purely local Hubbard model on the honeycomb lattice. We investigate the renormalizations of the local interactions by nearest-neighbor interaction only, just as we did in the two preceding sections for Hubbard model on a ring and the square lattice. We again use the DQMC method to calculate the charge correlation functions on a  $8 \times 8$  lattice with  $\beta = 9/t$ ,  $\Delta\tau = 0.025$ , 500 warm-up sweeps and 5000 measurement sweeps. We use the Savitzky-Golay filter with a window of  $\Delta\tilde{U}/t = 1.5$  and cubic polynomials to smoothen the data. The spatial behavior is shown in Fig. (3.8). The general behavior is very similar to the case of the square lattice, with an exponential decay of the correlation functions with increasing  $j$  (panel (a) and (b)). The oscillatory behavior of the local term is similar but slightly bigger than for the square lattice. For large interaction strength ( $\tilde{U} = 10.0$ ) the exponential decay is faster than in the case of the square lattice, at least if we consider not

the decay with distance ( $\mathbf{r}_0 - \mathbf{r}_j$ ) but with the number of the neighbors  $j$ . The square lattice is more densely packed, such that the distance between the sites labeled 0 and  $j$  is smaller than in the case of the honeycomb lattice. The derivatives of the charge correlation functions (multiplied by the coordination number  $N_j$ ) shown in panel (c) of Fig. (3.8) show a similar trend as in the case of the square lattice. The minimum of the local term is shifted to larger interaction strengths ( $\tilde{U}_M \sim 4.5$ ). The graphical representations on the lattice in Fig. (3.9) show that the oscillatory behavior of the sign below  $\tilde{U}_M$  is matched to the sub-lattice symmetry of the lattice. For  $\tilde{U} < \tilde{U}_M$ , the derivatives for the sublattice A are negative, those for sublattice B are positive. For  $\tilde{U} > \tilde{U}_M$  all derivatives but the local one are positive, as in the case of the square lattice.

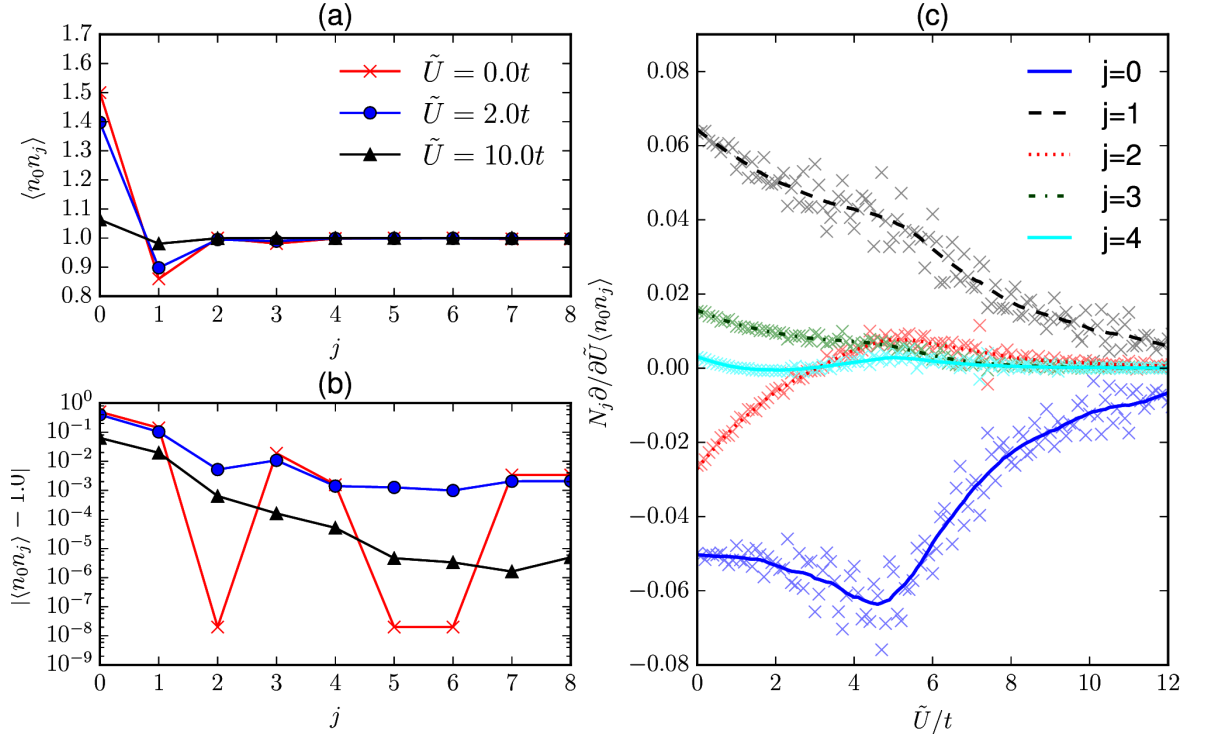


**Figure 3.8.:** Density-density correlation functions for a Hubbard model on a  $8 \times 8$  unit cells honeycomb lattice: (a) and (b) show the spatial behavior for different interaction strengths for the  $j$ th neighbor shell. The semilogarithmic plot in (b) shows the difference to a value of 1.0. Panel (c) shows the derivative with respect to  $\tilde{U}$  multiplied with the coordination number, for the first few nearest neighbors  $j$ . The crosses are from finite differences and the line is from analytic derivatives of the result of a Savitzky–Golay filtering.

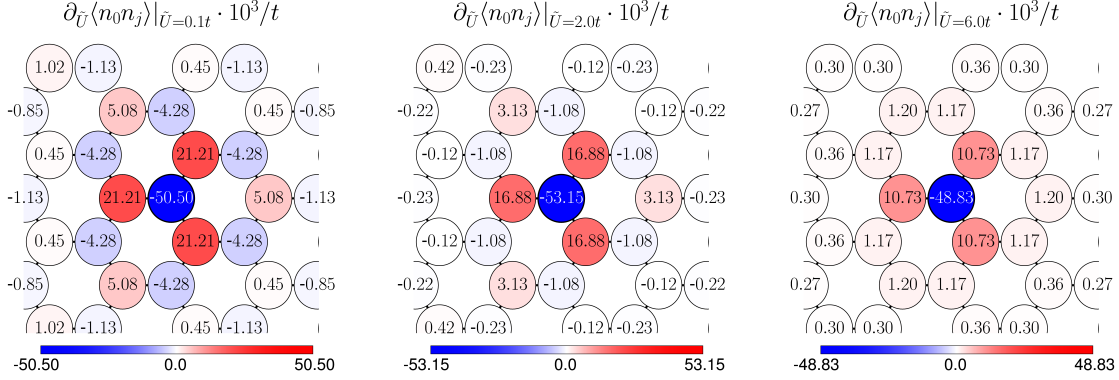


**Figure 3.9.:** Graphical representation of  $\partial/\partial\tilde{U}\langle n_0 n_j \rangle$  for  $\tilde{U}/t = 0.1, 2.0, 6.0$ .

The calculated renormalized local interactions  $\tilde{U}$  are presented in Fig. (3.10). We analyze the same Hubbard models (defined by  $U$  and  $V$ ) as in the two former cases. Depending on the strength of the nonlocal interactions, we find the strongest renormalization at  $U/t \sim 5$  to  $U/t \sim 7$ . Panel (b), which shows the difference of the exact treatment and the approximation  $\tilde{U} = U - V$ , reveals that for  $U/t \sim 2$  and nonlocal interactions up to  $V/U \sim 0.4$  the  $U - V$  approximation holds rather good. As in the case of the one-dimensional ring but in contrast to the case of the square lattice, we do find stronger renormalizations as in the case of the approximation for small interaction strengths. We find that the approximation overestimates the renormalization for large local interaction as in both other geometries.

The analysis of the nearest neighbor interaction strength  $\alpha(\tilde{U})$  underlines the findings from above: effective interaction strengths below  $\tilde{U}/t \approx 2$  lead to strong renormalizations with  $\alpha > 1$ . The non-interacting limit is close to the one-dimensional result,  $\alpha(0) \approx 1.2$ . We find the smallest renormalization,  $\alpha_{\min} \approx 0.6$ , for  $\tilde{U} \approx 5$ , which is the largest interaction strength at which we find the minimum for all three investigated lattices. As in the case of the six-site ring, we exclusively find  $\alpha(\tilde{U}) > 1$  for effective interaction strengths where  $\partial/\partial\tilde{U}\langle n_0 n_2 \rangle$  is negative.

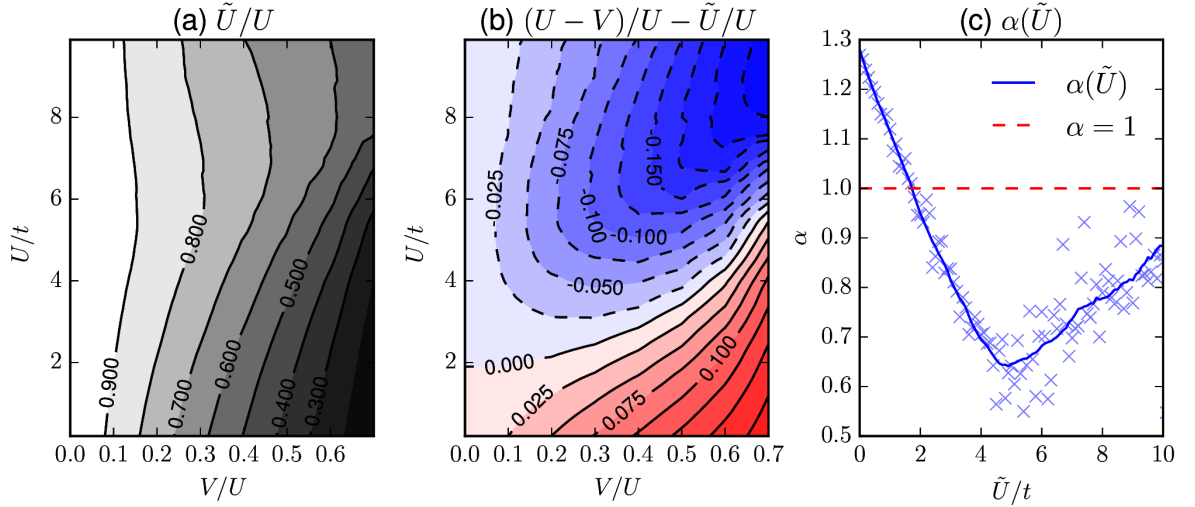


**Figure 3.10.:** (a) Renormalization of the local Coulomb interaction  $\tilde{U}/U$  (Eq. (3.8)) for half filled extended Hubbard models (defined by  $U/t$  and  $V/U$ ) on a honeycomb lattice. (b) shows the difference between the approximation that electrons are only displaced to nearest neighbors (Eq. (3.12)) and the exact treatment. (c) shows the nearest neighbor renormalization strength  $\alpha(\tilde{U})$ , compare Eq. (3.15). The crosses are from finite differences and the line is from analytic derivatives of fits. The red dashed line corresponds to the approximation  $\tilde{U} = U - V$ , i.e.,  $\alpha = 1$ .

In conclusion, we find a very similar behavior of the renormalization for all lattices: We find large renormalizations for small local interaction strengths. We find that in all cases the renormalization asymptotically reaches  $\alpha = 1$  for  $U/t \gg 1$  and  $U \gg V$ . The non-interacting renormalization strength differs between the lattices. It is similarly strong for one dimension and the honeycomb lattice ( $\alpha(0) \approx 1.2$ ) and considerably smaller for the square lattice ( $\alpha(0) \approx 0.8$ ). This difference seems to be related to the coordination number and the corresponding spatial spread of the derivatives of the correlation functions with respect to  $\tilde{U}$ . The values of the effective interaction at which we find the smallest renormalizations also depend on the geometry: Approximately, we find  $\alpha(\tilde{U} = 3.8) \approx 0.8$ ,  $\alpha(\tilde{U} = 3) \approx 0.4$  and  $\alpha(\tilde{U} = 4.7) \approx 0.6$  for the six-site ring, the square lattice and the honeycomb lattice, respectively.

### 3.6. Models for realistic materials: Graphene, silicene and benzene

To calculate  $\tilde{U}$  for realistic systems, we have to calculate model parameters for the corresponding extended Hubbard models. We do this in the sense of the derivation of model Hamiltonians from ab initio calculations, which we have already discussed in Sec. (2.4) in the context of LDA+DMFT.

We calculate values for the Coulomb interactions in the extended Hubbard model defined by Eq. (3.1). For graphene and silicene the values for the Coulomb interaction are calculated with the constrained random-phase approximation (cRPA, shortly introduced in Sec. (2.4.3)) as in [224], i.e., using cRPA on top of an LDA calculation. The resulting values of the Coulomb interactions are given in Table (3.1).

To define the single-particle Hamiltonian, we do not use the Kohn-Sham eigenfunctions and transform them into a localized basis, as in Sec. (2.4). Instead, we approximate the  $p_z$  band structure by a nearest-neighbor tight-binding Hamiltonian (compare Ref. [35]) with a hopping of  $t = 2.8$  eV for graphene and  $t = 1.14$  eV for silicene, which leads to a Fermi velocity at the Dirac point close to the LDA result. A comparison of the LDA band structure and the tight-binding band structure for the case of graphene and silicene is shown in Fig. (3.11).

For graphene, the occupied part of the LDA  $p_z$  band structure is approximated rather well by the tight-binding dispersion. The upper  $p_z$  band is, however, off by approximately 4 eV at the  $\Gamma$  point. For silicene, the buckling of the two-dimensional structure leads to hybridization of the  $p_z$  bands with other bands, visible near  $\Gamma$  and M, which is naturally not described by the nearest-neighbor tight-binding model with only one orbital per atom. Although we could improve the description of the single-particle part by including more hopping processes or enlarging the basis, we use the nearest-neighbor and single-orbital approximation, because it comes with the benefit of particle-hole symmetry, which eliminates the sign problem in DQMC simulations.

Let us keep in mind, that the single- and two-particle part of the extended Hubbard model, do not precisely match in the sense of LDA+DMFT, but that we use a different dispersion for the single-particle Hamiltonian than we have used to evaluate the Coulomb interaction via the cRPA. The severeness of this approximation is difficult to evaluate. At least the tight-binding approximation leads to a good general description of the LDA band structure and an excellent description of the Dirac point.

Finally, we stress that the LDA data themselves (the single-particle data and the cRPA data), are obtained from approximations, and thus an extended Hubbard model derived consequently in the LDA+DMFT sense does not necessarily have to be more

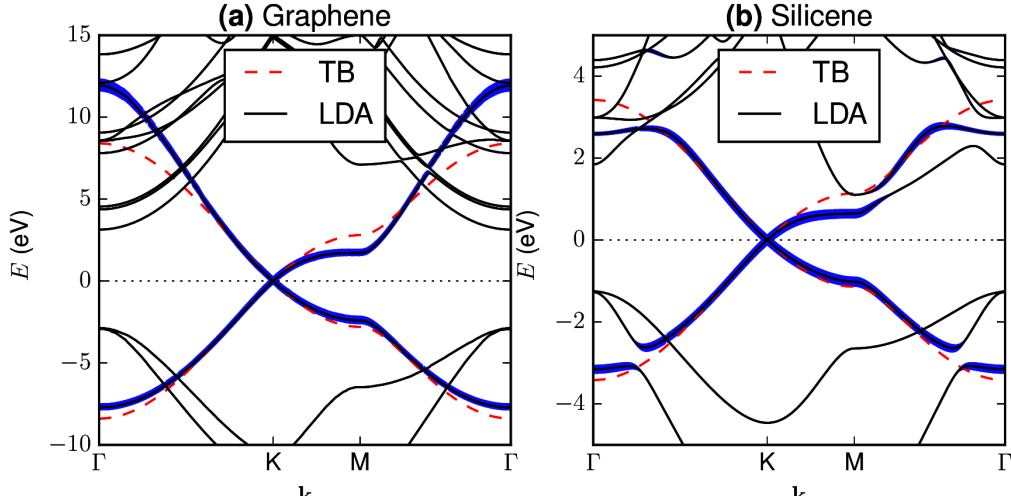


**Figure 3.11.:** Band structure of (a) graphene and (b) silicene from LDA calculations (black solid lines) and from the nearest-neighbor tight-binding approximation for the  $\pi$  and  $\pi^*$  band (red dashed lines) with  $t = 2.8$  eV for graphene (compare Ref. [35]) and  $t = 1.14$  eV for silicene (compare Ref. [48]) with the Fermi energy  $E_F = 0$  eV. The  $p_z$  character of the LDA bands is highlighted by fat bands (blue).

correct than the approach we have chosen.

For benzene, we use values of the Coulomb interaction and nearest neighbor-hopping from [31], which are obtained by fitting  $U$  and  $t$  to experimental spectra and calculating  $V_{ij}$  by Ohno interpolation [166], which reads

$$V_{ij}(\varepsilon) = \frac{U}{\sqrt{1 + (\alpha \varepsilon r_{ij})^2}} \quad (3.16)$$

with  $\alpha = U/e^2$ . The nonlocal Coulomb interaction can be tuned by an additional variable screening  $\varepsilon$  ranging from 0 to  $\infty$  to investigate model systems with different long-range behavior of the Coulomb interaction.  $\varepsilon = \infty$  corresponds to purely local interactions and  $\varepsilon = 0$  to ultimately nonlocal interactions with matrix elements not decaying with distance between sites.  $\varepsilon = 1$  corresponds to the model of benzene proposed in [31]. For benzene the values of the initial Coulomb interactions are given in Table (3.1).

The resulting values of the effective local Coulomb interaction  $\tilde{U}$  for graphene, silicene and benzene are summarized in the lower half of Tab. (3.1). The error bars stem from the statistical errors in the correlation functions from DQMC. The local Coulomb interaction is decreased by a factor of larger than two in all cases. For both, graphene and silicene the renormalized on-site interactions are far away from the transition to

a gapped spin liquid at  $\tilde{U}/t = 3.5$  [150]. The Dirac semimetal phase is thus stabilized by the nonlocal Coulomb interactions. We obtain the strongest renormalization of the on-site interaction for benzene. This is mostly due to the different ratio between local and nonlocal Coulomb interactions in benzene,  $V_{01}/U = 0.72$ , as compared to  $V_{01}/U = 0.56$  for graphene or  $V_{01}/U = 0.55$  for silicene.

**Table 3.1.:** First three rows: Coulomb matrix elements obtained with cRPA (graphene and silicene) and from [31] for benzene ( $t_{\text{graphene}} = 2.80$  eV,  $t_{\text{silicene}} = 1.14$  eV,  $t_{\text{benzene}} = 2.54$  eV). Last three rows: Effective local Coulomb matrix elements for half filling with and without the approximation that electrons are only displaced to nearest neighbors and factor by which the local Coulomb interaction is decreased.

	Graphene	Silicene	Benzene
$U/t$	3.63	4.19	3.96
$(V_{01}, V_{02})/t$	2.03, 1.45	2.31, 1.72	2.83, 2.01
$(V_{03}, V_{04})/t$	1.32, 1.14	1.55, 1.42	1.80, –
$\tilde{U}/t$	$1.6 \pm 0.2$	$2.0 \pm 0.3$	1.2
$(U - V_{01})/t$	1.6	1.9	1.1
$\tilde{U}/U$	$0.45 \pm 0.05$	$0.46 \pm 0.05$	0.3

### 3.6.1. Real space convergence of the effective interaction

For translationally invariant systems the equation for the effective interaction (Eq. (3.8)) includes a sum of derivatives of the correlation functions times the nonlocal Coulomb interaction over all neighbors  $j \neq 0$ . The spatial convergence depends on the  $r$  dependence of the correlation function and that of the nonlocal Coulomb interaction  $V_{0j}$ . The Coulomb interaction asymptotically decays as  $1/r$ . The derivatives fall off exponentially and their sign changes with the sublattice in the parameter range we expect from  $\tilde{U} \sim U - V$ . Altogether a quick convergence can be expected: Fig. (3.12) shows the results of the evaluation of Eq. (5) for different cutoff radii  $r_c$  for graphene and silicene respectively.  $r_c$  is the maximal distance between the sites with indexes  $i = 0$  and  $j$  included in the sum over  $j$  in Eq. (3.8).

As could be already expected from the  $\partial_{\tilde{U}} \langle n_{0\uparrow} n_{j\sigma'} \rangle_{\tilde{H}}$ -terms depicted in Fig. (3.8), the nearest-neighbor Coulomb interaction has the strongest impact on the renormalization of the on-site term  $\tilde{U}$ . Thus, the approximation of neglecting all non nearest-neighbors

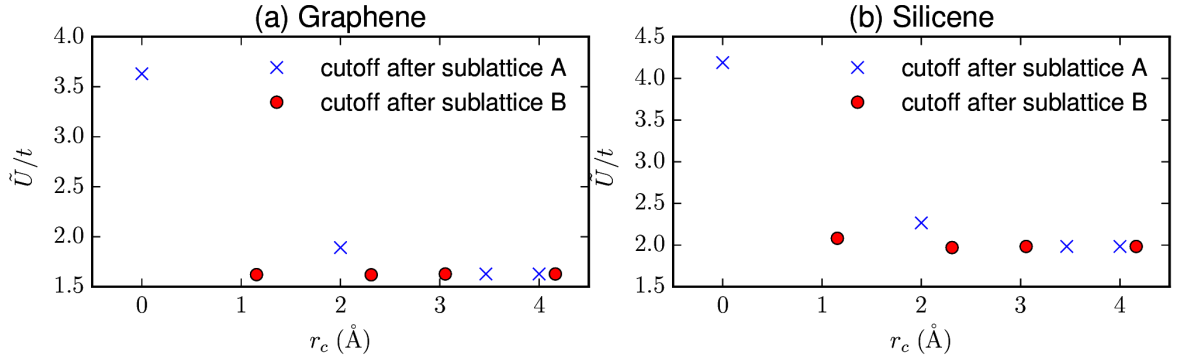


**Figure 3.12.:** Effective Coulomb interaction  $\tilde{U}/t$  for graphene and silicene against the position of the cutoff of the spatial sum used to evaluate Eq. (3.8).

terms is quite reasonable, here. Contributions from the same sublattice as the site  $i = 0$  tend to increase  $\tilde{U}$  and those from the other sublattice decrease  $\tilde{U}$ . It is obviously sufficient to introduce the cutoff after the fourth-nearest neighbors.

### 3.6.2. Finite-size analysis for graphene

The DQMC calculations are performed on finite lattices. To analyze if the results for finite lattices are relevant for the limit of infinitely large lattices, we have to compare calculations of systems with different sizes. Therefore, we compare the charge correlation  $\sum_{\sigma} \langle n_{0\uparrow} n_{j\sigma} \rangle$  of a Hubbard model on the honeycomb lattice on  $10 \times 10$  and  $16 \times 16$  unit cells for  $\tilde{U}/t = 1$  for all available distances  $|r_0 - r_j|$ . The result is presented in Fig. (3.13), where we compare the absolute values and the difference of the calculations with different numbers of lattice sites. The difference is on the order of per mille. Thus, the results seem not to be affected strongly by the finite size of the lattice. This analysis was performed for the honeycomb lattice up to interaction strengths of  $\tilde{U}/t = 3.5$  with basically the same result.

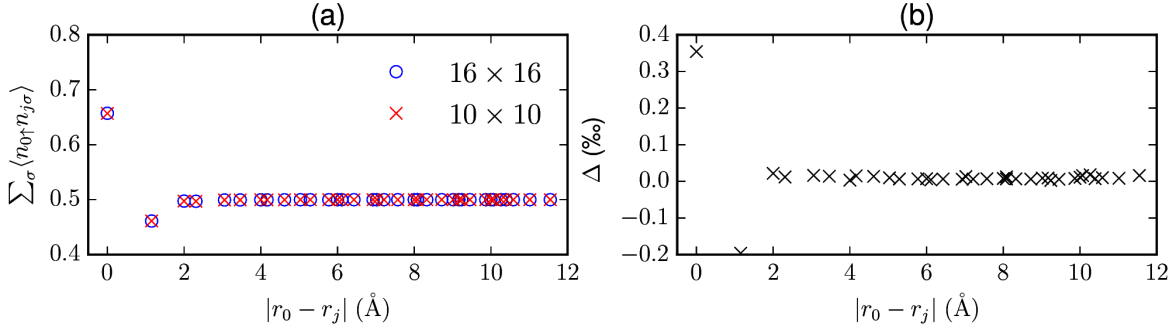


**Figure 3.13.:** Comparison of correlation functions of Hubbard models on the honeycomb lattice for  $U/t = 1$  with  $10 \times 10$  unit cells (red crosses) and  $16 \times 16$  unit cells (blue circles) on (a) an absolute scale and (b) a relative scale in per mille.

### 3.6.3. Temperature dependence of $\tilde{U}$ for graphene

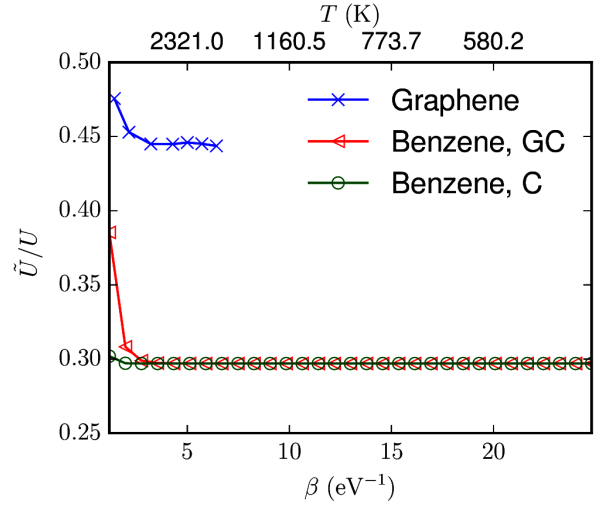
So far, we have obtained the renormalizations for all systems at a fixed temperature of  $\beta t = 9$  and have evaluated the expectation values in a grand canonical ensemble. Here we analyze the behavior of the renormalization with respect to the temperature of the system and the severeness of approximating the canonical expectation values with their grand canonical counterparts.

Therefore, we first calculate  $\tilde{U}/t$  for different temperatures ( $\beta t = (4, 6, 9, 12, 14, 16, 18)$ ) on a smaller super cell of  $8 \times 8$  unit cells because the calculations for smaller temperatures become increasingly heavy, computationally. The time discretization is fixed to  $\Delta\tau = 0.05$ .

Fig. (3.14) shows the resulting effective local interaction strengths versus the inverse temperature  $\beta$  (in units of  $\text{eV}^{-1}$  instead of  $\beta t$  in order to compare results obtained for benzene). We can observe a rise of  $\tilde{U}$  for higher temperatures ( $\beta \lesssim 3 \text{ eV}^{-1}$ ). However, for smaller temperatures ( $\beta \gtrsim 3 \text{ eV}^{-1}$ ) no dramatic change takes place.

Unfortunately, we can not draw any conclusion for very low temperatures as the DQMC method is limited in this regard. To check the behavior at lower temperature and compare canonical with grand canonical results we alternatively analyze the  $\tilde{U}(T)$  dependence for benzene. For benzene we calculate the correlation functions with exact diagonalization and thus have no computational limitations regarding the temperature. The resulting effective interaction strengths for the canonical and grand canonical case are presented in Fig. (3.14). In both cases the behavior is similar to that of graphene. The renormalization is basically constant and coincides for the grand canonical and canonical calculations for  $\beta \gtrsim 3 \text{ eV}^{-1}$ . While the rise of  $\tilde{U}/U$  for smaller  $\beta$  is sharp in the case of the grand canonical calculation, it is only slight in the canonical case.

**Figure 3.14:** Temperature dependence of  $\tilde{U}/U$  for graphene (blue crosses) and benzene (red triangles and green circles for evaluation of expectation values in the grand canonical and canonical ensemble, respectively). Lines are guides to the eye.



We conclude, that a weak temperature dependence of  $\tilde{U}$  indicates a low discrepancy between results from the grand canonical and the canonical expectation values. Therefore, the results obtained for the case of graphene at  $\beta t = 9$  are valid for the canonical ensemble.

We understand the decline of the renormalization in the case of the grand canonical expectation values with an even simpler model than that for benzene, namely with a two-site Hubbard cluster. Fig. (3.15) shows the correlation functions  $\langle n_0 n_j \rangle$  (left panels), where  $n_j = n_{j\uparrow} + n_{j\downarrow}$ , and their derivative with respect to  $U$  (right panels) in dependence of the temperature for  $j = 0$  and  $j = 1$  and the grand canonical (upper panels) and the canonical case (lower panels). The left panels show systems with two interaction strengths,  $U/t = 0.7$  and  $U/t = 1.3$ . We observe that in the grand canonical case the system undergoes a transition from correlated (evident by  $\langle n_i n_j \rangle \neq \langle n_i \rangle \langle n_j \rangle$ ) at low temperatures to uncorrelated (evident by  $\langle n_i n_j \rangle = \langle n_i \rangle \langle n_j \rangle$ ) for temperatures close to  $\beta = 0$ .

By comparing the transition for the two slightly different interaction strengths (dashed and solid lines) we find that the difference in the correlation functions diminishes faster for the nonlocal correlation than for the local interaction. This trend is underlined by the derivative in the right panel. The nonlocal derivative starts to drop at around  $U/t = 2$  whereas the local derivative shows a sharp drop at  $U/t \sim 0.5$ . In conclusion, the growing thermal fluctuations introduced by the high temperature destroy the influence of  $U$  on the nonlocal correlations faster than its influence on the local correlation. This leads to a decline of the ratio between  $\partial/\partial\tilde{U}\langle n_0 n_1 \rangle_{\tilde{H}}$  and  $\partial/\partial\tilde{U}\langle n_0 n_0 \rangle_{\tilde{H}}$  in Eq. (3.8) (i.e., a smaller nearest neighbor renormalization strength  $\alpha$ ) and thus a value of  $\tilde{U}$  closer to the original  $U$ . In conclusion, the high temperature

leads to a smaller renormalization.

In the case of the canonical ensemble, the lower left panel of Fig. (3.15) reveals that in contrast to the former case the system obeys the sum rule introduced in Eq. (3.10), i.e.,  $\langle n_0 n_0 \rangle + \langle n_0 n_1 \rangle$  is constant. This leads up to a sign to equal derivatives with respect to  $U$  at all temperatures, as is evident in the lower right panel of Fig. (3.15), and consequently to no temperature dependence of  $\tilde{U}$ . That this is not strictly the case for larger systems is apparent in the non zero  $\tilde{U}$  dependence for the canonical case shown in Fig. (3.14).

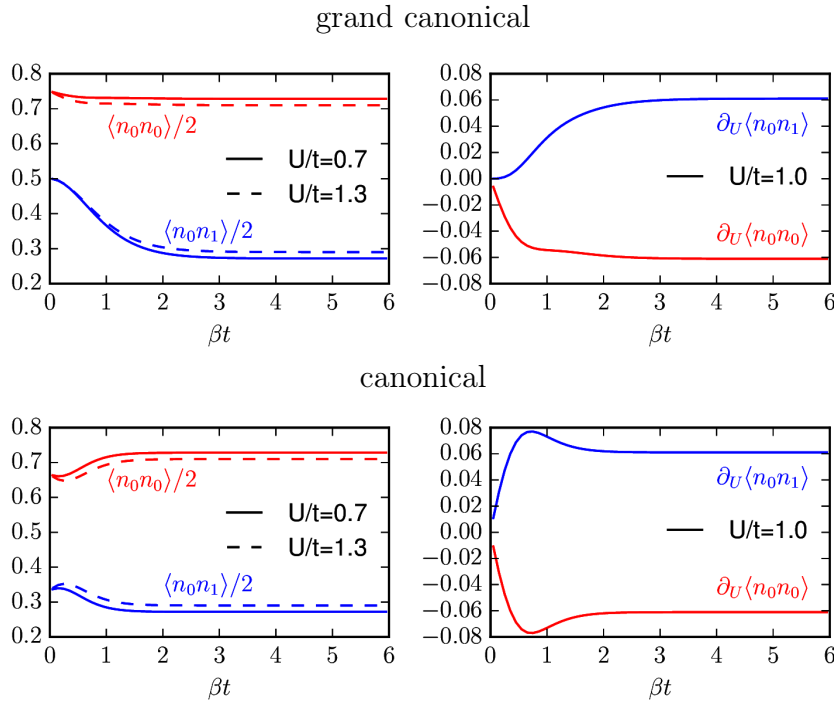


**Figure 3.15.:** Temperature dependence of the correlation functions  $\langle n_0 n_j \rangle$  evaluated in the grand canonical ensemble (upper panels) and in the canonical ensemble (lower panels) for  $U/t = 0.7$  and  $U/t = 1.3$  (left panels) and their derivatives at  $U/t = 1$  (right panels) for a two-site Hubbard model.

### 3.7. Filling dependence

It is interesting to see how the renormalization of the local Coulomb interaction depends on the filling of the system. Unfortunately, the sign problem in the DQMC method appears for non half-filled Hubbard models, which is prohibitively strong for the parameters we have chosen, compare Sec. (2.5.3). Therefore, we study the model

of benzene at arbitrary number of electrons  $N$  by means of exact diagonalization. The initial Coulomb matrix elements entering Eq. (3.8) are assumed to be doping independent.

The results for the filling dependent  $\tilde{U}/t$  in benzene for differently screened nonlocal Coulomb interaction  $V_{ij}(\varepsilon)$  parametrized via the Ohno interpolation (Eq. (3.16)) are shown in Fig. (3.16). Clearly, doping in the range of  $4 \leq N \leq 8$  has only little effect on  $\tilde{U}$ . This doping range corresponds to changing the number of electrons on the order of  $\pm 1/3$  per atom and thus covers fully the range of dopings which can be achieved in graphene by means of gate voltages or adsorbates.

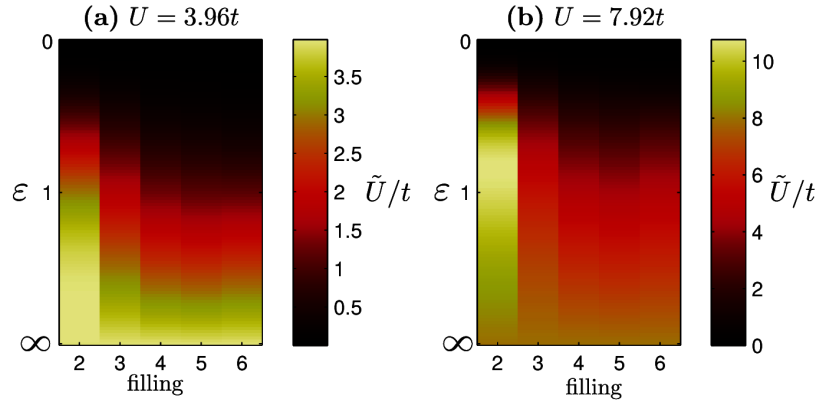


**Figure 3.16.:** Effective local Coulomb interaction  $\tilde{U}/t$  color coded for (a) benzene with  $U = 3.96/t$  and (b) benzene with  $U = 7.92/t$ , various screenings of  $V_{ij}(\varepsilon)$  and all fillings. Due to particle hole symmetry of the model only  $N \leq 6$  is shown.

Strong differences to the half-filled case arise however for extreme doping ( $N=2,10$ ), i.e., close to the nearly empty or almost completely filled case. The reduction of the effective local interaction  $\tilde{U}$  is considerably weaker (Fig. (3.16) (a)). For a stronger initial on-site interaction ( $U = 7.92t$ )  $\tilde{U}$  even exceeds the initial on-site interaction by a factor of up to  $\tilde{U}/U \approx 1.3$  (Fig. (3.16) (b)).

This effect is generally expected in nearly empty and almost filled systems: Fig. (3.17) shows  $\tilde{U}$  derivatives of charge correlation functions in a  $5 \times 5$  supercell of a honeycomb lattice occupied by  $N = 2$  electrons. As the Fock space is small enough, the correlation functions are calculated by exact diagonalization. Here,  $\partial_{\tilde{U}} \langle n_{0\uparrow} n_{j\downarrow} \rangle_{\tilde{H}}$  shows pronounced differences to the half-filled case. In addition to a suppression of double occupancy by increased  $\tilde{U}$  (i.e.,  $\partial_{\tilde{U}} \langle n_{0\uparrow} n_{0\downarrow} \rangle_{\tilde{H}} < 0$  as in the half-filled case)  $\partial_{\tilde{U}} \langle n_{0\uparrow} n_{j\downarrow} \rangle_{\tilde{H}}$  is negative in the vicinity of  $j = 0$ , too. Increasing local interactions with

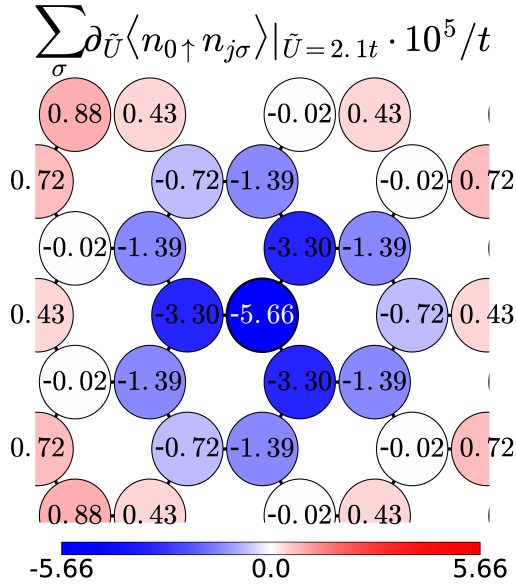


**Figure 3.17:** Color coded graphical representation of the derivatives of the correlation functions for  $\tilde{U}/t = 2.1$  for a nearly empty honeycomb lattice (2 electrons in  $5 \times 5$  super cell).

an electron at site  $j = 0$  expel other electrons also from its vicinity.

This corresponds to the process depicted in Fig. (3.18) and leads to effective on-site interactions being *increased* by nonlocal Coulomb terms: In a dilute system, two electronic wave packages can minimize their Coulomb energy by avoiding each other in real space while staying delocalized over many lattice spacings at the same time. For such delocalized wave packages the effect of on-site and, e.g., nearest-neighbor Coulomb interactions becomes very similar such that  $V$  increases the on-site interaction  $\tilde{U}$ .

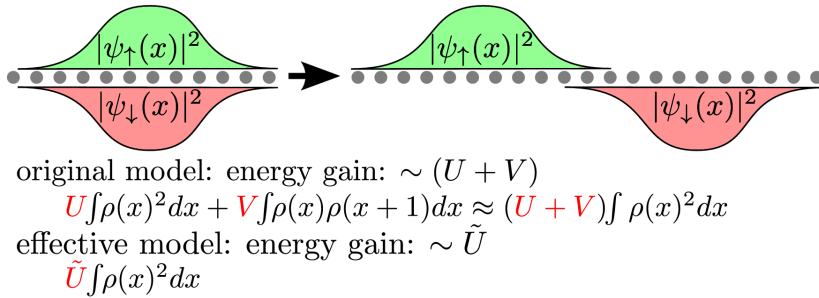


**Figure 3.18.:** Illustration of the physical process underlying Eq. (3.8) for nearly empty/full system: Wave packets of spin up and down electrons/holes ( $\rho(x) = |\psi_{\uparrow,\downarrow}(x)|^2$ ) are separated to the farthest possible position. If the packets are much wider than the lattice spacing, the energy gained in the original model is  $\sim (U + V)$  and  $\sim \tilde{U}$  in the effective model.

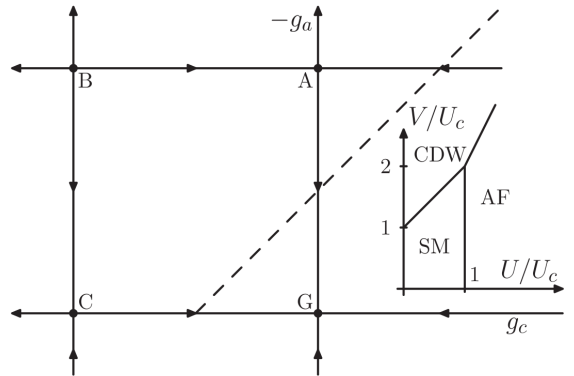
This can be understood in terms of Wigner crystallization [228]. In the full model the Coulomb energy wins over the kinetic energy for low electron/hole densities. Thus the carriers tend to localize. To approach a Wigner crystal in the auxiliary model, the effective local interaction is increased such that interaction energy dominates over kinetic energy.

### 3.8. Benchmark for the case of benzene

The question arises how accurate the effective model reflects the physical properties of the original model. The phase diagram of the extended Hubbard model on the honeycomb lattice includes an antiferromagnetic (AF), a semimetal (SM) and a charge density wave (CDW) phase (as reproduced in Fig. (3.19) from Ref. [80]) while the (repulsive) Hubbard model with strictly local interactions only features the first two phases. (The attractive Hubbard model does show, next to a superconducting phase [192], signs of a CDW instability [65]). Similarly, if the system is in a quantum Hall regime, i.e., in presence of strong magnetic fields, there are some many-body phenomena like the formation of stripes where the long-range tails of the Coulomb interaction are crucially important. In situations with such charge inhomogeneities the auxiliary model can likely fail to provide a physically correct description of the original system. If the parameters of the extended model are, however, clearly inside the AF or the SM phase, the effective model likely approximates the physical properties of the original model quite well.

We illustrate this expectation with the example of modified benzene. In this model, the nonlocal Coulomb interaction  $V_{ij}$  are calculated with the Ohno interpolation (3.16). A comparison of the spin and the density correlation functions ( $\langle S_z^{ij} \rangle = \langle m_i m_j \rangle$ , where  $m_i = n_{i\uparrow} - n_{i\downarrow}$  and  $\langle \rho^{ij} \rangle = \langle n_i n_j \rangle$ , where  $n_i = n_{i\uparrow} + n_{i\downarrow}$ ), for the extended and the

**Figure 3.19:** The inset shows the phase diagram of an extended Hubbard model on a honeycomb lattice with long range Coulomb interaction. Reprinted figure with permissions from [I. Herbut, Phys. Rev. Lett., **97**, 146401 (2006), [80]]. Copyright 2006 by the American Physical Society.



auxiliary local Hubbard model are shown in Fig. (3.20). The correlation functions have been calculated by exact diagonalization for, both, the original and the effective model. For  $\varepsilon = 0$  and  $\varepsilon \rightarrow \infty$  (non-interacting and local limit, respectively) the correlation functions of the effective and original model coincide as they should. CDW physics would manifest in  $\langle \rho^{ij} \rangle$  and here we find indeed some differences of  $\langle \rho^{ij} \rangle$  for the effective and the auxiliary model for intermediate screening ( $\varepsilon \sim 1$ ). However, nearly no deviation of  $\langle S_z^{ij} \rangle$  between the extended and effective model is found. To less extent, this behavior is found for all fillings and also different initial local interactions  $U$ , which can be seen in the overall comparison in Figs. (A.2) and (A.3) in the Appendix (A.2). The deviations for the spin correlation function are larger away from half filling. We thus expect that transitions into phases like an AF insulator (or a Mott insulator) are very well described by the effective model.

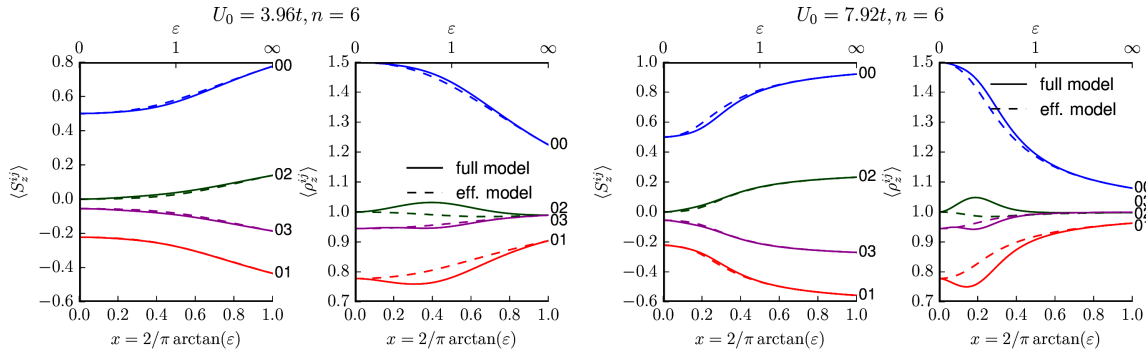


**Figure 3.20.:** Comparison of the spin and density correlation functions for modified benzene at half filling as functions of the screening for the extended Hubbard model (continuous lines) and the effective model (broken lines). The left panels show results for  $U = 3.96t$ , the right panels show results for  $U = 7.92t$ .

### 3.9. Low-level approximations of the effective system

So far, we have used exact, or in the case of DQMC close to statistical exact, solutions of finite Hubbard models to calculate the renormalization of the local interaction by nonlocal interaction. For multi-orbital Hubbard models, this is not possible because the numerical calculations are too expensive. An alternative to cope with more complex Hubbard models are approximations on a lower level.

We explore the quality of two approximations, namely Hartree-Fock and the random-

phase approximation, on the basis of the DQMC results for the square lattice in Sec. (3.4). We analyze the quality of the derivatives of the charge correlation functions with respect to  $\tilde{U}$  and the nearest-neighbor renormalizations strength  $\alpha(\tilde{U})$ . Another approximation worth inspecting is dynamical mean-field theory. However, the assessment of the quality of the DMFT for the calculation of  $\tilde{U}$  is not part of this work.

### 3.9.1. Hartree-Fock

Before we calculate the charge correlation functions in Hartree-Fock and use them in Eq. (3.8) to calculate  $\tilde{U}$  directly, we follow a different path towards a renormalized local interaction. We assume all nonlocal interactions to be static, decouple them in a mean-field manner and absorb the resulting one-particle terms into a renormalized hopping. The treatment of nonlocal interactions by Hartree-Fock is exact in infinite dimensions [156]. Because the properties of the Hubbard model are governed by the ratio of the interaction and the hopping  $U/t$ , we can equivalently regard a renormalized hopping as a renormalized interaction. The decoupling of nonlocal terms only is not precisely Hartree-Fock as it does not follow from the variational principle. However, this approach is in the spirit of Hartree-Fock.

We start by decoupling the nonlocal two-particle terms by

$$n_{i\sigma}n_{j\sigma'} = -c_{i\sigma}^\dagger c_{j\sigma'}^\dagger c_{i\sigma} c_{j\sigma'} \rightarrow -\langle c_{i\sigma}^\dagger c_{j\sigma'} \rangle c_{j\sigma'}^\dagger c_{i\sigma} - \langle c_{j\sigma'}^\dagger c_{i\sigma} \rangle c_{i\sigma}^\dagger c_{j\sigma'} + \langle n_{i\sigma} \rangle n_{j\sigma'} + \langle n_{j\sigma'} \rangle n_{i\sigma}, \quad (3.17)$$

where we have used  $i \neq j$ . The positive (Hartree-) terms lead to a constant shift in energy and can be absorbed into the chemical potential. Assuming spin symmetry, only expectation values with equal spin indices are nonzero,  $\langle c_{i\sigma}^\dagger c_{j\sigma'} \rangle = \delta_{\sigma\sigma'} \langle c_{i\sigma}^\dagger c_{j\sigma} \rangle$ . Inserting this expression into the Hamiltonian (3.1)<sup>5</sup> using  $V_{ij} = V_{ji}$  and relabeling of summation indices we arrive at

$$\begin{aligned} \tilde{H}_{\text{HF}} &= -t \sum_{ij\sigma} c_{i\sigma}^\dagger c_{j\sigma} + U \sum_i n_{i\uparrow} n_{i\downarrow} - \sum_\sigma \sum_{i \neq j} V_{ij} c_{i\sigma}^\dagger c_{j\sigma} \langle c_{j\sigma}^\dagger c_{i\sigma} \rangle \\ &= - \sum_{ij\sigma} \tilde{t}_{ij} c_{i\sigma}^\dagger c_{j\sigma} + U \sum_i n_{i\uparrow} n_{i\downarrow}, \end{aligned} \quad (3.18)$$

where

$$\tilde{t}_{ij} = \begin{cases} 0 & \text{if } i = j \\ t + V_{ij} \langle c_{j\sigma}^\dagger c_{i\sigma} \rangle & \text{if } i, j \text{ next neighbors} \\ V_{ij} \langle c_{j\sigma}^\dagger c_{i\sigma} \rangle & \text{else} \end{cases} \quad (3.19)$$

---

<sup>5</sup>In contrast to Eq. (3.1) we now explicitly assume a positive  $t$ ,  $U$ , and  $V_{ij}$  and write a minus sign in front of the one-particle term.

is the renormalized hopping. For general nonlocal interaction terms, the decoupling introduces long-range hopping parameters. For simplicity, and for the sake of comparability with the results from Sec. (3.4), we neglect all nonlocal interactions beyond nearest neighbor. Then, the effective Hamiltonian is a Hubbard Hamiltonian with only nearest-neighbor hopping and we can cast the band renormalization into a renormalization of  $U$  by demanding  $U/\tilde{t} = \tilde{U}/t$ . The renormalization of the nearest neighbor hopping is  $\tilde{t} = t + V_{01}\langle c_{0\sigma}^\dagger c_{1\sigma} \rangle$ .

Fixing the energy scale through  $t = 1$ , we arrive at a renormalized  $U$  of

$$\tilde{U} = \frac{U}{1 + V_{01}\langle c_{0\sigma}^\dagger c_{1\sigma} \rangle}. \quad (3.20)$$

The result of the self-consistent solution of Eq. (3.20), i.e., evaluating the expectation value for  $\tilde{U}$  (we use the DQMC solution here), for the square lattice with  $U/t$  from 0 to 9 and  $U/V$  from 0 to 0.7 is shown in Fig. (3.21) (b). The comparison with the result of the proper minimization of the free energy (see Fig. (3.7)) shows that the self-consistent treatment leads to reasonable results for  $U/t \gtrsim 4$  but strongly underestimates the renormalization for smaller interaction strengths. Using the non-interacting system to calculate the expectation value in Eq. (3.20) leads to slightly larger renormalizations, presented in Fig. (3.21) (a). The larger renormalization for the non self-consistent treatment is reasonable, as the value of  $\langle c_{0\sigma}^\dagger c_{1\sigma} \rangle$  declines with increasing interaction strength.

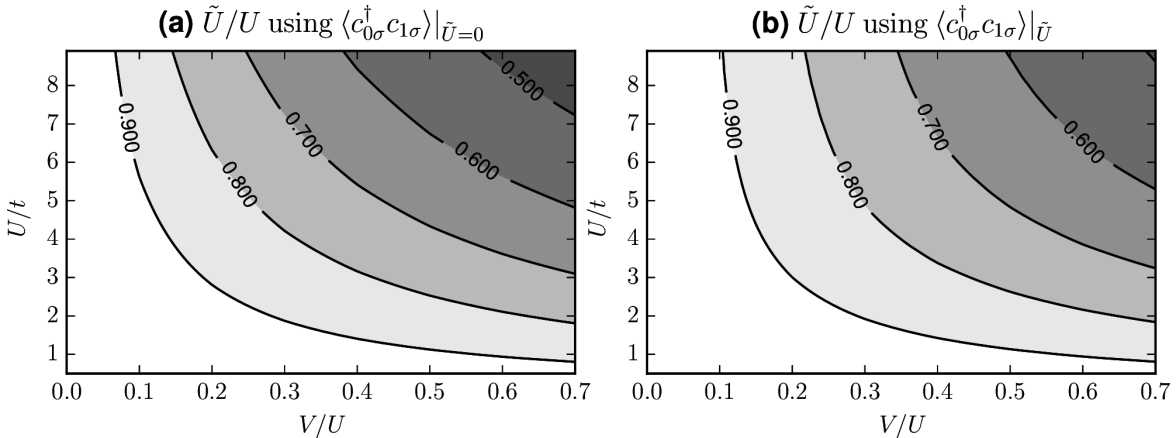


**Figure 3.21.:** Renormalization of the local interaction by a static treatment of non-local interaction terms by (a) a non-self consistent solution and (b) a self consistent solution of Eq. (3.20).

We continue the discussion on Hartree-Fock by calculating the charge correlation

### 3. Renormalizations of the Hubbard model by nonlocal interactions

---

functions in HF and using them to solve Eq. (3.8). We solve the HF Hamiltonian of the Hubbard model for half filling

$$H_{\text{HF}} = t \sum_{\langle ij \rangle \sigma} c_{i\sigma}^\dagger c_{j\sigma} + \sum_i \left[ U \langle n_{i\uparrow} \rangle n_{i\downarrow} + U \langle n_{i\downarrow} \rangle n_{i\uparrow} - \frac{U}{2} (\langle n_{i\uparrow} \rangle + \langle n_{i\downarrow} \rangle) \right] \quad (3.21)$$

self-consistently. In restricted Hartree-Fock ( $n_{i\uparrow} = n_{i\downarrow}$ ), where the decoupling of the local interaction term only leads to an on-site energy, which can be absorbed into the chemical potential, we don't get any dependence of the system on  $\tilde{U}$  at all. However, if we allow for broken spin symmetry, i.e., use unrestricted Hartree-Fock, we do get a dependence of the charge correlation functions on  $\tilde{U}$ . The ground state of the Hubbard model in HF is that with antiferromagnetic ordering [84]. However, we analyze the antiferromagnetic and ferromagnetic HF solutions. We use  $\langle n_{i\uparrow} \rangle \neq \langle n_{i\downarrow} \rangle$  to start the self-consistency in the case of ferromagnetic solutions. To enforce an antiferromagnetic solution we use  $\langle n_{i\uparrow} \rangle = 0.5 + (-1)^i m$  and  $\langle n_{i\downarrow} \rangle = 0.5 - (-1)^i m$  and  $m \neq 0$  in the beginning of the self-consistency cycle. In this case we solve the Hamiltonian in Eq. (3.21) on a  $2 \times 2$  unit cell and therefore have to diagonalize a  $4 \times 4$  matrix for the  $\uparrow$ -electrons reading

$$H(\mathbf{k}) = \begin{pmatrix} U \langle n_{1\downarrow} \rangle & 1 + e^{ik_x} & 1 + e^{ik_y} & 0 \\ 1 + e^{-ik_x} & U \langle n_{2\downarrow} \rangle & 0 & 1 + e^{ik_y} \\ 1 + e^{-ik_y} & 0 & U \langle n_{3\downarrow} \rangle & 1 + e^{ik_x} \\ 0 & 1 + e^{-ik_y} & 1 + e^{-ik_x} & U \langle n_{4\downarrow} \rangle \end{pmatrix} \quad (3.22)$$

at every  $\mathbf{k}$ -point, where  $t = 1$  and the sites in the unit cell are labeled as  $\begin{smallmatrix} 3 & 4 \\ 1 & 2 \end{smallmatrix}$ . We solve the equations on a grid of  $240 \times 240$   $k$ -points in the positive first quadrant of the Brillouin zone for a finite temperature of  $\beta t = 9$  and zero temperature, respectively. We calculate the charge correlation of the effective non-interacting system by the Wick theorem

$$\langle n_{0\sigma} n_{j\sigma'} \rangle = \langle n_{0\sigma} \rangle \langle n_{j\sigma'} \rangle - \langle c_{0\sigma}^\dagger c_{j\sigma'} \rangle \langle c_{j\sigma'}^\dagger c_{0\sigma} \rangle + \delta_{0j} \delta_{\sigma\sigma'} \langle n_{0\sigma} \rangle. \quad (3.23)$$

The derivatives of the charge correlations in the ferromagnetic case are shown in Fig. (3.22) (a). For finite temperature (solid lines) we observe a spontaneous magnetization for  $\tilde{U} \gtrsim 4$ . From the inspection of the Stoner criterion for magnetic solutions,  $\rho(E_F) \tilde{U} > 1$ , we would expect magnetic solutions for all  $\tilde{U}$ , because of the logarithmic divergence of the density of states  $\rho(E)$  [175, 176] at the Fermi energy  $E_F$  [84]. This simple version of the Stoner criterion is however only valid at  $T = 0$ . We indeed recognize non-zero derivatives from  $\tilde{U} = 0$  on at  $T = 0$  (dashed lines). In the ferromagnetic

regime we find a vaguely similar behavior to the exact treatment with DQMC (compare Fig. (3.5) (c)): The magnitude of the derivatives drops for increasing  $j$ . However, there is no agreement in the shape of the curves. Fig. (3.22) (b) shows the nearest neighbor interaction strength, see Eq. (3.15). For the case of finite temperature, we can not sensibly define  $\alpha$  for  $\tilde{U} \lesssim 4$ , the paramagnetic regime. For values of  $\tilde{U}$  above but close to the phase boundary we get an  $\alpha$  between 0.6 and 0.95 which is rather close to the value obtained from the DQMC calculations shown in Fig. (3.7). For larger interaction strengths, the renormalization begins to vanish, in contrast to the exact treatment. For zero temperature we observe a linear increase of  $\alpha$  for  $0 < \tilde{U} \lesssim 4$ . The renormalization strength shows a sharp drop at  $\tilde{U} \sim 8$ , where the system is fully polarized.

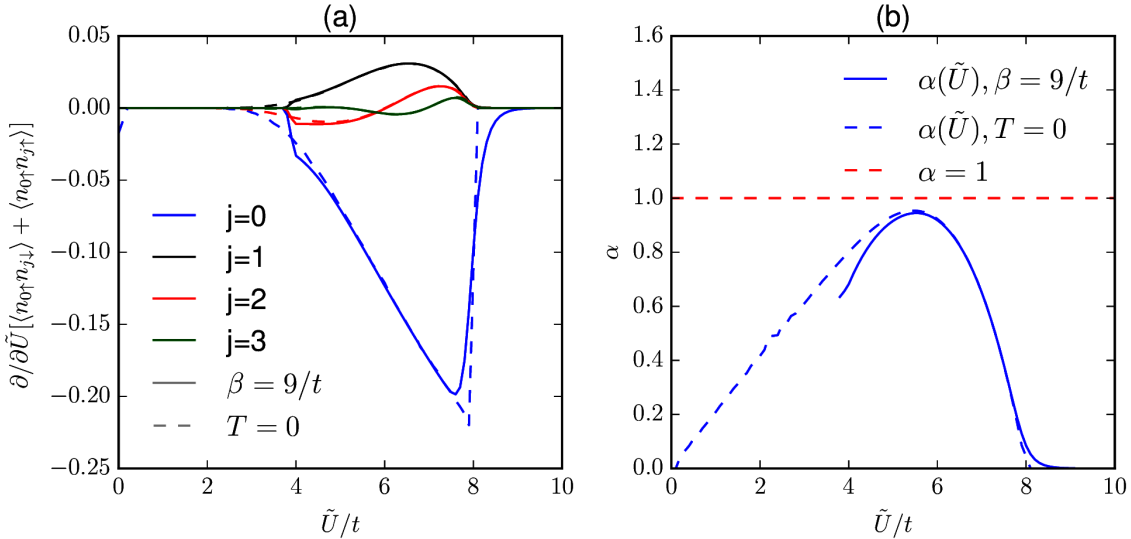


**Figure 3.22.:** (a): Derivative of the charge correlation functions with respect to  $\tilde{U}$  for the ferromagnetic HF treatment of a Hubbard model on the square lattice, for  $j = 0, 1, 2, 3$  and for  $\beta = 9/t$  (solid lines) and  $T = 0$  (dashed lines). (b): Nearest neighbor renormalization strength  $\alpha(\tilde{U})$  (compare Eq. (3.15)) for  $\beta = 9/t$  (solid blue line) and  $T = 0$  (dashed blue line). The red dashed line corresponds to the approximation  $\tilde{U} = U - V$ , i.e.,  $\alpha = 1$ .

The derivatives of the local and nearest-neighbor charge correlation functions in the case of antiferromagnetic ordering are presented in Fig. (3.23) (a) for finite temperature ( $\beta = 9/t$ , solid lines) and zero temperature (dashed lines). For finite temperature we find a paramagnetic phase for  $\tilde{U} \lesssim 2$ . For  $T = 0$  we find antiferromagnetic ordering

for all interaction strengths in line with Ref. [84]. In contrast to the DQMC solution and the ferromagnetic HF solution, the nearest-neighbor term dominates the local derivative. We observe a maximum of the derivative around  $\tilde{U} \sim 2$ , close to the finite temperature phase boundary. This results in a nearest-neighbor interaction strength  $\alpha$ , shown in Fig. (3.23) (b), which is by orders of magnitude larger than that from the exact treatment in the case of relatively small interaction strengths. For  $\tilde{U} \gg 1$ , the value of  $\alpha$  slowly seems to decay to  $\lim_{\tilde{U} \rightarrow \infty} \alpha(\tilde{U}) = 5$ . Obviously, the influence of the local interaction on the nonlocal charge correlation is strongly overestimated in the antiferromagnetic version of HF. In hindsight, it seems reasonable that using an antiferromagnetically symmetry broken state to calculate *charge* correlation functions leads to poor results.

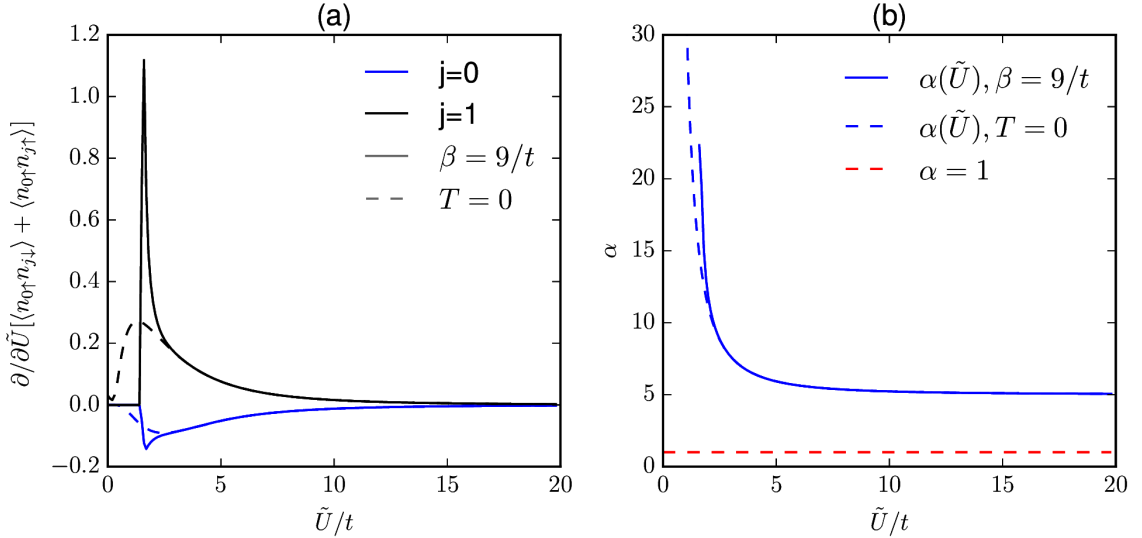


**Figure 3.23.:** (a): Derivative of the charge correlation functions with respect to  $\tilde{U}$  for the antiferromagnetic (checkerboard order) HF treatment of a Hubbard model on the square lattice, for  $j = 0$  and  $j = 1$  and for  $\beta = 9/t$  (solid lines) and  $T = 0$  (dashed lines). (b): Nearest neighbor renormalization strength  $\alpha(\tilde{U})$  (compare Eq. (3.15)) for  $\beta = 9/t$  (solid blue line) and  $T = 0$  (dashed blue line). The red dashed line corresponds to the approximation  $\tilde{U} = U - V$ , i.e.,  $\alpha = 1$ .

### 3.9.2. Random-phase approximation

The random-phase approximation is in some sense a generalization of the Hartree-Fock approximation, which introduces a frequency-dependent self-energy and thus should

lead to better results for  $\tilde{U}$  than HF.

To assess the quality of the random-phase approximation we calculate the charge correlation functions via Eq. (2.150). We have evaluated the charge susceptibility numerically with 90  $\mathbf{k}$  and  $\mathbf{q}$  points in the first quadrant of the Brillouin zone, 35 Matsubara frequencies and a temperature of  $\beta = 9/t$  for a Hubbard model on the square lattice.

The derivatives of the charge correlation functions  $\langle n_0 n_j \rangle$  with respect to  $\tilde{U}$  are presented in Fig. (3.24) (a). In general, the correlation functions resemble those obtained from DQMC (compare Fig. (3.5) (c)) especially for  $\tilde{U} \ll 1$  and presumably for  $\tilde{U} \gg 1$ . However, in RPA all functions are strictly monotonically decreasing and either convex or concave, depending on their sign. The DQMC results show maxima or at least a deviation of their respective convex or concave behavior at large  $\tilde{U}$  at about  $\tilde{U} = 3$ . This is completely missed by the RPA approximation. The nearest-neighbor renormalization strength  $\alpha$ , plotted in Fig. (3.24) (b), is monotonically decreasing and thus shows a similar trend as in the DQMC case for  $\tilde{U} \lesssim 3$ . In the exact case  $\alpha$  starts to grow above  $\tilde{U} \sim 3$  against 1. The RPA result gets worse with increasing  $\tilde{U}$ .

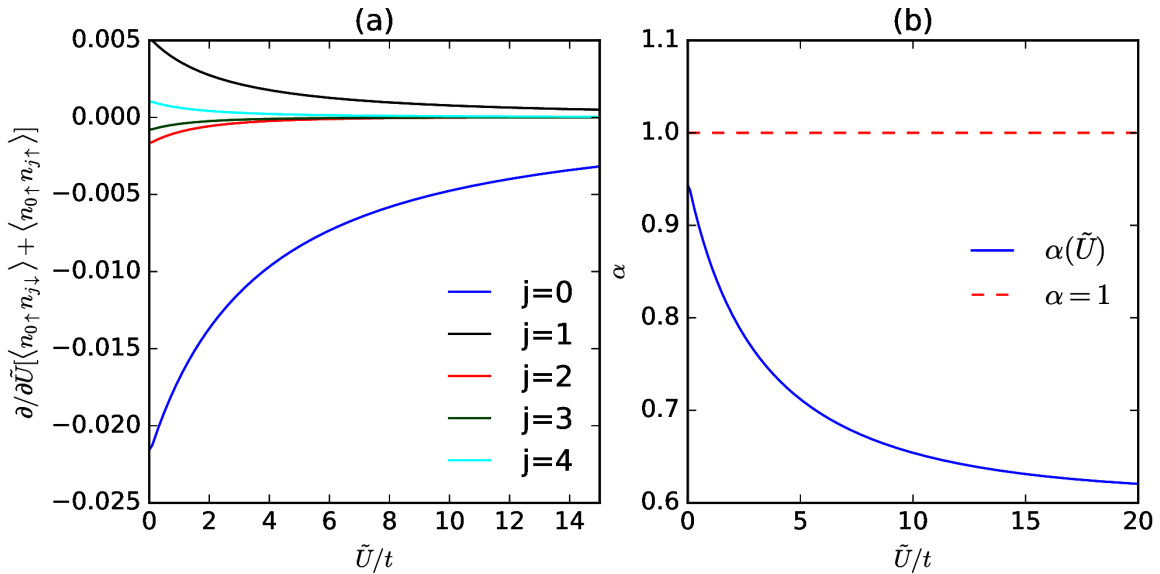


**Figure 3.24.:** (a) Derivative of the charge correlation functions with respect to  $\tilde{U}$  for the RPA treatment of a Hubbard model on the square lattice, for the first few nearest neighbors  $j$ . (b) Nearest neighbor renormalization strength  $\alpha(\tilde{U})$ , compare Eq. (3.15), which is the (negative) ratio of the  $j = 1$  and  $j = 0$  data from panel (a). The red dashed line corresponds to the approximation  $\tilde{U} = U - V$ , i.e.,  $\alpha = 1$ .

We should mention that the two equations to calculate  $\tilde{U}$ , Eqs. (3.8) and (3.9), differ by their denominator,  $\partial/\partial\tilde{U}\langle n_0n_0\rangle$  and  $\partial/\partial\tilde{U}\langle n_{0\uparrow}n_{0\downarrow}\rangle$ . The equations are interchangeable because the Pauli principle,  $n_{0\sigma}n_{0\sigma} = n_{0\sigma}$ , leads to  $\partial/\partial\tilde{U}\langle n_{0\sigma}n_{0\sigma}\rangle = 0$ . This is however only true if we calculate the correlation functions by methods that obey the Pauli principle. Because RPA violates the Pauli principle to second order in  $U$  [218] Eqs. (3.8) and (3.9) do give different results. In general, Eq. (3.8) should be preferred because it involves directly the charge correlation, which is a natural quantity in RPA ( $\langle n_{0\uparrow}n_{0\downarrow}\rangle$  has to be calculated from the difference of charge and spin correlation.). The error involved in the spin diagonal and spin off-diagonal terms from the RPA treatment cancel each other. Using Eq. (3.8) also means that we only calculate  $\chi^c(\mathbf{q},\omega)$  but not  $\chi^s(\mathbf{q},\omega)$ . The charge correlation function is numerically easier to calculate as it does not require such a fine  $\mathbf{q}$ -grid as the spin correlation function. There, the grid has to be fine to handle the divergences where  $1 = U\Gamma(\mathbf{q},\omega)$ <sup>6</sup>.

In conclusion, the RPA charge correlation functions lead to a satisfactory value of the nearest-neighbor renormalization strength  $\alpha(\tilde{U})$  for  $\tilde{U} \lesssim 3$  in the case of the square lattice. For larger interaction strengths,  $\partial/\partial\tilde{U}\langle n_0n_0\rangle$  spuriously dominates the  $\partial/\partial\tilde{U}\langle n_0n_j\rangle$  for  $j > 1$ , leading to a decline of  $\alpha$  to 0 for  $\tilde{U} \gg t$ . We can expect the RPA to perform similarly for all geometries.

### 3.10. Conclusion

In conclusion, we have derived a systematic map from lattice models with nonlocal Coulomb interactions to effective Hubbard models with strictly local Coulomb interactions  $\tilde{U}$ . The physical properties of the effective model reflect the original system nicely, especially regarding spin related properties. We find that the nonlocal Coulomb interactions can significantly renormalize the effective on-site interaction  $\tilde{U}$  as compared to the original local  $U$ . We find a universal drop of the nearest-neighbor renormalization at a specific effective interaction strength for all investigated geometries, but also find considerable differences in the details and the strength of the renormalization. In the cases of graphene and silicene with long-range interactions our calculations yield a renormalization of  $\tilde{U}/U < 0.5$  for half filling. Thus, the nonlocal Coulomb interactions stabilize the Dirac semimetallic phases in these materials against transitions to a gapped spin liquid or an antiferromagnetic insulator. In defective graphene or at edges local Coulomb interactions can lead to the formation of magnetic moments [99, 144, 229]. When describing these situations in terms of the Hubbard model, the value of  $\tilde{U} = 1.6t$  obtained here should be used. We have shown that this result

---

<sup>6</sup> $U$  and  $\Gamma(\mathbf{q},\omega)$  are positive, which can be seen by inspection of Eq. (2.151) for  $T = 0$ .

shows strong deviations for higher temperatures ( $\beta \lesssim 10/t$ ) but is robust for smaller temperatures. We have found that thermal fluctuations start destroying nonlocal interaction driven correlations faster than local ones. Whether or not a Hubbard model is generally appropriate to describe the physical properties of graphene is still a matter of debate and depends on the observable of interest. Our results suggest that a Hubbard model should be useful to judge the occurrence of edge magnetism and of AF insulator phases. Furthermore, our work indicates that nonlocal Coulomb interactions, in general, significantly weaken local correlation effects in *sp*-electron materials in a wide doping range. Additionally we have shown that for extreme low carrier densities (in the vicinity of the Wigner crystal instability) nonlocal interactions can increase the effective local interaction. For instance such systems should be realizable in any weakly doped semiconductor. It is interesting to see how the renormalization of effective on-site interactions generalizes to heterostructures with modified bands and additional van Hove singularities like in twisted bilayer graphene, gated (gapped) bilayer or to quantum Hall systems depending on Landau level filling factors. We have investigated the use of the Hartree-Fock and the random-phase approximation to obtain renormalizations, with promising results for small interaction strengths in the case of RPA.



# 4. Variational exact diagonalization method for the Anderson impurity model

M. Schüler, C. Renk, and T. O. Wehling, **Variational exact diagonalization method for Anderson impurity models**, Phys Rev. B **91** 235142 (2015)

All sections of this chapter but Sec. (4.6) are based on the publication given above and show considerable amount of overlap with the original manuscript, concerning both text and figures. The original text is mainly written by M. Schüler and proofread by all authors. The implementation of the exact diagonalization solver for this section is done by C. Renk. All other calculations and figures presented in the manuscript have been prepared by M. Schüler.

## 4.1. Introduction

We have introduced the Anderson impurity model (AIM) in Sec. (2.1.2) and discussed the possibility to solve the AIM by Monte-Carlo sampling of the partition function in Sec. (2.5.2). Here, we discuss a complementary approximative method to solve the AIM based on a variational simplification of the Hamiltonian and exact diagonalization. In contrast to CT-QMC, exact diagonalization based methods can cope with low symmetries, spin-orbit coupling and general Coulomb interaction terms at no additional cost, which makes it valuable especially in the case of AIMs related to realistic situations in the context of LDA++ approaches [133], where impurity models (or quantum lattice models, compare LDA+DMFT in Sec. (2.4)) are derived from first-principles calculations. The resulting models are typically multi-orbital models including complex hybridization between the impurity and a continuous bath of states from the surrounding material, which brings along two challenges: First, the numerical solution of the impurity models and secondly the interpretation of the physics contained in these generally complex models in more simple terms. Experiments are

for instance often interpreted in terms of atomic spins, crystal field, ligand field [15] or cluster approaches [44], which typically involve a small discrete set of bath states or no bath states at all. The link of the complex, *ab initio* derived models and simpler phenomenological models is a priori unclear and relates to the so-called bath-discretization problem of exact diagonalization solvers of the AIM.

The solution of the Anderson impurity model for general parameters has to be done numerically by means of, e.g., quantum Monte Carlo [66] (QMC), numerical renormalization group [30] (NRG), or exact diagonalization (ED) methods. While NRG and QMC are in principle numerically exact methods, they become computationally very demanding, when dealing with many orbitals, hybridization functions with low symmetry, spin-orbit coupling and general fermionic four-operator Coulomb vertices. ED methods deal with low symmetries and general Coulomb vertices at no additional computational cost but suffer from the so-called bath-discretization problem: Due to the exponential growth of the many-particle Fock space with the system size, it can handle only a few bath levels per orbital. A mapping of the continuous bath to a discrete version has to be found. Several approaches to this task have been introduced. One is to fit the hybridization function of the continuous bath on Matsubara frequencies introduced in Sec. (4.7), another is to represent the hybridization function by a continued fraction and to link its coefficients to the parameters of the bath [201].

These schemes are systematic in the sense that they converge to the full model when including more and more bath sites. However, in the multi-orbital case, the number of bath sites is limited (typically on the order of three or less for a five-orbital impurity problem), so the quality of the mapping can hardly be checked by an analysis of the convergence.

Basically two different strategies have been laid out to circumvent this problem. First, the many body Hilbert space can be truncated in the sense of configuration interaction (CI) expansions, which have a long tradition in the context of quantum impurity problems [222, 69] and are subject of recent developments [231, 141, 139]. CI expansions are variational, i.e., they deliver upper bounds for total energies, but they do not provide simplified auxiliary Hamiltonians. On the other hand, there are several approaches towards optimized cluster approximations to Anderson impurity problems. In this context, self-energy functional theory [178] is based on an extremal principle but it is not variational regarding total energies and does not allow for variations of interaction parameters or the interacting orbitals. More general optimizations are possible in the framework of the so-called self-energy embedding theory (SEET, [95]), which is however not variational.

In this chapter we combine ideas of variational approaches and optimized cluster approximations to the AIM. We introduce a strictly variational method of approximating

an AIM with continuous bath by an AIM with finite strongly reduced number of bath sites, which we call variational ED method. It guarantees an optimal approximation to the AIM for a given number of bath sites in the sense of thermodynamic ground state properties. The method is based on the Peierls-Feynman-Bogoliubov variational principle introduced as the variational principle for the grand potential in Sec. (2.9.2), which finds optimal effective models on the basis of an optimal density matrix by minimizing a free energy functional.

First, we consider how to calculate the free energy functional for the specific choice of the original and effective model and how to minimize it efficiently. Then, by treating a single-orbital model with the variational ED method, we analyze its performance in comparison to an exact treatment, established bath discretization methods [32], as well as Hartree-Fock theory. We demonstrate the applicability of the method to realistic five-orbital system with the example of Co impurities in bulk Cu and compare to QMC simulations. We apply the method to models of Fe on alkali surfaces, where we use the effective model to investigate spin and orbital moments under the influence of magnetic field and hybridization. We show that the variational ED method leads to systematically lower, i.e., more accurate, free energy estimates than unrestricted Hartree-Fock and traditional bath discretization schemes also in the multi-orbital case.

## 4.2. The effective model

In the framework of the variational principle (Sec. (2.9.2)), the original model is the Anderson model as defined in Sec. (2.1.2). The effective model is an exactly solvable version of an AIM. The structure of the effective Hamiltonian for the case of a single-impurity orbital is depicted in the right panel of Fig. (4.1). In contrast to the original model (left panel of Fig. (4.1)), the effective model consists of two decoupled parts: First, the effective impurity coupled to one bath site only and second the remaining bath sites. I.e., we partition the full Hilbert space  $\mathcal{H}$  into a correlated subspace  $\mathcal{C}$  (first part) and an uncorrelated rest  $\mathcal{R}$  (second part). Here, we consider for concreteness a cluster consisting of a multi-orbital impurity and one bath site per impurity orbital for the correlated space but other choices are similarly possible. The single-particle states of the effective model are related to those of the original model by a unitary transformation, which allows for mixing of original “bath” and “impurity” character in the effective model.

The optimal matrix elements of the effective model, as well as the optimal unitary transformation are found by minimizing the functional  $\tilde{\Phi}_{\text{GP}}$ , defined in Eq. (2.169). The subscript GP is omitted in the following.

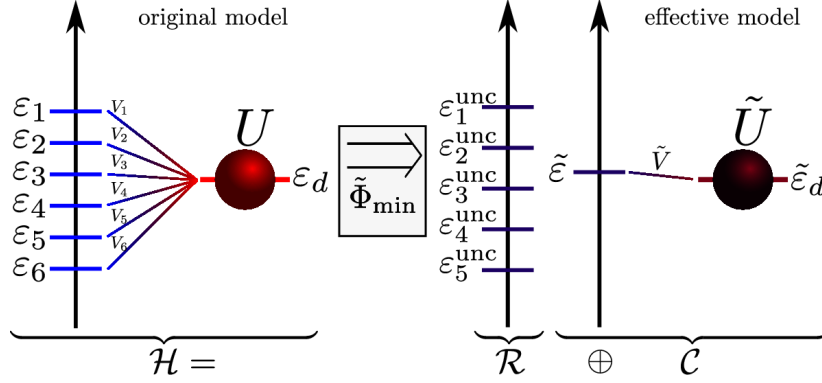


**Figure 4.1.:** Illustration of the original and effective model for the case of one orbital and six bath sites. Blue represents bath character and red impurity character: In the effective model bath and impurity states can be mixed.  $\varepsilon_n^{\text{unc}}$  are eigenvalues of  $h_{kk'}^{\mathcal{R}}$ .

The states spanning  $\mathcal{C}$  are defined by

$$|\tilde{d}_\alpha\rangle = u_{d_\alpha}^{d_\alpha} |d_\alpha\rangle + \sum_k u_{c_{\alpha k}}^{d_\alpha} |c_{\alpha k}\rangle, \quad (4.1)$$

$$|\tilde{c}_{\alpha 1}\rangle = u_{d_\alpha}^{c_{\alpha 1}} |d_\alpha\rangle + \sum_k u_{c_{\alpha k}}^{c_{\alpha 1}} |c_{\alpha k}\rangle, \quad (4.2)$$

where the coefficients  $u$  are chosen such that  $|\tilde{d}_\alpha\rangle$  and  $|\tilde{c}_{\alpha 1}\rangle$  form an orthonormal basis of  $\mathcal{C}$ . An orthonormal basis spanning  $\mathcal{R}$  is defined by

$$|\tilde{c}_{\alpha k}\rangle = u_{d_\alpha}^{c_{\alpha k}} |d_\alpha\rangle + \sum_{k'} u_{c_{\alpha k'}}^{c_{\alpha k}} |c_{\alpha k'}\rangle, k > 1. \quad (4.3)$$

As a whole, the coefficients  $u$  form a unitary matrix. In practice, we obtain the elements of this matrix from the QR decomposition of a matrix, in which the first two rows are defined by the coefficients of  $|\tilde{d}_\alpha\rangle$  and  $|\tilde{c}_{\alpha 1}\rangle$  and all other elements are zero. This leads to a new orthonormal basis for the full space  $\mathcal{H}$ , which provides the partitioning according to  $\mathcal{H} = \mathcal{C} \oplus \mathcal{R}$ . The ansatz for the effective Hamiltonian in this new basis explicitly reads

$$\tilde{H} = \tilde{H}^{\mathcal{C}} + \tilde{H}^{\mathcal{R}}, \quad (4.4)$$

with

$$\begin{aligned} \tilde{H}^{\mathcal{C}} = & \sum_{\alpha} \tilde{V}_{\alpha} \left( \tilde{c}_{\alpha 1}^{\dagger} \tilde{d}_{\alpha} + \tilde{d}_{\alpha}^{\dagger} \tilde{c}_{\alpha 1} \right) + \sum_{\alpha} \tilde{\varepsilon}_{\alpha 1} \tilde{c}_{\alpha 1}^{\dagger} \tilde{c}_{\alpha 1} \\ & + \sum_{\alpha} \tilde{\varepsilon}_{\alpha}^d \tilde{d}_{\alpha}^{\dagger} \tilde{d}_{\alpha} + \sum_{\alpha\beta\gamma\delta, \sigma\sigma'} \tilde{U}_{\alpha\beta\gamma\delta} \tilde{d}_{\alpha\sigma}^{\dagger} \tilde{d}_{\beta\sigma'}^{\dagger} \tilde{d}_{\gamma\sigma'} \tilde{d}_{\delta\sigma} \end{aligned} \quad (4.5)$$

and

$$\tilde{H}^{\mathcal{R}} = \sum_{\alpha, (k, k') > 1} h_{\alpha k k'}^{\mathcal{R}} \tilde{c}_{\alpha k}^{\dagger} \tilde{c}_{\alpha k'}. \quad (4.6)$$

It is stressed, that the new states are linear combinations of the original impurity states *and* the original bath states, leading to mixed basis states. The new impurity states can have some amount of bath character and vice versa. The Hamiltonian in Eq. (4.5) states a many-body problem which can be solved by exact diagonalization, as long as its Hilbert space is sufficiently small. In contrast, the Hamiltonian (4.6) states a one-particle problem and can be solved by diagonalizing the matrix  $h_{\alpha k k'}^{\mathcal{R}}$ . In summary, the Hamiltonian  $\tilde{H} = \tilde{H}^{\mathcal{C}} + \tilde{H}^{\mathcal{R}}$  defines an effective Hamiltonian, which can be solved exactly and thus  $\tilde{\Phi}$  can be calculated.

This ansatz implies several approximations. First, all couplings between  $\mathcal{C}$  and  $\mathcal{R}$  are neglected. Second, interaction terms are restricted to new effective impurity orbitals  $\tilde{d}_{\alpha}$  within  $\mathcal{C}$ , which is motivated by the fact that the original model includes only on-site interactions, too. The latter approximation can be relaxed to include arbitrary interactions within  $\mathcal{C}$ , but we keep it here for simplicity.

Finally, we note that the amount of variational degrees of freedom in the variational ED approach is such that it includes Hartree-Fock as the limiting case  $\tilde{U}_{\alpha\beta\gamma\delta} \rightarrow 0$ . Thus, we expect that variational ED generally gives more accurate energy estimates than Hartree-Fock.

### 4.2.1. Implementation of minimization

In order to perform the minimization in practice, the number of free parameters has to be kept sufficiently low. First, we assume that the Coulomb tensor  $\tilde{U}_{\alpha\beta\gamma\delta}$  is not varied. We choose it to be the same as in the original model. Test calculations have shown, that the variation of the Coulomb tensor is not crucial, as this can mostly be absorbed into the variation of the impurity level. The single-particle matrix elements of  $\tilde{H}^{\mathcal{C}}$  are assumed to be free parameters. In principle, the parameters of the uncorrelated Hamiltonian are free parameters, too. However, to further reduce the number of free parameters, we define  $h_{\alpha k k'}^{\mathcal{R}}$  by a projection of a Hartree-Fock solution of the original Hamiltonian onto the states  $|\tilde{c}_{\alpha k}\rangle$ . The Hartree-Fock solution of the original Hamiltonian (2.6) can be written as

$$H_{\text{HF}} = \sum_n \varepsilon_n^{\text{HF}} c_n^{\dagger} c_n, \quad (4.7)$$

where the eigenstates  $|n\rangle$  and energies  $\varepsilon_n^{\text{HF}}$  are found by applying the Hartree-Fock decoupling

$$\begin{aligned} d_{\alpha\sigma}^\dagger d_{\beta\sigma'}^\dagger d_{\gamma\sigma'} d_{\delta\sigma} &\rightarrow \langle d_{\alpha\sigma}^\dagger d_{\delta\sigma} \rangle d_{\beta\sigma'}^\dagger d_{\gamma\sigma'} + \langle d_{\beta\sigma'}^\dagger d_{\gamma\sigma'} \rangle d_{\alpha\sigma}^\dagger d_{\delta\sigma} \\ &\quad - \langle d_{\alpha\sigma}^\dagger d_{\gamma\sigma'} \rangle d_{\beta\sigma'}^\dagger d_{\delta\sigma} - \langle d_{\beta\sigma'}^\dagger d_{\delta\sigma} \rangle d_{\alpha\sigma}^\dagger d_{\gamma\sigma'} \end{aligned} \quad (4.8)$$

to Eq. (2.9) and solving the resulting non-interacting problem self-consistently. The single-particle matrix elements within the uncorrelated space  $\mathcal{R}$  explicitly read

$$h_{\alpha k k'}^{\mathcal{R}} = \sum_n \varepsilon_n^{\text{HF}} \langle \tilde{c}_{\alpha k} | n \rangle \langle n | \tilde{c}_{\alpha k'} \rangle. \quad (4.9)$$

In order to not break any spin-rotation symmetries, restricted Hartree-Fock is used.

The functional  $\tilde{\Phi}[\rho_{\tilde{H}}]$  now depends on the unitary transformation and on the matrix elements of  $\tilde{H}^{\mathcal{C}}$ . The minimum of the functional is searched by iterative methods. Thus, the functional  $\tilde{\Phi}[\rho_{\tilde{H}}]$  has to be calculated for various points of the variational space with the computationally most expensive part being here the diagonalizations of  $\tilde{H}^{\mathcal{C}}$ . Therefore, we first search for fixed parameters in  $\tilde{H}^{\mathcal{C}}$  a corresponding optimal unitary transformation matrix defining the optimal partitioning  $\mathcal{H} = \mathcal{C} \oplus \mathcal{R}$  using an SLSQP algorithm<sup>1</sup>. The search of the minimum with respect to the parameters of  $\tilde{H}^{\mathcal{C}}$  is then done by the Nelder-Mead algorithm<sup>2</sup>. The number of independent parameters can be further reduced when the original system shows symmetries like orbital degeneracies which are assumed not to be broken in the effective model.

### 4.3. Benchmark for a single-orbital Anderson impurity model

In this section the variational ED method is tested for its performance in reproducing the density operator as well as observables such as the occupation number, double occupancy and crystal orbital overlap populations of a simple original model. The original model we consider here is a single-orbital model with only 6 bath sites, which itself can be solved by exact diagonalization. The detailed setup of the model is as follows: The impurity level is  $\varepsilon_d = -2.0$  eV, the interaction strength is  $U = 4.0$  eV. The 6 bath levels are equally aligned around a mean bath energy  $\varepsilon_b$  in an interval of 2 eV (i.e., the bandwidth of the bath). The coupling is  $V_k = 0.9$  eV. The mean bath energy  $\varepsilon_b$  is swept from  $-6.0$  eV to  $6.0$  eV. All energies are measured with respect to

<sup>1</sup>A sequential least squares programming algorithm as implemented in the package `scipy.optimize.minimize` [117].

<sup>2</sup>A simplex algorithm as implemented in the python module `scipy.optimize.minimize` [158].

the Fermi energy  $\varepsilon_F = 0$ . The system is solved for  $T = 0$ . The model is first solved exactly, second by the variational ED method, third by unrestricted Hartree-Fock and finally by ED using reduced bath sites obtained by fitting of the hybridization functions on the imaginary Matsubara frequency axis [32]. The latter type of approaches require generally the introduction of a so-called weight function  $W_n$  for the fitting procedure, as explained in Sec. (4.7).

The central object for the assessment of the quality of the methods is the difference between  $\tilde{\Phi}[\rho_{\tilde{H}}]$  and the exact free energy  $\Phi_H$ , as shown in Fig. (4.2) (a). For bath sites energetically far away from the Fermi level and single-particle excitation energies of the impurity ( $|\varepsilon_b| > 4$  eV), all methods lead essentially to the correct free energy. Deviations occur, however, for bath levels closer to the Fermi energy. The Hartree-Fock free energy differs from the exact thermodynamical potential on the order of 100 meV basically in the whole range of  $|\varepsilon_b| < 4$  eV. The fitting of the hybridization function on the imaginary axis leads to rather accurate free energies as long as all bath sites are above or below the Fermi energy ( $|\varepsilon_b| > 1$  eV), while for  $|\varepsilon_b| < 1$  eV deviations from the exact thermodynamical potential on the order of 10 to 20 meV occur. The choice of an optimal weight function (see Sec. (4.7)) depends on details of the bath: For the case of bath sites on both sides of the Fermi level ( $|\varepsilon_b| < 1$  eV)  $W_n = 1/\omega_n$  leads to the lowest free energies. Otherwise, the constant weight function  $W_n = 1$  shows smallest deviations of the free energy functional from the exact solution. The variational ED method is generally very close to the exact solution. Only for the special case of a strictly symmetric distribution of the bath sites around the Fermi energy ( $\varepsilon_b = 0$  eV) a deviation on the order of meV occurs.

Fig. (4.2) (b)-(e) shows a comparison of several observables (chemical bond strength (b), bath occupation (c), impurity occupation (d) and double occupation (e)) calculated with the different methods. For the outermost regions ( $|\varepsilon_b| > 4$  eV) all methods describe the observables accurately. The fitting of hybridization functions on the Matsubara axis leads to deviations depending on the weight function, especially for the double occupation and chemical bond strength if the bath is centered around the Fermi energy ( $\varepsilon_b \approx 0$  eV). Hartree-Fock systematically overestimates the double occupancy for  $|\varepsilon_b| < 4$  eV. The variational ED method shows nearly no deviations from the exact solution at all.

It is instructive to examine the unitary transformation linking the basis of the original and effective model. Fig. (4.2) (f) shows the coefficients of the linear combination of the states spanning the correlated space  $|\tilde{d}\rangle$  and  $|\tilde{c}_1\rangle$  (see Eqs. (4.1) and (4.2)) for an original model with the bath centered around the energy  $\varepsilon_b = -0.3$  eV. The effective impurity has mainly  $|d\rangle$  character with small bath admixture and can approximately

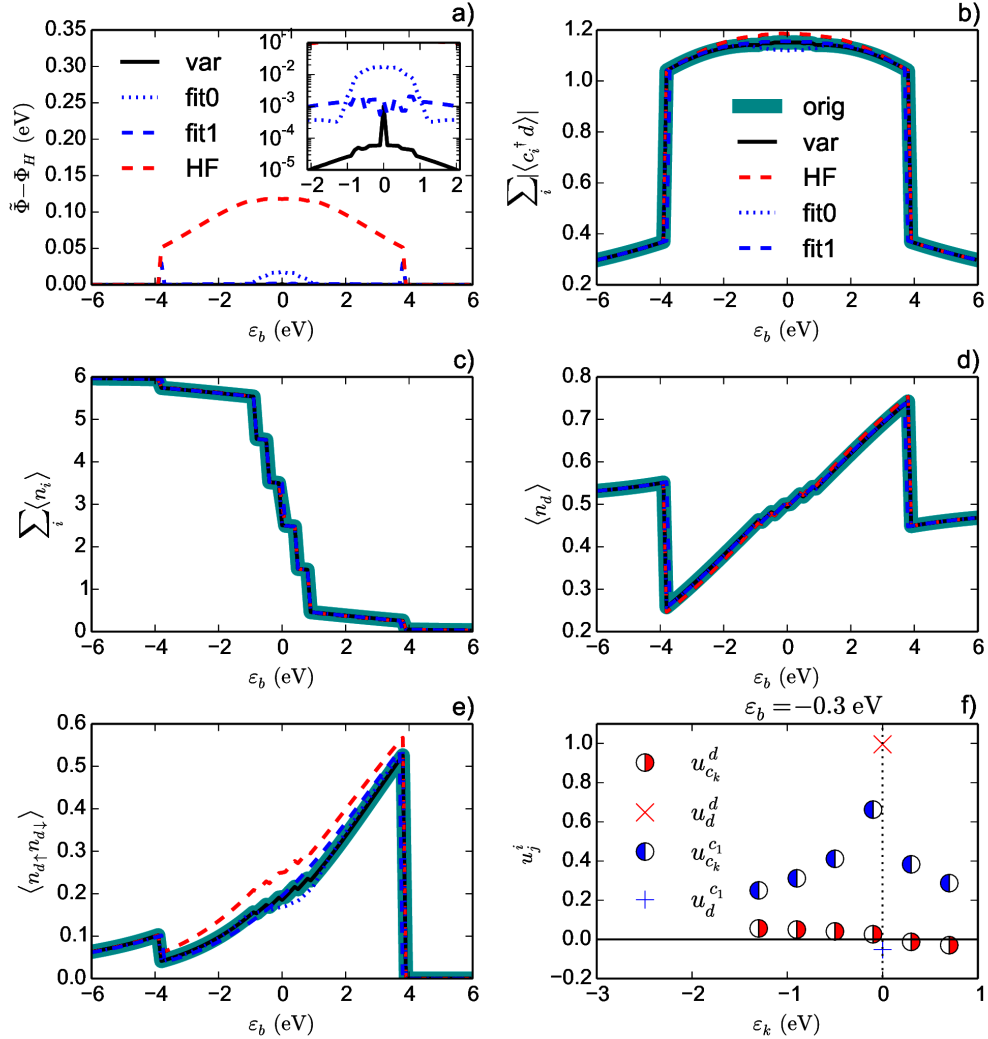


**Figure 4.2.:** Benchmark of different ED approaches and spin-polarized Hartree-Fock theory against an exact solution for single-orbital Anderson impurity models with a mean bath energy  $\varepsilon_b$ . (a) Difference between the free energy functional obtained by different approximate methods according to Eq. (2.169) and the free energy of the original model. The inset shows a close up view close to the Fermi energy on a logarithmic scale. (b)-(e): Comparison of local and non-local observables obtained from an exact solution (“orig”, bold cyan) and calculated by the four different approximate methods, i.e., the variational ED method (“var”, solid black), Hartree-Fock (“HF”, dashed red) and fits of hybridization functions on the imaginary axis with different weight functions ( $W_n = 1$ : “fit0”, dotted blue;  $W_n = 1/\omega_n$ : “fit1”, dashed blue.) Panel b) shows the chemical bond strength, c) shows the total bath occupation, d) the impurity occupation and e) the double occupation. Panel e) shows the coefficients of the unitary transformation linking the original model to the optimized effective model with one bath-site per spin orbital in  $\mathcal{C}$  for the example of  $\varepsilon_b = -0.3$  eV.

be interpreted as the old impurity state. The coupled effective bath state is nearly a pure linear combination of old bath states, where states closer to the Fermi energy contribute stronger than those further away. This behavior is very reminiscent of effective bath wavefunctions obtained in variational approaches like the Varma-Yafet [222] or the Gunnarsson-Schönhammer expansion [69].

For the treatment of original models with far more bath sites, it is important to note, that the coefficients defining the unitary transformation from the original bath states to the effective impurity and bath orbitals, i.e.,  $u_{c_k}^{c_1}$  and  $u_{c_k}^d$ , vary smoothly as function of the bath energies on either side of the Fermi energy.

## 4.4. Spectral functions

The variational principle results in an effective model which represents thermodynamic ground state properties in an optimal manner. This is a necessary but not a sufficient condition to give a good approximation also for excitation spectra. In the following, we study the one particle spectral function for single-orbital impurity benchmark systems from Sec. (4.3) with the bath states centered around  $\varepsilon_b = 0.3$  eV and two different hybridization strengths,  $V_k = 0.9$  eV and  $V_k = 0.3$  eV, respectively. The impurity spectral function is obtained from the Lehmann representation of the impurity Green function

$$G_\alpha(\omega) = \frac{1}{Z} \sum_{\mu\nu} \frac{|\langle \mu | d_\alpha^\dagger | \nu \rangle|^2}{\omega + E_\nu - E_\mu - i0^+} (e^{-\beta E_\nu} + e^{-\beta E_\mu}), \quad (4.10)$$

where in our calculations  $0^+$  is replaced by a broadening of  $\delta = 0.1$  eV and the inverse temperature is  $\beta = 3200$  eV<sup>-1</sup>, which is very close to the  $T = 0$  calculations of expectation values in Sec. (4.3).

We assess the quality of the spectra obtained from the variational ED method, from ED with the hybridization function fitted on the Matsubara axis (with two different weight functions  $W_n = 1$  and  $W_n = 1/\omega_n$ ) and from an unrestricted Hartree-Fock treatment by comparing to the exact spectrum of the original model. For the case of the parameters of the effective Hamiltonian obtained from fitting the hybridization function with  $W_n = 1/\omega_n$ , we additionally compare the impact of optimizing the transformation according to the variational principle. In particular, we compare the conventional result of fitting the hybridization function which we term “bath” and is equivalent to not mixing original bath and impurity states, to the case which we term “all” where we optimally mix the original bath and impurity states to form the effective bath state.

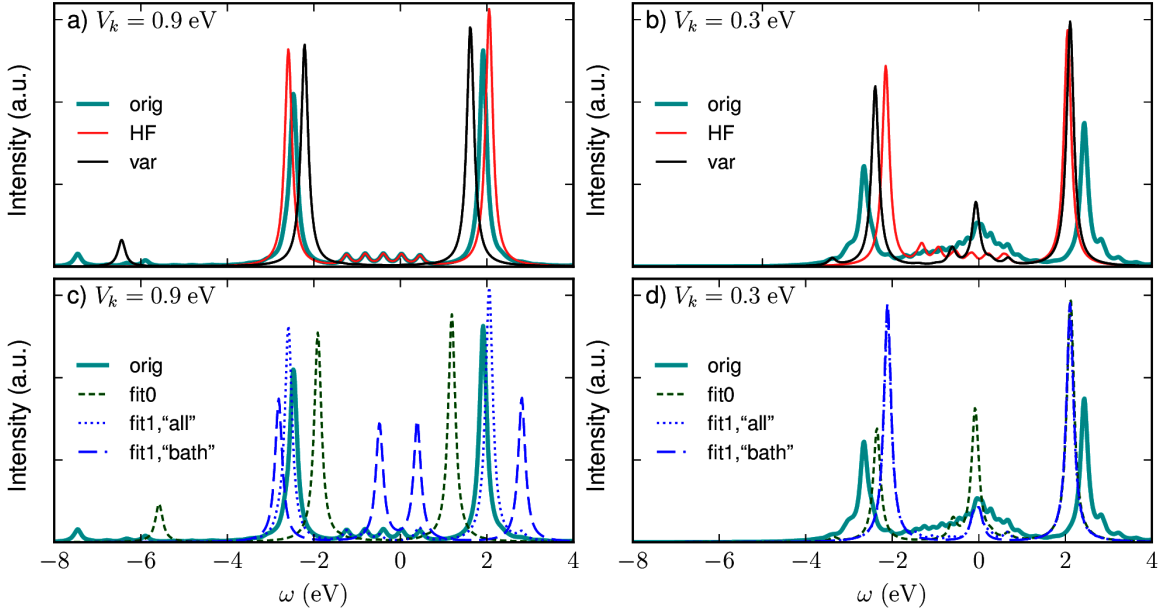


**Figure 4.3.:** One particle impurity spectral functions for the single-orbital benchmark model introduced in Sec. (4.3) with  $\varepsilon_b = -0.3$  eV and hybridization strengths  $V_k = 0.9$  eV ((a) and (c)) and  $V_k = 0.3$  eV ((b) and (d)). The spectral function from the exact solution of the original model is shown in bold cyan, from the Hartree-Fock calculation in red and from the variational ED method in black. Spectra from ED with fitted hybridization functions on the Matsubara axis are depicted in dashed green (“fit0”, i.e., weight function  $W_n = 1$ ), dotted blue (“fit1”,  $W_n = 1/\omega_n$  optimizing all states) and dashed blue (“fit1”,  $W_n = 1/\omega_n$  optimizing only bath states).

The dominant features of the original spectrum in the case of strong hybridization ( $V_k = 0.9$  eV, Fig. (4.3) a) and c)) are two major peaks at about  $-2.5$  eV and  $2$  eV (stemming from bonding and anti-bonding combinations of impurity and bath orbitals), two satellite peaks far from the Fermi energy and additional smaller peaks around the Fermi energy. An analysis of the original spectrum for various hybridization strengths is done in the appendix (A.3), which allows for an identification of the origin of the peaks. The spectral function from Hartree-Fock reproduces the bonding/anti bonding peaks and those close to the Fermi energy very well, while the satellites are missing. The variational ED method describes the positions of the main peaks well and also reproduces the satellite peaks, whereas the minor peaks around the Fermi energy are not present. The spectral function from a fit on the imaginary axis with a constant weight function ( $W_n = 1$ ) shows a similar picture but with major peaks and satellites shifted considerably towards the Fermi energy. The result for the weight function

emphasizing small Matsubara frequencies ( $W_n = 1/\omega_n$ ) leads to a good representation of the peaks around  $-2.5$  eV and  $2$  eV and some minor peaks around the Fermi energy but the satellites are missing completely. The resulting spectrum obtained by not mixing bath and impurity states (“bath”) shows only little resemblance to the original spectrum. I.e., in this case the mixing of bath and impurity basis states can not only improve total energies and thermodynamic potentials but also spectra quite significantly.

In the case of weaker hybridization ( $V_k = 0.3$  eV, Fig. (4.3) b) and d)) the original impurity spectral function shows two Hubbard peaks at about  $-2.6$  eV and  $2.4$  eV and in comparison to the former case more spectral weight and additional features close to the Fermi energy. Here, the Hartree-Fock description results in a spin-polarized ground state and describes the positions of the Hubbard peaks in the spectrum correctly. The enhanced spectral weight at the Fermi energy is however not reproduced. Exact diagonalization of the effective models obtained from the variational method and from the fits of the hybridization functions on imaginary axis give similar results. In addition to the upper and lower Hubbard peaks the ED methods also reproduce enhanced spectral weight at the Fermi level.

While the performance of the fit methods in reproducing the spectra of the original model differs between the case with strong and weak hybridization particularly for the weight function  $W_n = 1/\omega_n$ , the variational method gives satisfactory results in both cases. The spectra from variational ED are in both cases at least as close to the spectra of the original model as the best spectrum obtained with any of the two bath fitting procedures  $W_n = 1$  or  $1/\omega_n$ ) under investigation.

## 4.5. Co impurities in Cu: Application to a realistic five-orbital system

Partially filled transition metal atoms embedded in metallic hosts, such as Fe atoms in Au or Co atoms in Cu, are prototypical Kondo system and due to their structural simplicity easily available experimentally. From a theoretical point of view, such multi-orbital systems are computationally far more demanding than single-orbital systems, yet they exhibit a bigger class of phenomena, which makes multi-orbital systems intriguing to investigate. The additional orbital degree of freedom leads to Hund’s coupling, orbital-dependent crystal fields and hybridizations. The importance of effects related to Hund’s coupling has for instance recently been shown for Fe on Pt(111), a candidate for a building block of Hund’s metals [100].

Co atoms in Cu are a well established system, which is investigated both exper-

imentally and theoretically. Scanning tunneling experiments found a large Kondo temperature of  $T_K = (655 \pm 155)$  K [179]. This system has been studied by the LDA++ approach, introduced in Sec. (2.4.2), in Ref. [210]. There, an Anderson impurity model is derived from ab-initio calculation and solved with the continuous-time quantum Monte-Carlo method (compare Sec. (2.5.2)), revealing the formation of a strongly renormalized Fermi liquid with a Kondo temperature between  $T_K = 1100$  K and  $T_K = 1900$  K, depending on the orbital and the details of the calculations.

We use the numerically exact solution of the Anderson impurity model for Co in Cu derived in Ref. [210] in order to benchmark the variational ED method for multi-orbital systems (i.e., a five-orbital system). This is of great importance for the applicability of the method to realistic system as transition metal impurities constitute a large range of interesting systems, as discussed in the introduction of the Anderson impurity model (Sec. (2.1.2)).

The next section deals with the details of the Anderson impurity model from Ref. [210]. In Sec. (4.5.2), we discuss the issues of the implementation of the variational ED for the case of realistic five-orbital systems. Finally, in Sec. (4.5.3) we compare the results of the variational ED method to the solution obtained with the continuous-time quantum Monte Carlo method presented in Ref. [210].

### 4.5.1. The Anderson impurity model derived from LDA

The cubic symmetry of the Cu crystal leads to a splitting of the Co  $3d$  orbitals into blocks of  $t_{2g}$  and  $e_g$  symmetry. From the DFT hybridization function, which is a continuous function, we obtain our initial model assuming some large number of bath sites, here 100 per orbital. (This number does not present a limiting factor and could be chosen arbitrarily larger). The bath sites are assumed to be equidistantly distributed between  $-10$  eV and  $10$  eV, and the hybridization terms  $V_{\alpha k}$  are then found by fitting the imaginary part of a discretized hybridization function

$$\Delta_{\text{disc}}(\omega) = \sum_k \frac{V_{\alpha k}^* V_{\alpha k}}{\omega - \varepsilon_k + i\delta}, \quad (4.11)$$

with some broadening  $\delta = 0.1$  eV to the ab initio hybridization function  $\Delta(\omega)$  on the real axis. The  $V_{ik}$  are plotted in Figure (4.4). The crystal field obtained from the DFT calculation is  $\varepsilon_{e_g}^d - \varepsilon_{t_{2g}}^d = 0.136$  eV. As in Ref. [210], we consider a rotationally invariant Coulomb interaction defined by

$$U_{\alpha\beta\gamma\delta} = \sum_{k=0}^{2l} a_k(\alpha_m\beta_m, \gamma_m\delta_m) F^k, \quad (4.12)$$

where  $a_k(\alpha_m\beta_m, \gamma_m\delta_m)$  are the Gaunt coefficients [205, 49] and where  $F^0 = U$ ,  $F^2 = 14/(1 + 0.625)J$  and  $F^4 = 0.625F^2$  are Slater parameters with the average Coulomb interaction  $U = 4.0$  eV and Hund's exchange interaction  $J = 0.9$  eV. Due to the so-called double-counting problem inherent to LDA++ approaches, the filling of the impurity d-levels is not exactly known. Here, we consider the double-counting potential  $\mu = 27$  eV as in Ref. [210]. All data is obtained at a temperature of  $\beta = 40$ , like in the case of the QMC simulations. Finally, we assume that the cubic symmetry of the system prevails, which means that only two independent sets of matrix elements (for the  $t_{2g}$  and  $e_g$  states) have to be varied during the minimization of  $\tilde{\Phi}[\rho_{\tilde{H}}]$ .

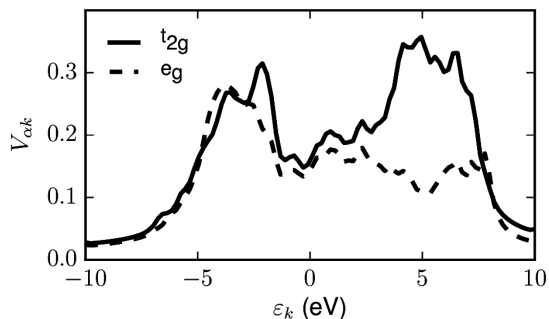


**Figure 4.4:** Hopping matrix elements  $V_{\alpha k}$  between the impurity orbitals and the bath from the original Anderson impurity model for Co impurities in Cu (solid  $t_{2g}$ , dashed  $e_g$ ).

#### 4.5.2. Implementation of the variational ED method for the five-orbital Anderson impurity model

We compare two different sets of variational degrees of freedom for the optimization of the single-particle basis, which we refer to as “bath” and “all”. In the “bath” case, only bath sites are optimized, i.e., we fix the expansion coefficients  $u_{d_\alpha}^{c_{\alpha 1}} = 0$ ,  $u_{c_{\alpha k}}^{d_\alpha} = 0$  and  $u_{d_\alpha}^{d_\alpha} = 1$ . This leads to considerably less variational parameters and a much smaller amount of expectation values to be calculated in each step of the iteration. In the second approach, “all”, which is computationally more demanding because the full two-particle density matrix of the effective system has to be calculated, we optimize the full one particle basis of the bath and that of the impurity.

Because a full optimization of the parameters of the effective model is computationally challenging, it is crucial to start the optimization from a good initial guess. We obtain such initial guesses for the parameters of the bath by fitting of hybridization functions on Matsubara frequencies as introduced in Sec. (4.7). We choose  $\tilde{\varepsilon}_\alpha^d = \varepsilon_\alpha^d$  as the initial guess for the parameters of the impurity. The resulting first guesses using different weight functions are summarized in the Table (4.1). While all weight func-

tions lead to setups with the  $t_{2g}$  bath sites above the Fermi energy and the  $e_g$  bath sites below, the details of their energetic positions and the hybridization strengths depend strongly on the form of  $W_n$ . Adding more weight on features on small Matsubara frequencies shifts the effective bath parameters to smaller values. The quality of these starting guesses in the context of the variational principle is discussed in the next section.

weight function	1	$1/\omega_n$	$1/\omega_n^2$	var
$\tilde{\varepsilon}_{t_{2g}1}$ (eV)	3.203	0.775	0.068	2.658
$\tilde{V}_{t_{2g}}$ (eV)	1.563	0.606	0.223	1.717
$\tilde{\varepsilon}_{e_g1}$ (eV)	-2.314	-0.019	-0.015	-1.995
$\tilde{V}_{e_g}$ (eV)	1.049	0.170	0.156	1.418
$\tilde{\varepsilon}_{t_{2g}}^d$ (eV)	-27.30	-27.30	-27.30	-26.57
$\tilde{\varepsilon}_{e_g}^d$ (eV)	-27.44	-27.44	-27.44	-27.87

**Table 4.1.:** Parameters of the effective model (see Eq. (4.5)) obtained by the fit of hybridization functions on imaginary frequencies using different weight functions ( $W_n = 1, 1/\omega_n, 1/\omega_n^2$ , see Sec. (4.7)) and the iterative optimization (“var”).

The large number of bath sites (100 per orbital) in the original model leads to 202 variational parameters defining the unitary transformation in the “all” case or 100 parameters in the “bath” case for each orbital. The observation, that  $u_{c_{\alpha k}}^{d\alpha}, u_{c_{\alpha k}}^{c\alpha 1}$  are smooth functions of energy (c.f. Fig. (4.2) (e) below and above  $E_F$ ), leads to the possibility of expanding them in a set of smooth functions and thereby reducing the number of variational parameters considerably. Here, we chose five Chebyshev polynomials  $T_n(k)$  per orbital for bath sites above and five for those below the Fermi energy. Therefore only 22 (or 10 in the case of “bath”) parameters per orbital have to be varied to find the optimal unitary transformation to embed the effective model into the full Hilbert space. To investigate the convergence behavior of the results with the number of Chebyshev polynomials, we calculate the optimal transformation for a one orbital Anderson impurity model, defined by the  $t_{2g}$  hybridization function of CoCu discretized with 30 bath sites, an on-site impurity energy  $\varepsilon_d = -2.0$  eV and a Coulomb interaction  $U = 4$  eV. The parameters of the effective model are fixed to  $\tilde{U} = 4$  eV,  $\tilde{\varepsilon}_d = -2.62$  eV,  $\tilde{V} = 0.57$  eV. The parameters of  $\mathcal{R}$  are defined in the simplest way by projecting the single-particle part of the original Hamiltonian onto  $\mathcal{R}$ . The left panel of Fig. (4.5) shows the convergence of the functional  $\tilde{\Phi}$ . The functional is virtually converged for five polynomials. The right panel of Fig. (4.5) shows the

expanded coefficients of the transformation for the effective bath,  $u_{c_k}^c$  in Eq. (4.2), for selected expansion orders and the result of the direct minimization. The coefficients from the expansion in seven polynomials can hardly be distinguished from the exact result. The results for five, six (not shown), and seven polynomials are very similar, indicating the fast convergence of the results with respect to the number of Chebyshev polynomials.

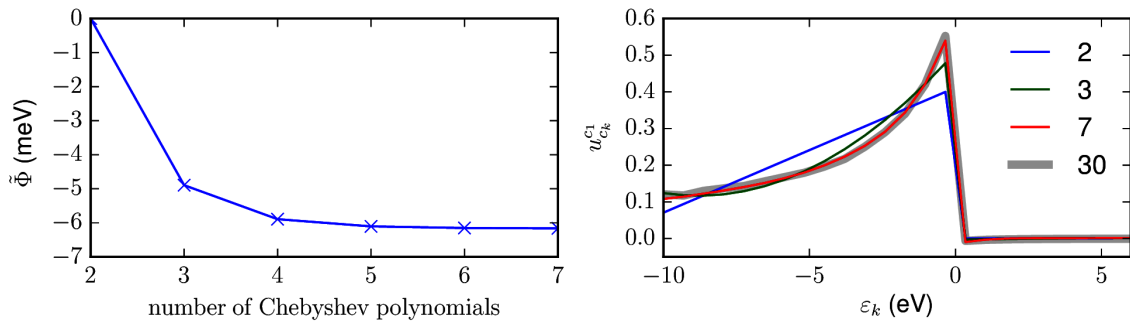


**Figure 4.5.:** Left panel: Convergence of the functional  $\tilde{\Phi}$  with respect to the number of Chebyshev polynomials the  $u_{c_k}^c$  are expanded in. The value of  $\tilde{\Phi}$  is relative to the value for two Chebyshev polynomials. Right panel: Expanded coefficients  $u_{c_k}^c$  from different number of Chebyshev polynomials. The line labeled “30” is the result of a minimization without any expansion.

### 4.5.3. Results

First, we compare free energy estimates as well as different local observables obtained from variational ED treatments to unrestricted Hartree-Fock as well as QMC calculations. Afterwards, we investigate the nature of the optimized effective bath and impurity states as obtained from the variational ED treatment.

#### Free energy functional and local observables

Table (4.2) shows the free energy functional  $\tilde{\Phi}$  (relative to unrestricted Hartree-Fock (UHF)), as obtained with different starting points and different amounts of variational degrees of freedom in the variational ED approach. In the case of “bath”, the constant

#### 4. Variational exact diagonalization method for the AIM

	$\Delta\tilde{\Phi}$ (eV)	$\langle n_d \rangle$	$S$
QMC		$7.78 \pm 0.05$	$0.92 \pm 0.02$
UHF	0	7.78	1.78
RHF	0.52	8.20	1.06
fit0,bath	0.05	7.75	1.06
fit1,bath	1.15	7.84	1.04
fit2,bath	2.77	7.92	1.03
fit0,all	-0.22	7.71	1.03
fit1,all	0.32	7.65	1.05
fit2,all	1.04	7.60	1.00
var,bath	0.00	7.76	1.05
var,all	-0.30	7.75	1.02

**Table 4.2.:** The free energy functional  $\tilde{\Phi}$ , the total impurity occupancy  $n_d$  and the local spin  $S$  as obtained from simulations of the AIM for Co impurities in Cu. The values of  $\tilde{\Phi}$  are shown as differences to the results from unrestricted Hartree-Fock (UHF):  $\Delta\tilde{\Phi} = \tilde{\Phi} - \tilde{\Phi}_{\text{UHF}}$ . Total impurity occupation and spin calculated with the variational ED method are compared to QMC solutions of the AIM from Ref. [210]. Different flavors of the variational ED method are considered: first “bath” and second “all” with the model parameters obtained from the fits of the hybridization function on the imaginary frequencies using different weight functions ( $W_n = 1$  “fit0”,  $W_n = 1/\omega_n$  “fit1” and  $W_n = 1/\omega_n^2$  “fit2”) and finally full optimization of transformation and model parameters labeled “var”. Restricted Hartree-Fock (RHF) and unrestricted HF (UHF) results are also shown.

weight function (“fit0”,  $W_n = 1$ ) leads to the lowest values of the  $\tilde{\Phi}[\rho]$ . The models derived using weight functions  $W_n = 1/\omega_n$  (“fit1”) and  $W_n = 1/\omega_n^2$  (“fit2”) lead to free energy estimates which are about 1 to 3 eV higher in energy. The situation for the case of “all” is similar. On this basis, we have chosen the starting guess obtained with the constant weight function for the full optimization of the effective model parameters. The resulting parameters are shown in the last column of Tab. (4.1) and are close to the starting guess. The full optimization schemes (“var,bath” and “var,all”) find parameters which lower the functional  $\tilde{\Phi}$  considerably for “all” and slightly for “bath”.

Regarding the impurity occupation ( $\langle n_d \rangle$ , see Tab. (4.2)), we see that the description by unrestricted Hartree-Fock is rather close to QMC, whereas restricted Hartree-Fock overestimates the occupation. All versions of exact diagonalization lead to occupations close to the QMC results, and many cases within the QMC error bars. The spin  $S$

(defined as  $\langle \hat{S}^2 \rangle = S(S+1)$ ), which is a two-particle observable, reveals the problems of the Hartree-Fock description.  $S$  is vastly overestimated by unrestricted Hartree-Fock. The variational ED methods, especially the “all” case for the constant weight function (“fit0”) and the full optimized ED model, lead to results close to QMC.

To compare the results of the variational ED method with those ED methods based on fitting of the hybridization function on the imaginary axis, we should compare the “fit0,bath”, “fit1,bath”, and “fit2,bath” cases to the corresponding “all” and “var,all” cases. We see that having more variational degrees of freedom leads to an improved description of the free energies, as it should be.

In general, we learn that only in the case of optimizing both effective bath and effective impurity states (termed “all”) we reach lower values of the free energy functional  $\tilde{\Phi}$  than with unrestricted Hartree-Fock: The freedom to form mixtures of bath and impurity states in the effective model is important to describe the free energy and local observables of the system adequately. As the variational ED method provides more accurate (free) energy estimates than unrestricted Hartree-Fock, the approach introduced here could be a way to improve LDA+U total energy schemes.

### The effective basis states

Now we analyze the unitary transformation relating the optimized basis states of the effective model and the original basis states. The transformation obtained for the models from the starting guesses with weight functions  $W_n = 1, 1/\omega_n,$  and  $1/\omega_n^2$  is shown in Fig. (4.6). We observe a clear trend that the admixture of the original bath states into the effective bath state ( $u_{c_{\alpha 1}}^{c_{\alpha k}}$ , blue lines) is strongest in the vicinity of the Fermi energy and the effective bath site energy  $\tilde{\epsilon}_{\alpha 1}$ . For bath states close to the Fermi energy we get a sharp cut off for states on the opposite side of the Fermi energy. This is very similar to first order configuration interaction treatments of the AIM [69, 222]. The original impurity admixture in the effective impurity ( $u_{d_{\alpha}}^d$ ) rises with the distance of the effective bath site from the Fermi energy.

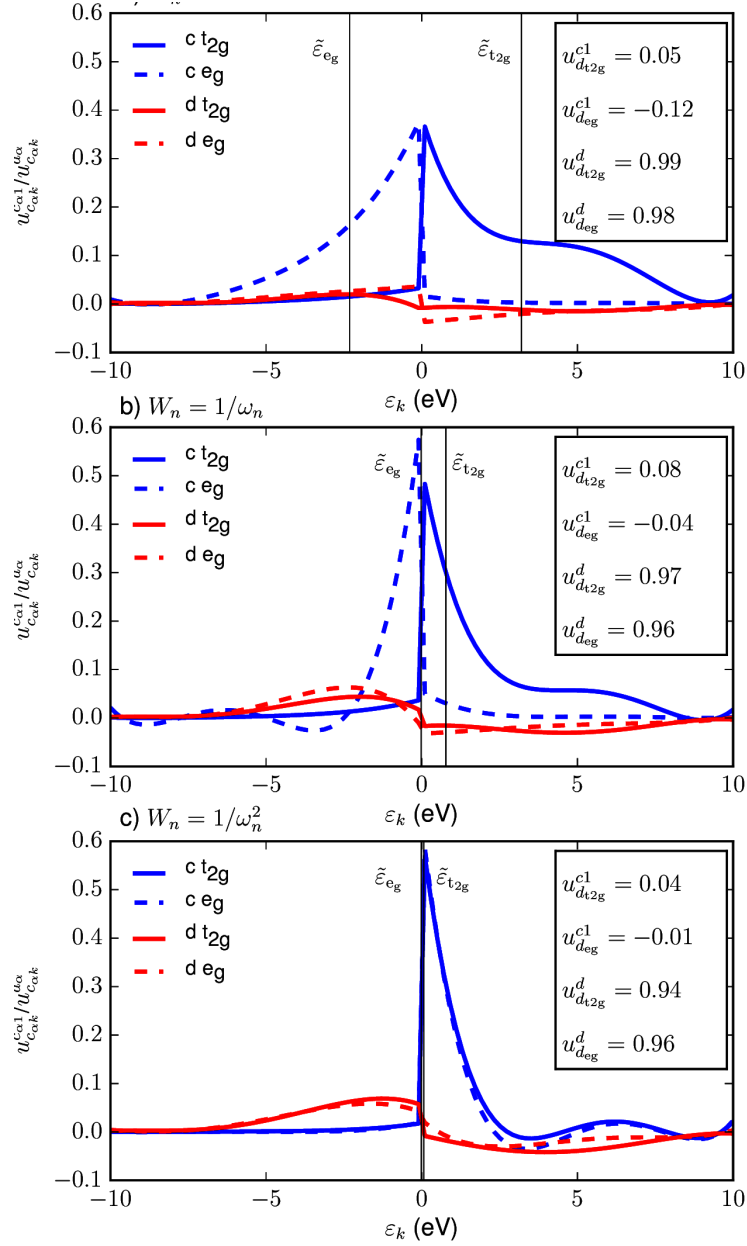


**Figure 4.6.:** Coefficients defining the optimal transformation from original bath states to effective bath states (blue/dark gray) and effective impurity states (red/light gray), c.f. Eqs. (4.1) and (4.2). Optimized transformations for different effective models defined through fits of the hybridization with weight functions  $W_n = 1$  (a),  $W_n = 1/\omega_n$  (b), and  $W_n = 1/\omega_n^2$  (c) are shown. The energies of the effective coupled bath sites  $\tilde{\epsilon}_\alpha$  are depicted as thin vertical lines. The numerical values of the transformation coefficients defining the admixture of original impurity states to the effective bath and impurity states are given as insets.

## 4.6. Fe on alkali surfaces

We further investigate the possibilities of the variational exact diagonalization method by applying it to a highly intriguing set of systems, namely Fe impurities on alkali surfaces. Here, we are not foremostly concerned with benchmarking the method but applying it in a meaningful way. The alkali metals are  $s$  electron metals which decrease their valence electron density with increasing atomic number due to larger bond distances. Impurities on alkali surfaces therefore experience decreasing hybridization strengths with increasing atomic number of the metal. Thus, by investigating Fe impurities on Li, Na, K, and Cs the evolution from a strongly coupled impurity for the case of Li to a weakly coupled, atomic like, impurity for the case of Cs can be observed. This is done in Ref. [33] by means of photo emission spectroscopy. The result is sketched in Fig. (4.7) by the density of states for different hybridization strengths. For weak hybridizations, the density of states shows an atomic multiplet structure. For strong hybridization a quasiparticle emerges at the Fermi energy ( $E_F$ ) due to spin-flips of  $s$  electrons at the magnetic impurity (Kondo effect). At intermediate hybridization strength a mixture of both regimes is found.

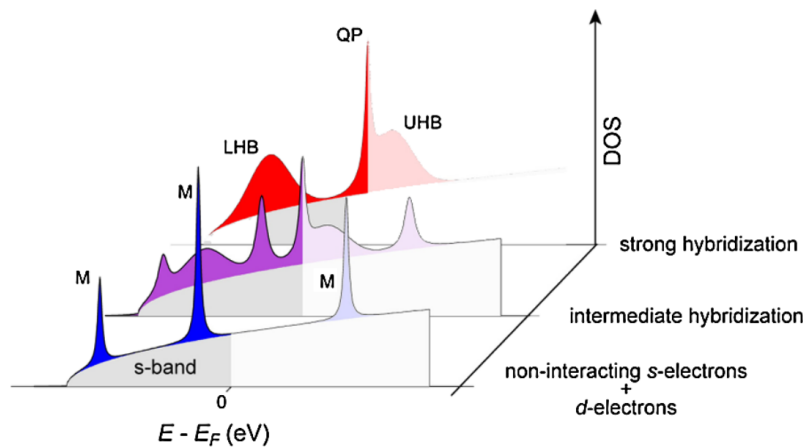


**Figure 4.7.:** Spectral function of a many-body  $d$ -electron impurity and host conduction electrons: localized impurity limit (bottom); intermediate coupling (middle); strong hybridization limit (top). Letters indicate multiplet (M), quasi-particle resonance (QP), lower and upper Hubbard bands (LHB, UHB) spectral features. Reprinted figure with permissions from [C. Carbone et al., Phys. Rev. Lett., **104**, 117601 (2010), [33]]. Copyright 2015 by the American Physical Society.

We explore not the spectral properties of Fe impurities on alkali metals but the magnetic ground-state properties. Using the variational exact diagonalization method

we aim to understand the evolution of the orbital and spin moment with increasing hybridization and under the influence of a magnetic field. To this end, we introduce the basic experimental techniques in Sec. (4.6.1), which have been used to obtain magnetization data in high magnetic fields. We derive from LDA calculations an Anderson impurity model with a continuous bath as in Sec. (4.6.2). Using the variational ED method in Sec. (4.6.3) we calculate magnetization curves and study the spin and orbital moment in dependence of the hybridization.

#### 4.6.1. X-ray magnetic circular dichroism measurements

X-ray magnetic circular dichroism (XMCD) spectroscopy is a certain version of x-ray absorption spectroscopy (XAS). XAS measures the absorption of x-ray photons from core  $p$  electrons (L-edge spectroscopy), which are excited to partially filled  $d$  states [73]. The comparison of experimental and simulated XAS spectra allows to determine the number of empty  $d$  states and thus the electronic configuration. XMCD is the difference signal of XAS with left ( $\sigma^+$ ) and right ( $\sigma^-$ ) circularly polarized light. The different polarization leads to separate excitations of the spin split  $L_2$  and  $L_3$  edge and the possibility to detect spin and orbitally resolved information. The resulting signal, integrated over different energetic parts, is related to spin and orbital moments  $S_z$  and  $L_z$  of the  $d$  shell via sum rules in an element specific manner [216, 34].

The currently unpublished XMCD measurements for Fe on Li, Na, K and Cs are done by S. Gardonio (University of Nova Gorica, Slovenia) and reproduced here with permission. The Fe impurities were prepared by evaporating minute quantities (0.02-0.001 monolayers) on alkali films condensed on Cu(111) at  $T = 10$  K. The XMCD measurements were performed at  $T = 4.5$  K.

Earlier XAS experiments of Fe on K in combination with theoretical simulations of XAS spectra have revealed a  $d^7$  configuration of the impurity [57]. XMCD was used to obtain the magnetic moment of the Fe impurities on alkali metals in a magnetic field up to  $B = 7$  T. The data for FeLi, FeNa, FeK and FeCs are presented in Fig. (4.8). We can see an increase of the susceptibility from FeLi to FeCs. For the case of FeLi, we can observe a nearly linear increase of the magnetization. For all other substrates, the magnetization shows a deviation from the linear behavior; it resembles a Brillouin function. The data can indeed be fitted by normalized Brillouin functions (compare Ref. [42]) reading

$$M = \alpha B_J(g\mu_B J B k_B T), \quad (4.13)$$

where  $k_B$  is the Boltzmann constant,  $T$  the temperature,  $g$  the Landé factor,  $J$  the total angular momentum quantum number,  $\alpha$  a scaling factor and  $B$  the magnetic

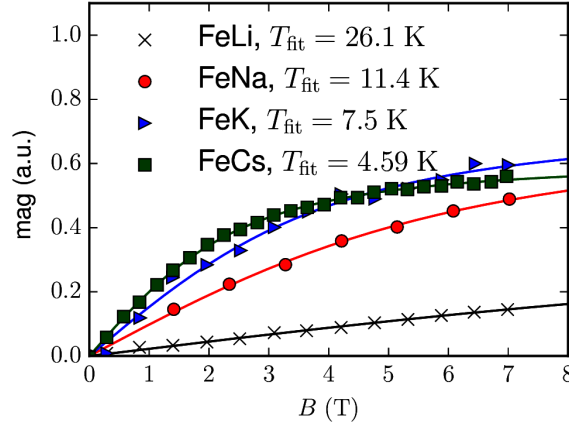


**Figure 4.8.:** Experimental magnetization data obtained from XMCD measurements for Fe on alkali substrates: Li (black crosses), Na (red circles), K (blue triangles) and Cs (green squares). Measured data are fitted (lines) with Brillouin functions (Eq. (4.13)) resulting in parameters presented in Tab. (4.3). Experimental data are measured by S. Gardonio, Materials Research Laboratory, University of Nova Gorica, Vipavska 13, 5000 Nova Gorica, Slovenia and reproduced with authorization.

field. The Brillouin function  $B_J(x)$  is defined by

$$B_J(x) = \frac{2J+1}{2J} \coth\left(\frac{2J+1}{2J}x\right) - \frac{1}{2J} \coth\left(\frac{x}{2J}\right). \quad (4.14)$$

Eq. (4.13) describes the magnetization of an ensemble of equal free magnetic moments  $\mathbf{J}$  in a magnetic field  $B = B_z$ . The assumption of free moments only approximates the experimental situation due to two reasons: First, the surface induces charge fluctuations, such that a description of the adatoms by moments may be inadequate. Secondly, the (supposed) moments are not free but coupled to the surface. Yet, the experimental data are well described by Brillouin functions if the temperature in Eq. (4.13) is treated as a parameter. The fits presented in Fig. (4.8) are obtained with the appropriate values of the total angular momentum  $J$  and the Landé factor  $g$  for a  $d^7$  configuration,  $J = 4.5$  and  $g = 4/3$ . In order to obtain satisfactory fits, the scaling  $\alpha$  and the temperature  $T$  are adjusted, resulting in values presented in Tab. (4.3). The fitted temperature considerably differs from the experimental temperature ( $T_{\text{exp}} = 4.5$  K) for all substrates but Cs. The discrepancy between fitted temperature and experimental temperature can be viewed as an indicator of how well the model of isolated moments is valid for Fe on different alkali surfaces. Obviously, this model is a good approximation for FeCs. The model loses its validity with increasing valence electron density, i.e., increasing hybridization strength.

In order to obtain an improved description of Fe on alkali surfaces, the impurities should rather be modeled by Anderson impurity models, taking into account charge fluctuations, local correlation effects on the impurity, and hybridization with the surface. Therefore, we derive an Anderson impurity model from ab-initio calculations in the next section. Then in Sec. (4.6.3), we use the variational exact diagonalization technique to investigate the behavior of the impurities in a simplified model.

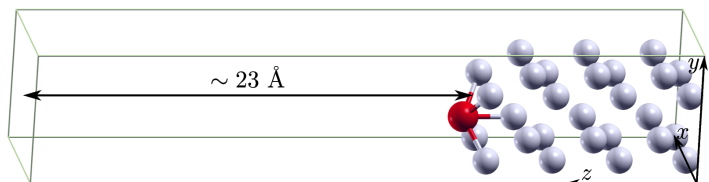
**Table 4.3:** Parameters obtained from fitting Brillouin functions with  $J = 4.5$  and  $g = 4/3$  (compare Eq. (4.13)) to magnetization data presented in Fig. (4.8).

substrate	$\alpha$	$T$ (K)
Li	0.361	26.07
Na	0.688	11.40
K	0.712	7.46
Cs	0.595	4.59

#### 4.6.2. Anderson impurity model derived from LDA

We have performed LDA calculations using supercells of 28 alkali atoms stacked in 7 layers (depicted in Fig. (4.9)) to model the alkali surfaces. The supercells include approximately 23 Å of vacuum distance. We have relaxed the positions of the two uppermost alkali layers and that of the Fe impurity in spin-polarized LDA. In order to extract hybridization functions as introduced in Sec. (2.4.2), we have performed spin unpolarized calculations.

**Figure 4.9:** Unit cell used to model Fe (red) on Li (gray). The figure is generated with XCrySDen [108].



Unfortunately, the LDA calculations for K and Cs showed a bad convergence behavior and could not be investigated further. Therefore, we only extract hybridization functions from LDA calculations for Fe impurities on Li and Na surfaces. We do so in the same way as in Sec. (4.5.1). The imaginary parts of the hybridization functions are shown in Figure (4.10). The orbital averaged hybridization function at the Fermi energy ( $\omega = 0$ ) is clearly stronger for Li than for Na. This is the expected trend from

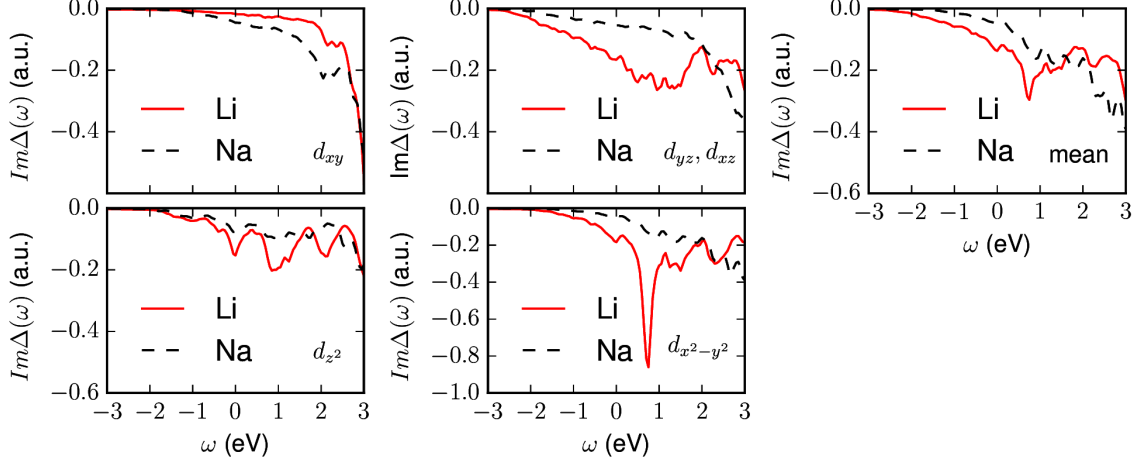


**Figure 4.10.:** Orbitally resolved and orbitally averaged hybridization functions from LDA simulations for Fe on Li and Na.

considering the electronic density of Li and Na. The only exception from this trend is the  $d_{xy}$  orbital, which shows stronger hybridization for Na.

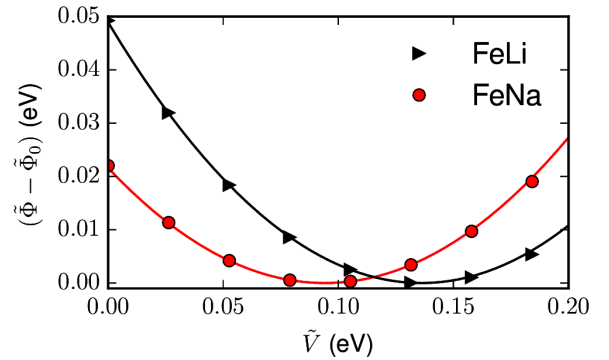
### 4.6.3. Calculation of magnetization

To calculate the response of the impurity to a magnetic field and the evolution of the spin and orbital moment for the different substrates we use the variational exact diagonalization method. We set up the simplest possible model that describes the essence of the magnetic behavior of FeLi and FeNa. Therefore, we neglect crystal field effects (i.e., assume degenerate  $d$  orbitals) and assume bath sites at the Fermi energy coupled with a hybridization of  $\tilde{V}$  to the impurity orbitals. We include spin-orbit coupling with a  $g$ -factor of  $g = 0.05$  eV which is between the atomic value and the value of an iron surface [202]. In order to simplify the calculation of impurity properties, we forbid mixing of impurity and bath sites ( $d_{\alpha}^{(\dagger)} = \tilde{d}_{\alpha}^{(\dagger)}$ ). The model Hamiltonian of the correlated subspace, for which we derive the remaining parameters, thus reads

$$\begin{aligned}
\tilde{H}^C = & \sum_{\alpha} \tilde{\varepsilon}_{\alpha}^d d_{\alpha}^{\dagger} d_{\alpha} + \sum_{\alpha} \tilde{\varepsilon}_{\alpha 1} \tilde{c}_{\alpha 1}^{\dagger} \tilde{c}_{\alpha 1} + \sum_{\alpha} \tilde{V}_{\alpha} \left( \tilde{c}_{\alpha 1}^{\dagger} d_{\alpha} + d_{\alpha}^{\dagger} \tilde{c}_{\alpha 1} \right) \\
& + \sum_{\alpha \beta \gamma \delta, \sigma \sigma'} U_{\alpha \beta \gamma \delta} d_{\alpha \sigma}^{\dagger} d_{\beta \sigma'}^{\dagger} d_{\gamma \sigma'} d_{\delta \sigma} + B_z \sum_{\alpha \sigma} (2m_{s\sigma} + m_{l\alpha}) d_{\alpha \sigma}^{\dagger} d_{\alpha \sigma} \\
& + g \sum_{\alpha \beta \sigma \sigma'} (\mathbf{L} \cdot \mathbf{S})_{\alpha \beta \sigma \sigma'} d_{\alpha \sigma}^{\dagger} d_{\beta \sigma'}.
\end{aligned} \tag{4.15}$$

We fix the impurity on-site energy  $\tilde{\varepsilon}_\alpha^d = -20.66$  eV by the constraint of 7 electrons on the impurity. For simplicity, we fix  $\tilde{\varepsilon}_{\alpha 1} = 0.0$  eV and set the Coulomb matrix as a rotational invariant version with the Slater parameters  $U = 3.3$  eV and  $J = 0.65$  eV (compare Refs. [33, 58] for similar parameters for Fe on alkali and Fe on Ag(100) ( $U = 8$  eV and  $J = 0.85$  eV and  $U = 3$  eV and  $J = 1.0$  eV, respectively)). The non-zero  $g$  factor and the magnetic field lead to a spin-polarized ground state and subsequently spin-dependent effective hybridization matrix elements. The simplest approximation neglecting this, is to set  $g = 0$  and  $B_z = 0$  in the process of minimizing the functional  $\tilde{\Phi}$ . Because we have fixed all parameters but the hybridization by external constrains or reasoning from the literature we only have to minimize the functional with respect to  $\tilde{V}$ . We do this straightforwardly by calculating  $\tilde{\Phi}[\tilde{V}]$  for a set of  $\tilde{V}$ . The resulting values of  $\tilde{\Phi}$  are presented in Fig. (4.11) relative to their respective minimal value. The minimum is found by fitting a quadratic function to the three data points with the smallest functional. The resulting optimal hybridization matrix elements are  $\tilde{V}_{\text{FeLi}} = 0.1371$  eV and  $\tilde{V}_{\text{FeNa}} = 0.0939$  eV. The coefficients defining the optimal transformation ( $u_{c_{\alpha k}}^{c_{\alpha 1}}$ , compare Eq. (4.2)) are in both cases sharply peaked at the Fermi energy, with the most weight at states below the Fermi energy (similar to the  $u_{c_{egk}}^{c_{eg1}}$  in the case of CoCu with the weight function  $W_n = \omega_n^{-1}$  shown in Fig. (4.6) (b)).

**Figure 4.11:** Relative value of the functional  $\tilde{\Phi}[\tilde{V}]$  (Eq. (2.169)) for models defined by  $\tilde{V}$ . Calculated data points for FeLi (triangles) and FeNa (circles) are shown together with quadratic fits (solid lines) to three points closest to the minimum.



Using these parameters we solve the Hamiltonian (4.15) including spin-orbit coupling and an increasing magnetic field up to  $B = 8$  T at a temperature of  $\beta = 2500$  eV<sup>-1</sup> corresponding to  $T = 4.5$  K. We calculate the  $z$  component of the spin and orbital moment,  $\langle S_z \rangle$  and  $\langle L_z \rangle$ . The total moment is defined by  $2\langle S_z \rangle + \langle L_z \rangle$ , which is plotted in Fig. (4.12). The shaded areas under the graph depicting the total moment indicate the summands  $2\langle S_z \rangle$  and  $\langle L_z \rangle$ . We observe a decline of the susceptibility with stronger hybridization: The total moment at  $B = 8$  T is 0.11 for FeLi and 0.27 for FeNa. The decrease of the magnetic moment with increasing hybridization is difficult to compare

with the experimental findings, as they are measured in arbitrary units. The simulated moment increases linear over the complete range of the investigated fields. The shape of the magnetization curve is not reproduced very well, especially for the case of FeNa.

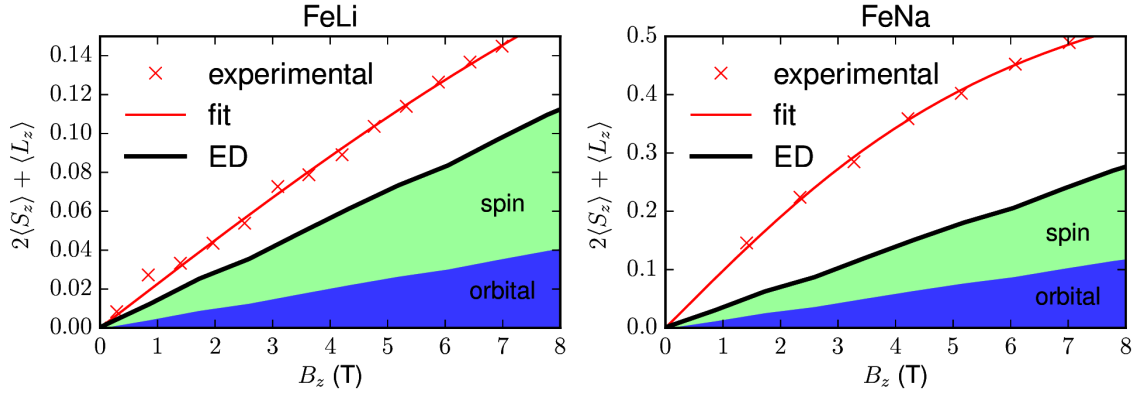


**Figure 4.12.:** Experimental (red crosses) and theoretical (solid black lines) magnetization curves for FeLi (left) and FeNa (right) from exact diagonalization calculations with parameters gained from the variational ED method. The moments from spin and orbital degrees of freedom are marked as shaded area below the black line.

However, we observe a change of the ratio of spin and orbital moment from the simulated data. For the case of strong hybridization the spin moment dominates the total moment. For the case of weaker hybridization the spin and orbital moment are on the same order. The hybridization seems to quench the orbital moment faster than the spin moment.

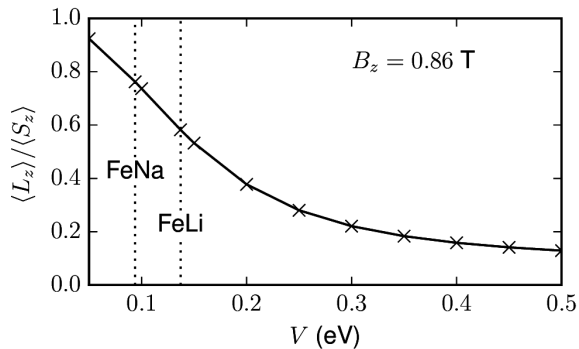


**Figure 4.13:** Orbital moment divided by spin moment for fixed magnetic field of  $B_z = 0.86\text{T}$  in dependence of the hybridization strength. The approximate hybridization strengths for the case of FeLi ( $V_{\text{FeLi}} = 0.1371\text{ eV}$ ) and FeNa ( $V_{\text{FeNa}} = 0.0939\text{ eV}$ ) are marked.

We analyze this behavior by calculating the ratio of spin and orbital moment  $\langle L_z \rangle / \langle S_z \rangle$  for more hybridization strengths  $V$  at a fixed magnetic field  $B = 0.86\text{ T}$ . The result is

presented in Fig. (4.13) and confirms our assumption from above: The orbital and spin moment are on the same order for weak hybridization. For increasing hybridization the orbital moment is quenched faster than the spin moment.

In order to compare this finding to the XMCD data (presented in Fig. (4.14)) we use a sum rule, which is valid for small spin-orbit interaction and weak crystal fields, to obtain a measure for  $\langle L_z \rangle / \langle S_z \rangle$  (compare Ref. [34]). The sum rule reads

$$\frac{\langle L_z \rangle}{\langle S_z \rangle} \approx \frac{2}{3} \frac{\delta_{L_3} + \delta_{L_2}}{\delta_{L_3} - 2\delta_{L_2}}, \quad (4.16)$$

where  $\delta_{L_i}$  is defined by the integral of the XMCD signal over the respective L-edge

$$\delta_{L_i} = \int_{L_i} (\sigma^+ - \sigma^-) dE. \quad (4.17)$$

The domains used to integrate the  $L$  edges are  $704 \text{ eV} < E < 715 \text{ eV}$  and  $715 \text{ eV} < E < 728 \text{ eV}$  for the  $L_3$  and  $L_2$  edge, respectively. The resulting ratios of the spin and orbital momenta, presented in Tab. (4.4), show a clear trend from strong (FeLi) to weak (FeCs) hybridization: The ratio is equally large for FeCs and FeK and smallest for FeLi. FeNa shows an intermediate ratio. This trend matches our findings from the model calculations with only one bath state. The absolute values of the ratios do not coincide with the theoretical values ( $\langle L_z \rangle / \langle S_z \rangle \approx 0.6$  and  $\langle L_z \rangle / \langle S_z \rangle \approx 0.75$  for FeLi and FeNa, respectively), which is mainly because the magnetic field in the experimental setup is significantly higher (up to 7 T).

**Table 4.4:** Approximate ratio between orbital and spin moment obtained from XMCD data via Eq. (4.16).

substrate	Li	Na	K	Cs
$\langle L_z \rangle / \langle S_z \rangle$	0.3	0.5	0.9	0.9

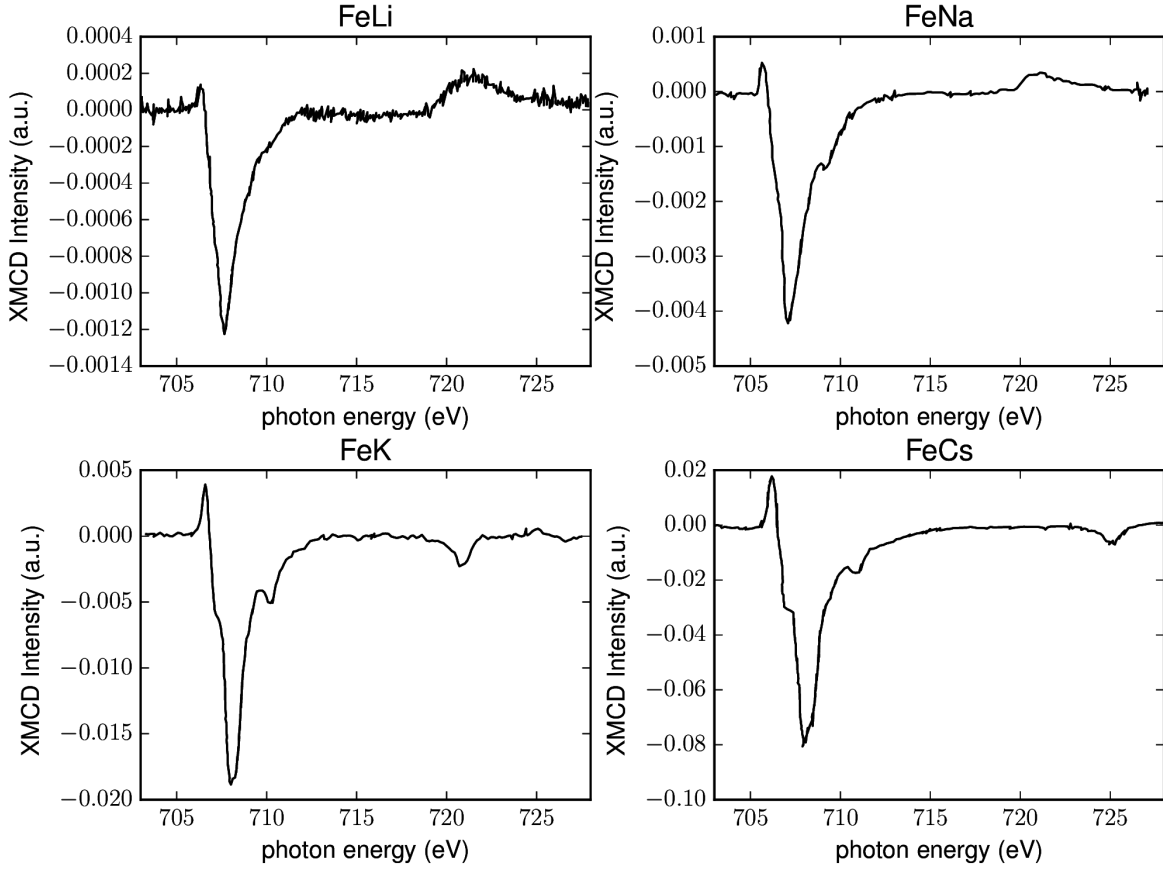


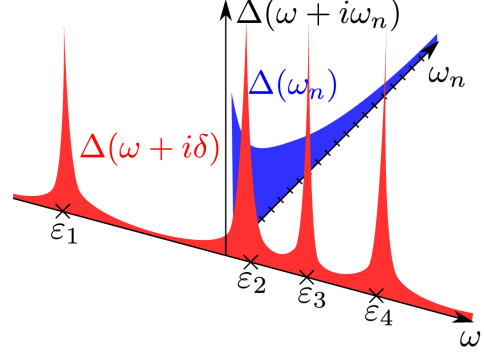
**Figure 4.14.:** XMCD intensity for Fe on all investigated alkali metals (Li, Na, K, and Cs). The  $L_3$  and  $L_2$  edges are located around  $\sim 707$  eV and  $\sim 723$  eV, respectively. Data are measured by S. Gardonio, Materials Research Laboratory, University of Nova Gorica, Vipavska 13, 5000 Nova Gorica, Slovenia and reproduced with authorization.

## 4.7. Fit of hybridization functions on the Matsubara axis

The method of fitting hybridization functions is shortly introduced for the sake of completeness. The method is first introduced in [32] where it is used in the context of dynamical mean field theory. The idea of the method is depicted in Fig. (4.15). The red and blue curves are an exemplary hybridization function (which is closely related to the inverse non-interacting Green function, compare Eq. (2.15)) of the original model, corresponding to Eq. (4.19), evaluated on real (red) and imaginary (blue) frequencies. A fit with a hybridization function with less poles ( $\tilde{\Delta}$ ) than the original hybridization function on the real axis is rather ill defined, due to the peaked structure of  $\Delta(\omega + i\delta)$

and especially  $\tilde{\Delta}(\omega + i\delta)$ . The result heavily depends on the imaginary offset  $\delta$ . The hybridization functions on the imaginary axis are, however, smooth functions which makes a fit well defined and robust.

**Figure 4.15:** Hybridization function in the complex plain, defined by Eq. (2.15) evaluated on Matsubara frequencies  $\omega_n$  (blue) and on the real axis  $\omega$  with an imaginary offset  $\delta$  (red). Figure inspired by Fig. (13) in Ref. [61].



The fit is defined by the minimization of a cost function for the inverse impurity Green function (or equivalently the hybridization function) of the discretized model and that of the original model, both defined on the imaginary frequency axis [32]. In the case of one effective bath site, the discrete impurity Green function is defined as

$$g_0(i\omega_n) = \left( i\omega_n - \epsilon_d - \mu - \frac{\tilde{V}^2}{i\omega_n - \tilde{\epsilon}_1} \right)^{-1} \quad (4.18)$$

and the Green function of the original model as

$$G_0(i\omega_n) = \left( i\omega_n - \epsilon_d - \mu - \sum_k \frac{V_k^2}{i\omega_n - \epsilon_k} \right)^{-1}. \quad (4.19)$$

The cost function then reads

$$\chi^2 = \frac{1}{n_{\max} + 1} \sum_{n=0}^{n_{\max}} W_n |G_0^{-1}(i\omega_n) - g_0^{-1}(i\omega_n)|^2, \quad (4.20)$$

where  $W_n$  is a weight function. Popular choices for the weight function are  $W_n = 1$ ,  $W_n = 1/\omega_n$  and  $W_n = 1/\omega_n^2$ , which put different emphasis of low/higher Matsubara frequencies [213]. Throughout this work, we have chosen  $\beta = 40$  and  $n_{\max} = 1000$ . This method only provides the effective parameters  $\tilde{\epsilon}_1$  and  $\tilde{V}$ . However, in order to calculate the functional  $\tilde{\Phi}[\rho_{\tilde{H}}]$  an optimal unitary transformation in above sense is calculated and the  $h_{ikk'}$  are found by a projection of a Hartree-Fock solution onto the basis states of  $\mathcal{R}$ . We assume that the effective energy of the impurity site is the same as in the original model ( $\tilde{\epsilon}_d = \epsilon_d$ ).

# 5. Many-body effects on Cr(001) surfaces: An LDA+DMFT study

M. Schüler, S. Barthel, M. Karolak, A. I. Poteryaev, A. I. Lichtenstein, M. I. Katsnelson, G. Sangiovanni, and T. O. Wehling, **Many-body effects on Cr(001) surfaces: An LDA+DMFT study**, arXiv **1512.01181** (2015), accepted in Phys. Rev. B (2016)

This chapter is based on the publication given above and shows considerable amount of overlap with the original manuscript, concerning both text and figures. The original text is mainly written by M. Schüler and proofread by all authors. The DFT calculations were done in collaboration with M. Karolak. The projector scheme was developed and implemented by S. Barthel, Tim Wehling and M. Schüler. All other calculations and figures presented in the manuscript have been prepared by M. Schüler.

## 5.1. Introduction

In this chapter we investigate the electronic structure of the Cr(001) surface by means of the LDA+DMFT method introduced in Sec. (2.4). We use a generalized approach of the LDA+DMFT method in order to take the spatially inhomogeneous Coulomb interaction and correlation effects of the surface into account. Thereby, we elucidate the role of interaction effects and its complex interplay with the surface band structure in forming a low-energy resonance, which we believe was unrecognized in earlier approaches to this problem. We investigate how the electronic structure obtained from LDA and spin polarized LDA calculations changes at the surface with respect to the bulk. We perform DMFT calculations to study how the differences in the single-particle part translates to effects in the interacting electronic spectrum. Thereby, we present the first realistic treatment of the electronic structure of Cr(001), which includes correlation effect on a non-perturbative level using the LDA+DMFT scheme.

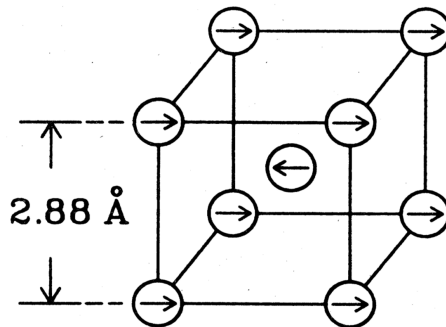
We start the discussion in Sec. (5.2) with a brief review of Cr related physics. In particular we discuss the experimental findings and theoretical attempts to the Cr(001) surface. In Sec. (5.3.1) we briefly introduce the experimental spectrum which

we compare our data to. We give a short overview of the LDA and DMFT methods as well as the physical and numerical parameters we have used in Sec. (5.3.2). The results of the single-particle methods are presented in Sec. (5.4.1) which are the basis for the detailed analysis of the DMFT results in Sec. (5.4.2), where we also prove the many-body nature of the central resonance and discuss the spatial properties of the self-energy. Finally, we give a conclusion in the last section.

## 5.2. Overview of Cr physics

Bulk Cr crystallizes in a body-centered crystal (bcc) structure [183]. Neutron diffraction experiments [200, 11] reveal a spin-density wave ordering of bulk Cr with a magnetic moment of about  $0.6\mu_B$  per atom at low temperatures and a Néel temperature of approximately  $T_N^{\text{bulk}} \sim 311$  K [180]. The spin density wave is close to a pure antiferromagnetic ordering [11] in which the lattice is described by a simple cubic (sc) unit cell, which contains two atoms of opposite spin polarization, of double the size of the bcc unit cell, compare Fig. (5.1). Following Ref. [71], we compare the GGA band structure of antiferromagnetic and paramagnetic bulk Cr in the sc unit cell, as presented in Fig. (5.2). Strikingly, the antiferromagnetic ordering (in GGA) induces one avoided crossing at the Fermi energy on the  $\Gamma M$  line and several at the X point. In Ref. [131] the magnetic structure of bulk Cr is similarly discussed on the basis of the paramagnetic electronic structure (in particularly the Fermi surface and its nesting properties).

**Figure 5.1:** Real-space spin-lattice of commensurate antiferromagnetic Cr. The topmost atoms define the (001) surface. Reprinted figure with permissions from [L. Klebanoff, S. Robey, G. Liu, D. Shirley, Phys. Rev. B, **31**, 6379 (1985), [102]]. Copyright 1985 by the American Physical Society.



Considering the lattice of antiferromagnetic Cr, depicted in Fig. (5.1), it is obvious that a cut along the (001) direction leads to a surface where atoms of layers parallel to the surface are ferromagnetically aligned. Thus, a ferromagnetic surface is formed. Intriguingly, the surface magnetic state persists up to much larger tempera-

tures ( $T_N^{\text{surf}} \sim 750 - 800$  K) than the bulk state, as measured in Refs. [103, 101] by angular resolved photo emission (ARPES) and Ref. [148] by magnetization measurements with Cr particles of different diameter. Theoretical calculations based on the tight-binding method found surface magnetic moments increased by a factor of 3-4 compared to the experimental bulk value and confirmed the large surface Néel temperature [4, 63, 75]. This large magnetic moment originates from the altered paramagnetic electronic structure: The surface introduces massively more states close to the Fermi energy (compare Fig. (5.7)), which spin split due to the exchange interaction and lead to a large surface moment [131].

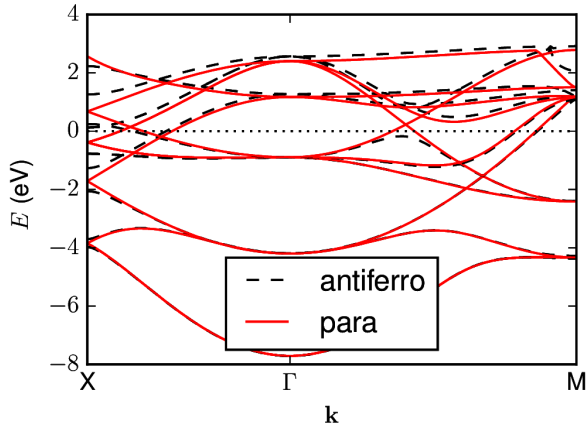


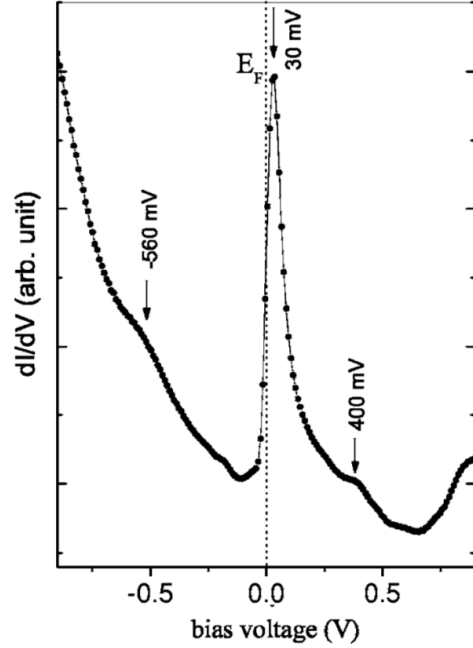
**Figure 5.2:** GGA band structure of antiferromagnetic (dashed black) and paramagnetic (solid red) bulk Cr for wave vectors of high symmetry lines of the sc unit cell with  $k_z = 0$ . The Fermi energy ( $E = 0.0$  eV) is depicted as dotted line.

Next to the (rather well understood) magnetic properties of Cr(001), the surface shows a distinct and basically unexplained feature in its spectroscopic electronic properties. This feature is a sharp resonance close to the Fermi energy and was first found in ARPES experiments [101, 102, 103]. The spectrum found in a subsequent scanning tunneling spectroscopy (STS) measurement [110], reproduced in Fig. (5.3), exemplifies the sharp feature close to the Fermi energy.

Since its first observation, the task of unraveling the origin of this sharp resonance has spawned many experimental and theoretical works. Inspired by scanning tunneling spectroscopy (STS) measurements [209] first theoretical explanations were single-particle models, showing a  $d_{z^2}$  character of the resonance, with the downside of having to adjust the amount of magnetic polarization of the surface to fit the experimental spectrum.

New light was shed on the system by combination of STS measurements on highly clean Cr(001) surfaces and theoretical many-body techniques which suggested many-body effects as the source of the resonance [109, 110]. In contrast to the conventional Kondo effect, where virtual transitions between degenerate spin states, mediated

**Figure 5.3:** Electronic resonance at 30 meV above the Fermi energy of Cr(001) in tunneling conductance measurements. Broad features at 560 meV below and 400 meV above the Fermi energy are also visible. For details on the experimental setup refer to the original work in Ref. [110]. Reprinted figure with permissions from [O. Kolesnychenko, G. Heijnen, A. Zhuravlev, R. de Kort, M. Katsnelson, A. Lichtenstein, H. van Kempen, Phys. Rev. B, **72**, 085456 (2005), [110]]. Copyright 2005 by the American Physical Society.



through metallic bath states, lead to a resonance at the Fermi energy, the many-body scenario suggested in Refs. [109, 110] is an orbital Kondo effect, where such virtual transitions occur between degenerate *orbital* states. In the case of the Cr(001) surface, these states are the  $d_{xz}$  and  $d_{yz}$  orbitals, which due to the crystal field of the surface are the only degenerate orbitals. The spectrum of a model calculation and the underlying process of the orbital Kondo effect are reproduced from [109] in Fig. (5.4). This explanation naturally comes with the premise of a resonance with  $d_{xz/yz}$  character, in contrast to the  $d_{z^2}$  character proposed in single-particle theories.

To decide if the orbital Kondo scenario or the single-particle picture is valid, two experiments have been performed: STS measurements have aimed to use the temperature dependence of the resonance to rule out one of the two scenarios but without a definite conclusion [72]. Newer measurements, combining STS, PES and inverse PES (IPES) [28], have directly probed the symmetry properties (i.e., the orbital character) of the spectrum, revealing a  $d_{z^2}$  symmetry of the supposedly Kondo peak. The spectrum is reproduced from Ref. [28] in Fig. (5.5). The  $d_{z^2}$  character of the resonance speaks against the orbital Kondo scenario. However, an alternative satisfactory explanation in terms of a single-particle theory is not at hand. The discussed electron-phonon interaction mechanisms, which are necessary to explain the temperature dependence of the shape of the single-particle resonance would require coupling matrix elements

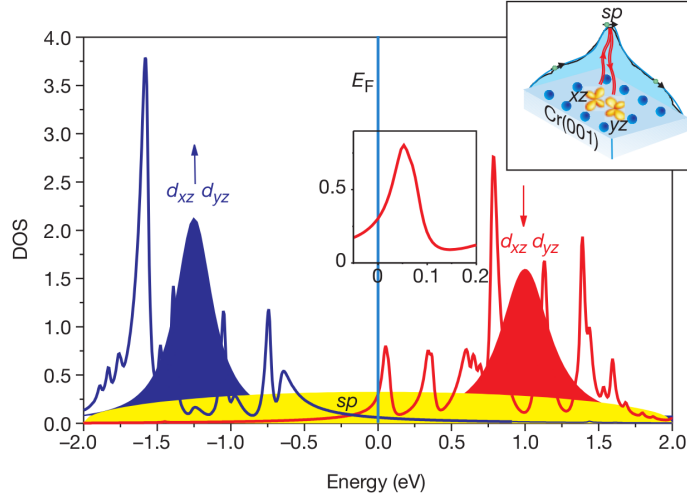


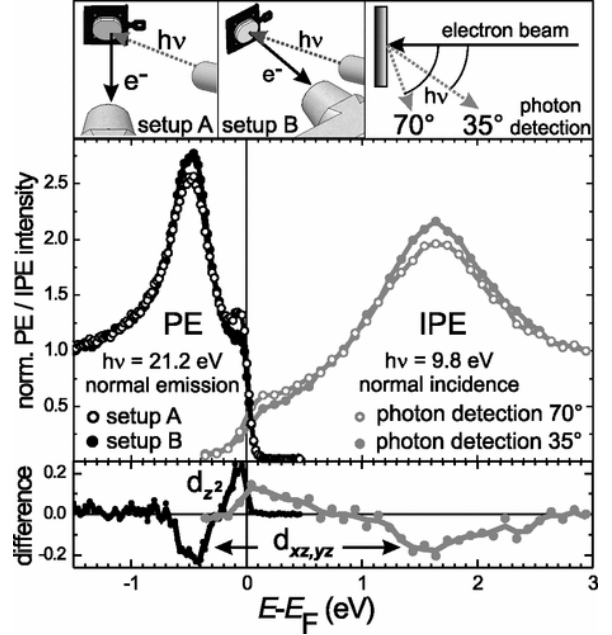
**Figure 5.4.:** Model calculation for the formation of the orbital Kondo resonance. Main panel: solid yellow shows ferromagnetic surface DOS of Cr(001). Solid blue and red show one-electron states for  $d_{xz/yz}$  spin up and down (in blue and red, respectively). The surface and interacting orbital states hybridize and are solved in exact diagonalization, leading to the correlated DOS in blue and red. The correlated peak near the Fermi energy is magnified in the central inset and is identified as Kondo resonance. The right inset shows a sketch of the physical process leading to the orbital Kondo effect. Virtual transitions between the degenerate  $d_{xz/yz}$  orbitals via the conduction states lead to the Kondo effect. For details refer to the original work in Ref. [109]. Reprinted by permission from Macmillan Publishers Ltd: O. Kolesnychenko, R. de Kort, M. Katsnelson, A. Lichtenstein, H. van Kempen, *Nature* **415** (2002) 6871 [109], copyright 2002.

for the surface of the order of 5-10 larger than the bulk value [72].

Newer PES measurements [1] show a strong temperature dependence of the resonance. Namely the emergence of a pseudogap below about  $T = 200$  K and the advent of a sharp resonance below  $T = 75$  K which speaks for a predominate many-body nature of the resonance. This was previously not found in STS measurements [72].

We believe that both routes (single-particle theory and the simplified model for the orbital Kondo effect) have problems describing the spectrum correctly for distinctive reasons. First, the single-particle theory misses correlation effects, which cannot be negligible in a system of transition metal atoms with considerable amount of spectral weight at the Fermi level in the paramagnetic phase [4]. Secondly, the model behind the orbital Kondo effect incorporates correlation effects but only deals with the  $d_{xz/yz}$  orbitals and such misses the specific electronic structure of the system by neglecting

**Figure 5.5:** PE and IPE spectra obtained at  $T = 295$  K in experimental geometries with different sensitivities to  $d_{z^2}$ -like (open dots) and  $d_{xz,yz}$ -like (filled dots) orbital characters (see text of original publication for details). The same symmetry assignment was obtained at ( $T = 160$  K) (not shown). Reprinted figure with permissions from [M. Budke, T. Allmers, M. Donth, and M. Bode, Phys. Rev. B, **77**, 233409 (2008), [28]]. Copyright 2015 by the American Physical Society.



three of the five  $d$  orbitals.

Our goal is to calculate and characterize the spectrum of Cr(001) including correlation effects on the basis of a realistic description of the electronic structure. The method of choice is the LDA+DMFT scheme, introduced in Sec. (2.4). The method incorporates effects stemming from strong correlations in a local approximation into the material specific framework of density functional theory. We show that local electronic correlations are key to understanding the electronic structure of Cr(001).

## 5.3. Models and Methods

### 5.3.1. Cr(001) surface

Combined PES and IPES measurements make a fairly direct comparison of experimental and calculated local density of states (DOS) of the surface possible. The most up to date combined PES *and* IPES measurements from Ref. [28], reprinted in Fig. (5.5), obtained at a temperature of  $T = 295$  K ( $\beta = 39.3$  eV $^{-1}$ ) reveal three main features in the spectrum. First, a broad peak at  $-0.5$  eV dominated by  $d_{xz/yz}$  character. Second a sharp peak around the Fermi energy at  $0.0$  eV  $\pm 0.05$  eV, which is mainly of  $d_{z^2}$  character. Third, a broad peak at  $1.65$  eV which is again dominated by  $d_{xz/yz}$  character.

In order to reproduce the three peak structure of the spectrum realistically, we model

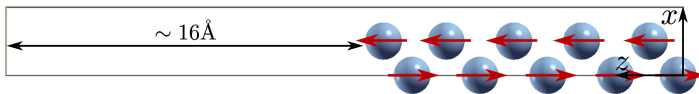


**Figure 5.6.:** Unit cell used to model the Cr(001) surface. The  $z$ -coordinates of the two outermost atoms per surface were relaxed in LDA. Arrows indicate the magnetic ordering. The figure is generated with XCrySDen [108].

the Cr(001) surface by a slab of 10 Cr atoms and a region of vacuum of about 16 Å stacked in  $z$  direction as depicted in Fig. (5.6). This slab is periodically continued in  $x$  and  $y$  direction. Earlier DFT calculations [71, 19] have shown that a slab of ten atoms is thick enough such that the innermost atoms behave like bulk atoms. We calculate the spectra near the experimental inverse temperature ( $\beta = 40 \text{ eV}^{-1}$ ). Additionally we analyze the temperature dependence of the spectrum by simulating one higher ( $\beta = 60 \text{ eV}^{-1}$ ) and one lower ( $\beta = 20 \text{ eV}^{-1}$ ) inverse temperature. As discussed in the previous section and depicted in Fig. (5.1), the magnetic ground state of the Cr(001) surface are antiferromagnetically ordered layers which themselves are ferromagnetically ordered [71] (see Fig. (5.6) for a side view of the surface). The cubic symmetry present in the bulk, leading to three degenerate  $t_{2g}$  and two  $e_g$   $d$  orbitals, is lifted at the surface, leaving only the  $d_{xz}$  and  $d_{yz}$  orbitals degenerate.

### 5.3.2. Details of the LDA+DMFT method for Cr(001)

We take structural changes in the vicinity of the surface into account by optimizing the coordinate perpendicular to the surface of the two uppermost and lowermost atoms. To perform many-body calculations on top of the paramagnetic LDA calculations a projection of delocalized low energy Kohn-Sham states to a localized basis is done as introduced in Sec. (2.4.1). We choose the 70 Kohn-Sham states lowest in energy for this task. The subspace in which Coulomb interaction is treated by DMFT is defined by the five  $3d$  orbitals on each Cr atom. The 20 spare states form the uncorrelated subspace. The projection yields a single-particle Hamilton matrix for each in-plane wave number  $\mathbf{k}$ :  $H(\mathbf{k})_{\alpha\beta}^{ij} = \langle i, \alpha | H(\mathbf{k}) | j, \beta \rangle$  in the localized basis  $|i, \alpha\rangle$ , labeled by a layer index  $i$  and a combined index  $\alpha$  for  $d$  orbitals and states of the orthogonal complement. The correlated states are augmented with the parametrized rotationally invariant local Coulomb interaction introduced in Sec. (2.4.3), which we choose to be

layer dependent as

$$U_{\alpha\beta\gamma\delta}^i = \sum_{k=0}^{2l} a_k(\alpha_m\beta_m, \gamma_m\delta_m) F_i^k. \quad (5.1)$$

The layer dependent average Coulomb interaction  $U_i$  and Hund's exchange interaction  $J_i$  are taken from ab initio constrained random phase approximation (cRPA, compare section (2.4.3)) calculations [190]. The Coulomb interaction has a strong layer dependence<sup>1</sup> ( $U_{1/10} = 3.44$  eV,  $U_{2/9} = 4.64$  eV,  $U_{3/8} = 4.73$  eV,  $U_{4/7} = 4.94$  eV and  $U_{5/6} = 4.95$  eV) while the Hund's exchange interaction is constant ( $J_i = 0.65$  eV). On first sight it seems counterintuitive that the Coulomb interaction is smaller at the surface than in the bulk, as screening should be less efficient due to a smaller screening volume. However, surface electronic structure effects such as the appearance of surface states and effective band narrowing can also increase screening at the surface. In the case of the Cr(001) surface, the electronic structure effect dominates the volume effect, thus leading to a decrease of the surface interaction matrix elements with respect to the bulk value, as discussed in detail in Ref. [190]. We neglect all Coulomb interaction terms besides density-density terms.

We solve the multi-orbital Hubbard model of the slab of ten atoms by multi-site DMFT which allows for spatially inhomogeneous Coulomb interaction and antiferromagnetic ordering [61]. Compare, e.g., Refs. [126] and [220] for a similar approach. In multi-site DMFT the lattice Green function reads

$$[G(i\omega_n, \mathbf{k})^{-1}]_{\alpha\beta}^{ij} = [(i\omega_n + \mu) \delta_{\alpha\beta} - \Sigma(i\omega_n)_{\alpha\beta}^i] \delta_{ij} - H(\mathbf{k})_{\alpha\beta}^{ij}, \quad (5.2)$$

where the DMFT approximation of a local, i.e.,  $\mathbf{k}$ -independent, self-energy is apparent. The double-counting term is absorbed into the self-energy. The local lattice Green function  $G(i\omega_n)$  is obtained by  $\mathbf{k}$ -averaging  $G(i\omega_n, \mathbf{k})$ . We compute the Weiss field,

$$[\mathcal{G}^0(i\omega_n)^{-1}]_{\alpha\beta}^i = [G(i\omega_n)^{-1}]_{\alpha\beta}^i + \Sigma(i\omega_n)_{\alpha\beta}^i, \quad (5.3)$$

for each Cr atom and solve the resulting effective impurity problems for each Cr atom until self-consistency in the DMFT loop is reached.

To solve the impurity problems we use the continuous-time quantum Monte Carlo (CTQMC) algorithm in the hybridization expansion [226, 225] implemented in the

---

<sup>1</sup>We have checked the sensitivity of our results with respect to the used Coulomb matrix elements by using constant average interaction of  $U_i = 4.95$  eV (the bulk value from the reference) and  $U_i = 2.0$  eV with  $J_i = 0.9$  from [37]. The former parameters lead to basically the same spectra as the layer dependent ones. The considerably smaller latter parameters lead to no resonance at the Fermi energy.

w2dynamics software package [168]. We cope with the double-counting problem, which is inherent to LDA++ approaches, by the requirement that the total occupation on each impurity obtained from the DMFT Green function  $G$  matches the corresponding occupation obtained from the bath Green function. This is called trace double-counting correction and reads

$$\text{Tr } \rho_{\alpha\beta}^{\text{imp}} = \text{Tr } \rho_{\alpha\beta}^{0,\text{loc}}, \quad (5.4)$$

where  $\rho$  is the density matrix for each atom. This leads to satisfactory results in metallic systems [96]. To assess the influence of the choice of the double-counting energy we have used an alternative double-counting scheme, namely enforcing 4.5 electrons on each Cr atom<sup>2</sup>.

For the analytic continuation from imaginary to real frequency spectral functions we use the maximum entropy method (compare Sec. (2.5.4)) as implemented in the w2dynamics software package. In the DMFT loop, the antiferromagnetic order is achieved by starting with a constant shift of the real part of the self energy in the first iteration of the DMFT loop. We stress the importance of global spin flips of configurations in the Markov chains in the presence of magnetic polarization in order to prevent getting stuck in local minima. After reasonable convergence of the self energy, some final iterations with high statistics ( $10^5 - 10^6$  measurements depending on the inverse temperature.) are done. The autocorrelation times for each inverse temperature are estimated by the ratio of the acceptance rate of inserting operators in the trace and the position of the maximum in the expansion histogram [160] leading to  $N_{\text{corr}} = 4500, 14000, 40000$  for  $\beta = (20, 40, 60) \text{ eV}^{-1}$ , respectively.

## 5.4. Results

### 5.4.1. LDA and LSDA spectra

The broadened local density of states for the paramagnetic LDA calculation are shown in Fig. (5.7) for (a) a surface atom and (b) an atom of the fifth layer, which is henceforth called bulk atom. The results are very close to tight-binding calculations [4]. At first glance, the structure of the spectrum resembles the experimental one, with three peaks at about the right positions. However, neglecting the magnetic order and correlation effects leads to many differences in detail: The peak at the Fermi energy is far too big and broad in comparison to the experiment (Fig. (5.5)). The orbital

<sup>2</sup>We replace the right hand side of Eq. (5.4) with 4.5. In contrast, the trace double counting leads to 4.7 electrons in the case of the surface atom.

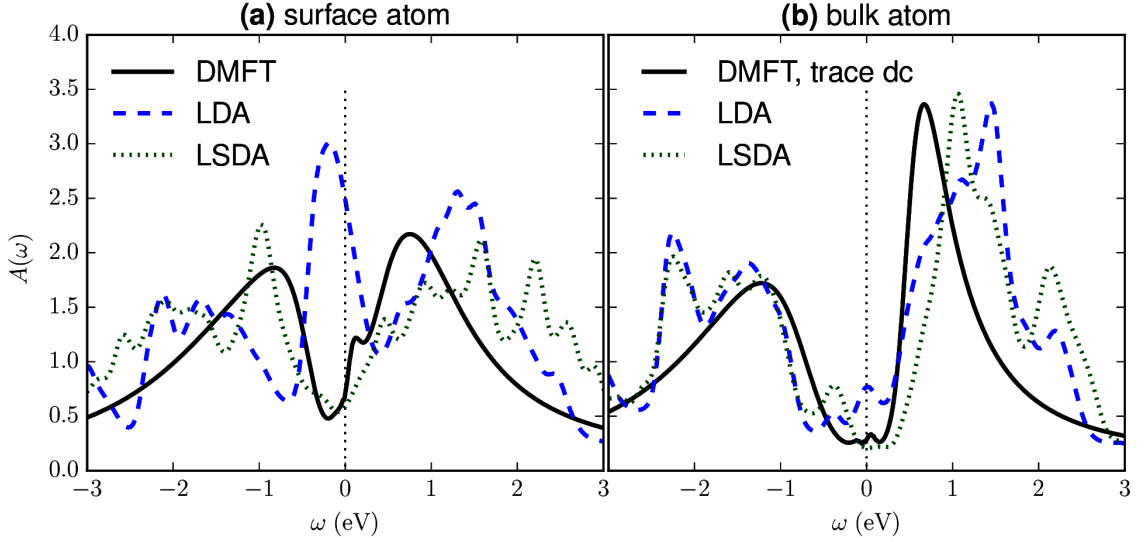


**Figure 5.7.:** Orbital and spin averaged local density of states (LDOS) from LDA+DMFT simulations at the temperature  $\beta = 40 \text{ eV}^{-1}$  (solid line), LDA (dashed lines) and LSDA (dotted lines) calculations. (a) shows the LDOS at the surface atom. (b) shows the LDOS of the center atom.

characters shown in Fig. (5.8) (a) do not coincide with the experimental data from Ref. [28] shown in Fig. (5.5). The peak at the Fermi energy has nearly evenly divided orbital weight among all  $d$  orbitals and the upper broad peak is mainly of  $d_{z^2}$  character. In contrast to the bulk atom, the high spectral weight at the Fermi energy together with a considerable Coulomb interaction ( $U_1 = 3.44 \text{ eV}$ ) is a possible basis for a large magnetic moment and strong many-body effects at the surface. The peak at the Fermi energy is absent in the bulk case.

The static mean-field treatment of spin polarization effects in the case of the LSDA calculations leads to a splitting of the states close to the Fermi energy. The position of the broad peaks is estimated to be  $-1.0 \text{ eV}$  and  $1.6 \text{ eV}$ , which corresponds roughly to the experimental positions ( $-0.5 \text{ eV}$  and  $1.65 \text{ eV}$ ). The large initial (“paramagnetic”) peak at the Fermi energy leads to a larger magnetization at the surface ( $|m| \sim 2.31\mu_B$ ) than for the bulk atoms ( $|m| \sim 1.25\mu_B$ ). The orbitally resolved density of states shown in Fig. (5.8) (b) reveals that the lower broad peak is of mainly  $d_{xz,yz}$  and  $d_{xy}$  character which is in line with the experimental findings. The upper peak has also  $d_{xz,yz}$  and  $d_{xy}$  character but considerable  $d_{x^2-y^2}$  weight is found, too. Instead of a resonance directly at the Fermi level, LSDA yields a feature of  $d_{z^2}$  character  $0.5 \text{ eV}$  above the Fermi

energy. In summary, LSDA is able to describe the broad peaks above and below the Fermi energy reasonably well, whereas the sharp feature at the Fermi energy is absent.

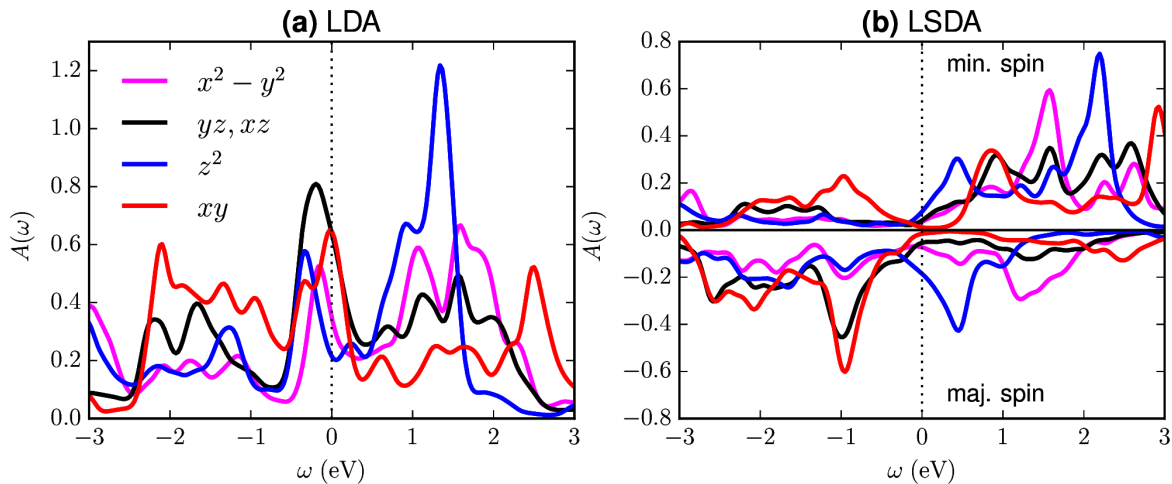


**Figure 5.8.:** Orbitally resolved local density of states of the surface atom from (a) LDA, (b) LSDA.

### 5.4.2. DMFT spectra

For all three investigated temperatures we have found antiferromagnetic solutions in DMFT. Similar to the LSDA calculation we find a larger magnetic moment for the surface atoms ( $|m| \sim 2.2\mu_B$ ,  $2.4\mu_B$  and  $3.0\mu_B$ ) than for the bulk atoms ( $|m| \sim 1.5\mu_B$ ,  $1.8\mu_B$  and  $2.5\mu_B$ ) for  $\beta = 20 \text{ eV}^{-1}$ ,  $40 \text{ eV}^{-1}$  and  $60 \text{ eV}^{-1}$ , respectively. Like in the case of LSDA this results from the larger LDA density of states at the Fermi energy (compare Fig. (5.7) (a) and (b)) and is therefore a consequence of the rearrangement of the electronic states at the surface. The magnetic moment shows a strong dependence on the temperature.

We first analyze the density of states obtained using the trace double-counting scheme: The local density of states at  $\beta = 40 \text{ eV}^{-1}$  summed over the  $d$  orbitals and spins for the surface atom is shown in comparison to the L(S)DA spectra in Fig. (5.7) (a). The same is shown for a bulk atom in Fig. (5.7) (b). A direct comparison of the experimental data and the DMFT spectra of the surface atom is given in Fig. (5.10). For the surface atom we can observe a three-peak structure resembling

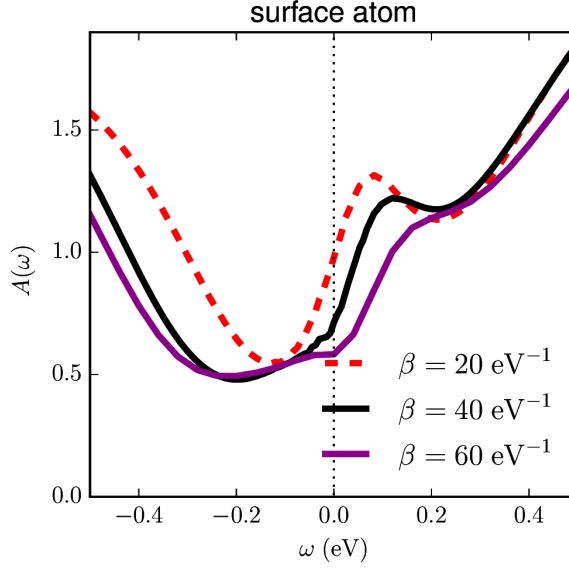


**Figure 5.9.:** Details of the orbital and spin averaged local density of states (LDOS) from LDA+DMFT simulations near the Fermi level for different temperatures,  $\beta = 20 \text{ eV}^{-1}$  (dashed line),  $\beta = 40 \text{ eV}^{-1}$  (solid black line) and  $\beta = 60 \text{ eV}^{-1}$  (solid magenta line).

the experimental situation. In particular, the lower and upper peak are located at  $-0.8 \text{ eV}$  and  $0.75 \text{ eV}$ . The peak at the Fermi level is shown in detail in Fig. (5.9) for all investigated temperatures. It is located at about  $0.1 \text{ eV}$  for  $\beta = 20 \text{ eV}^{-1}$  and  $\beta = 40 \text{ eV}^{-1}$ . The peak is shifted towards  $150 \text{ meV}$  above the Fermi level and appears as a shoulder for  $\beta = 60 \text{ eV}^{-1}$ . The resonance is slightly sharper for the simulation at  $\beta = 20 \text{ eV}^{-1}$ . While the position of the central peak fits nicely to the experiment, the position of the lower and upper peak is off by  $\sim 0.3 \text{ eV}$  and  $\sim 1 \text{ eV}$ , respectively.

To test the influence of the choice of the double-counting energy we have calculated spectra using the alternative double-counting scheme described above. For the surface atom, the double counting we arrive at is  $1.3 \text{ eV}$  smaller as in the case of the trace double counting ( $E_{\text{dc}}^{\text{trace}} \approx 13.5 \text{ eV}$  and  $E_{\text{dc}}^{4.5} \approx 12.2 \text{ eV}$ ). The resulting total density of states for the surface atom at  $\beta = 40 \text{ eV}^{-1}$  is presented in Fig. (5.10). The resonance at the Fermi energy is more pronounced and shifted by approximately  $100 \text{ meV}$  to the Fermi energy. The lower broad peak is shifted to considerably higher energy ( $-0.4 \text{ eV}$ ) and lies nearly on top of the corresponding experimental peak ( $-0.5 \text{ eV}$ ). The position of the upper broad peak is not affected by the smaller double-counting energy.

A source of the wrong spectral positions, especially of the upper broad peak for both

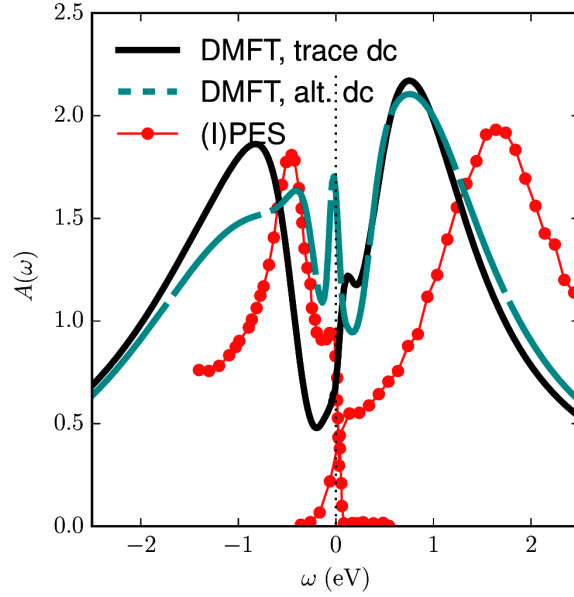


**Figure 5.10.:** DMFT surface spectra at  $\beta = 40 \text{ eV}^{-1}$  with two different double-counting schemes (trace double counting, solid line) and an alternative scheme (see text, dashed line) in comparison with experimental (I)PES data [28] (dots). (I)PES data are in arbitrary units.

double-counting schemes, could be neglecting the interaction mechanisms between the correlated and uncorrelated bands as well as those between the uncorrelated bands themselves, leading to a too small overall exchange splitting. Considering the lower peak and the resonance at the Fermi energy, the total spectrum from the smaller double-counting energy agrees better with the experimental data. The bulk spectra do not change dramatically with the temperature and are very close to the LSDA treatment: dynamic correlation effects seem to be less important far from the surface<sup>3</sup>, which is in agreement with Ref. [37]. Indeed, the spectrum for the second layer already shows nearly no peak at the Fermi level (not shown).

The orbital characters of the spectra obtained with the trace double counting for the two temperatures showing the resonance are presented in Fig. (5.11) (a) and (b). The broad peaks show very similar characters to the LSDA calculations: the lower peak is mainly of  $d_{xz/yz}$  and  $d_{xy}$  character, the upper peak is mainly of  $d_{xz,yx}$ ,  $d_{xy}$ ,  $d_{x^2-y^2}$  and slightly of  $d_{z^2}$  character. The sharp central peak is dominated by a feature in the

<sup>3</sup>From the analytically continued spectrum only it is hard to assess whether or not differences between static- and dynamical-mean field, as the ones discussed in Ref. [187] are present or not.

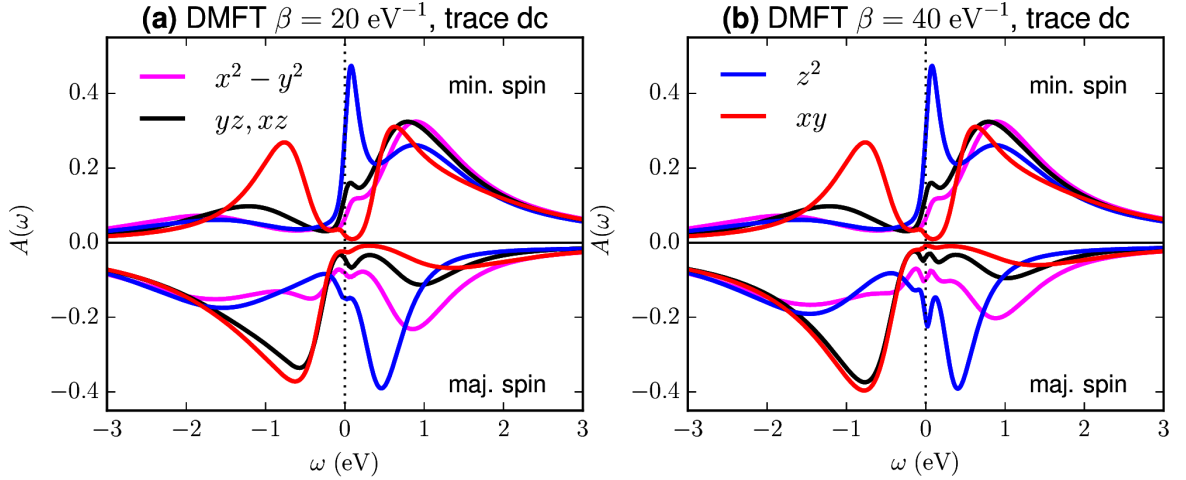


**Figure 5.11.:** Orbitaly resolved local density of states of the surface atom from LDA+DMFT simulations for trace double counting ( $E_{dc} \approx 13.5$  eV) and temperatures (a)  $\beta = 20$  eV $^{-1}$  and (b)  $\beta = 40$  eV $^{-1}$ .

minority spin channel with  $d_{z^2}$  character but also carries some spectral weight from the other  $d$  orbitals, particularly the  $d_{xz}$  and  $d_{yz}$  orbitals. For  $\beta = 40$  eV $^{-1}$  the  $d_{z^2}$  orbital also shows a sharp resonance in the majority spin channel.

The orbitaly resolved spectral functions for the surface atom in the case of the alternative double-counting scheme are shown in Fig. (5.12) (a) and (b) for the same temperatures as before. The overall character of the peaks is unaffected by the change of the double-counting energy. The  $t_{2g}$  contribution of the lower peak is sharper than in the former case and shifted towards the Fermi level. The smaller double-counting energy leads to additional minor  $d_{xy}$  character of the resonance. The resonance in the  $d_{z^2}$  majority spin part of the spectrum for the trace double counting present at  $\beta = 20$  eV $^{-1}$  and  $\beta = 40$  eV $^{-1}$  is absent in this case. In conclusion, the orbital character for both double-counting energies are in line with the experimental data reported in Ref. [28], which are shown in (5.5).

The comparison of the spectra at different temperatures (Fig. (5.9)) shows that the resonance at the Fermi level tends to shift from  $\beta = 40$  eV $^{-1}$  on. This shift is contradictory to temperature dependent STS measurements [72] of the resonance which show a resonance for temperatures from  $\beta = 33.5$  eV $^{-1}$  to  $\beta = 527$  eV $^{-1}$  which narrows with smaller temperature without any shift. This behavior in the simulations could be an artifact of the density-density approximation of the Coulomb-tensor and has to be investigated further. However, recent temperature dependent PES measurements [1]

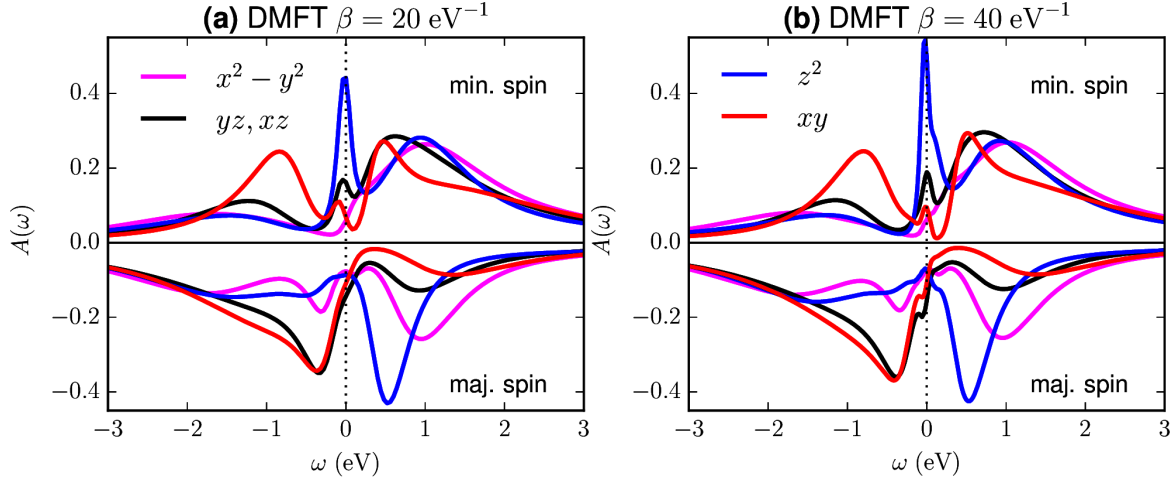


**Figure 5.12.:** Orbitaly resolved local density of states of the surface atom from LDA+DMFT simulations with the alternative double counting scheme ( $E_{\text{dc}} \approx 12.2$  eV) and temperatures (a)  $\beta = 20$  eV $^{-1}$  and (b)  $\beta = 40$  eV $^{-1}$ .

do find an emerging pseudogap above  $T = 200$  K ( $\beta = 58$  eV $^{-1}$ ), which is in qualitative agreement with the results of our simulations. The experimental data also show a sharp feature reappearing in the spectrum for temperatures below  $T = 50$  K; a temperature unfortunately computationally too expensive for the QMC method used in this work. In summary, while deviations in the energetic position of the broad peaks between experimental and DMFT data are apparent, the experimental orbital character of all three peaks could be confirmed by the DMFT simulations.

Kondo-like resonances originate from degenerate levels in contact with a bath. In the original sense of the Kondo effect, these levels are the spin levels. One characteristic property of Kondo-type resonances is their behavior under breaking of this degeneracy by an energy  $\Delta$ : Below a critical splitting on the scale of the Kondo temperature  $T_K$  the resonance is pinned to the Fermi energy. Above the critical energy the resonance is split by approximately  $\Delta$  and broadened [40]. In the case of Cr(001), the suggested *orbital* Kondo effect in Ref. [109] results from the degenerate  $d_{xz}$  and  $d_{yz}$  orbitals. To check if the  $d_{xz/yz}$  contribution of the above found resonance is of a Kondo-like nature, we test its robustness against a small splitting of the orbital energy, i.e., an artificial crystal field. Similarly, we test the many-body nature of the  $d_{z^2}$  contribution of the resonance by shifting the  $d_{z^2}$  orbital energy. To this end, we investigate five-orbital Anderson impurity models with artificially broken crystal symmetries. The impurity models are defined by the hybridization function of a surface atom found

in the DMFT self-consistency for the trace double counting, the appropriate chemical potential and Coulomb matrix. We first break the  $d_{xz/yz}$  degeneracy by simultaneously applying a negative crystal field to the  $d_{xz}$  orbital and a positive to the  $d_{yz}$  orbital. The strength of the crystal field is  $|\Delta_{xz/yz}| = 0.1$  eV and  $|\Delta_{xz/yz}| = 0.2$  eV. The resulting spectra of the  $d_{xz}$  and  $d_{yz}$  orbitals are depicted in Fig. (5.13) (a)-(b). While the broad peaks above and below the Fermi level experience a rigid shift in the direction of the respective crystal field, revealing them as single-particle peaks, the position of the central resonance is basically not changed. This speaks very much for a many-body nature of the resonance, as expected from the prior comparison of the GGA and DMFT spectra. We further analyze the resonance by shifting the  $d_{z^2}$  orbital by  $\Delta_{z^2} = 0.1$  eV and  $\Delta_{z^2} = 0.2$  eV. The  $d_{z^2}$  contributions of the spectra are shown in Fig. (5.13) (c). The central resonance again does not change with the crystal field, speaking for a many-body effect as the source of the resonance. In contrast, the maximum at  $\sim 0.5$  eV is rigidly shifted, revealing it as a single-particle feature.

The analysis of the resonance's behavior subject to a shift of single-particle energies rules out a pure single particle nature of the resonance. Its robustness is an indicator for a many-body nature. However, a conventional Kondo effect does not likely explain the resonance because the temperature dependence and symmetry breaking found in this work contradicts the expectations from the Kondo effect (sharpening of the resonance with lower temperatures, splitting under symmetry breaking) and the corresponding Kondo temperature would be extremely high ( $T_K \gtrsim 300$  K). The nature of the resonance seems to lay in the combination of the rearrangement of the electronic structure at the Cr(001) surface (massively more states at the Fermi energy in contrast to bulk Cr) and the multi-orbital interaction effects, especially in the  $d_{z^2}$  and  $d_{xz/yz}$  orbitals. The interaction introduces two major effects: First, the spin dependent splitting of mainly the  $d_{xz/yz}$  orbitals and secondly, the appearance of quasiparticle peaks in  $d_{z^2}$  and  $d_{xz/yz}$  orbitals. We conclude that the resonance is a complex many-body effect in the  $d_{z^2}$  and  $d_{xz/yz}$  orbitals due to dynamic local-correlation effects. The low-energy resonance discussed here for temperatures  $T > 190$  K compares best to the low-energy resonance observed in (I)PES in Ref. [28] and displays a clear temperature dependence in our calculations. The relation of this resonance to the temperature dependent low-energy resonance reported in STM studies [109, 72] remains however unclear and would require calculations at low temperatures.

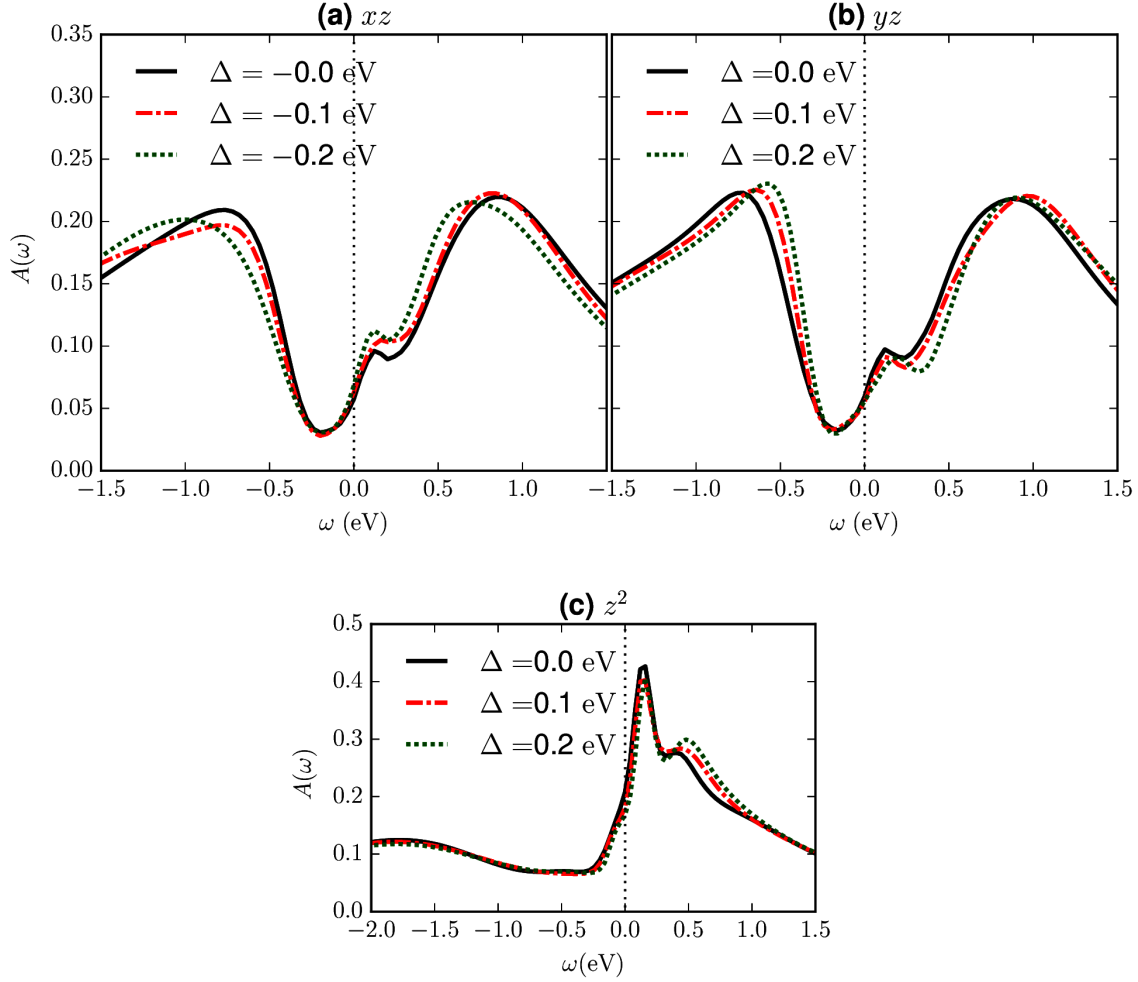


**Figure 5.13.:** (a) and (b): Spin averaged local density of states of the (a)  $d_{xz}$  orbital and (b) the  $d_{yz}$  orbital of the surface atom obtained from the solution of an AIM with the self-consistent hybridization function from DMFT at  $\beta = 40 \text{ eV}^{-1}$  and additional crystal field splitting of  $\Delta_{xz} = 0, -0.1, -0.2 \text{ eV}$  and  $\Delta_{yz} = 0, 0.1, 0.2 \text{ eV}$  with full, dashed and dotted lines. (c): Same for  $d_{z^2}$  orbital with crystal field of  $\Delta_{z^2} = 0, 0.1, 0.2 \text{ eV}$ .

### 5.4.3. Self-energy

In order to further understand the many-body properties of the Cr(001) surface, we investigate the behavior of the self-energy  $\Sigma(i\omega_n)$  and the quasiparticle weight  $Z$  for different orbitals, spins and layers. Here, we analyze the case of the experimental temperature  $\beta = 40 \text{ eV}^{-1}$  and the alternative double-counting scheme<sup>4</sup>. We start by comparing the self-energy of the surface atoms with that of the bulk atoms, presented in Fig. (5.14). For the surface, the imaginary part of the self-energy in the minority spin channel is nearly equally large for  $d_{z^2}$  and  $d_{yz/xz}$  orbitals. For the majority spin channel, the  $d_{yz/xz}$  and  $d_{xy}$  show the largest contribution. The  $d_{x^2-y^2}$  part of  $\text{Im } \Sigma$  is smallest for both spin channels. For all orbitals, the imaginary part of the self-energy approaches zero continuously, which indicates a Fermi liquid. In the case of the bulk atom (an atom of the fifth layer), the orbital differences are negligible for the minority spin channel. The orbital differences in the majority spin channel are similar, but smaller, than in the case of the surface.

To quantify the correlation effects for each layer, we calculate the quasiparticle weight  $Z$  for all orbitals and spin. The quasiparticle weight determines to which extent the concept of quasiparticles is actually valid, i.e., a Fermi surface exists.  $Z$  gives the jump of the occupation at the Fermi energy [145, 52]. Therefore,  $Z$  is bounded between  $Z = 1$  for non-interacting particles and  $Z = 0$  for non Fermi liquid systems. The quasiparticle weight  $Z$  is defined by

$$Z = \left[ 1 - \left. \frac{\partial \text{Re } \Sigma(\omega)}{\partial \omega} \right|_{\omega=0} \right]^{-1} \quad (5.5)$$

for a Fermi liquid, compare Ref. [142] for a derivation or Refs. [145, 47]. Following Ref. [12], we use

$$\left. \frac{\partial \text{Re } \Sigma(\omega)}{\partial \omega} \right|_{\omega=0} = \left. \frac{\text{Im } \Sigma(i\omega_n)}{\omega_n} \right|_{\omega_n \rightarrow 0} \quad (5.6)$$

to approximate  $Z$  with finite temperature results for the self-energy on Matsubara frequencies

$$Z \approx \left[ 1 - \frac{\text{Im } \Sigma(i\omega_{n=0})}{\omega_{n=0}} \right]^{-1}. \quad (5.7)$$

Fig. (5.15) shows the quasiparticle weight  $Z$  for all layers, orbitals and spins. The results directly correspond to the findings from the analysis of the imaginary part of

---

<sup>4</sup>The case of the trace double-counting is presented in the appendix (A.4).

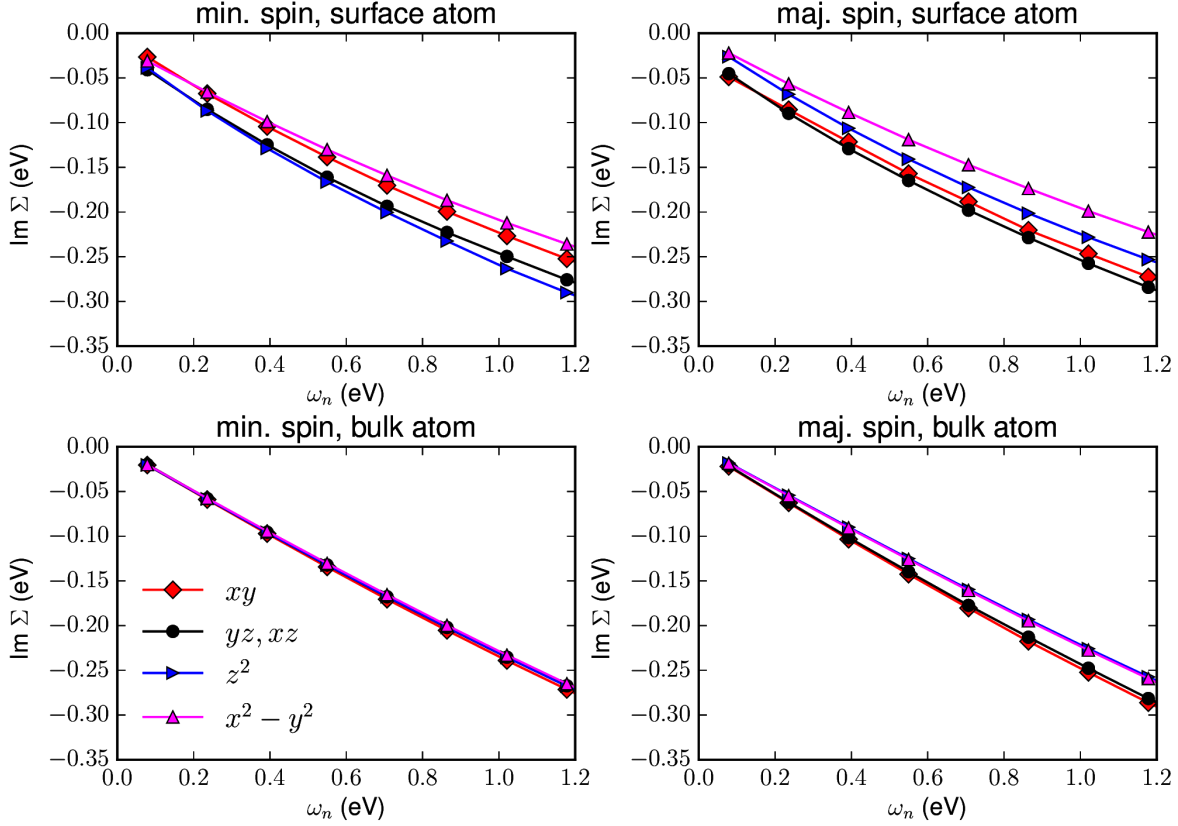


**Figure 5.14.:** Orbitally resolved imaginary part of the self-energy on Matsubara frequencies  $\omega_n$  for minority spin (left panels) and majority spin (right panels) for a surface atom (upper panels, atom of first layer) a bulk atom (lower panels, atom of fifth layer) simulated with alternative double counting and  $\beta = 40 \text{ eV}^{-1}$ .

the self-energy in Fig. (5.14). For all orbitals we observe a distinct trend of smaller quasiparticle weights at the surface than in the bulk. Strikingly, the atom of the second layer, shows the smallest correlation effects, apparent from the largest  $Z$ . At the surface, we find the smallest quasiparticle weight for the  $d_{z^2}$  and  $d_{yz/xz}$  orbitals for the minority spin and  $d_{xy}$  and  $d_{yz/xz}$  orbitals for the majority spin, in line with the analysis of the self energy. Interpreting the deviation of the quasiparticle weight from 1 as the amount of correlation effects, leads to a similar conclusion than the comparison between spectral functions from LSDA and DMFT. Those orbitals which show large differences to the LSDA treatment (cf. Fig. (5.8) and Fig. (5.12) for LSDA and DMFT spectra, respectively), show correspondingly low quasiparticle weight.

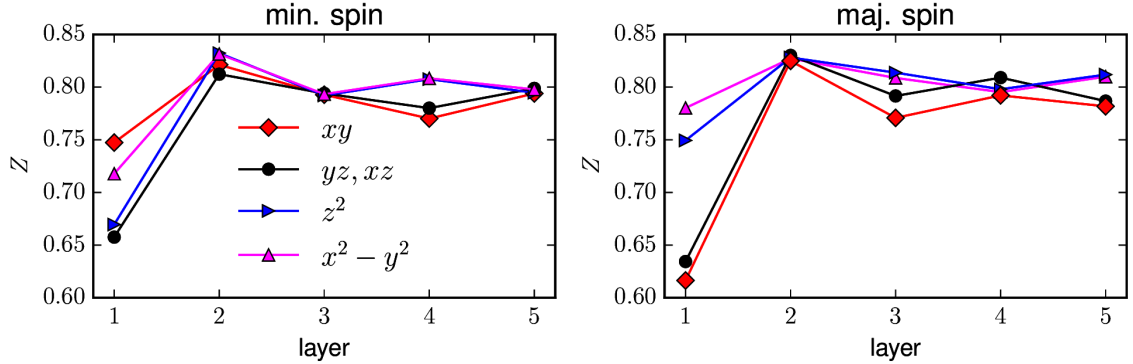


**Figure 5.15.:** Orbitaly resolved quasiparticle weight for atoms of different layers in the slab for minority spin (left panel) and majority spin (right panel) calculated for the alternative double counting and  $\beta = 40 \text{ eV}^{-1}$ . Layer 1 is the surface.

## 5.5. Conclusion

We have used the LDA+DMFT method to calculate the spectral function of the Cr(001) surface and have compared our results with experimental data on the spectral function at different temperatures. We have derived and chosen the parameters of the model based on ab-initio calculations. We could identify the main experimental features in our data and have found their orbital character to coincide with experimental findings. By the comparison of LSDA and DMFT calculations and an analysis of the DMFT spectrum by an artificial crystal field we could show that the resonance at the Fermi level is a many-body feature of mainly  $d_{z^2}$  and slightly  $d_{xz/yz}$  character. We could thus show that dynamic local-correlation effects play a key role to the electronic nature of the Cr(001) surface. The emergence of a pseudogap for inverse temperatures above  $\beta = 40 \text{ eV}^{-1}$  is in line with PES measurements but contradictory to STS measurements and its clarification needs more investigations.

## 6. Summary and outlook

In this thesis we have explored realistic models of low-dimensional correlated materials using many-body methods. We have investigated long-range interactions in Hubbard models, a method to approximate Anderson impurity models by exactly solvable effective models and the electronic structure of the Cr(001) surface.

Due to a small screening volume, long-range interactions cannot be neglected in low-energy lattice models (extended Hubbard models) for two-dimensional materials. This hinders the direct application of LDA+DMFT approaches to these materials, as only local interactions can be treated in single-site DMFT. To overcome this limitation, we have investigated the effect of long range interactions on the properties of the Hubbard model. To this end, we have introduced a variational method to map extended Hubbard models onto effective Hubbard models in Sec. (3). We have calculated the renormalization of the local interaction by non-local interaction terms and have thereby suggested a way to treat the more complicated extended Hubbard model by the rather well understood Hubbard model in an effective way. As pointed out above, this is of great importance in deriving low-energy models (i.e., Hubbard models) for real materials.

We could show that the local interaction is reduced by a weighted sum of the non-local terms. In the simplest approximation, the effective local interaction  $\tilde{U}$  for half-filled models reads  $\tilde{U} = U - V$ , where  $U$  is the local interaction and  $V$  the nearest-neighbor interaction in the extended Hubbard model. By examining Hubbard models on different geometries we could identify universal behaviors of the renormalization in terms of the effective system. For the case of ab-initio derived models for graphene and silicene, we could show that non-local interactions lead to a reduction of the local interaction by a factor of two. This clarifies which parameters to use in order to describe graphene and silicene in terms of a Hubbard model in an ab-initio fashion. Publications using our prescription are, e.g., Refs. [211, 132, 212, 170, 138].

For heavily doped (nearly empty or nearly full) systems we could show that the local interaction is increased by the non-local terms, which we understand in terms of Wigner crystallization. We have benchmarked the quality of the mapping using a six-site Hubbard model, which revealed that spin-related properties, in contrast to charge related properties, are well described in a large doping range around half filling.

We have explored different possibilities to calculate the renormalization and have concluded that for weak effective interaction strengths, the random phase approximation leads to satisfactory results, while Hartree-Fock leads to poor results for all interaction strengths.

Other authors tested the reliability of our approach for two-dimensional extended Hubbard models with GW+DMFT [14], EDMFT [88] and DQMC [214]. An additional method worth considering for benchmarking is the dual boson method [221]. Our scheme has inspired related work on correlated systems: The authors of Ref. [198] calculated the renormalization of interaction within a  $d$  shell by interactions between the  $d$  and  $p$  shell in multi-orbital models of transition metals.

Sec. (4) was devoted to the so-called bath discretization problem in exact diagonalization problems. We have introduced a variational scheme, which we call variational exact diagonalization method, to map an Anderson impurity model with an arbitrary number of bath sites to an effective model, which is separated into a non-interacting part and an interacting part with only a few sites (typically less than 10). The effective model is thus exactly solvable.

We have benchmarked the method's ability to reproduce ground-state properties by treating exactly solvable test cases. We have found that it outperforms Hartree-Fock theory and conventional approaches to the bath-discretization problem. By introducing methods to reduce the large amount of parameters to be optimized in the case of realistic methods, we could apply our method to a five-orbital model of Co in Cu. A benchmark against a QMC treatment of the same model revealed improvement over Hartree-Fock and conventional bath-discretization methods. Introducing a simplified scheme to find effective models in the presence of spin-orbit coupling and magnetic fields, we could set up models for Fe atoms on alkali surface. We have calculated magnetization curves, compared them to experimental data and could thereby reveal the mechanisms of quenching of the orbital and spin induced by hybridization effects: With increasing hybridization strength the orbital moment is quenched faster than the spin moment.

To date, an open issue of the variational exact diagonalization method is the aforementioned case of spin-orbit coupling. A consistent scheme to find optimal effective models under the influence of spin-orbit coupling is currently not implemented. The implementation and benchmarks are, however, currently work in progress. For the future, a user-friendly version of the developed code for the purpose of making it publicly available is also highly desirable.

The variational nature of the method leads to more accurate (free) energy estimates than unrestricted Hartree-Fock. Thus, the variational exact diagonalization method could be used to improve LDA+U total energy schemes. The method has to be further

---

investigated in order to understand under which circumstances spectra calculated from the effective model are satisfactory. This could in principle lead to the application of the variational exact diagonalization method for dynamical mean-field theory.

In Sec. (5) we have studied the electronic properties of the Cr(001) surface. Our main goal was to explain photoemission and inverse photoemission spectra which show an unexplained feature near the Fermi energy with  $d_{z^2}$  symmetry. To this end, we have combined density functional theory and dynamical mean-field theory in the LDA+DMFT framework to treat the electronic structure of the surface including local correlation effects at the experimental temperature realistically.

We have achieved a satisfactory agreement with the experimental data and concluded that the peak at the Fermi energy is due to a complicated interplay of electronic single-particle reconstruction at the surface and strong local interactions. The low-energy feature is composed of mainly  $d_{z^2}$  but also  $d_{xz/yz}$  orbitals. We have tested the nature of the feature by studying Anderson impurity models derived from the DMFT, but with broken crystal-field symmetries. We have found that both the  $d_{z^2}$  and the  $d_{xz/yz}$  contribution of the peak are robust against such shifts of single-particle energies. We have concluded that the peak at the Fermi energy is indeed a many-body feature.

So far, we have only investigated  $\mathbf{k}$ -independent features of the spectral function. It is intriguing to calculate  $\mathbf{k}$ -resolved spectral functions and to identify the parts of the Brillouin zone which are important for correlation effects. A comparison of calculated and measured Fermi surfaces is currently work in progress.

An open question which deserves further investigations is the evolution of the low-energy peak with the temperature. While scanning tunneling spectroscopy shows rather weak dependence of the spectra's shape on temperature, photoemission measurements reveal that the feature disappears for  $50 \text{ K} \lesssim T \lesssim 150 \text{ K}$  and reappears as an even sharper feature below  $T \sim 50 \text{ K}$ . Due to computational limitations of the methods we have used, clarifying these contradictory results is currently not possible. Here, different methods such as exact diagonalization could help.

Overall, we could proceed in closing the gap between ab-initio methods and model based methods incorporating interaction effects. The ultimate goal in this journey is specified in the title of the DFG research group 1346: "Dynamical Mean-Field Approach with Predictive Power for Strongly Correlated Materials". The predictive power of LDA+DMFT methods is a high aim which is certainly not reached yet, due to unsolved principle issues such as the double-counting problem and practical issues such as computational limitations, e.g., in incorporating  $\mathbf{k}$ -dependent self-energies in DMFT approaches. As pointed out in the outlook of Ref. [96], the current state of the LDA+DMFT approach is vastly successful in describing properties of many correlated materials, but rather as a tool for a posteriori explanations. We hope that the develop-

## 6. *Summary and outlook*

---

ments presented in this work, generalizing the LDA+DMFT approach to nanoscopic systems and finding simplified models, are a valuable step on the journey to predictive methods to strongly correlated materials.

# A. Appendix

## A.1. Smoothing QMC data: Savitzky-Golay filter

The noise in correlation functions obtained from DQMC calculations in Sec. (3) is problematic for the calculation of derivatives with respect to  $\tilde{U}$ . We compare four different approaches to overcome the noise. First, the direct calculation of finite differences. Second, taking the finite difference of data which is smoothed by a moving average. Third, fitting the data globally with a high order polynomial and taking the derivative analytically. Fourth, fitting data locally by low order polynomials and taking the derivatives analytically. We shortly introduce the last method. Consider numerical data  $F_i$  on a grid  $x_i$ . We introduce a window  $\Delta x$  and the order of polynomials  $p$ . The smoothed derivative  $f'(x)$  is defined by the function  $f(x)$  which reads

$$f(x) = p(x), \tag{A.1}$$

where  $p(x)$  is the least square fit of a  $p$ th order polynomial to the data  $F_i$  selected by  $|x_i - x| < \Delta x$ . This approach is based on the Savitzky-Golay filter (Ref. [191]). We analyze the performance of the different strategies for the example of the local correlation function  $\langle n_{0\uparrow} n_{0\downarrow} \rangle$  for the case of the square lattice. The results are presented in Fig. (A.1). The simple finite difference approach amplifies the noise of the data considerably. The polynomial fit of the order 13 leads to very smooth data but spurious oscillations for small  $\tilde{U}$ . The moving average over 30 data points leads to a strong reduction of the noise. Considering smoothness, the Savitzky-Golay filter with a window size of  $\Delta\tilde{U} = 1.5$  and cubic polynomials leads results comparable to the global fit and better results than the moving average, due to the larger averaging window. No spurious oscillations appear in the case of the local fitting. In conclusion, the Savitzky-Golay filter performs best in dealing with derivatives from noisy data and is thus used in this work to analyze derivatives on large ranges of  $\tilde{U}$ .

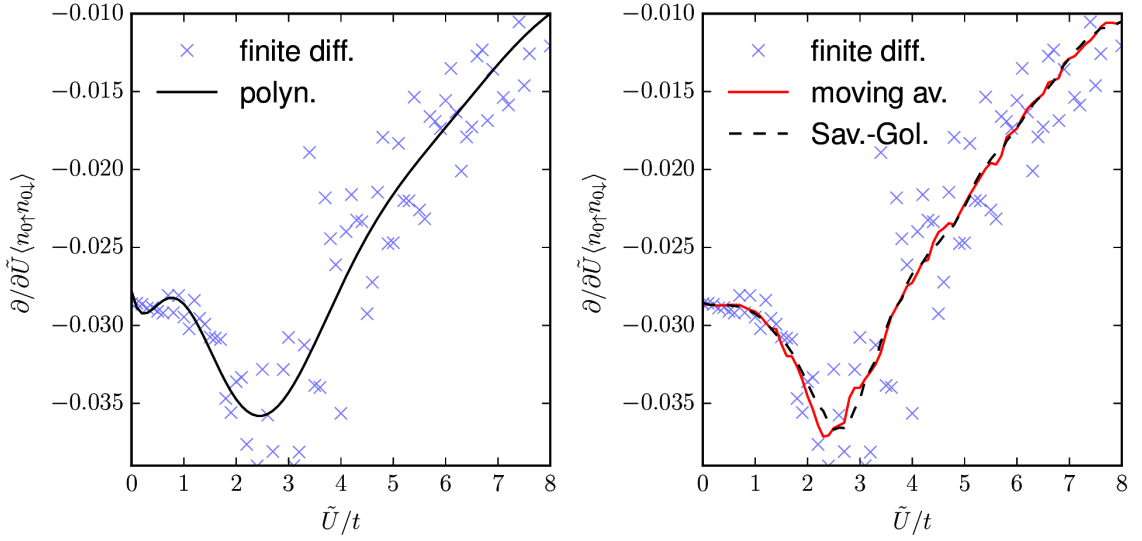


**Figure A.1.:** Comparison of different strategies to obtain smooth derivatives of correlation functions calculated with DQMC for the example of the local charge correlation. (i) The data are fitted by a 13th order polynomial which is differentiated analytically (left panel, solid line). (ii) The data are smoothed by a moving average of 30 data points (right panel, solid line). (iii) The derivative of Savitzky-Golay fits are taken analytically with a window size of  $\Delta\tilde{U} = 1.5$  and cubic polynomials. The results from finite differences are depicted as crosses.

## A.2. In depth benchmark of correlation functions for benzene

Here, we present benchmarks of effective models with purely local interactions for modified benzene (see Sec. (3.8)) for fillings away from half filling. For fillings far from half filling ( $n = 2, 10$ ), the deviations of the spin correlation functions are larger than for the half filled case. For all other fillings, ( $n = 3 - 9$ ), but especially for  $n = 5, 7$ , the deviations are similarly good as in the half filled case.

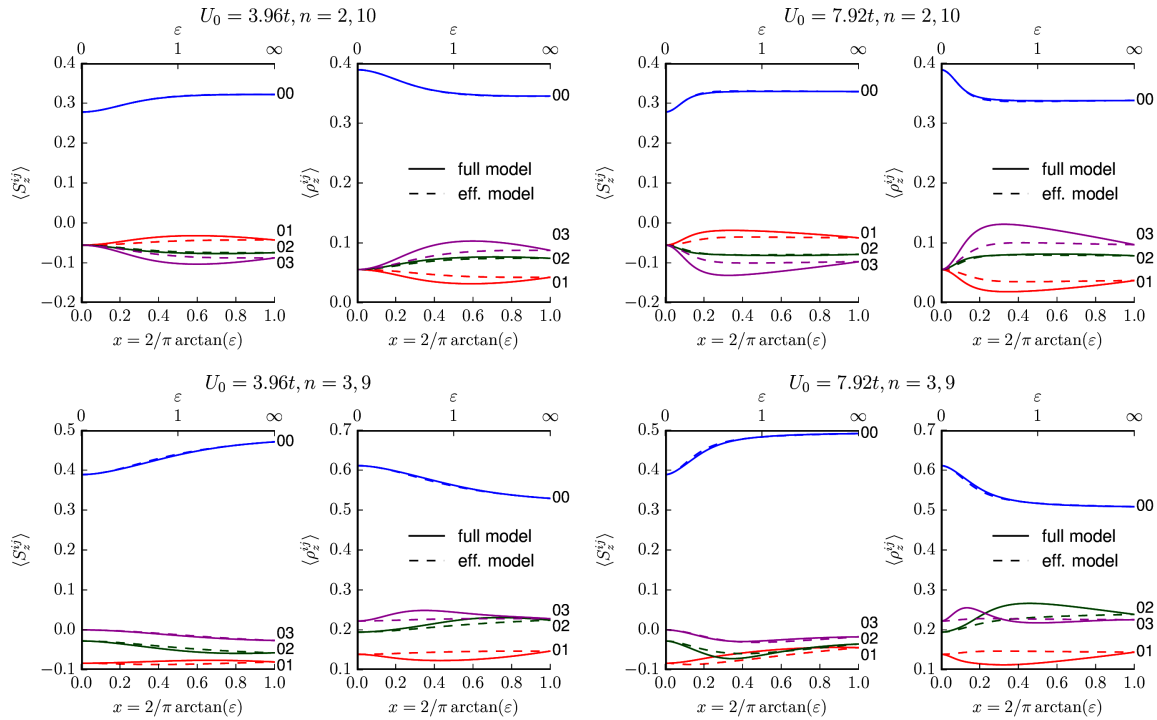


**Figure A.2.:** Comparison of the spin and density correlation function for modified benzene at fillings ( $n = 2, 10$  and  $n = 3, 9$ ) as functions of the screening for the extended Hubbard model (continuous lines) and the effective model (broken lines). The left panels show results for  $U = 3.96t$ , the right panels show results for  $U = 7.92t$ . From top to bottom, the panels show results for different fillings.

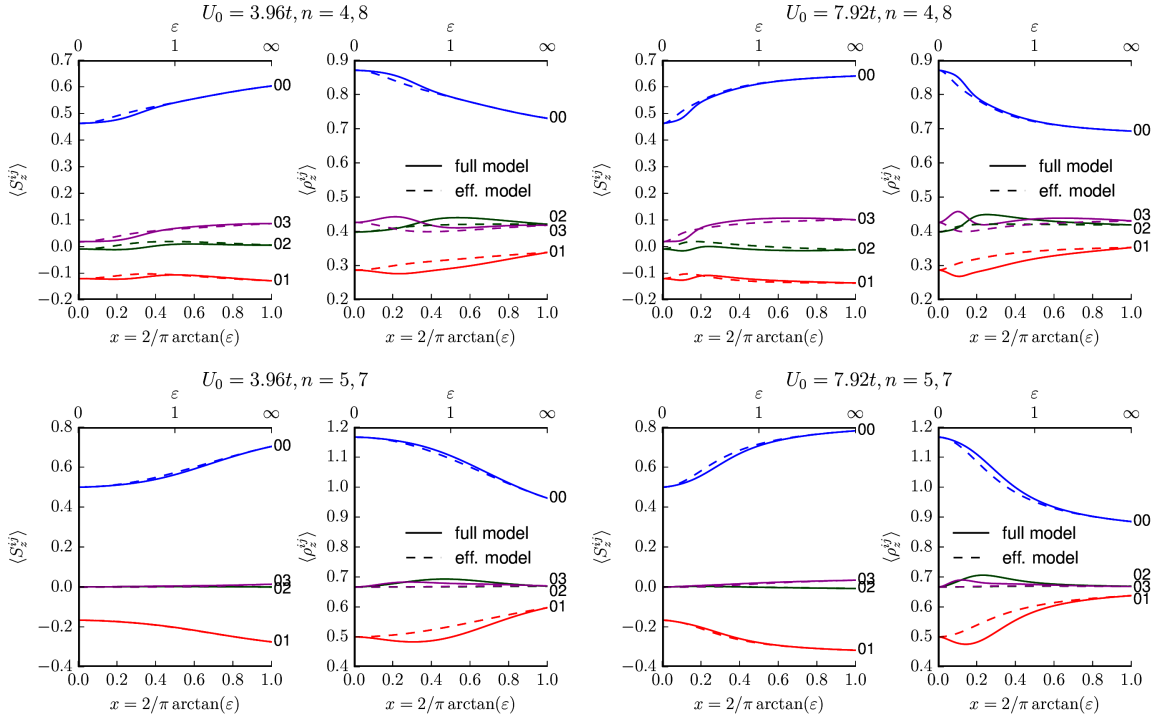


**Figure A.3.:** Comparison of the spin and density correlation function for modified benzene at fillings ( $n = 4, 8$  and  $n = 5, 7$ ) as functions of the screening for the extended Hubbard model (continuous lines) and the effective model (broken lines). The left panels show results for  $U = 3.96t$ , the right panels show results for  $U = 7.92t$ . From top to bottom, the panels show results for different fillings.

### A.3. Spectral function of a single-orbital AIM

Fig. (A.4) shows the evolution of the impurity spectral function of an AIM defined by  $\varepsilon_d = -2.0$ ,  $U = 4$ ,  $\varepsilon_k = -1.4, -1.0, -0.6, -0.2, 0.2, 0.6$  with increasing hybridization strength  $V_k$ . The spectral function is calculated from the Lehmann representation (Eq. (4.10)) at a temperature of  $\beta = 3200$  and a broadening of  $\delta = 0.1$ . For small hybridizations the spectrum shows major peaks approximately at the atomic excitation energies and minor peaks at the one-particle energies of the bath at  $\varepsilon_k$ . At intermediate hybridization strengths around  $V_k = 0.3$  we observe a resonance at the Fermi energy, resembling a Kondo-resonance. For large hybridization strengths the impurity and bath are fully coupled with two peaks corresponding to a bonding and an anti-bonding orbital.

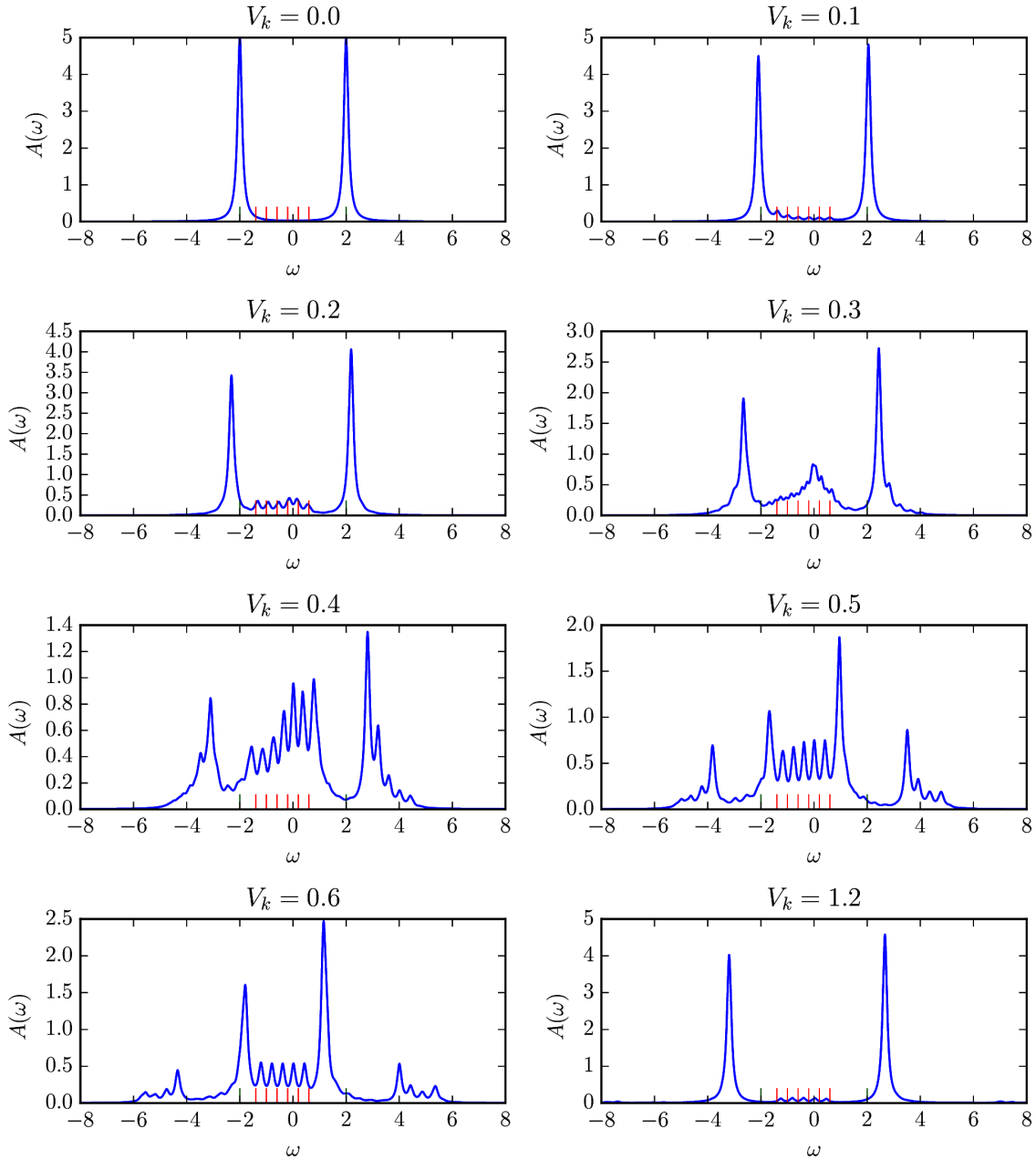


**Figure A.4.:** Evolution of the spectral function of a one-orbital AIM with increasing hybridization strength. The positions of the bath sites  $\varepsilon_k$  are marked by red lines. The excitation energies of the atomic limit ( $V_k = 0$ ) at  $-2.0$  and  $2.0$  are marked by green lines. An animated version is available at <http://pogcha.bplaced.net/physik/?p=4>.

## A.4. Self-energy of Cr(001) for the case of trace double counting

In line with the analysis of the self-energy for the simulations with the alternative double counting in Sec. (5.4.3), we investigate the self-energy for the trace double counting at  $\beta = 40 \text{ eV}^{-1}$ . The orbitally and spin resolved imaginary parts of the self-energy for the surface atom and a bulk atom (an atom of the fifth layer) are presented in Fig. (A.5). The result is very similar compared to that of the alternative double counting (Fig. (5.14)). Differences occur in the behavior of the  $d_{x^2-y^2}$  orbital for the minority spin of the surface atom, which is considerably larger. It is the largest contribution of all orbitals. The majority spin of the bulk atom also shows differences: While in the case of the alternative double counting the contribution of the  $d_{yz/xz}$  and  $d_{xy}$  orbitals are largest, in the case of the trace double counting the  $d_{z^2}$  and  $d_{x^2-y^2}$  orbitals dominate at small Matsubara frequencies.

We clarify the spatial behavior of the self-energy by investigating the quasiparticle weight  $Z$  for all layers, presented in the lower panels of Fig. (A.5). The  $d_{yz,xz}$  and  $d_{xy}$  orbitals show a similar behavior than in the case of the alternative double counting: The quasiparticle weight is smallest at the surface. However, the other orbitals, especially  $d_{x^2-y^2}$ , show large spatial oscillations.

In conclusion, the self-energy coincides up to some details for both double-counting schemes.

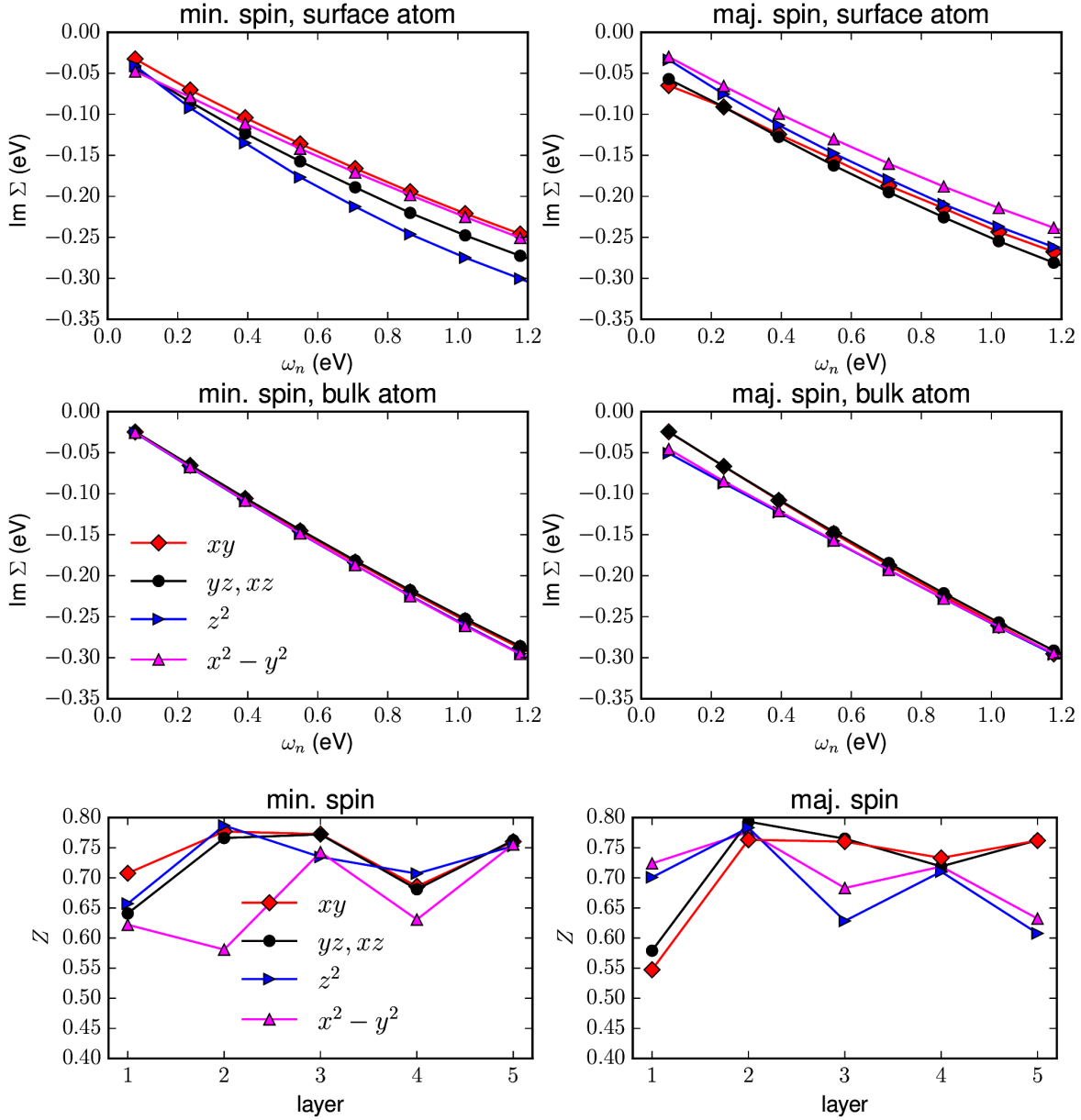


**Figure A.5.:** Orbitaly resolved imaginary part of the self-energy for minority spin (left panels) and majority spin (right panels) for a surface atom (upper panels, atom of first layer) a bulk atom (center panels, atom of fifth layer) simulated with trace double counting and  $\beta = 40 \text{ eV}^{-1}$ . Lower panels: Quasiparticle weight for atoms of all layers in the slab calculated for trace double counting and  $\beta = 40 \text{ eV}^{-1}$ . Layer 1 is the surface.



# List of publications

## In peer reviewed journals

- M. Schüler, M. Rösner, T. O. Wehling, A. I. Lichtenstein, M. I. Katsnelson, *Optimal Hubbard models for materials with nonlocal Coulomb interactions: graphene, silicene and benzene*, Phys. Rev. Lett. **111** (2013), 036601
- M. Schüler, C. Renk, T. O. Wehling, *Variational exact diagonalization method for Anderson impurity models*, Phys. Rev. B **91** (2015) 235142

## In preprint

- S. Bhandary, M. Schüler, P. Thunström, I. di Marco, B. Brena, O. Eriksson, T. O. Wehling, B. Sanyal, *Correlated electron behavior of metalorganic molecules: insights from density functional theory combined with many-body effects using exact diagonalization*, arXiv:1506.07973 (2015), accepted in Phys. Rev. B. (2016)
- M. Schüler, S. Barthel, M. Karolak, A. I. Poteryaev, A. I. Lichtenstein, M. I. Katsnelson, G. Sangiovanni, T. O. Wehling, *Many-body effects on Cr(001) surfaces: An LDA+DMFT study*, arXiv:1512.01181 (2015), accepted in Phys. Rev. B. (2016)
- M. Vondráček, J. Honolka, L. Cornils, J. Warmuth, L. Zhou, A. Kamlapure, A. A. Khajetoorians, R. Wiesendanger, J. Wiebe, M. Michiardi, M. Bianchi, J. Miwa, L. Barreto, P. Hofmann, C. Piamonteze, J. Minár, S. Mankovsky, St. Borek, H. Ebert, M. Schüler, T. O. Wehling, J.-L. Mi, B.-B. Iversen, *Non-magnetic ground state of Ni adatoms on Te-terminated bismuth chalcogenide topological insulators*, arXiv:1603.09689 (2016)
- S. Ulstrup, M. Schüler, M. Bianchi, F. Fromm, C. Raidel, T. Seyller, T. O. Wehling, P. Hofmann, *Manifestation of nonlocal electron-electron interaction in graphene*, arXiv:1604.00496 (2016)



# List of changes

The published version of this thesis includes slight corrections to the version originally handed in on April 27th, 2016.

Next to corrections concerning the orthography, which are not listed in detail, the following changes in equations have been made:

- In Eq. (2.86), the first occurrence of  $p_i$  was formerly  $p_j$ . This also concerns the  $\sum_i T_{ji} p_i$  directly above the equation.
- The signs of the denominators in Eqs. (2.126) and (2.127) have been changed.
- The sign of the second exponential in Eq. (4.10) has been changed.

The following changes concerning citations have been done:

- On page 8 and 13, references to [24, 60] have been added next to [152]. Similarly, on page 20, the reference to [152] has been replaced by [60].
- On page 84, a reference to [156] has been added.

Other changes are:

- Fig. (4.3) has been split into four panels instead of two.
- On page 62, “While the expression for the eigenstates...” has been changed to “While the expression for the eigenvalues...”.
- On page 118, “...from weak (FeLi) to strong (FeCs) hybridization:” has been changed to “...from strong (FeLi) to weak (FeCs) hybridization:”.



# Bibliography

Years are clickable links to online versions of the articles.

- [1] G. Adhikary, R. Bindu, S. Patil, and K. Maiti. *Complex evolution of the electronic structure of Cr with temperature*. Appl. Phys. Lett., **100** (2012), 042401.
- [2] L. A. Agapito, A. Ferretti, A. Calzolari, S. Curtarolo, and M. Buongiorno Nardelli. *Effective and accurate representation of extended Bloch states on finite Hilbert spaces*. Phys. Rev. B, **88** (2013), 165127.
- [3] L. A. Agapito, S. Ismail-Beigi, S. Curtarolo, M. Fornari, and M. B. Nardelli. *Accurate tight-binding Hamiltonian matrices from ab initio calculations: Minimal basis sets*. Phys. Rev. B, **93** (2016), 035104.
- [4] G. Allan. *Surface electronic structure of antiferromagnetic chromium*. Surface Science, **74** (1978), 79 .
- [5] A. Altland and B. Simons. *Condensed matter field theory*. Cambridge University Press, Cambridge ; New York, 2nd ed edition. ISBN 978-0-521-76975-4 (2010).
- [6] B. Amadon, F. Lechermann, A. Georges, F. Jollet, T. O. Wehling, and A. I. Lichtenstein. *Plane-wave based electronic structure calculations for correlated materials using dynamical mean-field theory and projected local orbitals*. Phys. Rev. B, **77** (2008), 205112.
- [7] P. W. Anderson. *Localized Magnetic States in Metals*. Phys. Rev., **124** (1961), 41.
- [8] V. I. Anisimov, F. Aryasetiawan, and A. I. Lichtenstein. *First-principles calculations of the electronic structure and spectra of strongly correlated systems: the LDA + U method*. J. Phys.: Condens. Matter, **9** (1997), 767.
- [9] V. I. Anisimov and O. Gunnarsson. *Density-functional calculation of effective Coulomb interactions in metals*. Phys. Rev. B, **43** (1991), 7570.
- [10] V. I. Anisimov, I. V. Solovyev, M. A. Korotin, M. T. Czyżyk, and G. A. Sawatzky. *Density-functional theory and NiO photoemission spectra*. Phys. Rev. B, **48** (1993), 16929.

- [11] A. Arrott, S. A. Werner, and H. Kendrick. *Neutron-Diffraction Study of Dilute Chromium Alloys with Iron*. Phys. Rev., **153** (1967), 624.
- [12] L.-F. Arsenault, P. Sémon, and A.-M. S. Tremblay. *Benchmark of a modified iterated perturbation theory approach on the fcc lattice at strong coupling*. Physical Review B, **86** (2012), 085133.
- [13] F. Aryasetiawan, M. Imada, A. Georges, G. Kotliar, S. Biermann, and A. I. Lichtenstein. *Frequency-dependent local interactions and low-energy effective models from electronic structure calculations*. Phys. Rev. B, **70** (2004), 195104.
- [14] T. Ayral, S. Biermann, and P. Werner. *Screening and Non-local Correlations in the Extended Hubbard Model from Self-Consistent Combined GW and Dynamical Mean Field Theory*. arXiv:1210.2712, (2012).
- [15] C. J. Ballhausen. *Ligand field theory*. McGraw Hill (1962).
- [16] K. S. D. Beach. *Identifying the maximum entropy method as a special limit of stochastic analytic continuation*. arXiv:cond-mat/0403055, (2004). ArXiv: cond-mat/0403055.
- [17] H. Bethe. *Zur Theorie der Metalle*. Z. Physik, **71** (1931), 205.
- [18] S. Biermann, A. Dallmeyer, C. Carbone, W. Eberhardt, C. Pampuch, O. Rader, M. I. Katsnelson, and A. I. Lichtenstein. *Observation of Hubbard bands in  $\gamma$ -manganese*. Jetp Lett., **80** (2004), 612.
- [19] G. Bihlmayer, T. Asada, and S. Blügel. *Electronic and magnetic structure of the (001) surfaces of V, Cr, and V/Cr*. Phys. Rev. B, **62** (2000), R11937.
- [20] R. Blankenbecler, D. J. Scalapino, and R. L. Sugar. *Monte Carlo calculations of coupled boson-fermion systems. I*. Phys. Rev. D, **24** (1981), 2278.
- [21] P. E. Blöchl. *Projector augmented-wave method*. Phys. Rev. B, **50** (1994), 17953.
- [22] N. N. Bogoliubov. Dokl. Akad. Nauk SSSR, **119** (1958), 244.
- [23] M. Born and R. Oppenheimer. *Zur Quantentheorie der Molekeln*. Ann. Phys., **389** (1927), 457.
- [24] U. Brandt and C. Mielsch. *Thermodynamics and correlation functions of the Falicov-Kimball model in large dimensions*. Zeitschrift für Physik B Condensed Matter, **75** (1989), 365.
- [25] J. Braun, J. Minár, H. Ebert, M. I. Katsnelson, and A. I. Lichtenstein. *Spectral Function of Ferromagnetic 3d Metals: A Self-Consistent LSDA+DMFT Approach Combined with the One-Step Model of Photoemission*. Phys. Rev. Lett., **97** (2006), 227601.

- 
- [26] H. Bruus and K. Flensberg. *Many-body quantum theory in condensed matter physics: an introduction*. Oxford Univ. Press, Oxford. ISBN 978-0-19-856633-5 (2007).
- [27] R. Bryan. *Maximum entropy analysis of oversampled data problems*. European Biophysics Journal, **18** (1990), 165.
- [28] M. Budke, T. Allmers, M. Donath, and M. Bode. *Surface state vs orbital Kondo resonance at Cr(001): Arguments for a surface state interpretation*. Phys. Rev. B, **77** (2008), 233409.
- [29] R. Bulla. *Zero Temperature Metal-Insulator Transition in the Infinite-Dimensional Hubbard Model*. Phys. Rev. Lett., **83** (1999), 136.
- [30] R. Bulla, T. Costi, and T. Pruschke. *The numerical renormalization group method for quantum impurity systems*. arXiv:cond-mat/0701105, (2007). Rev. Mod. Phys. 80, 395 (2008).
- [31] R. J. Bursill, C. Castleton, and W. Barford. *Optimal parametrisation of the Pariser–Parr–Pople Model for benzene and biphenyl*. Chemical Physics Letters, **294** (1998), 305.
- [32] M. Caffarel and W. Krauth. *Exact diagonalization approach to correlated fermions in infinite dimensions: Mott transition and superconductivity*. Phys. Rev. Lett., **72** (1994), 1545.
- [33] C. Carbone, M. Veronese, P. Moras, S. Gardonio, C. Grazioli, P. H. Zhou, O. Rader, A. Varykhalov, C. Krull, T. Balashov, A. Mugarza, P. Gambardella, S. Lebègue, O. Eriksson, M. I. Katsnelson, and A. I. Lichtenstein. *Correlated Electrons Step by Step: Itinerant-to-Localized Transition of Fe Impurities in Free-Electron Metal Hosts*. Phys. Rev. Lett., **104** (2010), 117601.
- [34] P. Carra, B. T. Thole, M. Altarelli, and X. Wang. *X-ray circular dichroism and local magnetic fields*. Phys. Rev. Lett., **70** (1993), 694.
- [35] A. H. Castro Neto, F. Guinea, N. M. R. Peres, K. S. Novoselov, and A. K. Geim. *The electronic properties of graphene*. Rev. Mod. Phys., **81** (2009), 109.
- [36] D. M. Ceperley and B. J. Alder. *Ground State of the Electron Gas by a Stochastic Method*. Phys. Rev. Lett., **45** (1980), 566.
- [37] L. Chioncel, L. Vitos, I. A. Abrikosov, J. Kollár, M. I. Katsnelson, and A. I. Lichtenstein. *Ab initio electronic structure calculations of correlated systems: An EMTO-DMFT approach*. Phys. Rev. B, **67** (2003), 235106.
- [38] C. L. Cleveland and R. A. Medina. *Obtaining a Heisenberg Hamiltonian from the Hubbard model*. American Journal of Physics, **44** (1976), 44.

- [39] M. Cococcioni and S. de Gironcoli. *Linear response approach to the calculation of the effective interaction parameters in the LDA + U method*. Phys. Rev. B, **71** (2005), 035105.
- [40] T. A. Costi. *Kondo Effect in a Magnetic Field and the Magnetoresistivity of Kondo Alloys*. Phys. Rev. Lett., **85** (2000), 1504.
- [41] T. S. Cubitt, D. Perez-Garcia, and M. M. Wolf. *Undecidability of the spectral gap*. Nature, **528** (2015), 207.
- [42] G. Czycholl. *Theoretische Festkörperphysik: Von den klassischen Modellen zu modernen Forschungsthemen*. Springer-Lehrbuch. Springer, Berlin, 3., aktualisierte Aufl. edition. ISBN 3540747893 and 978-3-540-74789-5 (2008).
- [43] M. T. Czyżyk and G. A. Sawatzky. *Local-density functional and on-site correlations: The electronic structure of  $\text{La}_2\text{CuO}_4$  and  $\text{LaCuO}_3$* . Phys. Rev. B, **49** (1994), 14211.
- [44] F. M. F. de Groot. *X-ray absorption and dichroism of transition metals and their compounds*. Journal of Electron Spectroscopy and Related Phenomena, **67** (1994), 529.
- [45] F. M. F. de Groot, J. C. Fuggle, B. T. Thole, and G. A. Sawatzky. *2 p x-ray absorption of 3 d transition-metal compounds: An atomic multiplet description including the crystal field*. Phys. Rev. B, **42** (1990), 5459.
- [46] H. De Raedt and W. von der Linden. *Quantum Lattice Problems*. In K. Binder, editor, *The Monte Carlo Method in Condensed Matter Physics*, volume 71 of *Topics in Applied Physics*. Springer, Berlin (1992).
- [47] S. Doniach and E. H. Sondheimer. *Green's Functions for Solid State Physicists*. Imperial College Press. ISBN 978-1-86094-080-4 (1998).
- [48] N. D. Drummond, V. Zólyomi, and V. I. Fal'ko. *Electrically tunable band gap in silicene*. Phys. Rev. B, **85** (2012), 075423.
- [49] Eder, Robert. *Multiplets in Transition Metal Ions*. In Pavarini, Eva and Koch, Erik and Anders, Frithjof and Jarrell, Mark, editor, *Correlated electrons: from models to materials*, Schriften des Forschungszentrums Jülich. Reihe Modeling and simulation. Forschungszentrum Jülich GmbH, Institute for Advanced Simulation (2012).
- [50] T. Eelbo, M. Waśniowska, P. Thakur, M. Gyamfi, B. Sachs, T. O. Wehling, S. Forti, U. Starke, C. Tieg, A. I. Lichtenstein, and R. Wiesendanger. *Adatoms and Clusters of 3d Transition Metals on Graphene: Electronic and Magnetic Configurations*. Phys. Rev. Lett., **110** (2013), 136804.
- [51] F. H. L. Eßler and H. Frahm. *Density correlations in the half-filled Hubbard model*. Phys. Rev. B, **60** (1999), 8540.

- 
- [52] P. Fazekas. *Lecture Notes on Electron Correlation and Magnetism*. Number v. 5 in Series in Modern Condensed Matter Physics. World Scientific Publishing Company. ISBN 978-981-02-2474-5 (1999).
- [53] R. P. Feynman. *Statistical Mechanics*. Benjamin, Reading Mass. (1972).
- [54] A. Flesch, E. Gorelov, E. Koch, and E. Pavarini. *Multiplet effects in orbital and spin ordering phenomena: A hybridization-expansion quantum impurity solver study*. Phys. Rev. B, **87** (2013), 195141.
- [55] R. H. Friend, R. W. Gymer, A. B. Holmes, J. H. Burroughes, R. N. Marks, C. Taliani, D. D. C. Bradley, D. A. D. Santos, J. L. Brédas, M. Lögdlund, and W. R. Salaneck. *Electroluminescence in conjugated polymers*. Nature, **397** (1999), 121.
- [56] S. Fuchs, T. Pruschke, and M. Jarrell. *Analytic continuation of quantum Monte Carlo data by stochastic analytical inference*. Phys. Rev. E, **81** (2010), 056701.
- [57] P. Gambardella, S. S. Dhesi, S. Gardonio, C. Grazioli, P. Ohresser, and C. Carbone. *Localized Magnetic States of Fe, Co, and Ni Impurities on Alkali Metal Films*. Phys. Rev. Lett., **88** (2002), 047202.
- [58] S. Gardonio, M. Karolak, T. O. Wehling, L. Petaccia, S. Lizzit, A. Goldoni, A. I. Lichtenstein, and C. Carbone. *Excitation Spectra of Transition-Metal Atoms on the Ag (100) Surface Controlled by Hund's Exchange*. Physical Review Letters, **110** (2013), 186404.
- [59] F. Gebhard. *The Mott metal-insulator transition*. Springer, Berlin. ISBN 3-540-61481-8 (1997).
- [60] A. Georges and G. Kotliar. *Hubbard model in infinite dimensions*. Physical Review B, **45** (1992), 6479.
- [61] A. Georges, G. Kotliar, W. Krauth, and M. J. Rozenberg. *Dynamical mean-field theory of strongly correlated fermion systems and the limit of infinite dimensions*. Rev. Mod. Phys., **68** (1996), 13.
- [62] Graham Woan. *The Cambridge handbook of physics formulas*. Cambridge Univ. Press, Cambridge [u.a.]. ISBN 0521573491 and 0521575079. 219 S ; 26 cm : Ill., graph. Darst (2000).
- [63] D. R. Grempel. *Surface magnetic ordering in chromium*. Physical Review B, **24** (1981), 3928.
- [64] N. Grewe and F. Steglich. *Handbook on the Physics and Chemistry of Rare Earths*. Vol. 14 North-Holland, Amsterdam, (1991), 343.

- [65] S.-J. Gu, S.-S. Deng, Y.-Q. Li, and H.-Q. Lin. *Entanglement and Quantum Phase Transition in the Extended Hubbard Model*. Physical Review Letters, **93** (2004), 086402.
- [66] E. Gull, P. Werner, S. Fuchs, B. Surer, T. Pruschke, and M. Troyer. *Continuous-time quantum Monte Carlo impurity solvers*. Computer Physics Communications, **182** (2011), 1078.
- [67] S. F. Gull and G. J. Daniell. *Image reconstruction from incomplete and noisy data*. Nature, **272** (1978), 686.
- [68] O. Gunnarsson, O. K. Andersen, O. Jepsen, and J. Zaanen. *Density-functional calculation of the parameters in the Anderson model: Application to Mn in CdTe*. Phys. Rev. B, **39** (1989), 1708.
- [69] O. Gunnarsson and K. Schönhammer. *Electron spectroscopies for Ce compounds in the impurity model*. Phys. Rev. B, **28** (1983), 4315.
- [70] Gunnarsson, Olle. *Strongly Correlated Electrons: Estimate of Model Parameters*. In Pavarini, Eva and Koch, Erik and Anders, Frithjof and Jarrell, Mark, editor, *Correlated electrons: from models to materials*, Schriften des Forschungszentrums Jülich. Reihe Modeling and simulation. Forschungszentrum Jülich GmbH, Institute for Advanced Simulation (2012).
- [71] P. Habibi, C. Barreteau, and A. Smogunov. *Electronic and magnetic structure of the Cr(001) surface*. J. Phys.: Condens. Matter, **25** (2013), 146002.
- [72] T. Hänke, M. Bode, S. Krause, L. Berbil-Bautista, and R. Wiesendanger. *Temperature-dependent scanning tunneling spectroscopy of Cr(001): Orbital Kondo resonance versus surface state*. Phys. Rev. B, **72** (2005), 085453.
- [73] J. P. Hannon, G. T. Trammell, M. Blume, and D. Gibbs. *X-Ray Resonance Exchange Scattering*. Phys. Rev. Lett., **61** (1988), 1245.
- [74] P. Hansmann, T. Ayrál, L. Vaugier, P. Werner, and S. Biermann. *Long-Range Coulomb Interactions in Surface Systems: A First-Principles Description within Self-Consistently Combined GW and Dynamical Mean-Field Theory*. Phys. Rev. Lett., **110** (2013), 166401.
- [75] H. Hasegawa. *Electronic structures and surface magnetism of Cr (100) at finite temperatures*. Journal of Physics F: Metal Physics, **16** (1986), 1555.
- [76] K. Haule. *Quantum Monte Carlo impurity solver for cluster dynamical mean-field theory and electronic structure calculations with adjustable cluster base*. Phys. Rev. B, **75** (2007), 155113.
- [77] W. Heisenberg. *Zur Theorie des Ferromagnetismus*. Z. Physik, **49** (1928), 619.

- 
- [78] K. Held, G. Keller, V. Eyert, D. Vollhardt, and V. I. Anisimov. *Mott-Hubbard Metal-Insulator Transition in Paramagnetic  $V_2O_3$ : An LDA + DMFT(QMC) Study*. Phys. Rev. Lett., **86** (2001), 5345.
- [79] K. Held, A. K. McMahan, and R. T. Scalettar. *Cerium Volume Collapse: Results from the Merger of Dynamical Mean-Field Theory and Local Density Approximation*. Phys. Rev. Lett., **87** (2001), 276404.
- [80] I. F. Herbut. *Interactions and Phase Transitions on Graphene's Honeycomb Lattice*. Phys. Rev. Lett., **97** (2006), 146401.
- [81] A. C. Hewson. *The Kondo problem to heavy fermions*. Cambridge studies in magnetism ; 2. Cambridge Univ. Press. ISBN 0-521-36382-9. XXI, 436 S : Ill., graph. Darst (1993).
- [82] C. F. Hirjibehedin, C. P. Lutz, and A. J. Heinrich. *Spin Coupling in Engineered Atomic Structures*. Science, **312** (2006), 1021.
- [83] J. E. Hirsch. *Discrete Hubbard-Stratonovich transformation for fermion lattice models*. Phys. Rev. B, **28** (1983), 4059.
- [84] J. E. Hirsch. *Two-dimensional Hubbard model: Numerical simulation study*. Phys. Rev. B, **31** (1985), 4403.
- [85] J. E. Hirsch. *Charge-Density-Wave to Spin-Density-Wave Transition in the Extended Hubbard Model*. Phys. Rev. Lett., **53** (1984), 2327.
- [86] P. Hohenberg and W. Kohn. *Inhomogeneous Electron Gas*. Phys. Rev., **136** (1964), B864.
- [87] C. Honerkamp. *Density Waves and Cooper Pairing on the Honeycomb Lattice*. Phys. Rev. Lett., **100** (2008), 146404.
- [88] L. Huang, T. Ayrál, S. Biermann, and P. Werner. *Extended dynamical mean-field study of the Hubbard model with long-range interactions*. Phys. Rev. B, **90** (2014), 195114.
- [89] J. Hubbard. *Electron Correlations in Narrow Energy Bands*. Proc. R. Soc. Lond. A, **276** (1963), 238.
- [90] M. Imada, A. Fujimori, and Y. Tokura. *Metal-insulator transitions*. Rev. Mod. Phys., **70** (1998), 1039.
- [91] D. Jacob, K. Haule, and G. Kotliar. *Kondo Effect and Conductance of Nanocontacts with Magnetic Impurities*. Phys. Rev. Lett., **103** (2009), 016803.
- [92] Jarrell, Mark. *Maximum Entropy Method*. In Pavarini, Eva and Koch, Erik and Anders, Frithjof and Jarrell, Mark, editor, *Correlated electrons: from models to*

- materials*, Schriften des Forschungszentrums Jülich. Reihe Modeling and simulation. Forschungszentrum Jülich GmbH, Institute for Advanced Simulation (2012).
- [93] R. O. Jones and O. Gunnarsson. *The density functional formalism, its applications and prospects*. Rev. Mod. Phys., **61** (1989), 689.
- [94] J. Jung and A. H. MacDonald. *Enhancement of nonlocal exchange near isolated band crossings in graphene*. Phys. Rev. B, **84** (2011), 085446.
- [95] A. A. Kananenka, E. Gull, and D. Zgid. *Systematically improvable multiscale solver for correlated electron systems*. Phys. Rev. B, **91** (2015), 121111.
- [96] M. Karolak. *Electronic Correlation Effects in Transition Metal Systems : From Bulk Crystals to Nanostructures*. Ph.D. thesis, University of Hamburg (2013).
- [97] M. Karolak, G. Ulm, T. Wehling, V. Mazurenko, A. Poteryaev, and A. Lichtenstein. *Double counting in LDA + DMFT-The example of NiO*. Journal of Electron Spectroscopy and Related Phenomena, **181** (2010), 11.
- [98] M. Karolak, T. O. Wehling, F. Lechermann, and A. I. Lichtenstein. *General DFT + + method implemented with projector augmented waves: electronic structure of SrVO<sub>3</sub> and the Mott transition in Ca<sub>2-x</sub>Sr<sub>x</sub>RuO<sub>4</sub>*. J. Phys.: Condens. Matter, **23** (2011), 085601.
- [99] M. I. Katsnelson. *Graphene: Carbon in Two Dimensions*. Cambridge University Press, 1 edition. ISBN 0-521-19540-3 (2012).
- [100] A. A. Khajetoorians, M. Valentyuk, M. Steinbrecher, T. Schlenk, A. Shick, J. Kolorenc, A. I. Lichtenstein, T. O. Wehling, R. Wiesendanger, and J. Wiebe. *Tuning emergent magnetism in a Hund's impurity*. Nature Nanotechnology, **10** (2015), 958.
- [101] L. E. Klebanoff, S. W. Robey, G. Liu, and D. A. Shirley. *Observation of a surface magnetic phase transition on Cr(100)*. Phys. Rev. B, **30** (1984), 1048.
- [102] L. E. Klebanoff, S. W. Robey, G. Liu, and D. A. Shirley. *Investigation of the near-surface electronic structure of Cr(001)*. Phys. Rev. B, **31** (1985), 6379.
- [103] L. E. Klebanoff, R. H. Victora, L. M. Falicov, and D. A. Shirley. *Experimental and theoretical investigations of Cr(001) surface electronic structure*. Phys. Rev. B, **32** (1985), 1997.
- [104] G. Knizia and G. K.-L. Chan. *Density Matrix Embedding: A Strong-Coupling Quantum Embedding Theory*. J. Chem. Theory Comput., **9** (2013), 1428.
- [105] G. Knizia and G. K.-L. Chan. *Density Matrix Embedding: A Simple Alternative to Dynamical Mean-Field Theory*. Phys. Rev. Lett., **109** (2012), 186404.

- 
- [106] Koch, Erik. *The Lanczos Method*. In Pavarini, Eva and Koch, Erik and Coleman, Piers, editor, *Many-Body Physics: From Kondo to Hubbard*, Schriften des Forschungszentrums Jülich. Reihe Modeling and simulation. Forschungszentrum Jülich GmbH, Institute for Advanced Simulation (2015).
- [107] W. Kohn and L. J. Sham. *Self-Consistent Equations Including Exchange and Correlation Effects*. Phys. Rev., **140** (1965), A1133.
- [108] A. Kokalj. *Computer graphics and graphical user interfaces as tools in simulations of matter at the atomic scale*. Comp. Mat. Sci., **28** (2003), 155.
- [109] O. Y. Kolesnychenko, R. de Kort, M. I. Katsnelson, A. I. Lichtenstein, and H. van Kempen. *Real-space imaging of an orbital Kondo resonance on the Cr(001) surface*. Nature, **415** (2002), 507.
- [110] O. Y. Kolesnychenko, G. M. M. Heijnen, A. K. Zhuravlev, R. de Kort, M. I. Katsnelson, A. I. Lichtenstein, and H. van Kempen. *Surface electronic structure of Cr(001): Experiment and theory*. Phys. Rev. B, **72** (2005), 085456.
- [111] J. Kondo. *Resistance Minimum in Dilute Magnetic Alloys*. Progress of Theoretical Physics, **32** (1964), 37.
- [112] T. Kotani. *Ab initio random-phase-approximation calculation of the frequency-dependent effective interaction between 3d electrons: Ni, Fe, and MnO*. J. Phys.: Condens. Matter, **12** (2000), 2413.
- [113] G. Kotliar, S. Y. Savrasov, K. Haule, V. S. Oudovenko, O. Parcollet, and C. A. Marianetti. *Electronic structure calculations with dynamical mean-field theory*. Rev. Mod. Phys., **78** (2006), 865.
- [114] G. Kotliar and D. Vollhardt. *Strongly correlated materials: Insights from dynamical mean-field theory*. Physics Today, **57** (2004), 53.
- [115] V. N. Kotov, B. Uchoa, V. M. Pereira, F. Guinea, and A. H. Castro Neto. *Electron-Electron Interactions in Graphene: Current Status and Perspectives*. Rev. Mod. Phys., **84** (2012), 1067.
- [116] L. Kouwenhoven and L. Glazman. *Revival of the Kondo effect*. Physics world, **14** (2001), 33.
- [117] D. Kraft. *A software package for sequential quadratic programming*. DFVLR Köln, Germany (1988).
- [118] W. Krauth. *Statistical Mechanics : Algorithms and Computations*. Oxford Master Series in Physics. Oxford University Press, UK, Oxford. ISBN 978-0-19-851535-7 (2006).

- [119] G. Kresse and D. Joubert. *From ultrasoft pseudopotentials to the projector augmented-wave method*. Phys. Rev. B, **59** (1999), 1758.
- [120] H. R. Krishna-murthy, J. W. Wilkins, and K. G. Wilson. *Renormalization-group approach to the Anderson model of dilute magnetic alloys. I. Static properties for the symmetric case*. Phys. Rev. B, **21** (1980), 1003.
- [121] A. N. Krylov. -. *Izv. Akad. Nauk SSSR, Otd. Mat. Estest.*, **7** (1931).
- [122] J. Kügel, M. Karolak, J. Senkpiel, P.-J. Hsu, G. Sangiovanni, and M. Bode. *Relevance of Hybridization and Filling of 3d Orbitals for the Kondo Effect in Transition Metal Phthalocyanines*. Nano Letters, **14** (2014), 3895.
- [123] Lanczos, Cornelius. *An iteration method for the solution of the eigenvalue problem of linear differential and integral operators*. J. Res. Nat'l Bur. Std, **45** (1950), 225.
- [124] D. P. Landau and K. Binder. *A Guide to Monte Carlo Simulations in Statistical Physics*. Cambridge University Press, Cambridge. ISBN 978-0-521-65314-5 (2000).
- [125] F. Lechermann, S. Biermann, and A. Georges. *Importance of Interorbital Charge Transfers for the Metal-to-Insulator Transition of  $BaVS_3$* . Phys. Rev. Lett., **94** (2005), 166402.
- [126] F. Lechermann and M. Obermeyer. *Towards Mott design by  $\delta$ -doping of strongly correlated titanates*. New Journal of Physics, **17** (2015), 043026.
- [127] R. B. Lehoucq, D. C. Sorensen, and C. Yang. *ARPACK Users' Guide: Solution of Large-scale Eigenvalue Problems with Implicitly Restarted Arnoldi Methods*. SIAM. ISBN 978-0-89871-407-4 (1998).
- [128] S. Lem. *Die Stimme des Herrn*. Volk und Welt (1983).
- [129] S. Lem. *His Master's Voice*. Mandarin, London. ISBN 978-0-7493-0490-4 (1990).
- [130] S. Lem. *Głos Pana*. Wydawn. Literackie, Kraków. ISBN 978-83-08-03318-0 (2002).
- [131] M.-A. Leroy, A. M. Bataille, F. Bertran, P. Le Fèvre, A. Taleb-Ibrahimi, and S. Andrieu. *Electronic structure of the Cr(001) surface and Cr/MgO interface*. Phys. Rev. B, **88** (2013), 205134.
- [132] Y. Li, J. He, X. Kong, and S.-P. Kou. *Vacancy-induced intrinsic magnetic impurity with quasilocalized spin moment in graphene*. Phys. Rev. B, **90** (2014), 201406.
- [133] A. I. Lichtenstein and M. I. Katsnelson. *Ab initio calculations of quasiparticle band structure in correlated systems: LDA++ approach*. Phys. Rev. B, **57** (1998), 6884.

- 
- [134] A. I. Lichtenstein, M. I. Katsnelson, and G. Kotliar. *Finite-Temperature Magnetism of Transition Metals: An ab initio Dynamical Mean-Field Theory*. Phys. Rev. Lett., **87** (2001), 067205.
- [135] E. H. Lieb and F. Y. Wu. *The one-dimensional Hubbard model: a reminiscence*. Physica A: Statistical Mechanics and its Applications, **321** (2003), 1.
- [136] E. H. Lieb and F. Y. Wu. *Absence of Mott Transition in an Exact Solution of the Short-Range, One-Band Model in One Dimension*. Phys. Rev. Lett., **20** (1968), 1445.
- [137] A. I. Liechtenstein, V. I. Anisimov, and J. Zaanen. *Density-functional theory and strong interactions: Orbital ordering in Mott-Hubbard insulators*. Phys. Rev. B, **52** (1995), R5467.
- [138] L. R. F. Lima and C. H. Lewenkopf. *Disorder-assisted transmission due to charge puddles in monolayer graphene: Transmission enhancement and local currents*. Phys. Rev. B, **93** (2016), 045404.
- [139] C. Lin and A. A. Demkov. *Efficient variational approach to the impurity problem and its application to the dynamical mean-field theory*. Phys. Rev. B, **88** (2013), 035123.
- [140] H. Q. Lin, J. E. Hirsch, and D. J. Scalapino. *Pairing in the two-dimensional Hubbard model: An exact diagonalization study*. Phys. Rev. B, **37** (1988), 7359.
- [141] Y. Lu, M. Höppner, O. Gunnarsson, and M. W. Haverkort. *Efficient real-frequency solver for dynamical mean-field theory*. Phys. Rev. B, **90** (2014), 085102.
- [142] B. I. Lundqvist. *Some Numerical Results on Quasiparticle Properties in the Electron Gas*. physica status solidi (b), **32** (1969), 273.
- [143] A. M. Läuchli and P. Werner. *Krylov implementation of the hybridization expansion impurity solver and application to 5-orbital models*. Phys. Rev. B, **80** (2009), 235117.
- [144] M. P. López-Sancho, F. de Juan, and M. A. H. Vozmediano. *Magnetic moments in the presence of topological defects in graphene*. Phys. Rev. B, **79** (2009), 075413.
- [145] G. D. Mahan. *Many-Particle Physics*. Springer Science & Business Media. ISBN 978-1-4757-5714-9 (2013).
- [146] R. M. Martin. *Electronic Structure: Basic Theory and Practical Methods*. Cambridge University Press. ISBN 978-0-521-78285-2 (2004).
- [147] N. Marzari and D. Vanderbilt. *Maximally localized generalized Wannier functions for composite energy bands*. Phys. Rev. B, **56** (1997), 12847.

- [148] S. Matsuo and I. Nishida. *Magnetic Properties of a New Magnetic Phase in Fine bcc Chromium Particles Prepared by Gas Evaporation Method*. Journal of the Physical Society of Japan, **49** (1980), 1005.
- [149] A. K. McMahan, R. M. Martin, and S. Satpathy. *Calculated effective Hamiltonian for  $La_2CuO_4$  and solution in the impurity Anderson approximation*. Phys. Rev. B, **38** (1988), 6650.
- [150] Z. Y. Meng, T. C. Lang, S. Wessel, F. F. Assaad, and A. Muramatsu. *Quantum spin liquid emerging in two-dimensional correlated Dirac fermions*. Nature, **464** (2010), 847.
- [151] N. Metropolis, A. W. Rosenbluth, M. N. Rosenbluth, A. H. Teller, and E. Teller. *Equation of State Calculations by Fast Computing Machines*. The Journal of Chemical Physics, **21** (1953), 1087.
- [152] W. Metzner and D. Vollhardt. *Correlated Lattice Fermions in  $d = \infty$  Dimensions*. Phys. Rev. Lett., **62** (1989), 324.
- [153] C. Michael. *Fast heat-bath algorithm for the Ising model*. Phys. Rev. B, **33** (1986), 7861.
- [154] A. S. Mishchenko, N. V. Prokof'ev, A. Sakamoto, and B. V. Svistunov. *Diagrammatic quantum Monte Carlo study of the Fröhlich polaron*. Phys. Rev. B, **62** (2000), 6317.
- [155] Mishchenko, A S. *Stochastic Optimization Method for Analytic Continuation*. In Pavarini, Eva and Koch, Erik and Anders, Frithjof and Jarrell, Mark, editor, *Correlated electrons: from models to materials*, Schriften des Forschungszentrums Jülich. Reihe Modeling and simulation. Forschungszentrum Jülich GmbH, Institute for Advanced Simulation (2012).
- [156] E. Müller-Hartmann. *Correlated fermions on a lattice in high dimensions*. Zeitschrift für Physik B Condensed Matter, **74** (1989), 507.
- [157] K. Nakamura, R. Arita, Y. Yoshimoto, and S. Tsuneyuki. *First-principles calculation of effective onsite Coulomb interactions of 3d transition metals: Constrained local density functional approach with maximally localized Wannier functions*. Phys. Rev. B, **74** (2006), 235113.
- [158] J. A. Nelder and R. Mead. *A Simplex Method for Function Minimization*. The Computer Journal, **7** (1965), 308.
- [159] M. E. J. Newman and G. T. Barkema. *Monte Carlo Methods in Statistical Physics*. Oxford University Press, Oxford. ISBN 978-0-19-851797-9 (1999).
- [160] Nicolaus Parragh. *Strongly Correlated Multi-Orbital Systems, A Continuous-Time Quantum Monte Carlo Analysis*. Ph.D. thesis, University of Würzburg (2013).

- 
- [161] T. Niu and A. Li. *From two-dimensional materials to heterostructures*. Progress in Surface Science, **90** (2015), 21.
- [162] W. Nolting. *Grundkurs Theoretische Physik 5/2 Quantenmechanik - Methoden und Anwendungen*. Springer-Lehrbuch. DOI: 10.1007/978-3-540-47616-0 (2006).
- [163] W. Nolting. *Grundkurs Theoretische Physik 5/1*. Springer Berlin Heidelberg, Berlin, Heidelberg. ISBN 978-3-540-68868-6 (2009).
- [164] Y. Nomura, M. Kaltak, K. Nakamura, C. Taranto, S. Sakai, A. Toschi, R. Arita, K. Held, G. Kresse, and M. Imada. *Effective on-site interaction for dynamical mean-field theory*. Phys. Rev. B, **86** (2012), 085117.
- [165] N. Néel, J. Kröger, R. Berndt, T. O. Wehling, A. I. Lichtenstein, and M. I. Katsnelson. *Controlling the Kondo Effect in  $\text{CoCu}_n$  Clusters Atom by Atom*. Phys. Rev. Lett., **101** (2008), 266803.
- [166] K. Ohno. *Some remarks on the Pariser-Parr-Pople method*. Theoret. Chim. Acta, **2** (1964), 219.
- [167] R. Pariser and R. G. Parr. *A Semi-Empirical Theory of the Electronic Spectra and Electronic Structure of Complex Unsaturated Molecules. II*. The Journal of Chemical Physics, **21** (1953), 767.
- [168] N. Parragh, A. Toschi, K. Held, and G. Sangiovanni. *Conserved quantities of  $SU(2)$ -invariant interactions for correlated fermions and the advantages for quantum Monte Carlo simulations*. Phys. Rev. B, **86** (2012), 155158.
- [169] Pavarini, Eva. *The LDA+DMFT Approach*. In Pavarini, Eva and Koch, Erik and Vollhardt, Dieter and Lichtenstein, Alexander, editor, *The LDA+DMFT approach to strongly correlated materials: lecture notes of the autumn school 2011*, Schriften des Forschungszentrums Jülich. Reihe Modeling and simulation. Forschungszentrum Jülich GmbH, Institute for Advanced Simulation (2011).
- [170] T. G. Pedersen. *Self-consistent model of edge doping in graphene*. Phys. Rev. B, **91** (2015), 085428.
- [171] R. E. Peierls. Phys. Rev., **54** (1938), 918.
- [172] J. P. Perdew, K. Burke, and M. Ernzerhof. *Generalized Gradient Approximation Made Simple*. Phys. Rev. Lett., **77** (1996), 3865.
- [173] J. P. Perdew and Y. Wang. *Accurate and simple analytic representation of the electron-gas correlation energy*. Phys. Rev. B, **45** (1992), 13244.

- [174] C. A. Perroni, H. Ishida, and A. Liebsch. *Exact diagonalization dynamical mean-field theory for multiband materials: Effect of Coulomb correlations on the Fermi surface of  $Na_{0.3}CoO_2$* . Phys. Rev. B, **75** (2007), 045125.
- [175] K. Pesz and R. W. Munn. *Densities of states and anisotropy in tight-binding models*. J. Phys. C: Solid State Phys., **19** (1986), 2499.
- [176] R. Piasecki. *Density of electron states in a rectangular lattice under uniaxial stress*. arXiv:0804.1037 [cond-mat], (2008). ArXiv: 0804.1037.
- [177] J. Pople. *Electron interaction in unsaturated hydrocarbons*. Transactions of the Faraday Society, **49** (1953), 1375.
- [178] M. Potthoff, M. Aichhorn, and C. Dahnken. *Variational Cluster Approach to Correlated Electron Systems in Low Dimensions*. Phys. Rev. Lett., **91** (2003), 206402.
- [179] H. Prüser, M. Wenderoth, P. E. Dargel, A. Weismann, R. Peters, T. Pruschke, and R. G. Ulbrich. *Long-range Kondo signature of a single magnetic impurity*. Nature Physics, **7** (2011), 203.
- [180] Ö. Rapp, G. Benediktsson, H. U. Åström, S. Arajs, and K. V. Rao. *Electrical resistivity of antiferromagnetic chromium near the Néel temperature*. Physical Review B, **18** (1978), 3665.
- [181] T. Ribic, E. Assmann, A. Tóth, and K. Held. *Cubic interaction parameters for  $t_{2g}$  Wannier orbitals*. Phys. Rev. B, **90** (2014), 165105.
- [182] A. Rieder. *Keine Probleme mit inversen Problemen: eine Einführung in ihre stabile Lösung*. Vieweg, Wiesbaden, 1 edition. ISBN 3528031980 and 9783528031985. XIV, 300 S. : Ill., graph. Darst. (2003).
- [183] R. G. Ross and W. Hume-Rothery. *High temperature X-ray metallography*. Journal of the Less Common Metals, **5** (1963), 258.
- [184] D. Rost, F. Assaad, and N. Blümer. *Quasi-continuous-time impurity solver for the dynamical mean-field theory with linear scaling in the inverse temperature*. Phys. Rev. E, **87** (2013), 053305.
- [185] A. N. Rubtsov, V. V. Savkin, and A. I. Lichtenstein. *Continuous-time quantum Monte Carlo method for fermions*. Phys. Rev. B, **72** (2005), 035122.
- [186] A. W. Sandvik. *Stochastic method for analytic continuation of quantum Monte Carlo data*. Phys. Rev. B, **57** (1998), 10287.

- 
- [187] G. Sangiovanni, A. Toschi, E. Koch, K. Held, M. Capone, C. Castellani, O. Gunnarsson, S.-K. Mo, J. W. Allen, H.-D. Kim, A. Sekiyama, A. Yamasaki, S. Suga, and P. Metcalf. *Static versus dynamical mean-field theory of Mott antiferromagnets*. Phys. Rev. B, **73** (2006), 205121.
- [188] R. R. d. Santos. *Introduction to quantum Monte Carlo simulations for fermionic systems*. Brazilian Journal of Physics, **33** (2003), 36.
- [189] E. Şaşıoğlu, C. Friedrich, and S. Blügel. *Effective Coulomb interaction in transition metals from constrained random-phase approximation*. Phys. Rev. B, **83** (2011), 121101.
- [190] E. Şaşıoğlu, C. Friedrich, and S. Blügel. *Strength of the Effective Coulomb Interaction at Metal and Insulator Surfaces*. Phys. Rev. Lett., **109** (2012), 146401.
- [191] A. Savitzky and M. J. E. Golay. *Smoothing and Differentiation of Data by Simplified Least Squares Procedures*. Anal. Chem., **36** (1964), 1627.
- [192] R. T. Scalettar, E. Y. Loh, J. E. Gubernatis, A. Moreo, S. R. White, D. J. Scalapino, R. L. Sugar, and E. Dagotto. *Phase diagram of the two-dimensional negative-  $U$  Hubbard model*. Physical Review Letters, **62** (1989), 1407.
- [193] M. M. Scherer, S. Uebelacker, D. D. Scherer, and C. Honerkamp. *Interacting electrons on trilayer honeycomb lattices*. Phys. Rev. B, **86** (2012), 155415.
- [194] J. R. Schrieffer and J. S. Brooks. *Handbook of high-temperature superconductivity*. Springer Science+ Business Media, LLC (2007).
- [195] J. R. Schrieffer and P. A. Wolff. *Relation between the Anderson and Kondo Hamiltonians*. Phys. Rev., **149** (1966), 491.
- [196] H. J. Schulz. *Correlation exponents and the metal-insulator transition in the one-dimensional Hubbard model*. Phys. Rev. Lett., **64** (1990), 2831.
- [197] M. Schüler. *Tight-Binding-Modellierung von magnetischen Störstellen in Metallen*. Master Thesis, University of Bremen (2012).
- [198] P. Seth, P. Hansmann, A. van Roekeghem, L. Vaugier, and S. Biermann. *Towards a first-principles determination of effective Coulomb interactions in correlated electron materials: Role of intershell interactions*. arXiv:1508.07466 [cond-mat], (2015). ArXiv: 1508.07466.
- [199] H. Shinaoka, M. Troyer, and P. Werner. *Accuracy of downfolding based on the constrained random-phase approximation*. Phys. Rev. B, **91** (2015), 245156.
- [200] G. Shirane and W. J. Takei. *Neutron Diffraction Study of Chromium Single Crystals*. J. Phys. Soc. Japan, **Vol: 17: Suppl. B-III** (1962).

- [201] Q. Si, M. J. Rozenberg, G. Kotliar, and A. E. Ruckenstein. *Correlation induced insulator to metal transitions*. Phys. Rev. Lett., **72** (1994), 2761.
- [202] M. Singh, C. S. Wang, and J. Callaway. *Spin-orbit coupling, Fermi surface, and optical conductivity of ferromagnetic iron*. Phys. Rev. B, **11** (1975), 287.
- [203] J. Skilling. *Maximum Entropy and Bayesian Methods: Cambridge, England, 1988*. Springer Science & Business Media. ISBN 978-94-015-7860-8 (2013).
- [204] J. Skilling and R. K. Bryan. *Maximum entropy image reconstruction: general algorithm*. MNRAS, **211** (1984), 111.
- [205] J. C. Slater. *Quantum theory of atomic structure*, volume 1. McGraw-Hill New York (1960).
- [206] Z. G. Soos, S. Ramasesha, and D. S. Galvão. *Band to correlated crossover in alternating Hubbard and Pariser-Parr-Pople chains: Nature of the lowest singlet excitation of conjugated polymers*. Phys. Rev. Lett., **71** (1993), 1609.
- [207] I. Souza, N. Marzari, and D. Vanderbilt. *Maximally localized Wannier functions for entangled energy bands*. Phys. Rev. B, **65** (2001), 035109.
- [208] M. Springer and F. Aryasetiawan. *Frequency-dependent screened interaction in Ni within the random-phase approximation*. Phys. Rev. B, **57** (1998), 4364.
- [209] J. A. Strosio, D. T. Pierce, A. Davies, R. J. Celotta, and M. Weinert. *Tunneling Spectroscopy of bcc (001) Surface States*. Phys. Rev. Lett., **75** (1995), 2960.
- [210] B. Surer, M. Troyer, P. Werner, T. O. Wehling, A. M. Läuchli, A. Wilhelm, and A. I. Lichtenstein. *Multiorbital Kondo physics of Co in Cu hosts*. Phys. Rev. B, **85** (2012), 085114.
- [211] K. Szałowski. *Ground-state magnetic phase diagram of bow-tie graphene nanoflakes in external magnetic field*. Journal of Applied Physics, **114** (2013), 243908.
- [212] K. Szałowski. *Electric field control of the indirect magnetic coupling through a short graphene nanoribbon*. Phys. Rev. B, **90** (2014), 085410.
- [213] D. Sénéchal. *Bath optimization in the cellular dynamical mean-field theory*. Phys. Rev. B, **81** (2010), 235125.
- [214] H.-K. Tang, E. Laksono, J. Rodrigues, P. Sengupta, F. Assaad, and S. Adam. *Interaction-Driven Metal-Insulator Transition in Strained Graphene*. Phys. Rev. Lett., **115** (2015), 186602.

- 
- [215] C. Taranto, M. Kaltak, N. Parragh, G. Sangiovanni, G. Kresse, A. Toschi, and K. Held. *Comparing quasiparticle GW+DMFT and LDA+DMFT for the test bed material SrVO<sub>3</sub>*. Phys. Rev. B, **88** (2013), 165119.
- [216] B. T. Thole, P. Carra, F. Sette, and G. van der Laan. *X-ray circular dichroism as a probe of orbital magnetization*. Phys. Rev. Lett., **68** (1992), 1943.
- [217] J. M. Tomczak and S. Biermann. *Optical properties of correlated materials – Or why intelligent windows may look dirty*. physica status solidi (b), **246** (2009), 1996.
- [218] A.-M. S. Tremblay. *Two-Particle-Self-Consistent Approach for the Hubbard Model*. arXiv:1107.1534 [cond-mat], **171** (2012), 409. ArXiv: 1107.1534.
- [219] unknown. *The Monte Carlo method*. Published: Homepage Online <http://quest.ucdavis.edu/tutorial/mcrev2.pdf> 08 20 2015. (2015).
- [220] A. Valli, G. Sangiovanni, O. Gunnarsson, A. Toschi, and K. Held. *Dynamical Vertex Approximation for Nanoscopic Systems*. Phys. Rev. Lett., **104** (2010), 246402.
- [221] E. G. C. P. van Loon, A. I. Lichtenstein, M. I. Katsnelson, O. Parcollet, and H. Hafermann. *Beyond extended dynamical mean-field theory: Dual boson approach to the two-dimensional extended Hubbard model*. Phys. Rev. B, **90** (2014), 235135.
- [222] C. M. Varma and Y. Yafet. *Magnetic susceptibility of mixed-valence rare-earth compounds*. Phys. Rev. B, **13** (1976), 2950.
- [223] T. O. Wehling, A. V. Balatsky, M. I. Katsnelson, A. I. Lichtenstein, and A. Rosch. *Orbitally controlled Kondo effect of Co adatoms on graphene*. Phys. Rev. B, **81** (2010), 115427.
- [224] T. O. Wehling, E. Şaşıoğlu, C. Friedrich, A. I. Lichtenstein, M. I. Katsnelson, and S. Blügel. *Strength of Effective Coulomb Interactions in Graphene and Graphite*. Phys. Rev. Lett., **106** (2011), 236805.
- [225] P. Werner, A. Comanac, L. de’ Medici, M. Troyer, and A. J. Millis. *Continuous-Time Solver for Quantum Impurity Models*. Phys. Rev. Lett., **97** (2006), 076405.
- [226] P. Werner and A. J. Millis. *Hybridization expansion impurity solver: General formulation and application to Kondo lattice and two-orbital models*. Phys. Rev. B, **74** (2006), 155107.
- [227] S. R. White, D. J. Scalapino, R. L. Sugar, N. E. Bickers, and R. T. Scalettar. *Attractive and repulsive pairing interaction vertices for the two-dimensional Hubbard model*. Phys. Rev. B, **39** (1989), 839.
- [228] E. Wigner. *On the Interaction of Electrons in Metals*. Phys. Rev., **46** (1934), 1002.

- [229] O. V. Yazyev. *Emergence of magnetism in graphene materials and nanostructures*. Reports on Progress in Physics, **73** (2010), 056501.
- [230] Z. Bai, W. Chen, R.T. Scalettar, I. Yamazaki. *Numerical methods for quantum Monte Carlo simulations of the Hubbard model*. In *Multi-Scale Phenomena in Complex Fluids : Modeling, Analysis and Numerical Simulations*, number 12 in Series in Contemporary Applied Mathematics, pages 1–110. World Scientific, Singapore (2009).
- [231] D. Zgid, E. Gull, and G. K.-L. Chan. *Truncated configuration interaction expansions as solvers for correlated quantum impurity models and dynamical mean-field theory*. Phys. Rev. B, **86** (2012), 165128.
- [232] B.-X. Zheng and G. K.-L. Chan. *Ground-state phase diagram of the square lattice Hubbard model from density matrix embedding theory*. Phys. Rev. B, **93** (2016), 035126.
- [233] M. B. Zöfl, I. A. Nekrasov, T. Pruschke, V. I. Anisimov, and J. Keller. *Spectral and Magnetic Properties of  $\alpha$ - and  $\gamma$ -Ce from Dynamical Mean-Field Theory and Local Density Approximation*. Phys. Rev. Lett., **87** (2001), 276403.

# Acknowledgments

Many people have contributed to this work. Here, I would like to thank hopefully all of them. I am indebted to Tim Wehling, who gave me the possibility to write this thesis and pushed me invaluablely by many discussions, inspirations, and a great working atmosphere. I thank Gerd Czycholl for an open door and ear throughout the thesis, Alexander Lichtenstein for many ideas and enthusiasm (not only for my photographic skills), and Mikhail Katsnelson for inspiration.

I thank all of the working group in Bremen, not only for a great scientific environment, but also for all the essential distractions from physics. In particular, I would like to thank Daniel Mourad for sharing his vast knowledge, Stefan Barthel for Fortran and VASP expertise, Christian Renk for his code developments and those certain sailing chats, and my long-term office mate Malte Rösner; sharing this long way certainly made it easier and more fun. I thank Babak Vosughian for the inherited office flowers, which should have received more attention. I would like to thank Sarah Farley and Ania Mohammadi for helping with the administrative problems of the academic life. I also thank Klaus Bowe and Andreas Beuthner for taming the hardware and software at the ITP.

I thank Sandra Gardonio for the courtesy of sharing her ‘archaeological’ data and her patience. I thank Erik van Loon for giving me a different view on renormalizations in the Hubbard model. I had a lovely time in Würzburg at the group of Giorgio Sangiovanni; thank you for your hospitality. I especially thank Giorgio, Michael Karolak, Andi Hausoel and Nico Parragh for support with w2dynamics and much more.

I thank my family, Hanna, Peter, and Lennart, for all their diverse support. I express my special gratitude to Sarah, who brightens my day each and every time.

I greatly acknowledge financial support by the Simons foundation, the DFG via FOR 1346, and the DPG via the WE-Heraeus-Förderprogramm, which made visits of many workshops, schools, and conferences possible.